

Raman Sideband Cooling

$^{171}\text{Yb}^+$ Across Zeeman

Sub-levels

Jordan Raymond Scarabel

Bachelor of Photonics and Nanoscience (with Honours)

School of Environment and Science

Centre for Quantum Dynamics

Griffith University

Submitted in fulfilment of the requirements of the degree of

Doctor of Philosophy

July 11, 2022

Abstract

This thesis presents two demonstrations of Zeeman sub-level Raman sideband transitions on trapped $^{171}\text{Yb}^+$ ions that are to be used for the demonstration of a proof-of-concept quantum spin-heat engine (SHE)[1]. This Raman transition scheme has previously not been demonstrated on any $I = 1/2$ ion and relies on a single continuous wave (CW) laser and two acousto-optic modulators (AOMs) making it relatively cheap and easy to set up compared to other methods involving exotic pulsed lasers[2, 3] or complex optical setups[4, 5]. Using these novel transitions, I have demonstrated Raman sideband cooling below the Doppler limit on the two most strongly coupled modes of a trapped ion's motion and have shown good agreement with the theory for light-motion coupling of bound atoms.

I also developed methods and prepared control systems to realise a high fidelity single trapped ion qubit. Average qubit measurement fidelities around 99.5% were routinely measured, with single qubit operation fidelities estimated at $\sim 99.99\%$ and qubit initialisation fidelities estimated at $\sim 99.9999\%$. The qubit is based on the $^2\text{S}_{1/2}$ ground state hyperfine clock transition with a measured T_2 coherence time of 4.72(13) ms that is coherently driven by resonant microwaves at a maximum measured Rabi rate of 408.88(8) kHz.

Lastly, I perform an in depth frequency stability analysis of a 399 nm laser locked to the $^1\text{S}_0 \leftrightarrow ^1\text{P}_0$ transition in neutral ytterbium via the polarization enhanced absorption spectroscopy (POLEAS) technique. This locking technique is used for the required excitation of neutral ytterbium in the two-

photon isotope-selective ionization technique used in this ion trap research to generate isotopically pure $^{171}\text{Yb}^+$ or $^{174}\text{Yb}^+$ ions.

Statement of Originality

This work has not previously been submitted for a degree or diploma in any university. To the best of my knowledge and belief, the thesis contains no material previously published or written by another person except where due reference is made in the thesis itself.

A handwritten signature in black ink, appearing to read "J. Scarabel".

Jordan Scarabel

Thank you Mum, Dad, Sheree, Nicole, Kael, Ruby, Nanni, Nonno, Grandma, Poppy, Tim and Dan, my loving family for all your support.

Thank you Steven, Valdis, Moji, Marcin, Liz, Mark, you taught me how to actually do experimental work in a lab.

Thank you Alex, Kenji, Michael, Rose and Liam, my peers who have been a joy to work alongside.

Thank you to my supervisors;

Erik, your deep and wide understanding of experimental research has been instrumental and your advice has been invaluable in this research.

Mirko, you have been a great role model, teaching and instilling good scientific practices into my research.

Nora, thank you for coming on board late in the game.

Lastly, thank you to all my friends in and around Brisbane who have supported me through these years.

Contents

1	Introduction	15
1.1	Thesis Overview	16
1.2	Semantics	17
1.2.1	Uncertainties	17
1.2.2	Atomic states	17
2	Literature Review	18
2.1	Early ion trapping	18
2.2	Trapped ions for quantum computing	20
2.3	$^{171}\text{Yb}^+$ Raman transition demonstrations	25
2.4	Trapped ion heat engine demonstrations	30
3	Theory	37
3.1	Trapped Ion Motion	37
3.1.1	Mathieu Equations of Trapped Ion Motion	38
3.1.2	Quantum Harmonic Oscillator	43
3.2	Hydrogen-like atoms	47
3.2.1	Fine Structure, Hyperfine Structure and Zeeman Shift .	48
3.2.2	The two-level atom	51
3.2.3	Electric Dipole Moment and External Fields	51
3.2.4	Spontaneous Emission and open quantum systems	56
3.2.5	The optical Bloch equations	58
3.3	Light-Motion Coupling	61

3.3.1	The Lamb-Dicke regime	62
3.3.2	Beyond the Lamb-Dicke regime	64
3.3.3	Spontaneous Emission's effect on motion	65
3.3.4	Doppler cooling	67
3.3.5	Raman Transitions	68
3.3.6	Resolved Motional Sideband Raman Transitions	70
3.4	Experimental considerations	72
3.4.1	Qubit dephasing from resonance fluctuations	72
3.4.2	Dark states	76
3.4.3	Selection rules and coupling coefficients	77
3.4.4	Beam polarisation and propagation axis	79
3.5	Application of theory to $^{171}\text{Yb}^+$	79
3.5.1	The closed cycle transition	81
3.5.2	Off-resonant excitation and leakage	84
3.6	Trapped ion qubit readout	87
3.6.1	Dark counts	88
3.6.2	State mixing	89
3.6.3	Binomial proportion confidence interval	92
4	Methods	94
4.1	Experiment hardware	96
4.1.1	Micro-fabricated surface electrode ion trap	96
4.1.2	Vacuum systems	100
4.1.3	Laser systems	101
4.1.4	Frequency references and laser stabilisation	105
4.2	Control, measurement protocols, and analysis	106
4.2.1	Qubit readout parameter optimisation	106
4.2.2	Single shot atomic state readout	109
4.2.3	Laser polarisation scan for optimising ion fluorescence . .	111
4.2.4	Optical pumping into $^2S_{1/2} F = 0$	113

4.2.5	Optical pumping into $^2S_{1/2} F = 1$ Zeeman sub-levels	114
4.2.6	Qubit characterisation	117
5	Raman Motional Sideband Cooling on Zeeman-split states	124
5.1	Motivation	127
5.2	Z-axis motion-coupled Raman transitions	128
5.2.1	Experiment protocol and results	130
5.3	Reconfiguration for 3D addressability	135
5.3.1	3D Raman sideband cooling	136
5.4	Reconfiguration for more pure transitions	141
5.4.1	Setup	143
5.4.2	Power instability	144
5.4.3	Motional resonances and trap strength	145
5.4.4	Zero light-shift resonance	151
5.4.5	Raman Sideband Cooling	151
5.5	Conclusions	153
6	Enhanced Spectroscopy Techniques with Ytterbium	154
6.1	Polarization Spectroscopy	164
6.2	Polarization Enhanced Absorption Spectroscopy	167
6.3	Stability analysis	169
6.3.1	Allan Deviations of stabilized laser frequency	172
7	Conclusion	176
7.1	Achievements	176
7.2	Outlook	177
A	Other publications	179
B	Calculations	205
B.1	Fluorescence distribution under state mixing	205
B.2	Electric dipole calculation	206

B.2.1	π -transitions	206
B.2.2	σ^+ -transitions	207
B.3	Detuned Ramsey unitary	208
B.4	Comprehensive master equation model for ${}^2S_{1/2} \leftrightarrow {}^2P_{1/2}$ system	209
B.5	Raman self-interference	212
C	Code	214
C.1	Ideal readout parameter estimation	214
C.2	Angular Momentum Coupling Coefficient Calculator	217
C.3	Laser power stabilization algorithm	220
C.4	Resonances Computed for Raman Thermometry	221
D	Microwave amplifier schematic	222

List of Figures

1.1	Number of published ion trap papers (1960-2020)	15
2.1	Brayton cycle heat engine implemented by Roßnagel et al.[74]	31
3.1	Mathieu equation a-q stability plot	41
3.2	Trapped ion's motion in 1D	42
3.3	Rod trap basic structure	42
3.4	Rabi model excited state population as a function of pulse area.	55
3.5	Optical Bloch equation solution spectra varying Ω .	61
3.6	Lamb-Dicke regime 2-level atom spectrum.	63
3.7	Light-motion coupling terms outside Lamb-Dicke regime.	65
3.8	Wavefunction illustration of light-motion coupling.	66
3.9	Doppler cooling temperature spectrum.	68
3.10	Qubit dephasing for different B-field noise spectra.	75
3.11	A Grotrian diagram of $^{171}\text{Yb}^+$	80
3.12	Clebsch-Gordon terms for $^{171}\text{Yb}^+ \ ^2S_{1/2} \leftrightarrow \ ^2P_{1/2}$	82
3.13	Theory curves for $^{171}\text{Yb}^+ \ ^2P_{1/2} \ F = 0$ population.	85
3.14	Count histogram example of trapped ion qubit readout.	89
3.15	Off-resonant mixing affecting count histograms.	92
3.16	Wilson score interval visualized.	93
4.1	Schematic of ion trap used in experiment.	96
4.2	Single sideband phase noise of used microwave source.	99
4.3	Diagram of vacuum system used in experiment.	101

4.4	Diagram of transitions addressed by lasers used in experiment.	101
4.5	Protocol for taking fluorescence measurements.	107
4.6	Saturation curve of $^{171}\text{Yb}^+$ $^2S_{1/2}$ $F = 1 \leftrightarrow ^2P_{1/2}$ $F = 0$	109
4.7	Experimental qubit readout count histograms.	110
4.8	Laser polarization vs. ion fluorescence scan.	112
4.9	$^2S_{1/2}$ $F = 0$ preparation pump-out curve.	113
4.10	$^2S_{1/2}$ $F = 1$ $m_F = +1$ preparation pump-out curve	116
4.11	$^2S_{1/2}$ $F = 0 \leftrightarrow ^2S_{1/2}$ $F = 1$ $m_F = +1$ Rabi oscillations	118
4.12	$^2S_{1/2}$ $F = 0 \leftrightarrow ^2S_{1/2}$ $F = 1$ $m_F = +1$ spectrum sweep.	119
4.13	Ramsey interferometry of microwave transitions.	122
5.1	$^2S_{1/2}$ $F = 1$ $m_F = 0 \leftrightarrow m_F = +1$ Raman transition diagram.	. .	128
5.2	Raman sideband cooling pulse pattern	130
5.3	Z-mode Raman transition spectrum and Rabi oscillations.	. . .	132
5.4	Raman transition Rabi rate vs. motional eigenstate	134
5.5	Raman spectrum after/before sideband cooling.	137
5.6	Raman transition Rabi oscillations after/before sideband cooling	140	
5.7	Cooling/heating rate estimate from temperature estimate.	. . .	140
5.8	$^2S_{1/2}$ $F = 1$ $m_F = +1 \leftrightarrow m_F = -1$ Raman transition diagram	. .	142
5.9	Comparison of the two Raman schemes' population dynamics.	. .	143
5.10	Optical setup of σ^+ reset beam and σ^- Raman beam.	144
5.11	Plots of Raman beams' laser power noise.	145
5.12	Raman spectra varying trapping voltage.	147
5.13	Trapped ion motional resonances vs trapping voltage amplitude.	148	
5.14	a-q stability plot and experimentally determined a-q parameters	149	
5.15	Raman spectra with varying light shift.	150
5.16	Raman sideband cooling on the z-axis motional mode	152
6.1	Optical setup of the 399 nm spectroscopy and locking system.	. .	168
6.2	Frequency correlation plot of locked 399 nm and 780 nm lasers.	170	

6.3	Allan deviation plots between different frequency references. . .	173
B.1	Simulation of the Raman transitions using 8 atomic eigenstates	211
B.2	Empirical trends found from Raman transition simulations. . .	212

A list of supplementary material, if any.

Acknowledgements

A statement acknowledging the extent and nature of any assistance received in the pursuit of the research and preparation of the thesis. This should include a list of any work published in the course of the research that is included in whole or in major part in the thesis itself, editorial assistance, etc.

An acknowledgement of published papers included in the thesis. This acknowledgement is relevant only for submitting candidates who choose to include full copies of published papers in chapters of their thesis, rather than write the full thesis in standard thesis style with reference to published papers or inserting the papers as appendices.

Griffith formatting page

Chapter 1

Introduction

The field of ion trapping has lead to significant contributions in physics evidenced by two Nobel prize awards. The first in 1989 for the development of the ion trapping technique by Wolfgang Paul and Hans Georg Dehmelt[6] (1/4 prize each) and secondly in 2012 for probing individual quantum systems by David J. Wineland[7] (1/2 prize). Ion trapping as a research field has grown exponentially from 1960 to 2020 (figure 1.1), with there now being, on average, multiple papers published each day on the topic.

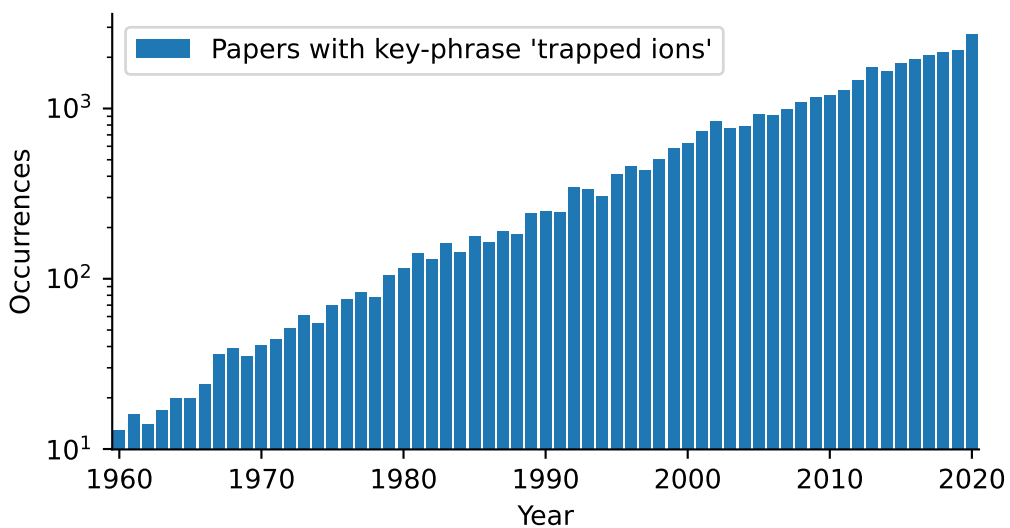


Figure 1.1: The number of papers with the phrase ‘trapped ions’ from 1960 to 2020. Counted by web scraping Google scholar[8].

A notable use-case of trapped ion systems are atomic clocks, which have

achieved low systematic uncertainties of 9.4×10^{-19} [9]. Advances in 2022 however have demonstrated neutral atom strontium lattice clocks with uncertainties at 8.9×10^{-20} [10] and 7.6×10^{-21} [11]. Ion trap systems are also used for the development of high performance quantum computers by companies such as Honeywell[12], Oxford Ionics[13] and IonQ, which became the first publicly traded pure-play quantum computing company in 2021[14].

Beyond high performance quantum computers and precision metrology, ion trap systems have demonstrated many world first quantum phenomena, including quantum jumps[15], photon anti-bunching[16] and the entanglement of two atoms[17].

Quantum thermodynamics is a research area that ion trap systems are also well suited for[18, 19]. A new heat engine design, the quantum spin-heat engine[1] is capable of heat-to-work efficiencies higher than the Carnot limit. Proof of concept experiments may be performed with trapped ion systems that would show this improvement in a lab setting. To demonstrate this, fine control over the motion of a trapped ion with near degenerate Zeeman states is required.

1.1 Thesis Overview

In this thesis, I demonstrate methods of Raman sideband cooling trapped ions with $I = 1/2$ spin across Zeeman split states. This has been previously explored in $I = 0$ atoms where the dynamics are different because of the different atomic state couplings. This particular Raman scheme requires only a single CW laser and two AOMs to bridge a small Zeeman shift in the atomic states. The simple optical setup makes it more financially accessible than other methods that require more complex laser and optical systems[3, 5, 4, 20, 2], at the cost of short coherence times since the transition is performed across a Zeeman qubit rather than a magnetic field insensitive hyperfine qubit.

Chapter 2 is a literature review going over the advancement of ion trap

technology, previously used Raman transition techniques in $I = 1/2$ trapped ions, and the quantum spin heat engine for which this research lays the foundation for manipulating and probing the trapped ion's motion. Chapter 3 describes all relevant theory for trapped ions and atomic transitions while chapter 4 introduces the experiment apparatus and how we achieve precise control of our trapped ion qubits. In chapter 5, the Raman transition scheme is presented, along with measurements and validation of the scheme to theory. It also presents attempts at Raman sideband cooling which shows cooling below the Doppler limit. Chapter 6 presents some aside research on neutral Ytterbium spectroscopy in hollow cathode lamps.

1.2 Semantics

1.2.1 Uncertainties

Uncertainties are expressed both in bracket notation and \pm notation throughout the thesis. Uncertainties expressed in brackets follow the convention,

$$1.9 \pm 1.6 \rightarrow 1.9(16). \quad (1.1)$$

This should be noted so that it will not misinterpreted as 1.9 ± 16 .

1.2.2 Atomic states

Throughout the thesis atomic states in $^{171}\text{Yb}^+$ are short-handed to bra-ket notation in the form $|L, F, m_F\rangle$, where L , F and m_F are quantum numbers. Only states within the $^2S_{1/2}$ and $^2P_{1/2}$ orbitals are presented in this way so the J quantum number (which is $1/2$ in both cases) is never specified. For example,

$$^2S_{1/2} \ F = 1, \ m_F = 0 \rightarrow |S, 1, 0\rangle. \quad (1.2)$$

Chapter 2

Literature Review

The goal of this review is to assess the viability of trapped ions for demonstrating a new type of heat engine technology[1]. This literature review will be split into four sections:

1. A short history and the emergence of modern ion trap techniques.
2. The development of ion trap systems to adapt to their application in quantum computing.
3. Comparison of different methods of performing motionally coupled Raman transitions in $^{171}\text{Yb}^+$
4. Heat engine demonstrations in trapped ions to date and the viability of a new method[1] using trapped ions.

2.1 Early ion trapping

Early trapped ion research began in the 1950s with Paul's work on the stability of charged particles in combinations of oscillating and static quadrupole electric fields[21]. Into the 1960s-70s, the use of Penning traps¹ in Dehmelt's lab led to motional spectroscopy measurements of both ions and single electrons[22].

¹Penning traps use a combination of a uniform magnetic field and static quadrupole electric field to confine charged particles.

Necessity of lasers

In 1973, the group of Günter Werth, experimenting with trapped $^{199}\text{Hg}^+$ ions, demonstrated optical pumping of hyperfine ground states, as well as microwave spectroscopy of the ground state hyperfine transition with optical detection of trapped ion fluorescence[23]. Their methods of fluorescing the ions at this stage involved shining a $^{202}\text{Hg}^+$ lamp onto the $^{199}\text{Hg}^+$ ions, which fortuitously matched resonances to within the lamp's thermal broadening. They commented that the signal-to-noise of such fluorescence was extremely poor[23]. In a later paper they demonstrated greatly improved optical detection of trapped ions with lasers[24] owing to their coherence, higher intensity and directionality.

Wineland, who worked in Dehmelt's lab went on to work at the National Institute of Standards and Technology (NIST)² and in 1978 achieved Doppler cooling of ions confined in a Penning trap[25] at the same time as another group[26] who had been working with Dehmelt who showed the cooling in a Paul trap. Doppler cooling opened up the potential for trapped ion systems to be used in more precise optical spectroscopy measurements, since Doppler shift and relativistic shifts could be greatly reduced by the cooling of the motion of the single ions and interrogation times could be greatly increased now that ions would not escape from the trap due to having high thermal energy.

Single perpetually trapped ions

In 1980, Toschek's group reported the trapping of a single Doppler cooled Barium ion in a Paul trap[27]. This was a major milestone in ion trap research where now an individual, suspended and long-lived atom could be studied. Neuhauser et al.[27] saw the potential for single Doppler cooled ions to be used in atomic clocks.

In 1983, Werth along with colleague Rainer Blatt measured to very high

²NIST was known as the National Bureau of Standards at the time.

precision the microwave resonance of $^{171}\text{Yb}^+$'s hyperfine ground state[28]. The ytterbium ion isotope is studied in greater detail through the following years by Werth, Blatt and others for its recognised potential as a very accurate atomic clock candidate[29, 30, 31, 32, 33]. Wineland and his colleague Wayne Itano using a single $^{198}\text{Hg}^+$ ion later demonstrated the quantum phenomena of quantum jumps[15] and resolved motional sideband cooling[34] using two different accessible transitions in the Mercury ion. Its fast fluorescing $^2S_{1/2} \leftrightarrow ^2P_{1/2}$ 194 nm (deep ultraviolet (UV)) transition allowed measurement of fluorescence of the ion and the narrow linewidth $^2S_{1/2} \leftrightarrow ^2D_{5/2}$ 281.5 nm transition could resolve motional sidebands and Zeeman split states. At a similar time Frank Diedrich and Herbert Walther showed trapped ions are a single-photon emitter with their measurement of photon anti-bunching[16].

2.2 Trapped ions for quantum computing

In 1992 the NIST group demonstrated the crystallisation of trapped ions into a linear chain using $^{199}\text{Hg}^+$ [35] and later showed single shot measurement of the hyperfine ground state qubit using state selective fluorescence and photon counting[36]. The conclusion and prospects written in these papers were interpreted in terms of spectroscopic limits and frequency standards. These techniques however formed the basis for qubit registers and quantum state readout.

Subsequent years saw the group now joined by Chris Monroe continue to achieve important results that laid the foundation for quantum computing with trapped ions. Using a radio frequency (RF) resonator, they increased the strength of the RF trapping quadrupole field, making lower motional states and the Lamb-Dicke regime more attainable through only Doppler cooling[37]. Via Raman sideband cooling, they also showed the ability to prepare an ion into its 3D ground state with a probability of 92%[38].

The group continued to show more deterministic control over the motional

state of trapped ions. For example, the Wigner function and density matrices of non-classical states of motion[39, 40] were prepared and reconstructed through measurement. By 1998, entanglement of two trapped ions using a breathing mode of a Beryllium ion pair[17] was demonstrated.

Cirac-Zoller gate

The idea of trapped ions as quantum logic processors only came about when Ignacio Cirac and Peter Zoller proposed a method of using trapped ion crystals and their shared motion as an intermediary coupling to perform a two-qubit gate (the Cirac-Zoller gate)[41].

Soon after the proposal, the NIST group demonstrated a CNOT-gate implemented using the hyperfine split ground states of a Beryllium-9 ion, and the n=0 and n=1 motional states of one of its three trapping modes[42]. This is different to what was envisioned in the Cirac-Zoller paper, where two trapped ions could be entangled through their intermediary motional mode. It does not find practical application because of the difficulty in simultaneous readout of both the ion's atomic and motional state.

By 2003, Blatt demonstrated the first true Cirac-Zoller gate using two $^{40}\text{Ca}^+$ ions and the $^2S_{1/2} \leftrightarrow ^2D_{5/2}$ optical transition qubit[43]. To date, the Cirac-Zoller gate is not widely used because of its strict condition of requiring the shared mode of the trapped ion qubits to be in the lowest motional state.

Mølmer-Sørensen gate

In 1999-2000, Mølmer and Sørensen presented a theoretical description of a two-qubit gate that could entangle internal atomic states without changing the motional state (if the coupling is in the Lamb-Dicke regime)[44, 45]. This gate was much more robust to heating compared to the Cirac-Zoller gate, since it did not require the ion to be in the motional ground state. It has been realised experimentally[2, 5] with published fidelities of 97.5%[46] on cloud quantum

computing platforms.

Garcia-Ripoll gate

Another important proposal of a gate was the Garcia-Ripoll fast entangling gate[47]. This gate did not spectrally address the ion’s motion like previous proposals and instead spatially addressed the ion’s motion with carefully timed laser pulses. These gates do not rely on resolved resonances so its gate speed is not limited to the frequency of ion motion and could be made arbitrarily fast. Efforts as of 2022 are being made by Blatt’s[48, 49] and our group[50, 51] to engineer ultrafast laser interactions suitable for implementation of the gate.

Similar entanglement operations using ultrafast Raman transitions[52] have been demonstrated with fidelities of $76\pm1\%$. This technique using Raman transitions induces a spin-flip with each ultrafast pulse, so has added complexity over a resonant pulse pair, which leaves the computational state unchanged.

Scaling ion trap quantum computers

The limit of the length of chains of trapped ions disallowed scaling of quantum computers so a method to extend trapped ion entangling gates beyond their local crystal was proposed[53] and partially demonstrated[54]. In the proposal, two frequency photon qubits entangled with the state of two trapped ion qubits could be interfered and measured to produce an entangled state between the trapped ion qubits. If those qubits themselves were part of a larger chain in their respective traps, the performance of quantum computation with the combined traps was shown to increase even though the entangling gate was probabilistic. They demonstrated remote entanglement using $^{171}\text{Yb}^+$ trapped ions in separate vacuum chambers distanced by 1 meter. They technically did not demonstrate it as an entangling gate nor did they claim to, but rather demonstrated an entanglement generation protocol. This is because they deviated from their original proposal in that their demonstration required the

ions to begin from a single initial quantum state.

Another method to scale the number of trapped ion qubits beyond the number permitted by a stable ion chain is to shuttle ions or chains of ions apart and together. This technique is being pursued by both IonQ and Honeywell[55].

The choice of $^{171}\text{Yb}^+$

A viability study[56] was carried out comparing different trapped ion species and their theoretical detection fidelity using a charge-coupled device (CCD) imager. Its focus was choosing the correct ion species for the scaling of trapped ion quantum computers with these CCDs. As a proof of concept, it demonstrated simultaneous readout with a CCD using three $^{111}\text{Cd}^+$ ions. Their comparison looked at $I = 1/2$ rare-earth alkalis $^{111}\text{Cd}^+$, $^{171}\text{Yb}^+$ and $^{199}\text{Hg}^+$ because of their simple atomic structure suitable for fast preparation and readout of ground state hyperfine qubits. Their study excluded species that were based around optical qubits³ (Ca^+ , Sr^+ , Ba^+) because of the added complexity in state preparation, optical shelving and need for optical regime (opposed to microwave regime) control of single qubits. The author's also note Be^+ , Mg^+ and Zn^+ are suitable candidates except they lack long lived or stable isotopes with nuclear spin $I = 1/2$. Ions with higher nuclear spin (e.g. $I = 3/2$) have more than one Zeeman sub-level in the ground S-orbital with lowest F-number, so can not be prepared through frequency separated transitions alone, but would require either specific polarization in lasers for preparation or coherent transfer of population between Zeeman states via resonant driven magnetic fields. Table 2.1 shows comparisons reproduced from their study[56] along with values for $^{133}\text{Ba}^+$ [57, 58] ($I = 1/2$, $\tau_{1/2} = 10.51$ years[59]), which has more recently been identified as a good candidate for ion trap quantum computing despite its radioactivity. They compared four properties of the atoms:

1. **Fluorescent transition wavelength** Longer wavelengths are gener-

³Trapped ion qubits split across optical transitions rather than hyperfine-split ground states.

	$^{111}\text{Cd}^+$	$^{171}\text{Yb}^+$	$^{199}\text{Hg}^+$	$^{133}\text{Ba}^+$
λ_{S-P} (nm)	226.5	369.5	194	493.5
$\gamma/2\pi$ (MHz)	50	19.6	70	20.1(2)
$\Delta_{HFS}/2\pi$ (GHz)	14.5	12.6	40.5	9.931(2)
$\Delta_{HFP}/2\pi$ (GHz)	2	2.1	6.9	1.840(2)
$\mathcal{F}(\eta = 0.001)$	94.11%	98.91%	98.78%	98.47%
$\mathcal{F}(\eta = 0.01)$	99.31%	99.88%	99.86%	99.83%
$\mathcal{F}(\eta = 0.3)$	99.97%	99.996%	99.995%	99.994%

Table 2.1: A comparison of trapped ion species properties relevant to qubit state readout. Transcribed from Acton et al.[56]. Barium P state linewidth from Guet and Johnson[58] and all other Barium values from Hucul et al.[57]. Fidelity calculations were re-performed following the theory in section 3.6 (Code in appendix C.1) for fair comparison to $^{133}\text{Ba}^+$. Average readout fidelity \mathcal{F} of the two qubit states was determined for different total detection efficiencies η . Fidelities assume no dark counts. The linewidth of $^{171}\text{Yb}^+$ was updated to match measurements of Berends et al.[60].

ally favoured because precision optics have less stringent engineering requirements and lasers generally perform better at longer wavelength. Also typically detectors have higher quantum efficiencies at longer wavelengths (UV-blue range). Operating at longer wavelengths also reduces unwanted effects like trap charging from the photo-electric effect and non-linearities in media like optical fibre.

2. **Transition linewidth** The advantage of a fast fluorescing transition is that the rate of emitted photons per second is higher, improving readout detection. A disadvantage is that the temperature of an ion at the Doppler limit increases with transition linewidth.
3. **Hyperfine splitting energies** Small ground state hyperfine splittings are more accessible using microwave electronics and electro-optics. However, higher hyperfine splittings improve optical readout of the qubit state since the optical state resonances are split by larger energies and so less state mixing occurs.
4. **Optical readout fidelities** For readout on a CCD it was found $^{171}\text{Yb}^+$ and $^{199}\text{Hg}^+$ performed equally better than $^{111}\text{Cd}^+$.

Informed by their analysis, Monroe’s group demonstrated with $^{171}\text{Yb}^+$ optical pumping to the $^2S_{1/2} F = 0$ ground state, driving of the $^2S_{1/2} F = 0 \leftrightarrow F = 1$ transition with resonant microwaves and qubit state readout using a photomultiplier tube (PMT)[61]. While Ytterbium ions had been studied decades before for their clock transition[28], this was the first demonstration in the context of quantum computing.

Improving readout fidelity

With the understood potential of $^{171}\text{Yb}^+$ as a useful species for ion trap research [28, 56], greater study went into understanding the fluorescence of $^{171}\text{Yb}^+$. Ejtemae et al. [62] performed a comprehensive study into the fluorescence of the $^2S_{1/2} \leftrightarrow ^2P_{1/2}$ transition in both $^{174}\text{Yb}^+$ and $^{171}\text{Yb}^+$. The difference of nuclear spin in each of the isotopes leads to very different atomic dynamics. Ejtemae was not the first to consider the atomic dynamics of these transitions, with Berkeland and Boshier[63] solving the dynamics in 2002. Ejtemae et al.’s work had an emphasis on experimental verification and optimising fluorescence for high fidelity deterministic readout of trapped ion qubits. Wölk et al. found a way to improve further the readout of a trapped ion qubit by extracting useful information from the arrival time of photo-electron events from PMTs and avalanche photo-diodes (APDs) using a time tagger.

2.3 $^{171}\text{Yb}^+$ Raman transition demonstrations

Many of the trapped ion entangling gate proposals required coherent and deterministic control of trapped ion motion, since it is an intermediary coupling between two separate trapped ions’ internal qubit states. While narrow linewidth transitions had served well in demonstrating sub-doppler cooling in the 1980s[34], their performance was constrained by photon recoil. Coherent Raman transitions do not lead to any excitation recoil. This is because far-

detuned Raman beams transfer virtually no population to the excited state[3]. However, problems in Raman transitions can arise from unwanted couplings to other states close in energy and AC-stark shifts[2, 3] that add error in the resonance and fidelity of implemented gates.

Terahertz-detuned CW beam with phase modulated sidebands

With phase coherence being a key requirement of driving highly coherent Raman transitions, narrow linewidth CW lasers are a natural choice. To have the Raman transition bridge the hyperfine transition of an ion, the frequency difference in the Raman beams needs to be match the hyperfine splitting, which is on the order of 12.6 GHz for $^{171}\text{Yb}^+$ (table 2.1). This can be achieved with coherent sidebands generated by an electro-optic modulator (EOM). Using EOMs for Raman transitions was first demonstrated by Monroe's group in 2003 with Cadmium ions[4]. They achieved ground-state cooling using this method a year later[64]. A comb generated by an EOM contains sidebands centered around the carrier frequency with symmetric intensity and spaced by the modulation frequency. The phase of opposite sidebands are anti-symmetric which causes destructive interference of Raman transitions throughout the optical frequency comb, reducing the effective Rabi rate to zero[4]. This interference occurs if the EOM is resonant with the hyperfine frequency or its half-tone. To avoid this, they propose in the same paper three different methods of generating a phase difference in the Raman beams which recovers the Rabi rate. They experimentally demonstrated the method with a Mach-Zehnder interferometer and an AOM in each arm.

Monroe's group later applied this method to $^{171}\text{Yb}^+$ across the hyperfine ground states using an EOM tuned to the half-tone of the ground state splitting and AOMs to adjust the transition resonance and drive appropriate motional sideband transitions[5]. They demonstrated a quantum simulation of an Ising model using this technique of Raman transitions as the intermediary

coupling between trapped ion qubits in a chain, using Mølmer-Sørensen gates. They reported the Raman beams were red-detuned by 0.5-2.7 THz from the $^2P_{1/2}$ $F = 1$ $m_F = \pm 1$ excited states of the transition. There are two scales of frequency that this detuning can be compared to:

1. The natural linewidth of the excited state (19.6 MHz) is 26,000-140,000 times smaller than the detuning.
2. The fine structure splitting of the $^2P_{1/2}$ and $^2P_{3/2}$ states is ~ 100 THz, which is comparable to the detuning.

The distance from the natural linewidth is large so that off-resonant excitation is negligible, however the coupling to the $^2P_{3/2}$ state must be considered at these far detunings, which can induce extra light shifts in the Raman resonances.

Terahertz-detuned mode-locked lasers

In 2010 Monroe's group showed how a mode-locked laser highly detuned from an optical transition could be used to reliably drive Raman transitions across $^{171}\text{Yb}^+$'s clock state[2] as well as across its motional sidebands.

The high intra-pulse coherence of a mode-locked laser means it can reliably drive Raman transitions which require high phase coherence between the pump and (anti-)Stokes beams. A frequency-doubled mode-locked Ti:Sapphire laser at $\lambda = 374$ nm (9 THz red detuned), repetition rate 80.76 MHz and pulse duration ~ 1 ps was used. The large detuning from the atomic resonance (500,000 natural linewidths) makes the probability of off-resonant spontaneous emission practically zero. The spectral bandwidth of their used pulsed laser $(1 \text{ ps})^{-1} \approx 1 \text{ THz}$ spans beyond the bandwidth of the ground state hyperfine transition of $^{171}\text{Yb}^+$ at 12.6 GHz[65]. Unlike the comb-teeth produced by an EOM[5], a mode-locked laser's teeth all have the same sign phase, so no destructive interference in a Raman transition would occur. By tuning the

repetition rate such that the hyperfine ground state resonance is an integer multiple of it, the comb-teeth become resonant with a Raman transition between hyperfine ground states. Light shift from comb-teeth being different intensities is negligible since the laser's spectral envelope is large compared to the hyperfine transition frequency. They also demonstrated a two-qubit Mølmer-Sørensen gate by tuning one of the Raman beam comb teeth with an AOM to have a multi-colour tone that produces a beat note, off-resonantly driving a motional sideband on both the blue and red side, creating a spin-dependent force[44, 45].

Monroe's group demonstrated a different method of driving Raman transitions across the hyperfine qubit using a single picked pulse from a mode-locked frequency tripled yttrium vanadate laser[3]. The specifications were $\lambda = 355$ nm, 121 MHz repetition rate and 14.8 ps pulse duration. This laser was 33 THz blue detuned from the $^2P_{1/2}$ manifold and coincidentally ~ 66 THz red of the $^2P_{3/2}$ manifold. This detuning was chosen to minimise AC Stark shift of the qubit states between the two fine-split states, and near-optimally minimise spontaneous emission from them as well. Since the Raman transition was being driven by a single laser at a single frequency (no comb teeth since only a single pulse is used), there was no detuning between the two Raman beams. This meant the detuning of the Raman transition would match the qubit resonance. Despite this, the power broadening in the Raman transition was sufficient to invert the population by more than 50%. By splitting the pulse into two counter-propagating pulses with a specific delay between them, full population transfer could be achieved. The Raman transition's Rabi rate is on the order of the pulse spectrum (100 GHz), so its power broadening is much wider than the harmonic motion energy spacing (~ 1 MHz). This means the qubit transition simultaneously drives a large number of motional transitions. This strong coupling was used to implement two-qubit entanglement in a similar manner to the Garcia-Ripoll gate[47, 52, 66].

Using this same laser, Monroe’s group demonstrated coherent Raman transitions between comb teeth as they had with the frequency doubled Ti:Sapphire mode-locked laser[67]. They performed a robust Mølmer-Sørensen gate with a maximum fidelity of 95%. With improvements, as of 2019, the 2-qubit gate fidelity was bench-marked to 97.5% in an 11-ion register[46].

No demonstrations across Zeeman sub-levels

While the magnetic field insensitive $|F = 0, m_F = 0\rangle$ and $|F = 1, m_F = 0\rangle$ states of $^{171}\text{Yb}^+$ ’s ground state hyperfine transition remains an obvious choice to realise a qubit for quantum computing, the near-degenerate Zeeman sub-levels of the $^2S_{1/2}$ $F = 1$ manifold (only split in energy by external magnetic fields), can be used to enable quantum technologies including quantum heat engines and magnetic field sensors, where the energy spacing between states is MHz to kHz under readily available laboratory conditions. This is small compared to the ground state hyperfine splitting meaning the Zeeman shift is in the weak-field regime of the Breit-Rabi formula.

Coherent stimulated Raman transitions across Zeeman-split states that can drive motional sidebands have been demonstrated in species with no hyperfine structure like $^{138}\text{Ba}^+$ [68] and $^{40}\text{Ca}^+$ [69]. The absence of hyperfine splitting in even isotope atoms requires the use of Raman transitions across Zeeman split states to perform Raman sideband cooling and quantum logic spectroscopy. Narrow linewidth transitions could be used but are fundamentally limited in their coherence and versatility by their intrinsic properties. Similarly, electromagnetically-induced-transparency (EIT) cooling could be used as a method of ground state cooling even isotope ions, as has been done with $^{40}\text{Ca}^+$ [70], $^{138}\text{Ba}^+$ [71] and $^{174}\text{Yb}^+$ [72], but a method of trapped ion thermometry is still required to confirm cooling.

Another type of coupling between Zeeman sub-levels and motion was observed in $^{173}\text{Yb}^+$ called Zeeman coherences[33]. The coupling is believed to

be mediated via magnetic field gradients. This process could be exploited for designing similar quantum technologies.

2.4 Trapped ion heat engine demonstrations

Thermodynamic processes allow useful classical technologies like heat engines and refrigerators. The field of quantum thermodynamics explores thermodynamic processes like work extraction and change in entropy in quantum systems[73]. While heat engines and refrigerators at the single atom level have been demonstrated using trapped ion systems[18, 19, 74], they remain explainable in terms of classical thermodynamic processes. Quantum thermodynamics interestingly allows a phenomena not possible in classical thermodynamics, heat engines with efficiencies beyond the classical limit[1] by leveraging additional quantum exclusive resources.

Classical atomic Brayton heat engines

Roßnagel et al.[74] use the transfer of heat into and out of the x- and y-axes of motion of a trapped ion to coherently drive the z-axis harmonic motion. The authors comment the engine performs a Carnot cycle (isothermal/adiabatic), however the engine can be argued to follow a Brayton cycle(isobaric/adiabatic)[75] (figure 2.1).

In terms of the four stages of the Brayton cycle, the engine begins with the trapped ion being heated by electric field noise in the RF quadrupole (x-y) plane of the trap (isobaric expansion). Isobaric expansion is characterised by an increase in the temperature, volume and entropy of a working fluid while its pressure remains constant. This is opposed to the equivalent stage of a Carnot cycle, isothermal expansion, where the working fluid's volume and entropy would increase while pressure would decrease and temperature would remain the same. In experiment, this stage causes heating and expansion of the ion in its x-y spatial distribution. This fits more with the description of isobaric

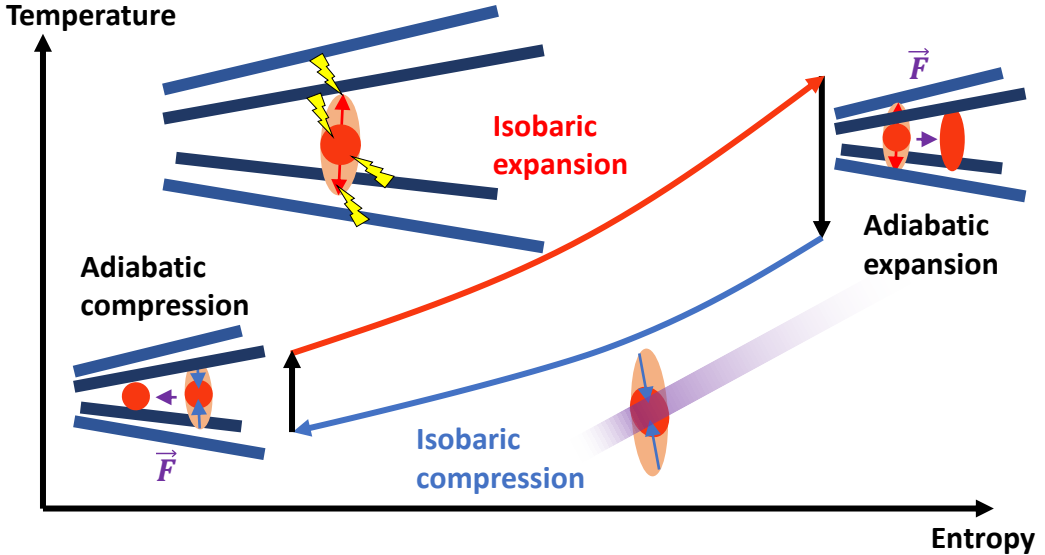


Figure 2.1: The Brayton cycle and how it was implemented by Roßnagel et al.[74]. The cycle begins by electrically heating the ion (isobaric expansion) which induces a z-axis force because of the tapered trap geometry (adiabatic expansion). The ion is then Doppler cooled (isobaric compression), which induces the opposite z-axis force (adiabatic compression). When this cycle is performed at the rate of the z-axis harmonic motion, the ion motion in that axis is driven and becomes more coherent (useful work).

expansion, hence a Brayton cycle.

Owing to the tapered shape of the rod trap, this thermal expansion generates a force in the axial (z) direction of the trap (adiabatic expansion). Next, the ion is Doppler cooled, which reduces its spatial distribution (isobaric compression). The ion feels a restorative force from the tapered trap's electric field completing the cycle (adiabatic compression). When this cycle is driven at the rate of the ion's axial secular frequency, the ion's motion in that direction increases coherently.

Lindenfels et al.[19] demonstrate a similar Carnot engine cycle. Instead of a tapered trap potential to generate temperature dependent forces, an optical standing wave with a node centered at the ion generates a spin dependent force[76]. By optically pumping the ion between Zeeman states of opposite spins in time with the secular frequency of the ion along the standing wave direction, the ion's motion was coherently driven.

Quantum SHE

The Maxwell’s demon thought experiment poses a scenario where two thermal baths in equilibrium can exchange particles via a portal that is opened and closed by an external agent (Maxwell’s demon). If the demon has sufficient knowledge of the state of the system, they could separate low and high energy particles between the baths, taking the baths out of equilibrium, lowering total entropy and violating the second law of thermodynamics. The second law holds however when the entropy cost of erasing the demon’s information (memory) is also considered[77].

Landauer’s principle states that the energy cost of erasing 1 bit of information is $\ln(2)k_B T$. However, as shown by Vaccaro and Barnett, the quantity of temperature in Landauer’s principle is not general and in fact the cost of erasing information can be paid for by any conserved measurable physical quantity. This ties into the maximum entropy principle of E. T. Jaynes in statistical mechanics where any conserved measurable physical quantity has an associated measure of entropy[78, 79].

Combining these concepts, Wright et al.[1] then proposed a type of heat engine that could use energy degenerate information erasure to extract useful work from an energetic thermal reservoir. Transfer of entropy from the thermal reservoir to an energy degenerate spin-reservoir satisfies the second law[80]. This could allow heat engines that perform above the Carnot efficiency limit since there is no fundamental loss in efficiency in the heat engine. The resetting of the spin-heat engine does not require a minimum energy $\ln(2)k_B T$, but rather a decrease in polarisation of a spin reservoir.

The engine proposed in the paper is described using a quantum dot system however it could be extended to any appropriate quantum system. The engine has different stages compared to classical heat engines. Its three stages are:

1. **Heat extraction** Energy in a thermal motional degree of freedom is transferred into an excited state in the quantum dot via an optical trans-

sition.

2. **Optical work output** Via stimulated emission or spontaneous decay, the energy now in the atomic state is released as a higher energy photon than that used to optically excite the quantum dot (anti-Stokes scattering).
3. **Erasure** The energy degenerate quantum dot spin qubit's entropy is decreased by interacting with a spin reservoir. The coupling between spin reservoir and spin qubit would be mediated through spin-exchange collisions of the nuclei within the quantum dot's valence electron wavefunction.

SHE viability in an ion trap system

To assess the viability of the SHE, an implementation of each stage of the engine in an ion trap will be proposed. Heat extraction and optical work output in trapped ion systems is well understood in literature in the context of the decades of research into the different cooling methods that have come about through necessity in ion trapping[26, 38, 67]. Three methods of heat extraction are proposed:

Heat extraction and generation of work

1. Coherent Raman transitions offer the ability to transfer energy from a motional degree of freedom into a photon via stimulated emission using an appropriately tuned anti-Stokes beam. This would simultaneously complete the heat extraction and optical work output steps of the engine, however the work photon would be difficult to discern within the noise of the anti-Stokes beam's laser power.
2. Another method would be to excite the ion on a fluorescent transition and observe probabilistic anti-Stokes spontaneous decay scattering. This

method would allow easier probing of the isotropically emitted work photon, however it would only probabilistically contain more energy because of the nature of the motion-light coupling.

3. The last proposal for heat extraction is to exploit the phenomena of EIT to favourably produce anti-Stokes spontaneous emission. EIT works by dressing the eigenenergies of a multi-level atom by driving a strong blue-detuned laser on a certain transition[81]. This alters the absorption profile on another transition such that anti-Stokes scattering can be favourably driven over Stokes scattering. This is unlike the method 2, where exciting a singular transition produces roughly the same amount of Stokes and anti-Stokes scattering through spontaneous decay.

To determine the true optical work output of the photon, precision spectroscopy (<MHz precision) could be performed to observe the anti-Stokes resonances.

Spin reset

Finally, methods of information erasure will be considered. The goal of information erasure is to reset degenerate spin atomic states via spin exchange with a spin reservoir. Two proposals are made:

1. Spin exchange has been observed between trapped ions and spin-polarised neutral atoms through spin exchange collisions[82, 83]. In this process, population transfer between Zeeman states in $^{174}\text{Yb}^+$ via spin-exchange with ultracold ^{87}Rb has been observed at a rate⁴ $\gamma_{SE}/(2\pi) \sim 30$ Hz. As a spin-reset operation, this process is not perfect and is limited by another process, spin-relaxation, a T1 decay type process with rate $\gamma_{SR} \sim 50$ Hz [82]. Another much slower ($\sim 10^{-5}\gamma_{SR}$) process of concern is charge-exchange collision, where electrons transfer to the ion, neutralising it and ejecting it from the trap, which limits ion life-time.

⁴ γ_{SE} and γ_{SR} are approximated from values from Ratschbacher et al.[82]

Extending this process to $^{171}\text{Yb}^+$ introduced a new problematic process where amplitude decoherence causes transfer of population to the lowest energy state ${}^2S_{1/2} F = 0$ in $^{171}\text{Yb}^+$, an energy transfer process which would ruin the efficiency of the spin-heat engine. Instead, an $I = 1/2+$ isotope ion with positive nuclear parity would have the ${}^2S_{1/2} F = 1$ manifold as its ground state. This would allow spin-transfer mechanisms without amplitude decoherence. Suitable isotopes for ion trapping where $I = 1/2+$ are $^{133}\text{Ba}^+(\tau_{1/2} = 10.51 \text{ years})$, $^{111}\text{Cd}^+$ or $^{113}\text{Cd}^+(\tau_{1/2} = 7.7 \times 10^{15} \text{ years})$ [59]. Other valued positive-parity nuclear spins could be used but $I = 1/2+$ offers the closest comparison to the physics of $^{171}\text{Yb}^+$ with $I = 1/2-$.

2. Self-induced Zeeman coherence[33] is a mechanism where the magnetic dipole between two Zeeman states couples to the ion motion via a magnetic field gradient in space[33]. It is a coherent process and is not energy degenerate because energy is being transferred from the motional degree of freedom to the spin degree of freedom in the trapped ion. However since energy transfer is self-contained within the ion and is sourced from the thermal motion, it is at no expense to the heat engine efficiency. The spin exchange mechanism in self-induced Zeeman coherences is unclear but may be spin exchange with the source of the external magnetic field that is producing the necessary magnetic field gradient.

Given these proposals, the best approach to produce a spin-heat engine using trapped ions is likely a combination of EIT transitions to produce optical work in the form of anti-Stokes-favoured spontaneous emission and a spin-polarised atomic vapour interacting with the ion with $I=1/2+$ nuclear spin. Demonstrations of EIT cooling in trapped ion with $I = 1/2$ hyperfine structure like $^{171}\text{Yb}^+$ [84] have lagged behind demonstrations in $I = 0$ atoms[85] because of their more complex atomic structure.

The outlook of this thesis focuses on the previously unexplored generation

of Raman transitions on the Zeeman sub-levels of $^{171}\text{Yb}^+$ for coherent control and measurement its the motional states for later characterisation of the SHE.

Chapter 3

Theory

This chapter describes the physics behind typical ion trap experiments, looking specifically at Ytterbium-171 ions. It will cover theory that is the baseline to understanding modern ion trap systems from which experiments in quantum-communication, -thermodynamics and -computing can be performed. This chapter will begin with trapped ion motion, looking both at the classical description of quadrupole ion traps as well as quantum harmonic oscillators (QHOs). It will then go over atomic theory relevant to the behaviour of trapped ions. Combining trapped ion motion and atomic theory, it will look at light-motion coupling and its applications in laser cooling. Finally, it will be shown how theory has been adapted in literature to describe $^{171}\text{Yb}^+$ ion trap systems.

3.1 Trapped Ion Motion

Trapped ions are bound by Coulomb potentials produced by external electric fields from electrodes. They can remain bound without being cooled for periods longer than other methods based on optical and/or magnetic forces because they produce tighter and deeper trapping potentials[86, 87].

An ion trap's main purpose is to provide an electric field that keeps a charged particle in stable motion in otherwise empty space. Earnshaw's theorem states this can not be achieved by static electric fields alone. Consider

a static electric field that provides a restorative force for positively charged particles in all three dimensions,

$$\mathbf{E}(x, y, z) = -\frac{E_0}{R_0}(\alpha x \mathbf{x} + \beta y \mathbf{y} + \gamma z \mathbf{z}) \quad (3.1)$$

where α , β & γ are scaling factors for the forces which must all be positive to produce a static trapping electric field. Applying Gauss's Law,

$$\nabla \cdot \mathbf{E} = -\frac{E_0}{R_0}(\alpha + \beta + \gamma) = \frac{\rho}{\epsilon_0} \neq 0, \quad (3.2)$$

it is found the charge density in this space is non-zero while the scaling factors are all positive. Note Earnshaw's theorem considers specifically electric fields producing a trapping field for a stationary particle, however 3-D trapping potentials can be produced by using combinations of static electric and magnetic fields (Penning traps) or non-stationary trapping fields using only static electric fields (orbitraps).

Instead of a static field, through an oscillating field, an average restorative (ponderomotive) force over many oscillations is capable of trapping a charged particle at a single point in space. The dynamics of a charged particle in such a field are described by the Mathieu differential equation.

3.1.1 Mathieu Equations of Trapped Ion Motion

The Mathieu differential equation

$$\frac{d^2\xi}{d\tau^2} = -(a - 2q \cos 2\tau)\xi \quad (3.3)$$

is used to describe the motion of particles in static and sinusoidally varying quadratic potentials. In ion traps, electrodes are typically arranged in symmetric pairs of equal voltage so that near the centre of an electrode pair, the electric field gradient is constant and passes through $\mathbf{E} = \vec{0}$. The electrode

pair can be driven with any combination of DC and AC voltages (typically RF band frequencies for trapping atomic ions) at the trap frequency Ω . The resulting trapping potentials take the general form,

$$\phi(x, y, z, t) = \frac{U_0}{2z_0^2}(\alpha_{DC}x^2 + \beta_{DC}y^2 + \gamma_{DC}z^2) + \frac{V_0}{2R_0^2} \cos \Omega t (\alpha_{RF}x^2 + \beta_{RF}y^2 + \gamma_{RF}z^2). \quad (3.4)$$

Parameters U_0 and z_0 scale the DC electric potential and V_0 and R_0 scale the RF potential. To abide by Gauss' law, the field must meet the conditions,

$$\begin{aligned} 0 &= \alpha_{DC} + \beta_{DC} + \gamma_{DC} \\ 0 &= \alpha_{RF} + \beta_{RF} + \gamma_{RF}. \end{aligned} \quad (3.5)$$

The motion of a charged particle in ϕ is described using Newton's second law and calculating the force $\mathbf{F} = -Q\nabla\phi$,

$$\begin{aligned} F_x &= m \frac{d^2x}{dt^2} = -Q(\alpha_{DC}\frac{U_0}{z_0^2} + \alpha_{RF}\frac{V_0}{R_0^2} \cos \Omega t)x \\ F_y &= m \frac{d^2y}{dt^2} = -Q(\beta_{DC}\frac{U_0}{z_0^2} + \beta_{RF}\frac{V_0}{R_0^2} \cos \Omega t)y \\ F_z &= m \frac{d^2z}{dt^2} = -Q(\gamma_{DC}\frac{U_0}{z_0^2} + \gamma_{RF}\frac{V_0}{R_0^2} \cos \Omega t)z. \end{aligned} \quad (3.6)$$

Equation 3.6 is of identical form to equation 3.3 with the reparametrisation of a and q ,

$$\begin{aligned} a_x &= \frac{4\alpha_{DC}QU_0}{m\Omega^2z_0^2}, \quad q_x = -\frac{2\alpha_{RF}QV_0}{m\Omega^2R_0^2} \\ a_y &= \frac{4\beta_{DC}QU_0}{m\Omega^2z_0^2}, \quad q_y = -\frac{2\beta_{RF}QV_0}{m\Omega^2R_0^2} \\ a_z &= \frac{4\gamma_{DC}QU_0}{m\Omega^2z_0^2}, \quad q_z = -\frac{2\gamma_{RF}QV_0}{m\Omega^2R_0^2}. \end{aligned} \quad (3.7)$$

Homogeneous solutions to equation 3.3[88, Eq. 28.2.18] exist,

$$\xi(\tau) = \sum_{n=-\infty}^{\infty} c_{2n} e^{i(\beta+2n)\tau}, \quad (3.8)$$

The solution of equation 3.8 can be made real by adding a conjugate solution

$$\xi(\tau) = 2 \sum_{n=-\infty}^{\infty} c_{2n} \cos((\beta + 2n)\tau). \quad (3.9)$$

Coefficients c_{2n} satisfy[88, Eq. 28.2.19]

$$qc_{2n+2} - (a - (\beta + 2n)^2)c_{2n} + qc_{2n-2} = 0, \quad (3.10)$$

and[89]

$$\beta = a + \frac{q^2}{(\beta + 2)^2 - a - \frac{q^2}{(\beta + 4)^2 - a - \frac{q^2}{(\beta + 6)^2 - a - \dots}}} + \frac{q^2}{(\beta - 2)^2 - a - \frac{q^2}{(\beta - 4)^2 - a - \frac{q^2}{(\beta - 6)^2 - a - \dots}}} \quad (3.11)$$

which in the range $0 \leq q \lesssim 0.4$ can be approximated to

$$\beta \approx \sqrt{a + \frac{q^2}{2}}. \quad (3.12)$$

There exists a set of a and q parameters that permit bounded trajectories described by the Mathieu differential equation. A subset of these solutions, where a is in the region of 0 are bound by the curves[90],

$$\begin{aligned} a &\gtrapprox -\frac{q^2}{2} + \frac{7q^4}{128} - \frac{29q^6}{2304} + \frac{68687q^8}{18874368} \dots \\ a &\lessapprox 1 - q - \frac{q^2}{8} + \frac{q^3}{64} - \frac{q^4}{1536} - \frac{11q^5}{36864} + \frac{49q^6}{589824} - \frac{55q^7}{9437184} - \frac{83q^8}{35389440} \dots, \end{aligned} \quad (3.13)$$

which when plotted, gives figure 3.1. Equation 3.13 is only true for positive q and solutions for $q < 0$ are mirrored. When a and q for all three axes are in the domain of figure 3.1, the charged particle is bound in 3D space. When $c_{-2} = c_{+2} = -\frac{q}{4}c_0$ [91] and all higher order terms are ignored,

$$\xi(\tau) \approx 2c_0(1 - \frac{q}{2} \cos 2\tau) \cos \beta\tau, \quad (3.14)$$

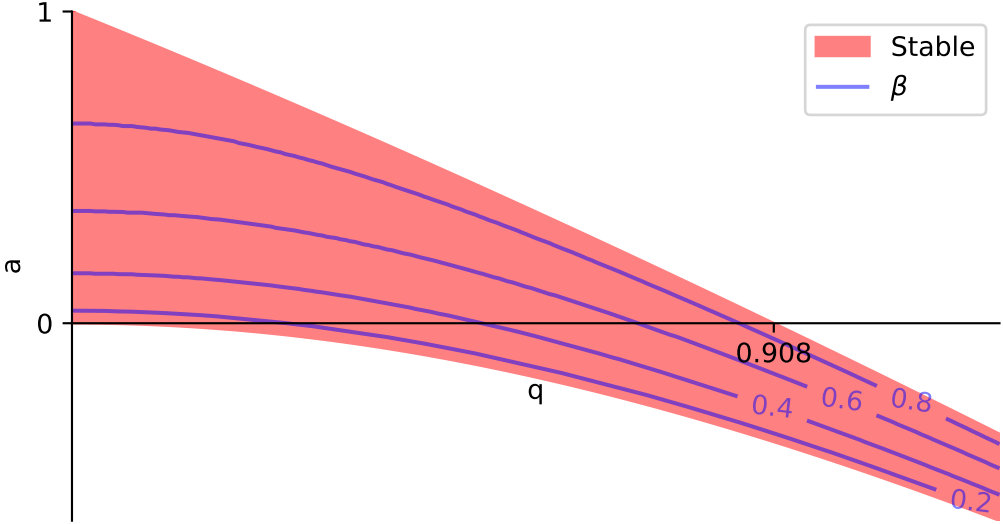


Figure 3.1: A region where a and q parameters give stable solutions to the Mathieu differential equation. Equipotential lines show how the β parameter varies with a and q , calculated using equation 3.11.

which can then be put in terms of the trap frequency $\Omega t = 2\tau$,

$$\xi(t) = 2c_0 \left(1 - \frac{q}{2} \cos(\Omega t) \right) \cos \left(\frac{\beta\Omega}{2} t \right), \quad (3.15)$$

where the secular frequency arises $\omega_s = \frac{\beta}{2}\Omega$ which describes the harmonic-like motion the ion takes. Figure 3.2 shows the characteristics of 1D ion motion in a trap.

Quadrupole rod trap

This theory will be applied to a specific geometry of ion traps, quadrupole rod traps (figure 3.3). These resemble the planar trap design used experimentally (figure 4.1) where R_0 can be re-scaled so the theory is equivalent. Let the x-y plane have a time varying quadrupole field and the z-axis have an electric field that gives a restorative force around $z = 0$. First consider the electric potential from the static electric field in the z plane. To have a trapping potential along the z-axis, $\gamma_{DC} = 1$. To satisfy Gauss's law and consequently Laplace's equation $\nabla^2\phi = 0$, then $\alpha_{DC} = -1/2 + \Delta$ and $\beta_{DC} = -1/2 - \Delta$.

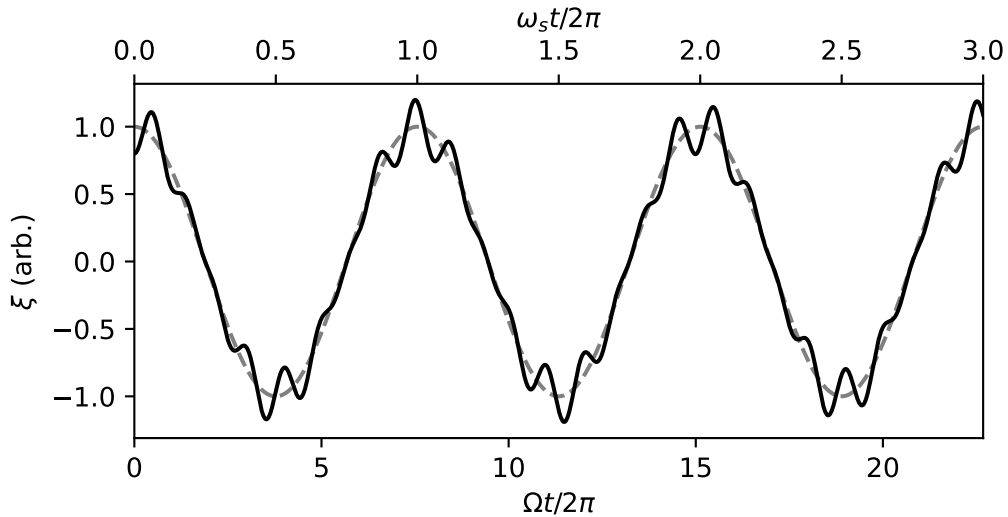


Figure 3.2: The 1D motion of a particle in an ion trap described by equation 3.15 (solid black line) with $q = 0.4$ and $a = -0.01$. The high value of q is used to exaggerate the oscillations due to the $\cos \Omega t$ term. Simple harmonic motion (dashed gray line) at frequency ω_s is a valid approximation to the motion of the trapped ion, when q is small.

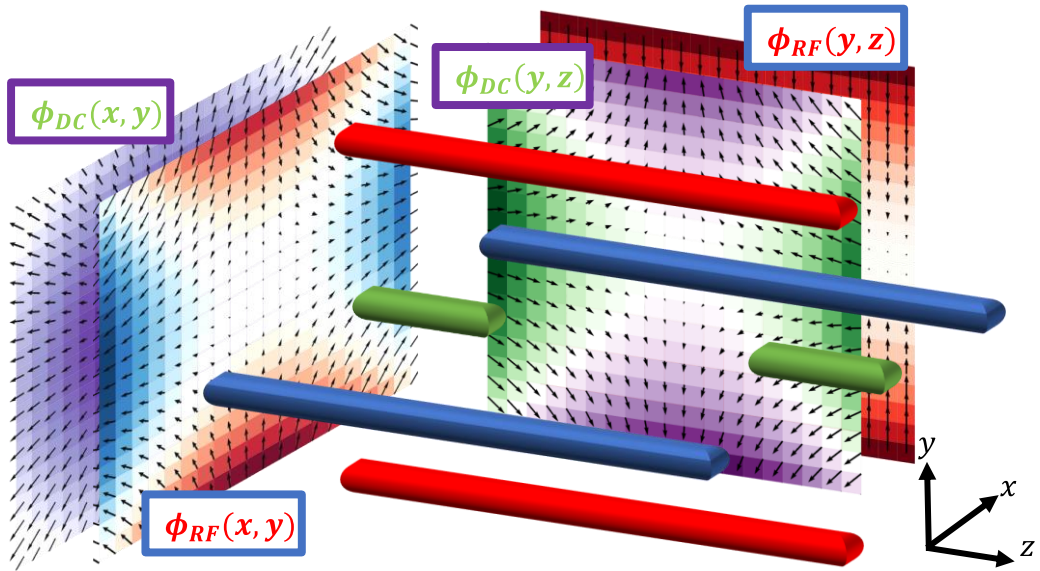


Figure 3.3: The basic structure of a rod trap. Alternating trapping(anti-trapping) potentials from the RF electrodes (ϕ_{RF}) are shown red(blue). The DC electrode trapping(anti-trapping) potential (ϕ_{DC}) is shown in green(purple).

Δ when non-zero, lifts the degeneracy of the x and y secular frequencies. An unstable field exists in the x-y plane because of the slope of its potential, which can be made stable adding the time varying quadrupole potential where $\alpha_{RF} = 1$, $\beta_{RF} = -1$ and $\gamma_{RF} = 0$ to satisfy Laplace's equation. The motion of a charged particle in such a field is described by the a and q parameters of equation 3.3,

$$\begin{aligned} a_z &= \frac{4QU_0}{m\Omega_{RF}^2 z_0^2} \\ a_x &= \left(-\frac{1}{2} + \Delta\right) a_z \\ a_y &= \left(-\frac{1}{2} - \Delta\right) a_z \\ q_x = -q_y &= -\frac{2QV_0}{m\Omega^2 R_0^2} \\ q_z &= 0 \end{aligned} \tag{3.16}$$

Different trap geometries will have different α , β & γ parameters, so will have different a & q solutions compared to equation 3.16. Expanding the secular frequency in terms of equation 3.16 gives,

$$\begin{aligned} \omega_R &= \frac{QV_0}{\sqrt{2m\Omega R_0^2}} \\ \omega_z &= \sqrt{\frac{QU_0}{mz_0^2}} \\ \omega_x &= \sqrt{\omega_R^2 - \left(\frac{1}{2} - \Delta\right)\omega_z^2} \\ \omega_y &= \sqrt{\omega_R^2 - \left(\frac{1}{2} + \Delta\right)\omega_z^2}, \end{aligned} \tag{3.17}$$

which are secular frequencies specific to quadrupole rod traps. ω_R represents the secular frequency of the motion radial to the z-mode, when there is no trapping DC field. The degeneracy of the x and y axes is lifted by Δ describing a small DC electric potential which increases a_x and decreases a_y . It preserves Laplace's equation but changes the x and y frequencies in opposite directions.

3.1.2 Quantum Harmonic Oscillator

From equation 3.15 it was found the motion of a trapped ion approximates simple harmonic motion for small values of q . The ion trap then approximates

a static quadratic potential in all 3 axes¹. Using the Hamiltonian for a particle in a quadratic potential,

$$\hat{H} = \frac{\hat{p}^2}{2m} + \frac{1}{2}m\omega_s^2\hat{x}^2, \quad (3.18)$$

wavefunction solutions exist

$$\psi_n(x) = \sqrt{\frac{a_0}{\sqrt{\pi}2^n n!}} e^{\frac{-x^2}{2a_0^2}} \mathcal{H}_n\left(\frac{x}{a_0}\right) \quad (3.19)$$

with associated energies

$$E_n = \hbar\omega_s\left(\frac{1}{2} + n\right) \quad (3.20)$$

where \mathcal{H}_n are the Hermite polynomials[88, Eq. 18.5.13] (table 3.1) and $a_0^2 = \frac{\hbar}{m\omega_s}$ is the difference in spatial variance between eigenstates. There are count-

n	$H_n(x)$
0	1
1	$2x$
2	$4x^2 - 2$
3	$8x^3 - 12x$
4	$16x^4 - 48x^2 + 12$

Table 3.1: The first few physicist's Hermite polynomials.

ably infinite solutions with evenly spaced energy. The variance of these wavefunctions,

$$\langle \hat{x}^2 \rangle = (2n + 1) \frac{\hbar}{2m\omega_s}, \quad (3.21)$$

shows a linear dependence of variance with n and consequently E_n . The standard deviation $\sqrt{\langle \hat{x}^2 \rangle}$ gives a quantum analog to the root mean square (RMS) amplitude of oscillation of a classical harmonic oscillator. The standard deviation increases with the square root of energy, as does the amplitude in a classical harmonic oscillator.

¹Far from the trapping centre its trapping potential will deviate from a quadratic potential.

Creation and Annihilation Operators

In a QHO, the position and momentum operators can be written in terms of the annihilation operator \hat{a} ,

$$\begin{aligned}\hat{x} &= \sqrt{\frac{\hbar}{2m\omega_s}}(\hat{a}^\dagger + \hat{a}) \\ \hat{p} &= i\sqrt{\frac{\hbar m\omega_s}{2}}(\hat{a}^\dagger - \hat{a}),\end{aligned}\tag{3.22}$$

This operator and its conjugate transpose (creation operator) show more clearly the relation between the eigenstates of a QHO. The operators can be written in matrix form,

$$\hat{a} = \begin{pmatrix} 0 & \sqrt{1} & 0 & 0 & 0 & \dots \\ 0 & 0 & \sqrt{2} & 0 & 0 & \dots \\ 0 & 0 & 0 & \sqrt{3} & 0 & \dots \\ 0 & 0 & 0 & 0 & \sqrt{4} & \dots \\ 0 & 0 & 0 & 0 & 0 & \dots \\ \vdots & \vdots & \vdots & \vdots & \vdots & \ddots \end{pmatrix},\tag{3.23}$$

which shows a coupling between nearest energy states $n \rightarrow n - 1$. The Hamiltonian of the QHO written in terms of this operator becomes

$$\hat{H} = \hbar\omega_s \left(\hat{a}^\dagger \hat{a} + \frac{1}{2} \right).\tag{3.24}$$

The ground state energy (zero point energy) $\hbar\omega_s/2$ is the inherent energy of the trapped particle because the variance in its position and momentum together can not be zero due to the Heisenberg uncertainty principle.

Thermalisation and heating

QHOs may couple to other quantum systems that are difficult to describe in terms of a complete Hamiltonian. For example, in ion traps, the ion motion as a QHO couples to the thermally fluctuating electric field of nearby electrodes, which is a very large and macroscopic system that is difficult to describe as

a pure quantum system. The interaction with this thermal bath with heat $\hbar\omega_s\bar{n}_t$ and coupling to the QHO Γ_t can be described by collapse operators in a Lindblad master equation[92, Eq. 12]

$$\dot{\rho} = -\frac{i}{\hbar}[\hbar\omega_s\hat{a}^\dagger\hat{a}, \rho] + \mathcal{D}[\sqrt{\Gamma_t\bar{n}_t}\hat{a}]\rho + \mathcal{D}[\sqrt{\Gamma_t(\bar{n}_t+1)}\hat{a}^\dagger]\rho. \quad (3.25)$$

The Lindblad master equation is a generalisation of the time-dependent Schrödinger equation (TDSE) that allows evolution into mixed states via collapse operators. These collapse operators are performed within the super-operator $\mathcal{D}[\hat{F}]\rho = \hat{F}\rho\hat{F}^\dagger - 1/2(\hat{F}^\dagger\hat{F}\rho + \rho\hat{F}^\dagger\hat{F})$ which preserves the trace (total probability of all the states) of the density matrix ρ in the Lindblad master equation. In the steady state solution of equation 3.25, the thermal distribution for a QHO is found

$$\rho_{n,n} = \frac{\bar{n}_t^n}{(\bar{n}_t+1)^{n+1}}. \quad (3.26)$$

Even in cryogenic ion traps in equilibrium with the temperature of liquid helium (4.15 K), the energy spacing of the motional states is much greater than the thermal bath $\hbar\omega_s/k_B \approx 50$ mK. In this regime where $\bar{n}_t \gg 1$, the approximation holds $\Gamma_t\bar{n}_t \approx \Gamma_t(\bar{n}_t+1) \equiv R_h$, where R_h is the heating rate of the QHO with units of quanta per second. In trapped ion experiments, the heating rate is an important parameter which describes on what timescale an ion may remain in a known motional state. It is measurable through spectroscopic techniques including motional Raman sideband transitions and measurement of thermal line broadening. Both these techniques are made possible through the coupling of the atom's motion and atomic states through interacting photons.

Another technique for measuring temperature is spatial thermometry[93]. The spatial distribution of a trapped ion in a thermal mixed state is a Gaussian distribution² with variance the same as equation 3.21. By imaging an atom via its fluorescence, the temperature can be estimated by measuring the variance

²Weigh the absolute squares of the harmonic oscillator spatial wavefunctions (equation 3.19) against the density matrix for a thermal harmonic oscillator (equation 3.26).

in its spatial distribution. Performance-wise, the Abbe diffraction limit is the lower bound of the Gaussian diameter of a point-like source of light imaged by a system with numerical aperture NA,

$$2W_0 \geq \frac{2\lambda}{\pi NA}. \quad (3.27)$$

A high numerical aperture (NA) imaging system is required since the Abbe limit convolutes the ion's spatial distribution.

3.2 Hydrogen-like atoms

The choice of atom for trapped ion experiments is usually hydrogen-like atoms. These are atoms that hold a single unpaired electron in one of its outer orbitals. Trapped ions are also typically singly ionised, because of the low energy requirement for ionisation. Typical choices of atom are then found in the second group of the periodic table, Be^+ , Mg^+ , Ca^+ , Sr^+ and Ba^+ , since their singly ionised form contains an unpaired outer-orbital electron. Other examples of hydrogen-like trapped ions are $^{171}\text{Yb}^+$ and $^{229}\text{Th}^{3+}$. This section presents atomic theory that can be used to accurately describe the fluorescence and energy levels of $^{171}\text{Yb}^+$.

The energies of Hydrogen-like atoms were solved using the time-indepedent Schrödinger equation (TISE) by Erwin Schrödinger in the same paper he introduced the equation[94]. The TISE includes the kinetic and potential energy of an electron with charge e and mass m_e bound by a nucleus with charge Ze and mass $m_{nuc.}$,

$$E\psi(r, \theta, \phi) = \left(-\frac{\hbar^2}{2\mu}\nabla^2 - k\frac{Ze^2}{r}\right)\psi(r, \theta, \phi). \quad (3.28)$$

where the kinetic energy is described with the nucleus-electron reduced mass $\mu = (m_e^{-1} + m_{nuc.}^{-1})^{-1}$ and $k = (4\pi\epsilon_0)^{-1}$. Solutions are found by separating ψ

into separate functions for the radial and angular coordinates, $\psi_{n,l,m}(r, \theta, \phi) = R_{n,l}(r)Y_{l,m}(\theta, \phi)$. In terms of the atomic scale, $a_0 = \frac{\hbar^2}{k\mu e^2}$, the energy eigenvalues,

$$E_n = \frac{-1}{2a_0} \left(\frac{Ze}{n} \right)^2 \quad (3.29)$$

depend on quantum number n which describes what shell the electron is in, much like the Bohr model. The eigenvalues of equation 3.29 are independent of l & m absent the inclusion of additional physics. In reality, different energies are observed for different l & m numbered-states. This is because the Coulomb interaction between electron and nucleus alone does not account for other physical processes. For example, adding the first order relativistic term $-\frac{p^4}{8m_e^3c^2}$ to the Hamiltonian leads to an l dependent shift in the energy state of Hydrogen-like atoms, giving $l = 0, 1, 2, 3 \dots$ (S, P, D, F...) orbitals a non-degenerate energies. Quantum numbers l and m describe the angular component of the wavefunction and relate to the orbital angular momentum and its quantisation. Wavefunction solutions from Allen & Eberly[95] are used later in section 3.2.2 to derive electric dipole moments.

3.2.1 Fine Structure, Hyperfine Structure and Zeeman Shift

In the frame of an electron with non-zero orbital angular momentum quantum number L , the nucleus appears as a moving charge, which gives rise to a magnetic field. This magnetic field interacts with the intrinsic magnetic dipole moment of the electron, whose spin is $S = \frac{1}{2}$. This interaction produces an energy shift of states dependent on the values of L and S . A new total angular momentum quantum number $\vec{J} = \vec{L} + \vec{S}$ accounts for both the electron's orbital angular momentum and spin. The $L S$ coupling leads to energy splittings (fine structure) in all l orbitals besides S ($l = 0$) and energy spacing shifts between different l orbitals. For example, the P ($l = 1$) orbital breaks into two different

energies with different total angular momentum numbers $J = |L - S| = \frac{1}{2}$ and $J = L + S = \frac{3}{2}$.

The hyperfine structure comes about for similar reasons to the fine structure. Nuclei with an odd number of fermionic nucleons with spins $\pm \frac{1}{2}$ have a total spin I which must be non-zero. This spin couples to the magnetic field produced by an orbiting electron with total angular momentum J to produce a potential shift in the energy of the electron's state. This shift is much smaller than the fine structure because the magnetic dipole moment scales inversely with mass, so the nuclear magnetic moment is smaller by a factor of the order $m_n/m_e \approx 1836$ [96] where m_n is the mass of a nucleon. Total angular momentum is then given by the new quantum number $\vec{F} = \vec{J} + \vec{I}$ called the hyperfine quantum number.

The spin and orbital angular momentum of the atom can produce a magnetic moment. When these spins interact with an external magnetic field, an energy shift occurs (Zeeman shift in weak magnetic fields). The component of angular momentum along the magnetic field \vec{B} is quantised according to the quantum numbers m_F or m_J ($I \neq 0$ or $I = 0$).

The Breit-Rabi formula[97], which is an accurate model of energy splittings in hyperfine transitions when $J = \frac{1}{2}$ gives the perturbations in energy of the atomic states. With nuclear magnetic moments omitted³ the energy of states with quantum number F and m_F are,

$$E(B)_{F=I\pm 1/2} \approx -\frac{E_{HF}}{2(2I+1)} \pm \sqrt{(E_{HF})^2 + \frac{4m_F}{2I+1}g_J\mu_B BE_{HF} + (g_J\mu_B B)^2}, \quad (3.30)$$

where $\mu_B = \frac{e\hbar}{2m_e}$. It can be approximated using a Taylor series with respect to B for an atom with $I = 1/2$ to find the hyperfine transition resonance,

$$E(B)_{F=1} - E(B)_{F=0} \approx E_{HF} + m_F \frac{g_J}{2} \mu_B B + \left(\frac{1}{2} - \left(\frac{m_F}{2} \right)^2 \right) \frac{(g_J\mu_B)^2}{E_{HF}} B^2. \quad (3.31)$$

³The nuclear magneton is on the order $m_p/m_e \sim 1836$ times smaller than the Bohr magneton, so can be omitted in this case where only general trends and not precision measurements are being shown.

The zero-field splitting E_{HF} is recovered when $B = 0$. The term linear with B is the first order Zeeman shift. The second order term has a much smaller scaling due to the inverse E_{HF} term. For example in $^{171}\text{Yb}^+$, the second order scaling of the $^2S_{1/2}$ $F = 0$ $m_F = 0 \leftrightarrow F = 1$ $m_F = 0$ transition goes as 310.8 Hz/G²[65].

For weak magnetic fields, where the energy shift is small relative to the fine and hyperfine splittings, Zeeman shift in atoms with no hyperfine splitting goes as

$$\hbar\delta_B = m_J g_J \mu_B B. \quad (3.32)$$

For atoms with hyperfine splitting, replace J with F , where the Landé g-factor is[96]

$$g_J \approx 1 + \frac{J(J+1) + S(S+1) - L(L+1)}{2J(J+1)} \quad (3.33)$$

$$g_F \approx g_J \frac{F(F+1) - I(I+1) + J(J+1)}{2F(F+1)}.$$

This is identical to the linear term in equation 3.31 since $g_J = 2g_F$ when $J = 1/2$ and $I = 1/2$.

The relativistic corrections from the Dirac equation, fine structure, hyperfine structure and Zeeman shift are some of the major degeneracy breaking splittings that give atomic states their unique energies. States are referred to under the naming convention $N^{2S+1}L_J$ where quantum number L is replaced with the orbital names (S, P, D, F...) and quantum number m_J maybe be specified after or F and m_F if the atom has hyperfine structure. Another naming convention is used for electron configuration which refers to the filling of the orbitals and can be used to describe more complex states. It is written as $[X]^{N_1}L_1^{n_1}N_2L_2^{n_2}\dots$ where $[X]$ represents all the inner orbitals that the largest noble gas, with element abbreviation X, equivalently occupies. $N_iL_i^{n_i}$ represents electrons in the orbital with quantum numbers N and L (L replaced with the orbital names) and n being the number of electrons in that orbital. In Yb^+ , there exists an un-hydrogen-like state shorthanded $^3D[3/2]_{1/2}$ [98]. Its electron configuration is $[\text{Xe}]4f^{13}5d\ 6s$ and describes two unpaired electrons

in the 5d and 6s orbitals and the 4f orbital missing one electron from its usual full set of 14.

3.2.2 The two-level atom

A simplified atomic model comprising of two electron orbital wave-functions helps show some of the phenomena of atom-light interactions. The $(n, l, m) = (1, 0, 0)$ & $(2, 1, 1)$ states will be represented as $|g\rangle$ & $|e\rangle$ respectively as are chosen by Allen & Eberly[95]. The electron wave-functions are orthogonal, which can be shown by calculating $\iiint_V \psi_e^* \psi_g dV = 0$. Defining the energy eigenvalues of states $|g\rangle$ as E_1 and $|e\rangle$ as E_2 , the Hamiltonian can be written as,

$$\hat{H}_{atom} = E_1 |g\rangle \langle g| + E_2 |e\rangle \langle e|. \quad (3.34)$$

The general solution to the TDSE is

$$\psi(t) = e^{-iE_1 t/\hbar} c_g |g\rangle + e^{-iE_2 t/\hbar} c_e |e\rangle. \quad (3.35)$$

Solutions can be modified by adding a time-dependent phase factor that evolves with time like $e^{-iEt/\hbar}\psi(t)$. This effectively adds an energy shift to the Hamiltonian of $E\hat{I}$ without changing any of the dynamics. Typically, $E = E_1$ is chosen to make the phase of the ground state time-independent. The wave-function for an atom can then be simplified to $\psi(t) = c_g |g\rangle + e^{-i\omega_0 t} c_e |e\rangle$ where $\omega_0 = (E_2 - E_1)/\hbar$ is the resonant frequency of electromagnetic radiation to the transition according to the Planck relation.

3.2.3 Electric Dipole Moment and External Fields

Consider the change in potential an electron may experience from external electric fields $\mathbf{E}_0(t)$,

$$\hat{V}(t) = -q\vec{\mathbf{E}}_0(t) \cdot \hat{\mathbf{r}}, \quad (3.36)$$

where the electric field vector is uniform across the space the nucleus and electron occupy and $\hat{\mathbf{r}}$ is the position operator of the electron relative to the nucleus. A uniform electric field is a reasonable approximation for the electric field of a laser experienced by a stationary atom. Typical order of magnitude of nucleus-to-electron radius is 100 pm while typical laser wavelength is of order 100 nm and beam radius is of order 10 μm . However, the spread of the wavefunction of a trapped ion is comparable to optical wavelengths and in section 3.3 the effect of motion on the potential in equation 3.36 is considered. Using the identity relation, $I_2 = |g\rangle\langle g| + |e\rangle\langle e|$, equation 3.36 can be re-written as,

$$\begin{aligned}\hat{V}(t) &= I_2 \hat{V}(t) I_2 = \\ -q\vec{\mathbf{E}}_0(t) \cdot (&(\langle g | \hat{\mathbf{r}} | g \rangle |g\rangle\langle g| + \langle e | \hat{\mathbf{r}} | e \rangle |e\rangle\langle e| + \langle g | \hat{\mathbf{r}} | e \rangle |g\rangle\langle e| + \langle e | \hat{\mathbf{r}} | g \rangle |e\rangle\langle g|)).\end{aligned}\quad (3.37)$$

These terms can be solved by performing integrals over the wave-functions and operators. The integral as in Allen & Eberly[95] finds the off-diagonal terms of \hat{V} ,

$$\begin{aligned}q\langle e | \hat{\mathbf{r}} | g \rangle &= q \int_0^\infty \int_0^{2\pi} \int_0^\pi \psi_{2,1,1}^*(r, \theta, \phi) \vec{\mathbf{r}} \psi_{1,0,0}(r, \theta, \phi) r^2 \sin(\phi) d\phi d\theta dr \\ &= -\frac{2^7}{3^5} qa_0 (\hat{\mathbf{x}} - i\hat{\mathbf{y}}),\end{aligned}\quad (3.38)$$

where $\vec{\mathbf{r}} \equiv r(\hat{\mathbf{x}} \sin \theta \cos \phi + \hat{\mathbf{y}} \sin \theta \sin \phi + \hat{\mathbf{z}} \cos \theta)$. $\langle g | \hat{\mathbf{r}} | e \rangle = \langle e | \hat{\mathbf{r}} | g \rangle^*$ is found to be true by taking the conjugate of equation 3.38. The $\langle g | \hat{\mathbf{r}} | g \rangle$ and $\langle e | \hat{\mathbf{r}} | e \rangle$ terms integrate to zero, specifically in the θ integral. Redefining equation 3.38 as $\vec{\mathbf{d}}_{eg}$, and knowing diagonal terms of equation 3.36 equal zero, the interaction term can be re-written.

$$\hat{V}(t) = -\vec{\mathbf{E}}_0(t) \cdot (\vec{\mathbf{d}}_{eg} |e\rangle\langle g| + \vec{\mathbf{d}}_{eg}^* |g\rangle\langle e|) \quad (3.39)$$

For the chosen electron wavefunctions, the quantum number m is 0 in the ground state and +1 in the excited state. Let

$$\vec{E}_0(t) = E_0(\cos(\omega t)\hat{x} + \sin(\omega t)\hat{y})/\sqrt{2} \quad (3.40)$$

be circularly polarised since the unit vector of equation 3.38 appears to couple strongest to circularly polarised electric fields. To solve the evolution of state under this interaction, the Hamiltonian is transformed into the interaction picture. The interaction picture allows the comparatively weak interaction potential ($|\vec{d}_{eg}|E_0 \ll \hbar\omega_0$) to be added to the already solved hydrogen-like atom as a small perturbation,

$$\hat{V}_I = e^{i\hat{H}_{atom}t/\hbar}\hat{V}e^{-i\hat{H}_{atom}t/\hbar} = \frac{|\vec{d}_{eg}|E_0}{2}(e^{-i(\omega-\omega_0)t}|e\rangle\langle g| + e^{i(\omega-\omega_0)t}|g\rangle\langle e|) \quad (3.41)$$

In equation 3.41, \hat{H}_{atom} is first shifted by $-E_1\hat{I}$ so that it can be expressed more simply as $\hat{H}_{atom} = \hbar\omega_0|e\rangle\langle e|$. Expanding out the first exponential in equation 3.41 in the form of a Taylor series yields,

$$e^{i\hat{H}_{atom}t/\hbar} = \hat{I} + \sum_{k=1}^{\infty} (i\omega_0 t)^k (|e\rangle\langle e|)^k / k! = |g\rangle\langle g| + e^{i\omega_0 t}|e\rangle\langle e|, \quad (3.42)$$

where $(|e\rangle\langle e|)^k = |e\rangle\langle e|$. $e^{-i\hat{H}_{atom}t/\hbar}$ can be found taking the conjugate. The Rabi rate,

$$\Omega = \frac{\vec{d}_{eg} \cdot \vec{E}_0}{\hbar}. \quad (3.43)$$

is the rate at which the atom changes state when driven by an on-resonant external electric field, shown in equation 3.47. The TDSE is applied to the Hamiltonian in the interaction picture. When it is written in vector notation,

$$\frac{d}{dt} \begin{bmatrix} c_e(t) \\ c_g(t) \end{bmatrix} = \begin{bmatrix} 0 & -\frac{i\Omega}{2}e^{-i(\omega-\omega_0)t} \\ -\frac{i\Omega}{2}e^{i(\omega-\omega_0)t} & 0 \end{bmatrix} \begin{bmatrix} c_e(t) \\ c_g(t) \end{bmatrix}, \quad (3.44)$$

it produces two coupled ordinary differential equations (ODEs). c_g & c_e are coefficients of states $|g\rangle$ & $|e\rangle$ for the superposition ψ .

Since the electric field is always real, its spectrum consists of both positive and negative frequency components. This can create a phase term with frequency $\pm(\omega + \omega_0)t$ that arises when the electric field has terms that oscillate counter to the electric dipole moment in the interaction picture (Appendix B.2.1). In the regime where $\omega - \omega_0 \sim \Omega \ll \omega + \omega_0$, counter-rotating terms precess Rabi oscillations much faster than the Rabi rate itself. Their effect in typical atomic experiments where $\omega + \omega_0 \sim 10^8 \times \Omega$ is an unnoticeable precession of the Bloch vector. For this reason, they can be omitted for most cases from models under the rotating wave approximation (RWA).

Noticeably equation 3.44 has no counter-rotating terms. Appendix B.2 shows the calculations for why counter-rotating terms appear in π -transitions ($\Delta m = 0$) driven by linearly polarised light and not in σ^\pm -transitions ($\Delta m = \pm 1$) driven by circularly polarised light.

The coupled ODEs can be manipulated into two uncoupled second-order ODEs,

$$\begin{aligned} 0 &= \frac{d^2}{dt^2}c_e(t) + i\Delta\frac{d}{dt}c_e(t) + (\frac{\Omega}{2})^2c_e(t) \\ 0 &= \frac{d^2}{dt^2}c_g(t) - i\Delta\frac{d}{dt}c_g(t) + (\frac{\Omega}{2})^2c_g(t) \end{aligned} \quad (3.45)$$

where $\Delta \equiv \omega - \omega_0$. Proposing solutions, $c_e(t) = c_{e,0}e^{i\beta t}$ & $c_g(t) = c_{g,0}e^{i\alpha t}$ finds two solutions for each ODE, $\beta_\pm = -\Delta/2 \pm \sqrt{\Delta^2 + \Omega^2}/2$ and $\alpha_\pm = \Delta/2 \pm \sqrt{\Delta^2 + \Omega^2}/2$. Now initial conditions can be considered. Take the case of the ground state $c_g(0) = 1$ and $c_e(0) = 0$. The solutions to these conditions in the interaction picture are,

$$|\psi(t)\rangle = e^{i\frac{\Delta t}{2}} \left(\cos \frac{\Omega' t}{2} - i \frac{\Delta}{\Omega'} \sin \frac{\Omega' t}{2} \right) |g\rangle - ie^{-i\frac{\Delta t}{2}} \frac{\Omega}{\Omega'} \sin \frac{\Omega' t}{2} |e\rangle \quad (3.46)$$

where $\Omega' = \sqrt{\Delta^2 + \Omega^2}$. These solutions are useful in experiments where population of an atomic state is measured after excitation by a pulsed external

field. Excited state population scales as the absolute squared of $c_e(t)$ where,

$$|c_e(t)|^2 = \frac{\Omega^2}{\Omega'^2} \sin^2 \frac{\Omega' t}{2}. \quad (3.47)$$

Figure 3.4 shows Rabi oscillations in terms of the excited state population at different detunings. The solutions are only useful in cases where states

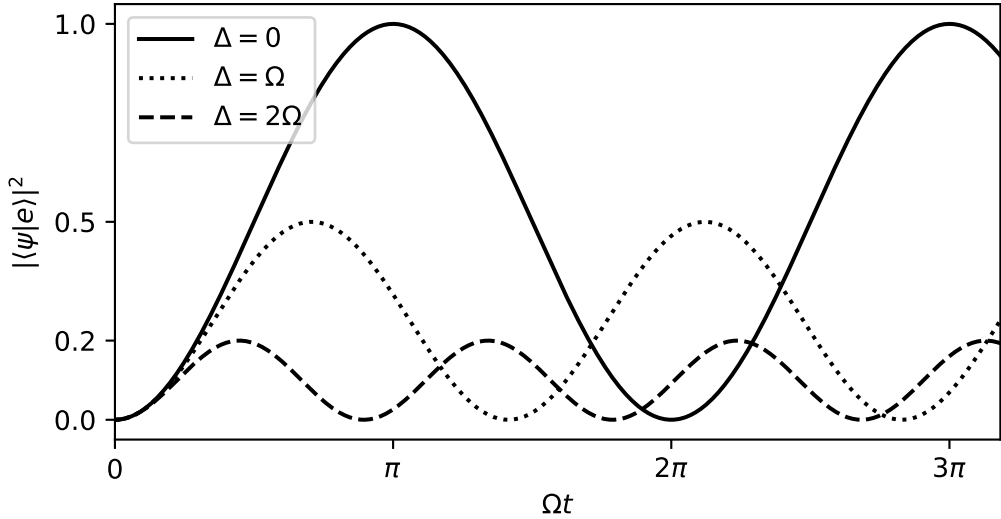


Figure 3.4: The excited state population as a function of pulse area (Ωt) for detunings in terms of the Rabi rate. Notice how the effective Rabi rate Ω' increases with increased detuning while the maximum transferable population decreases.

remain coherent over the time of excitation and measurement. The phase of the initial state changes sign after one oscillation of period $\frac{2\pi}{\Omega'}$. This sign change is important in the Cirac-Zoller gate[41].

Another Hamiltonian with similar solution,

$$\frac{\hat{H}}{\hbar} = \frac{\Delta}{2} \hat{\sigma}_z + \frac{\Omega}{2} \hat{\sigma}_x \quad (3.48)$$

can also be used to describe atom-light interactions. $\hat{\sigma}_x$ and $\hat{\sigma}_z$ are Pauli

matrices,

$$\hat{\sigma}_x = \begin{pmatrix} 0 & 1 \\ 1 & 0 \end{pmatrix}, \quad \hat{\sigma}_y = \begin{pmatrix} 0 & -i \\ i & 0 \end{pmatrix}, \quad \hat{\sigma}_z = \begin{pmatrix} 1 & 0 \\ 0 & -1 \end{pmatrix}. \quad (3.49)$$

Equation 3.48 can be derived by taking the interaction picture using the laser's frequency instead of the atom's resonant frequency

$$\begin{aligned} \hat{H}_0 &\rightarrow \hbar\omega |e\rangle\langle e| \\ \hat{V}(t) &\rightarrow \hat{V}(t) + \hbar(\omega_0 - \omega) |e\rangle\langle e|. \end{aligned} \quad (3.50)$$

In this picture, instead of the atom-light interaction evolving between σ_x and σ_y operators at rate Δ , the phase evolves at a rate Δ with the σ_z operator in equation 3.48. Its solution is the same as equation 3.46 except it does not contain the $e^{\pm i\frac{\Delta t}{2}}$ terms. This interaction picture is limited in that it becomes messy trying to describe multiple frequencies of light interacting with the same transition, but it is useful because it has no time-dependent components, making it easier to work with in other cases.

Magnetic dipole transitions also occur when two states are coupled by a magnetic dipole moment. Unlike electric dipole moments which are zero between states in the same orbital, the magnetic dipole can be non-zero. Similar to electric dipole moments, they can interact with electromagnetic fields and lead to the same dynamics as in equation 3.46. The Rabi rate $\Omega = \langle e | \hat{\mu} | g \rangle \cdot \vec{B}$ in magnetic dipole transitions are generally weaker than in electric dipole transitions in laboratory settings because of the limits in realistically producible magnetic field strengths compared to electric fields.

3.2.4 Spontaneous Emission and open quantum systems

The excited state in an electric dipole transition will decay into the ground state, even when the transition is not driven. This excited state lifetime, $\tau = 1/\Gamma$, where Γ is the spontaneous decay rate can be found by treating

the electric field amplitude as quantum and solving the dipole interaction for an excited state $|e\rangle$ interacting with many electric field modes (k) in their vacuum states $|e\rangle\langle e|\otimes_k|0_k\rangle\langle 0_k|$. The coupling out of $|e\rangle\langle e|\otimes_k|0_k\rangle\langle 0_k|$ to the ground state with any populated field mode, l , $|g\rangle\langle g|\otimes_{k=0}^{l-1}|0_k\rangle\langle 0_k|\otimes|1_l\rangle\langle 1_l|\otimes_{k=l+1}^{\infty}|0_k\rangle\langle 0_k|$ is strong because there are many transitions the system can use to reach the final state for an arbitrary excited mode l . The reverse process is much weaker because $|g\rangle\langle g|\otimes_{k=0}^{l-1}|0_k\rangle\langle 0_k|\otimes|1_l\rangle\langle 1_l|\otimes_{k=l+1}^{\infty}|0_k\rangle\langle 0_k|$ with specific mode l couples to only one other state, $|e\rangle\langle e|\otimes_k|0_k\rangle\langle 0_k|$. This mostly irreversible process transfers the information of the system to the quantised electro-magnetic (EM) field modes.

Derivation of the spontaneous emission rate (decay rate), ignoring the Hilbert space associated with the quantised EM field, leads to the rate equations[96, 99],

$$\begin{aligned}\frac{d}{dt}c_e(t) &= -\frac{\Gamma}{2}c_e(t) \\ \frac{d}{dt}c_g(t) &= \frac{\Gamma}{2}c_e(t),\end{aligned}\tag{3.51}$$

where,

$$\Gamma = \frac{\omega_0^3 d_{ge}^2}{3\pi\epsilon_0\hbar c^3}\tag{3.52}$$

A classical interpretation of spontaneous decay is that the atomic dipole is damped because the energised orbiting valence electron acts like an emitting antenna, producing EM radiation. Magnetic dipole transitions similarly have decay rates that also scale with their dipole strength squared and ω_0^3 [100]. Since magnetic dipole resonances in hyperfine transitions are usually in the microwave range and their dipole strengths are weak, spontaneous emission decay times are much slower (\sim 11 million years for hydrogen's ${}^2S_{1/2} F = 1 \rightarrow F = 0$ transition)[100, Eq. 26] compared to those in electric dipole transitions (\sim 8.1 nanoseconds in Yb $^+$'s ${}^2P_{1/2} \rightarrow {}^2S_{1/2}$ transition)[60].

3.2.5 The optical Bloch equations

The 2-level atom in section 3.2.3 (not including spontaneous emission) is a closed quantum system because it has been described fully in terms of Hermitian operators. Note a classical electric field was used, but the Hamiltonian was still Hermitian. Using the Lindblad master equation,

$$\frac{d\rho}{dt} = -\frac{i}{\hbar}[\hat{H}, \rho] + \mathcal{D}[\hat{F}]\rho, \quad (3.53)$$

the Rabi model can be extended to include spontaneous emission as a collapse operator $\hat{F} = \sqrt{\Gamma}|g\rangle\langle e|$ that can degrade the density matrix ρ into a mixed state. Steady state solutions to the Lindblad master equation (where $\dot{\rho} = 0$) can be found for an atom driven by an electric field described by the Hamiltonian of equation 3.48 and the spontaneous emission collapse operator \hat{F} . The terms of the density matrices are named according to $\rho_{ij} = c_i c_j^*$, where c are state coefficients used previously.

$$\begin{pmatrix} \dot{\rho}_{gg} \\ \dot{\rho}_{ge} \\ \dot{\rho}_{eg} \\ \dot{\rho}_{ee} \end{pmatrix} = \begin{pmatrix} 0 & \frac{i\Omega}{2} & \frac{-i\Omega}{2} & \Gamma \\ \frac{i\Omega}{2} & -i\Delta - \Gamma/2 & 0 & \frac{-i\Omega}{2} \\ \frac{-i\Omega}{2} & 0 & i\Delta - \Gamma/2 & \frac{i\Omega}{2} \\ 0 & \frac{-i\Omega}{2} & \frac{i\Omega}{2} & -\Gamma \end{pmatrix} \begin{pmatrix} \rho_{gg} \\ \rho_{ge} \\ \rho_{eg} \\ \rho_{ee} \end{pmatrix} \quad (3.54)$$

The matrix shows two decay rates, the longitudinal decay rate (Γ) and the transverse decay rate ($\Gamma/2$). The longitudinal decay rate moves population from ρ_{ee} to ρ_{gg} while the transverse decay process reduces off-diagonal terms of the density matrix to zero.

The medical and research fields of magnetic resonance imaging (MRI) and nuclear magnetic resonance (NMR) spectroscopy use three values to describe similar processes in magnetic dipole transitions:

1. T_1 time, the 1/e decay time for the longitudinal relaxation of a qubit.

This can be caused by interaction with a thermal bath, where the qubit

state populations relax into a Boltzmann distribution. It is similar to spontaneous emission in that both are longitudinal relaxations of the qubit.

2. T_2 time, the time for the off diagonal terms of a density matrix $|e\rangle\langle g|$, $|g\rangle\langle e|$ to reduce by a factor of e^{-1} . These off diagonal terms measure the coherence between the two states. It is a measure of the timescale for when phase information between the states is lost and the state can be considered mixed.
3. T_2^* time, faster than T_2 , it accounts for an ensemble of simultaneously probed qubits with varying transition energies, whose ensemble average phase will dephase quicker.

These processes in NMR-related fields are dominated by coupling of the environment (atom-atom collisions, magnetic field noise) to the qubit, unlike the pure radiative decay as described in equation 3.54.

Rows 1 and 4 of the 4×4 matrix in equation 3.54 are similar such that solving the equation in the steady state requires an extra equation. Normalisation ($\rho_{ee} + \rho_{gg} = 1$) must also be considered. The steady state solution of the optical Bloch equation for each of the density matrix coefficients are,

$$\begin{aligned}\rho_{gg} &= \frac{\Omega^2 + 4\Delta^2 + \Gamma^2}{2\Omega^2 + 4\Delta^2 + \Gamma^2} \\ \rho_{ge} &= \frac{-\Omega(2\Delta + i\Gamma)}{2\Omega^2 + 4\Delta^2 + \Gamma^2} \\ \rho_{eg} &= \frac{-\Omega(2\Delta - i\Gamma)}{2\Omega^2 + 4\Delta^2 + \Gamma^2} \\ \rho_{ee} &= \frac{\Omega^2}{2\Omega^2 + 4\Delta^2 + \Gamma^2},\end{aligned}\tag{3.55}$$

where ρ_{ee} describes a very important quantity in atomic physics, the excited state population of an atom driven on an electric dipole transition. Two key features of this equation are:

1. As Ω (proportional to electric field amplitude) approaches infinity, the excited state population approaches $\frac{1}{2}$.

2. The resonance appears as a Lorentzian distribution with respect to Δ with a full width at half maximum (FWHM) of $\sqrt{\Gamma^2 + 2\Omega^2}$. The natural linewidth of Γ is recovered in the case where $\Omega = 0$, while increase in linewidth due to increase in Ω is known as power broadening. Other broadening mechanisms exist, such as pressure broadening, where atom-atom collisions can increase the dephasing rate[101].

It is useful to express Rabi rate in terms of laser intensity. Laser intensity is an easily inferred quantity experimentally by measuring a laser beam's spatial profile along with its power. In a vacuum, its relation to the electric field magnitude is[102]

$$I = \frac{|E|^2}{2} \sqrt{\frac{\epsilon_0}{\mu_0}} = \frac{1}{2} c \epsilon_0 |E|^2. \quad (3.56)$$

By incorporating equations 3.43 and 3.52, an alternate expression for Rabi rate is found,

$$\Omega = \Gamma \sqrt{\frac{I}{2I_0}}, \quad (3.57)$$

where

$$I_0 = \frac{\hbar \Gamma \omega_0^3}{12 \pi c^2} \quad (3.58)$$

is the saturation intensity. In the dipole approximation it is an intrinsic property of a dipole transition depending on its transition frequency and linewidth. ρ_{ee} can then be written in terms of the on-resonant saturation parameter $s = I/I_0$ which leads to,

$$\rho_{ee} = \frac{1}{2} \frac{s}{s + 1 + (\frac{2\Delta}{\Gamma})^2}, \quad (3.59)$$

which when plotted as in figure 3.5 shows the power broadening as well as the $\rho_{ee} < 0.5$ limit. The excited state population in experiment can be inferred by measuring an atom's spontaneous emission rate. This is because the depopulation of the excited state is accompanied by an increase in quanta of coupled EM modes at a rate proportional to the excited state population

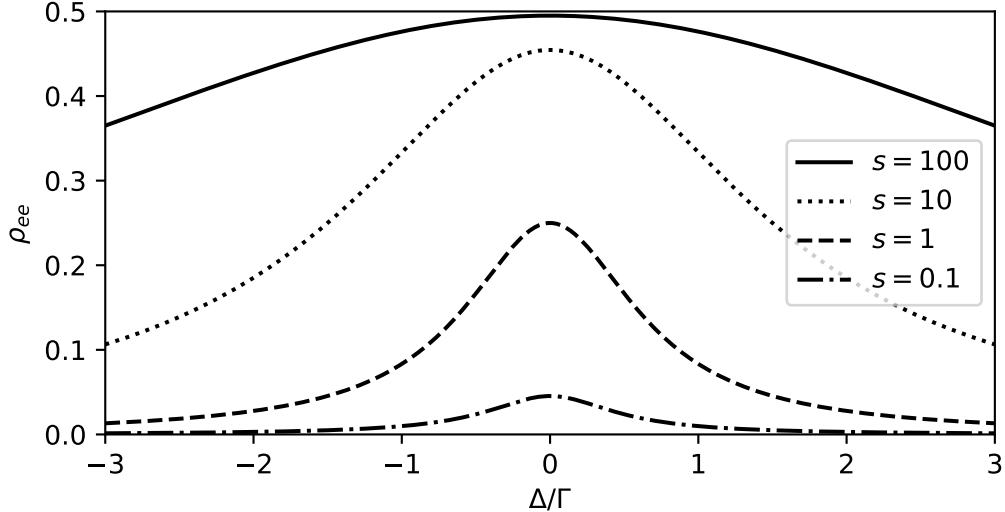


Figure 3.5: The excited state population of an atom driven by an electric field as a function of detuning in units of natural linewidth for different saturation parameters.

(equation 3.51). The rate of spontaneous emission of the atom into all these modes combined is $\Gamma \rho_{ee}$ with dimensions quanta per unit time.

3.3 Light-Motion Coupling

Motional states are coupled to atomic states because the optical field not only influences atomic states but also induces a change in momentum through recoil kicks of absorbed and emitted photons. Equation 3.39 can be modified to include a position operator to find the electric field of the plane wave at the ion,

$$\hat{V}(t) = -\mathbf{E}_0 e^{i\omega t} e^{-ik\hat{x}} \cdot \mathbf{d}_{eg} |e\rangle \langle g| + h.c. \quad (3.60)$$

This is a travelling plane wave electric field where \mathbf{k} is the wavevector and \hat{x} is the position operator of the ion (equation 3.22). When the wave is travelling in a vacuum, $k = \omega/c$ so $k\hat{x} = \frac{\omega}{c} \sqrt{\frac{\hbar}{2m\omega_s}} (a^\dagger + a)$. The unitless Lamb-Dicke parameter

$$\eta = \frac{\omega}{c} \sqrt{\frac{\hbar}{2m\omega_s}}, \quad (3.61)$$

describes the strength of the atom-light interaction. The Lamb-Dicke parameter is also interpreted in terms of particle collisions $\eta = \sqrt{\omega_{rec}/\omega_s}$ where a photon transfers

$$\hbar\omega_{rec} = \frac{(\hbar k)^2}{2m} \quad (3.62)$$

recoil energy to the atom after it is absorbed (derived considering an inelastic collision between photon and atom). Beyond 1D cases, the dot product between the ion motion and the wavevector must be considered. This can reduce the Lamb-Dicke parameter by $\cos\theta$, where θ is the motion-wavevector difference in angle. The position operator in the exponent of equation 3.60 can be interpreted with a Taylor series,

$$e^{-ik\hat{x}} = e^{-i\eta(\hat{a}^\dagger + \hat{a})} \approx \hat{I} - i\eta(\hat{a}^\dagger + \hat{a}) - \frac{\eta^2}{2}(\hat{a}^\dagger + \hat{a})^2 + i\frac{\eta^3}{3!}(\hat{a}^\dagger + \hat{a})^3 + \dots \quad (3.63)$$

3.3.1 The Lamb-Dicke regime

An atom with a spatial distribution much smaller than the wavelength of an interacting optical field, $\langle x^2 \rangle \ll (\lambda/2\pi)^2$, will experience only very small differences in the optical field over its wavefunction. This regime is exactly the Lamb-Dicke regime, which is reached when trapped ions are in a sufficiently low motional state for a specific value of the Lamb-Dicke parameter,

$$\eta^2(2\langle \hat{a}^\dagger \hat{a} \rangle + 1) \ll 1. \quad (3.64)$$

In this regime, the first two terms of equation 3.63 dominate the dynamics and the other terms can be omitted. The Hamiltonian describing the atomic states (equation 3.48) and motion (equation 3.24) consequently become much simpler and can be expressed in a short Hamiltonian by expanding the Hilbert space with a tensor product, along with the interaction term in the Lamb-Dicke

regime,

$$\hat{H} = \frac{1}{2}\Delta\hat{I} \otimes \hat{\sigma}_z + \omega_s \left(\hat{a}^\dagger \hat{a} \otimes \hat{I} + \frac{1}{2} \right) + \frac{1}{2}\Omega(\hat{I} \otimes \hat{\sigma}_x - \eta(\hat{a}^\dagger + \hat{a}) \otimes \hat{\sigma}_y). \quad (3.65)$$

There are 3 atomic transition resonances per motional state (2 when in the motional ground state) with coupling strengths,

$$\begin{aligned} \Omega_{n \rightarrow n} &= \Omega \\ \Omega_{n \rightarrow n-1} &= \sqrt{n}\eta\Omega \\ \Omega_{n \rightarrow n+1} &= \sqrt{n+1}\eta\Omega, \end{aligned} \quad (3.66)$$

as illustrated spectrally in figure 3.6.

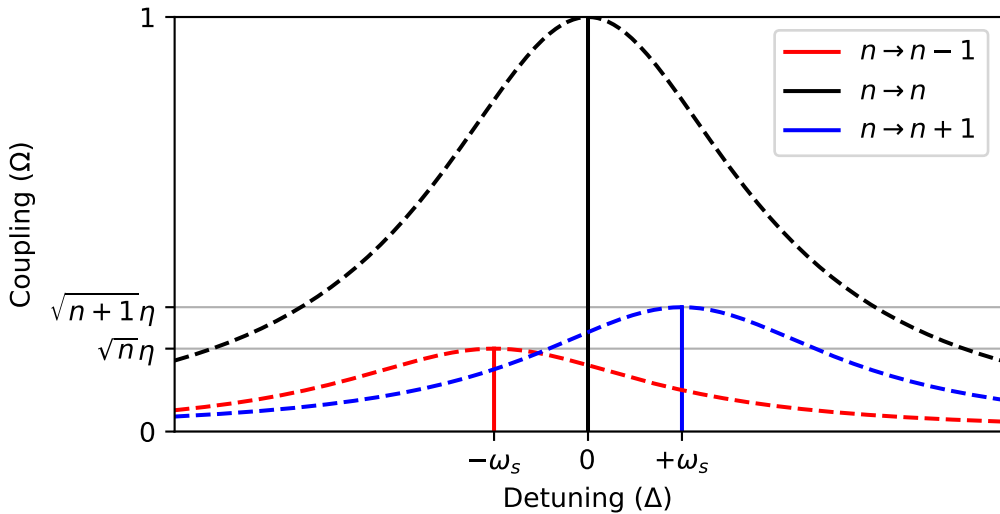


Figure 3.6: The resonances (solid vertical lines) of an atom with harmonic motion in the Lamb-Dicke Regime. In electric dipole transitions, the natural linewidth due to spontaneous emission (dashed lines) typically broadens the resonances with a linewidth much greater than the motional mode spacing. This is a technological limit that could be overcome by engineering strong traps with high ω_s values. Alternatively, atomic transitions with narrow natural linewidths, such as quadrupole transitions, can resolve these resonances[34].

3.3.2 Beyond the Lamb-Dicke regime

When the higher order terms of equation 3.63 can not be approximated to zero, a more general solution of all Rabi rates exist[103],

$$\begin{aligned} A_{n \rightarrow n} &= \Omega_{n \rightarrow n}/\Omega = e^{-\frac{\eta^2}{2}} L_n^0(\eta^2) \\ A_{n \rightarrow n-k} &= \Omega_{n \rightarrow n-k}/\Omega = e^{-\frac{\eta^2}{2}} \sqrt{\frac{(n-k)!}{n!}} \eta^k L_{n-k}^k(\eta^2) \\ A_{n \rightarrow n+k} &= \Omega_{n \rightarrow n+k}/\Omega = e^{-\frac{\eta^2}{2}} \sqrt{\frac{n!}{(n+k)!}} \eta^k L_n^k(\eta^2), \end{aligned} \quad (3.67)$$

where $L_n^k(x)$ are the generalised Laguerre polynomials[88, Eq. 18.5.12] (table 3.2). Equation 3.67 has a similar trend to Bessel functions of the first

$L_n^k(x)$	$n = 0$	$n = 1$	$n = 2$	$n = 3$
$k = 0$	1	$-x + 1$	$\frac{x^2}{2} - 2x + 1$	$-\frac{x^3}{6} + \frac{3x^2}{2} - 3x + 1$
$k = 1$	1	$-x + 2$	$\frac{x^2}{2} - 3x + 3$	$-\frac{x^3}{6} + 2x^2 - 6x + 4$
$k = 2$	1	$-x + 3$	$\frac{x^2}{2} - 4x + 6$	$-\frac{x^3}{6} + \frac{5x^2}{2} - 10x + 10$
$k = 3$	1	$-x + 4$	$\frac{x^2}{2} - 5x + 10$	$-\frac{x^3}{6} + 3x^2 - 15x + 20$

Table 3.2: The first few generalised Laguerre polynomials[88, Eq. 18.5.12].

kind, which describe the strength of sidebands of a phase modulated signal. Classically, the $k\hat{x}$ term in equation 3.60 acts as a sinusoidal phase modulation term (equation 3.15). So classically, the laser's carrier frequency appears to the ion to have sidebands split by the ion's secular frequency and strength described by Bessel functions of the first kind. Equation 3.67 is plotted in figure 3.7 for the first few positive values of k and is seen to follow the same trend as Bessel functions. Figure 3.8 shows the overlap of the wavefunctions and comparisons against the wavelength of light, which help visualise how the couplings in figure 3.7 come about.

As an atom in a thermal state increases in average motional quanta, higher order transitions beyond the Lamb-Dicke regime have greater coupling to light. Since the higher order transitions are spaced in resonance by ω_s , they cause thermal Doppler broadening of the transition.

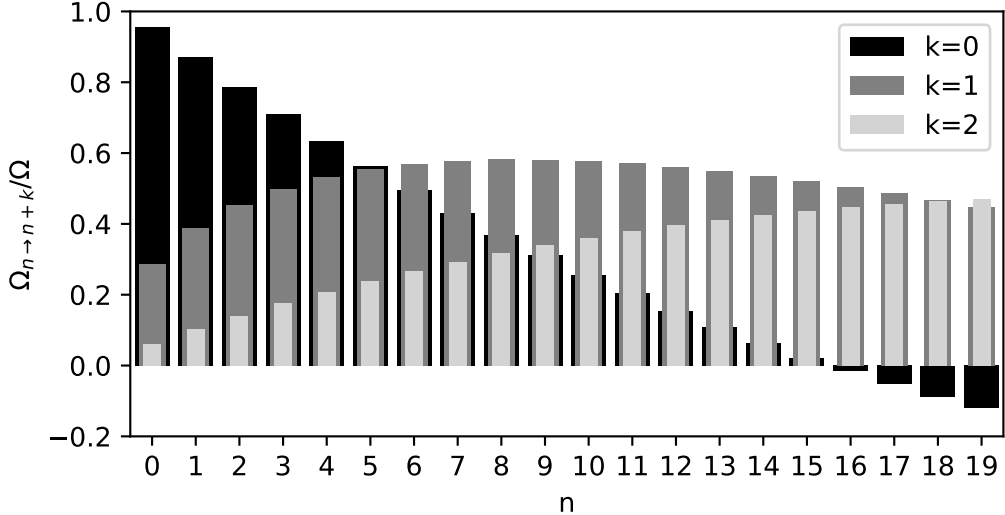


Figure 3.7: Equation 3.67 plotted against motional state n for the first few positive k values for $\eta = 0.3$. Unlike in the Lamb-Dicke Regime, the strength of the $k = 0$ transitions are not constant through n and even reverse phase at $n = 16$. This reversal occurs when the spatial distribution is on the order of $\lambda/2$. The $k = 1$ transitions do not continue increasing as \sqrt{n} and higher order modes are non-zero.

3.3.3 Spontaneous Emission's effect on motion

The collapse operator, $\hat{F} = \sqrt{\Gamma} |g\rangle \langle e|$ from section 3.2.5 can now be modified to include its effect on motion due to photon recoil[104],

$$\begin{aligned}\hat{F}_L &= \sqrt{\frac{\Gamma}{2}} e^{i\eta(a^\dagger + a)} \otimes |g\rangle \langle e| \\ \hat{F}_R &= \sqrt{\frac{\Gamma}{2}} e^{-i\eta(a^\dagger + a)} \otimes |g\rangle \langle e|,\end{aligned}\quad (3.68)$$

where there are now two separate collapse operators for spontaneous emission where photons travelling left or right in this 1-D motion system can be distinguished. Because couplings to $n \rightarrow n + k$ are slightly more preferential at low temperatures than $n \rightarrow n - k$ (equation 3.66), there is a slight heating due spontaneous emission in the Lamb-Dicke regime. By numerically simulating the Lindblad master equation[105], it was found spontaneous emission increases the average motional quanta on average by η^2 per emission event. For typical ion trap systems where $\eta \sim 0.1$, this is an increase of $\Delta\bar{n} \sim 0.01$.

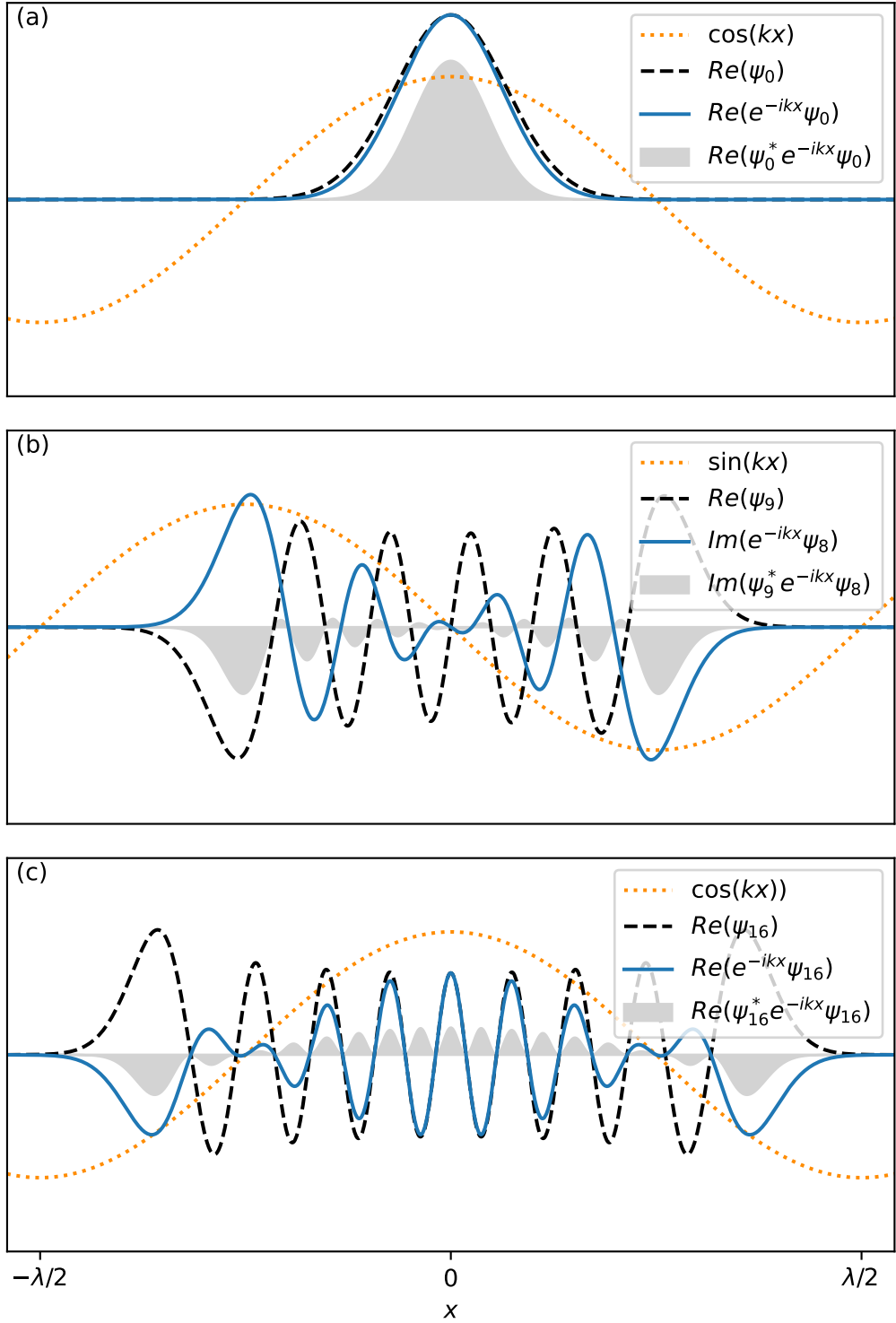


Figure 3.8: Fock states of trapped ion motion before $\psi_n(x)$ and after $e^{-ik\hat{x}}\psi_n(x)$ being optically excited. (a) $\psi_0(x)$ is in the Lamb-Dicke regime where the change in wavefunction from the excitation is small. (b) The imaginary part of the wavefunction of $e^{-ik\hat{x}}\psi_8(x)$ after excitation couples strongly to the real part of $\psi_9(x)$, shown by the negative overlap. (c) An excited $\psi_{16}(x)$ wavefunction, $e^{-ik\hat{x}}\psi_{16}(x)$, couples weakly to itself, shown by the wavefunction overlap which integrates nearly to zero. $\eta = 0.3$ was chosen for these plots.

3.3.4 Doppler cooling

A useful exploitation of this light-motion coupling is Doppler cooling. By detuning a laser to a frequency lower than the atomic resonance, red sidebands (figure 3.6) can be favourably driven over blue sidebands. These red sideband transitions carry population from $|n, g\rangle$ to $|n - k, e\rangle$, while spontaneous emission often resets the atomic state from $|n, e\rangle$ to $|n, g\rangle$. This creates a Doppler cooling cycle where on average, over time, the average motional quanta decreases. When the rate of heating from the off-resonant blue sideband transitions equals the rate of cooling, the ion's average motional quanta reaches a steady state. The associated minimum possible energy of a bound atom is the Doppler limit[106],

$$\hbar\omega_s \left(\bar{n} + \frac{1}{2} \right) \geq \frac{\hbar\Gamma}{2}, \quad (3.69)$$

and can be reached when the detuning of the incident light from resonance is $\Delta = -\Gamma/2$ and the Rabi rate is small such that power broadening is negligible. This equation is only true in the weak binding regime where $\omega_s \ll \Gamma$. In stronger regimes, blue sidebands are rarely excited and the limit is influenced more by spontaneous emission recoil[106]. This weak binding limit is illustrated (figure 3.9) by simulating the quantum system described by the master equation with collapse operators from equation 3.68 and light-motion coupling not in the Lamb-Dicke regime with a numerical steady state solver[105]. Equations used for this simulation are,

$$\dot{\rho} = -\frac{i}{\hbar} [\hat{H}, \rho] + \mathcal{D}[\hat{F}_L]\rho + \mathcal{D}[\hat{F}_R]\rho, \quad (3.70)$$

where,

$$\frac{\hat{H}}{\hbar} = \frac{1}{2}\Delta\hat{I} \otimes \sigma_z + \omega a^\dagger a \otimes \hat{I} + \frac{1}{2}\Omega(e^{i\eta(a^\dagger + a)} \otimes |g\rangle\langle e| + h.c.). \quad (3.71)$$

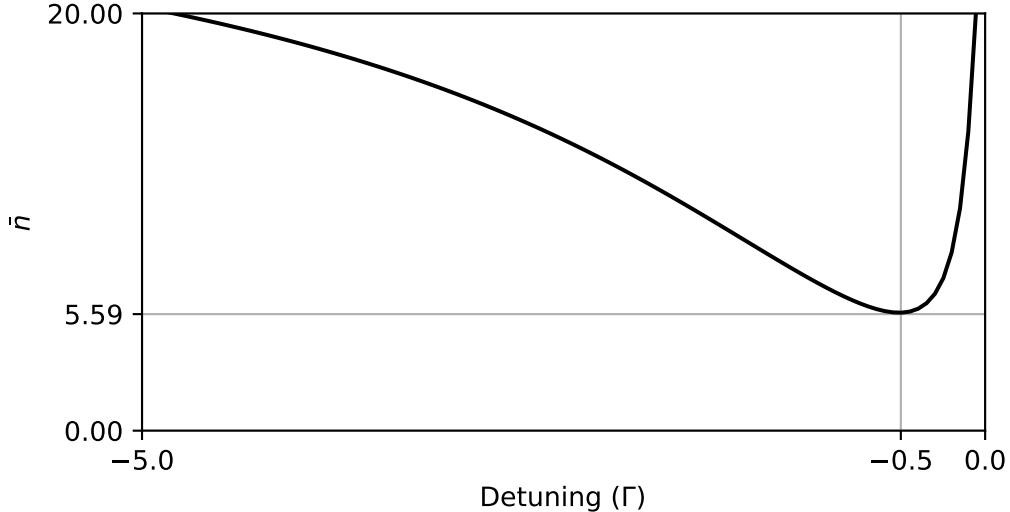


Figure 3.9: Numerical steady state solution to the average motional quanta given equations 3.70 and 3.71. The detuning is in units of natural linewidth and a small coupling $\Omega = 0.01\Gamma$ was chosen for the simulation. Typical experimental values were used for parameters $\omega_s = 0.082\Gamma$ and $\eta = 0.073$. The expected Doppler cooling limit $\bar{n} = \Gamma/2\omega_s - 0.5 \approx 5.59$ and the optimal detuning $\Delta = -\Gamma/2$ are consistent with the simulation. 60 motional states were used in the simulation and only the first four Taylor series terms of $e^{-i\eta(a^\dagger + a)}$.

3.3.5 Raman Transitions

Extending to three level atoms, Raman transitions are ground-to-ground-state transitions where transfer of population is mediated via an excited state. It finds wide application in chemistry where lasers are used to excite molecules from one vibrational ground state and observe their fluorescence as Stokes(anti-Stokes) scattered photons lose(gain) energy as they decay into another rovibronic (rotational-vibrational-electronic) state of higher(lower) energy.

Similarly, rovibronic resonances in molecular trapped ions have been observed [107], however these transitions were excited directly rather than observing Raman scattering. The motional state energy spacings in singular trapped ions are much smaller than rovibronic resonances (MHz compared to THz) making observing energy shifts spectroscopically very difficult.

Instead, trapped ions can use coherent Raman transitions, where both excitation and (anti-)Stokes scattering are stimulated using lasers typically far-

detuned from the excited state resonance. Instead of fluorescence spectroscopy, state selective fluorescence (section 3.6) is used to measure the population transferred by a Raman transition.

Similar to equation 3.48, a Hamiltonian describing this system (omitting motional coupling, which will be added in section 3.3.6) can be written as,

$$\frac{\hat{H}}{\hbar} = \delta |\uparrow\rangle\langle\uparrow| + \Delta |e\rangle\langle e| + \left(\frac{\Omega_P}{2} |\downarrow\rangle\langle e| + \frac{\Omega_S}{2} |\uparrow\rangle\langle e| + h.c. \right), \quad (3.72)$$

where Ω_P and Ω_S represent the pump and Stokes transitions' Rabi rates respectively. The Pump electric field has detuning Δ from the excited state resonance and the Stokes field has detuning $\Delta - \delta$. A large detuning from resonance is chosen for coherent optical Raman transitions to suppress spontaneous emission processes (equation 3.51). When Δ is large compared to the Rabi rates, as in a two level system, both the change in- and the overall occupation of excited state population remains low (equation 3.46). Using the TDSE, three coupled differential equations are produced [103],

$$\begin{aligned} \dot{c}_\downarrow &= -i\frac{\Omega_P}{2}c_e \\ \dot{c}_\uparrow &= -i\left(\frac{\Omega_S}{2}c_e + \delta c_\uparrow\right) \\ \dot{c}_e &= -i\left(\frac{\Omega_P}{2}c_\downarrow + \frac{\Omega_S}{2}c_\uparrow + \Delta c_e\right), \end{aligned} \quad (3.73)$$

where in the case of large detuning, it is reasonable to approximate $\dot{c}_e \approx 0$ under the adiabatic approximation. The system can be simplified into two coupled ODEs,

$$\begin{aligned} \dot{c}_\downarrow &= \frac{i\Omega_P}{4\Delta}(\Omega_P c_\downarrow + \Omega_S c_\uparrow) \\ \dot{c}_\uparrow &= \frac{i\Omega_S}{4\Delta}(\Omega_P c_\downarrow + \Omega_S c_\uparrow) - i\delta c_\uparrow, \end{aligned} \quad (3.74)$$

where a simplified Hamiltonian describing this system can be written in terms of Pauli matrices,

$$\frac{\hat{H}}{\hbar} = \left(\frac{\delta}{2} - \frac{\Omega_S^2 + \Omega_P^2}{8\Delta} \right) \hat{I} + \left(-\frac{\delta}{2} + \frac{\Omega_S^2 - \Omega_P^2}{8\Delta} \right) \hat{\sigma}_z - \frac{\Omega_S \Omega_P}{4\Delta} \hat{\sigma}_x. \quad (3.75)$$

This Hamiltonian can be simplified further by considering a rotating frame that makes the \hat{I} term disappear. The Hamiltonian then has identical structure to a two level system (equation 3.48). The equivalent Rabi rate for a Raman transition is

$$\Omega_R = \frac{\Omega_P \Omega_S}{2\Delta} \quad (3.76)$$

and detuning is

$$\Delta_R = \frac{\Omega_S^2 - \Omega_P^2}{4\Delta} - \delta \quad (3.77)$$

The $\frac{\Omega_S^2 - \Omega_P^2}{4\Delta}$ component of the detuning is the light shift, which can be cancelled by having equal pump and (anti-)Stokes couplings to both transitions.

An important feature of Raman transitions is they are not broadened by any natural linewidth which means they can be made arbitrarily narrow by decreasing the Rabi rate by either increasing Δ or reducing the pump and Stokes beams' powers. Linewidth will only sharpen up to the point where decoherence from other processes become significant. A narrow linewidth is useful in addressing transitions close in energy that would otherwise be unresolved by the broad natural a fast decaying electric dipole transitions driven by a single laser. The quantised states of harmonic motion in trapped ions are such examples of closely spaced energy levels ($\omega_s \sim 1$ MHz).

3.3.6 Resolved Motional Sideband Raman Transitions

To cool beyond the Doppler limit, the line broadening from the natural linewidth of the electric dipole transitions needs to be avoided so that $n \rightarrow n + k$ transitions are not being off-resonantly driven. This can be achieved with Raman transitions. From section 3.3.5 it was found a quantum state remains coherent through an entire Raman transition because the excited state $|e\rangle$ is rarely populated enough to spontaneously decay. This avoids the resulting line broadening that would come from this decay. This means only the power broadening due to the Rabi rate contributes to transition linewidths. Following

the derivation from Steinbach et al[108], the adiabatic approximation can be made with the motion terms considered. The effective Hamiltonian, in the same form as equation 3.72

$$\frac{\hat{H}_{eff}}{\hbar} = \omega_s a^\dagger a + \left(-\frac{\delta}{2} + \frac{\Omega_S^2 - \Omega_P^2}{8\Delta} \right) \sigma_z + \frac{\Omega_P \Omega_S}{4\Delta} (e^{i(\eta_P - \eta_S)(\hat{a}^\dagger + \hat{a})} |\uparrow\rangle \langle \downarrow| + h.c.) \quad (3.78)$$

now contains motional energy and interaction terms with Lamb-Dicke parameters from the pump and Stokes beams. Since the only line broadening is from power broadening which scales as the Raman transition's Rabi rate $\Omega_R \equiv \frac{\Omega_P \Omega_S}{2\Delta}$, individual motional resonances can be selected out spectrally when $\Omega_R \ll \omega_s$. Also, the new effective Lamb-Dicke parameter is the difference in the separate beams' Lamb-Dicke parameters so if beams are co-propagating, they will not drive any motional sidebands. If the beams are counter-propagating, the effective Lamb-Dicke parameter increases. By tuning the resonance of the Raman transition such that,

$$k\omega_s = \delta - \frac{\Omega_S^2 - \Omega_P^2}{4\Delta}, \quad (3.79)$$

$n \rightarrow n + k$ transitions can be driven with coupling that follows equation 3.67. The ability to drive singular motional transitions with the coherent narrow-linewidth Raman transitions opens up the possibility to perform exact operations on the motional state of a trapped ion. The two main uses of resolved motional sideband Raman transitions are ground state cooling and performing entangling operations by taking advantage of the shared motional mode of two ions in the same ion trap.

3D Resolved Motional Sideband Raman Transitions

The motion of a trapped ion is well described by three uncoupled quantum harmonic oscillators at the three different secular frequencies. This is sup-

ported by the observation of highly anisotropic temperatures (< 60 mK and > 15 K) in different motional modes of a single ion[93], which suggests the coupling between these modes is on the order of $250\times$ smaller than the interaction strength of the Doppler cooling beam on the cold mode in that experiment. Three Lamb-Dicke parameters can be described for the coupling of the pump and Stokes lasers to the modes according to the laser's wavevector \vec{k} and the mode directions $\eta_x = \vec{k} \cdot \hat{x}x_0$, $\eta_y = \vec{k} \cdot \hat{y}y_0$ and $\eta_z = \vec{k} \cdot \hat{z}z_0$. The effective Hamiltonian could then be re-written

$$\begin{aligned} \frac{\hat{H}_{eff}}{\hbar} = & \sum_{i=x,y,z} \omega_i \hat{a}_i^\dagger \hat{a}_i + \left(-\frac{\delta}{2} + \frac{\Omega_S^2 - \Omega_P^2}{8\Delta} \right) \sigma_z \\ & + \frac{\Omega_P \Omega_S}{4\Delta} (e^{i(\eta_{P,x} - \eta_{S,x})(\hat{a}_x^\dagger + \hat{a}_x)} \otimes e^{i(\eta_{P,y} - \eta_{S,y})(\hat{a}_y^\dagger + \hat{a}_y)} \otimes e^{i(\eta_{P,z} - \eta_{S,z})(\hat{a}_z^\dagger + \hat{a}_z)} |\uparrow\rangle\langle\downarrow| + h.c.). \end{aligned} \quad (3.80)$$

Which describes resonances that appear at combinations of the three secular frequencies,

$$\sum_{i=x,y,z} k_i \omega_i = \delta - \frac{\Omega_S^2 - \Omega_P^2}{4\Delta}, \quad (3.81)$$

where k_i are integers corresponding to three combined transitions $n_i \rightarrow n_i + k_i$ with Rabi rates multiplied three times by equation 3.67 for each of the motional modes.

3.4 Experimental considerations

3.4.1 Qubit dephasing from resonance fluctuations

Two-level atomic systems with long T_1 and T_2 coherence times serve well as memory qubits. Typically coherence of these memory qubits is limited by the observer's knowledge of the fluctuations of the qubit's phase due to the environment. Coherence will be defined using the relative phase ϕ of the qubit states as $\langle e^{i\phi} \rangle$. In the interaction picture, the phase evolution of an atomic

qubit is governed by the detuning between the qubit's resonant energy and the resonance of the driving field[109, 110]. Both can be affected by noise and fluctuate over time.

Qubit energy fluctuations

Consider a magnetic dipole transition where the energy of the excited state $|e\rangle$ experiences a Zeeman shift from a noisy external magnetic field with magnitude $B(t) = B_0 + \Delta B(t)$. The resonance Zeeman shift $\Delta\omega(t)$ over time would be given by equation 3.32 and the solution to the TDSE would then give a state similar to equation 3.35 but with the extra phase term in the excited state,

$$e^{i\phi(t)} = e^{i \int_0^t \Delta\omega(t') dt'}. \quad (3.82)$$

The fluctuation in $\Delta\omega(t)$ is a stochastic process, so $\langle e^{i\phi(t)} \rangle$ is of interest. Sousa[109] derives,

$$\langle e^{i\phi(t)} \rangle = e^{-\frac{1}{2}\sigma_t^2} \quad (3.83)$$

where

$$\sigma_t^2 = 2 \int_0^t (t - t') S(t') dt' \quad (3.84)$$

and

$$S(t') = \langle \Delta\omega(t') \Delta\omega(0) \rangle. \quad (3.85)$$

$S(t')$ is an auto-correlation function of the fluctuation of the resonance shift. Using the Wiener-Khinchin theorem[111], it can be expressed in terms of its power spectrum $\tilde{S}(\omega)$ (the tilde represents a Fourier transform has been performed on S),

$$S(t') = \frac{1}{2\pi} \int_0^\infty \tilde{S}(\omega) \cos(\omega t') d\omega. \quad (3.86)$$

It is useful to think of the dimensions of the power spectrum $\tilde{S}(\omega)$ as frequency-squared-per-frequency-band since it is a measure of the spectral density of the variance of the resonant frequency. The time integral in equation 3.84 can

then be solved,

$$\sigma_t^2 = \frac{2}{\pi} \int_0^\infty \tilde{S}(\omega) \frac{\sin^2(\frac{1}{2}\omega t)}{\omega^2} d\omega. \quad (3.87)$$

This solution shows that the evolution of the dephasing is dependent of the power spectrum of the noise. Three common noise sources that can be considered are white noise, cut-off white noise and a pure tone.

White noise

White noise is characterised as having flat spectral response across the entire spectrum, s.t. $\tilde{S}(f) = \tilde{S}_0$. Solving equation 3.87 with this spectrum gives the expectation value of phase,

$$\langle e^{i\phi(t)} \rangle_{white} = e^{-\frac{\tilde{S}_0 t}{4}}. \quad (3.88)$$

The trend is an exponential decay in phase that increases in rate with higher spectral power.

Cut-off white noise

In some cases, white noise sources may be only prominent in a certain band, from DC up to some cutoff frequency f_c . In this case, the noise spectrum could be written in terms of the Heaviside step function, $\tilde{S}(\omega) = \tilde{S}_0 H(\omega) H(\omega_c - \omega)$. The resultant expectation value of the phase,

$$\langle e^{i\phi(t)} \rangle_{white\ cut} = e^{-\frac{\tilde{S}_0}{2\pi} (t \text{Si}(\omega_c t) - 2\omega_c^{-1} \sin^2(\frac{1}{2}\omega_c t))}, \quad (3.89)$$

contains a $t \text{Si}(\omega_c t)$ term where $\text{Si}(x) = \int_0^x \frac{\sin(t)}{t} dt$. The expectation value follows a Gaussian, $\langle e^{i\phi(t)} \rangle \approx e^{-\frac{\tilde{S}_0}{2\pi} \omega_c t^2}$, when $t \lesssim \omega_c^{-1}$ and follows an exponential decay (equation 3.88) when $t \gtrsim \omega_c^{-1}$.

Pure tone

Pure tones are important when considering narrow band noise sources such as stray RF signals or 50 Hz mains noise. A pure tone's power spectrum is a Dirac delta function centered around a specific frequency $\tilde{S}(\omega) = \sigma_{\Delta\omega}^2 \delta(\omega - \omega_{noise})$ and leads to the phase expectation value,

$$\langle e^{i\phi(t)} \rangle_{tone} = e^{-\frac{\sigma_{\Delta\omega}^2}{\pi} \frac{\sin^2(\frac{1}{2}\omega_{noise}t)}{\omega_{noise}^2}}. \quad (3.90)$$

The phase has an oscillatory nature, because the integral in equation 3.82 returns back to 0 with each period of the tone.

If a noise spectrum has components of more than one type of noise, they can be added linearly and solved in the same manner. Figure 3.10 shows the characteristics of these types of decay processes.

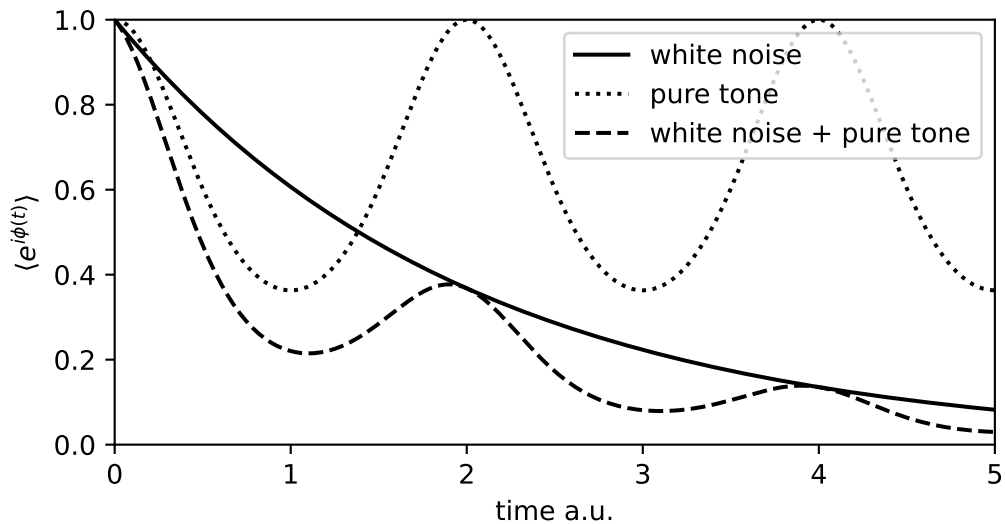


Figure 3.10: The expectation value of phase of a qubit whose excited state's energy fluctuates according to different noise sources. White noise is characterised by an exponential decay while a pure tone causes periodic dips in phase followed by coherence revivals. A noise spectrum containing both types is also shown.

Driving field fluctuations

In ground state hyperfine qubits, the magnetic dipole is driven by a resonant, stable microwave source. The instantaneous detuning of the microwave source to the qubit resonance can be related to its phase noise spectrum[110], $\bar{\mathcal{L}}(\omega)$ in units of dBc/Hz, where dBc is the ratio of the noise power relative to the carrier power in decibels. The phase noise spectrum is essentially a measurement of the linewidth of the driving field. Similar to the magnetic field noise from a qubit, it induces a dephasing equal to

$$\langle e^{i\phi(t)} \rangle = \frac{2}{\pi} \int_0^\infty 10^{\frac{\bar{\mathcal{L}}(\omega)}{10}} \sin^2 \frac{\omega t}{2} d\omega \quad (3.91)$$

for π -pulses⁴.

3.4.2 Dark states

In naturally occurring atoms, states couple to more than one other state, so the two-level atom is only useful as an approximation. A useful extension is considering an excited state coupled to two ground states (Λ -system). Dark states (states with no excited state population) in Λ -systems mainly occur via two related processes, coherent population trapping and optical pumping.

Coherent population trapping

Consider a Λ -system with states $|\downarrow\rangle$, $|\uparrow\rangle$ and $|e\rangle$. Both transitions are driven on-resonantly in the interaction picture,

$$\hat{H}_I = \frac{\Omega_\downarrow}{2} |e\rangle \langle \downarrow| + \frac{\Omega_\uparrow}{2} |e\rangle \langle \uparrow| + h.c. \quad (3.92)$$

⁴resonant Rabi oscillations that rotate the qubit along the Bloch sphere by π radians

One of the three eigenstates of the system is,

$$\psi_0 = -\frac{\Omega_\uparrow}{\sqrt{\Omega_\uparrow^2 + \Omega_\downarrow^2}} |\downarrow\rangle + \frac{\Omega_\downarrow}{\sqrt{\Omega_\uparrow^2 + \Omega_\downarrow^2}} |\uparrow\rangle, \quad (3.93)$$

where no population is in the excited state even though the atom is being driven by resonant fields. The state is reached stochastically from any other initial state via the spontaneous decay process. Void of any change to the Hamiltonian, the atom will stay in this state indefinitely.

This effect is sometimes unwanted if the desired outcome is to have the system in an excited state. For example in $^{171}\text{Yb}^+$, the $^2S_{1/2}$, $F = 1$ Zeeman substructure and the $^2P_{1/2}$, $F = 0$ excited state form a tripod system (which is similar to a Λ system but with three ground states), where coherent population trapping (CPT) can limit the excited state population, thereby limiting processes including Doppler cooling and state readout. This degeneracy can be overcome by generating a Zeeman shift between the ground states by introducing an external magnetic field[63]. This changes the eigenstate of equation 3.93 and introduces an excited state component to it.

Optical pumping

A similar process to coherent population trapping is optical pumping where the atom is driven on a single transition in the Λ -system. In the case where $\Omega_\uparrow = 0$, the eigenstate in equation 3.93 simplifies to $\psi_0 = |\uparrow\rangle$. This is useful in experiment for initialising to a particular atomic state for quantum operations.

3.4.3 Selection rules and coupling coefficients

When an electric dipole is driven by the electric field from a photon, angular momentum has to be conserved between the photon spin angular momentum and the initial and final orbital angular momentum of the valence electron, the nuclear spin and the electron spin. The conservation and transfer of angular

momentum between these quantities can lead to a reduction of the electric dipole moment, or if a transition simply can not conserve angular momentum then the coupling goes to zero. This reduces the Rabi rate as calculated in equation 3.38. When the angular momentum coupling is considered, the new value is called the reduced Rabi rate.

In Dirac notation, the combination of two angular momenta, $|j_1, m_1; j_2, m_2\rangle$ can project onto a third angular momentum $|j_3, m_3\rangle$,

$$C = \langle j_1, m_1; j_2, m_2 | j_3, m_3 \rangle, \quad (3.94)$$

where C is the Clebsch-Gordon coefficient, j represents an angular momentum and m represents its quantised component. The Clebsch-Gordon coefficient is given explicitly by Steck[96] and Allen & Eberly[95]. In the case of single photon interactions $j_2 = 1$, because the photon is a boson. The angular momenta that must be considered for an electric dipole hyperfine transition are: the nuclear spin I , the ground and excited total hyperfine angular momenta F_g & F_e , the ground and excited quantised total hyperfine angular momenta m_g & m_e and the ground and excited total angular momenta J_g & J_e . The reduced Rabi rate of an atom with electric dipole hyperfine transitions is[96],

$$\Omega_{reduced} = (-1)^{F_e+J_g+1+I} \frac{2J_e + 1}{2J_g + 1} \sqrt{(2F_e + 1)(2J_g + 1)} \\ \times \langle F_e, m_e; 1, -(m_e - m_g) | F_g, m_g \rangle \left\{ \begin{matrix} J_e & J_g & 1 \\ F_g & F_e & I \end{matrix} \right\} \Omega \quad (3.95)$$

Where the 6-term matrix is called the Wigner 6-j symbol and is related to the Clebsch-Gordon coefficient and is also given explicitly in Steck[96]. Calculation of the coupling coefficients specifically for $^{171}\text{Yb}^+$ is carried out by following Daniel Steck [96] and shown in figure 3.12. Code for calculation of the coupling terms of an atom with hyperfine structure is given in appendix C.

3.4.4 Beam polarisation and propagation axis

When an atom experiences a Zeeman shift from an external magnetic field, the quantisation axis of its total angular momentum will align along the external magnetic field direction. In equation 3.38, this quantisation axis is along the \vec{z} direction while the electric dipole had direction $\vec{x} - i\vec{y}$. This electric dipole direction relative to the quantisation axis is the same for all transitions where $\Delta m = +1$. Solving for the other two possible electric dipoles, $(n, l, m) \equiv (1, 0, 0) \leftrightarrow (2, 1, -1)$ and $(1, 0, 0) \leftrightarrow (2, 1, 0)$, finds for $\Delta m = -1$, the dipole has direction $\vec{x} + i\vec{y}$ and for $\Delta m = 0$, \vec{z} . Since the electric field of a photon is orthogonal to its direction of propagation in free space, there are constraints on the polarisation and direction of the incoming laser with respect to the external magnetic field direction experienced by the atom when trying to drive specific transitions.

To purely drive $\Delta m = 0$ (π) transitions, the beam must propagate in the x-y plane and its polarisation must be linear and parallel with the z axis. To drive $\Delta m = +1$ (σ^+) transitions, the beam must be co-propagating along the z axis with right hand circular (RHC) polarisation, or counter-propagating with left hand circular (LHC) polarisation. Driving $\Delta m = -1$ (σ^-) transitions requires LHC polarised light co-propagating along the z axis or RHC counter-propagating.

3.5 Application of theory to $^{171}\text{Yb}^+$

With 14.086(20)% natural abundance and $I = 1/2$ nuclear spin, ^{171}Yb is one of seven stable Ytterbium isotopes[112]. Neutral ^{171}Yb has a fully populated 4f valence orbital, however electrons in the 6s orbital are excitable[113], and in fact after ionisation, the ground state of $^{171}\text{Yb}^+$ is [Xe] $6s^1 4f^{14}$ [114]. This makes the singly ionised Ytterbium hydrogen-like with a singly populated outer 6s orbital. This atomic structure is unique to the lanthanide series where the

6s, 4f and 5d orbitals are the prominent valence orbitals, and is a useful atomic structure for use in ion trapping with many optically accessible transitions. Figure 3.11 shows the easily accessible states of $^{171}\text{Yb}^+$ via incident lasers used in this research.

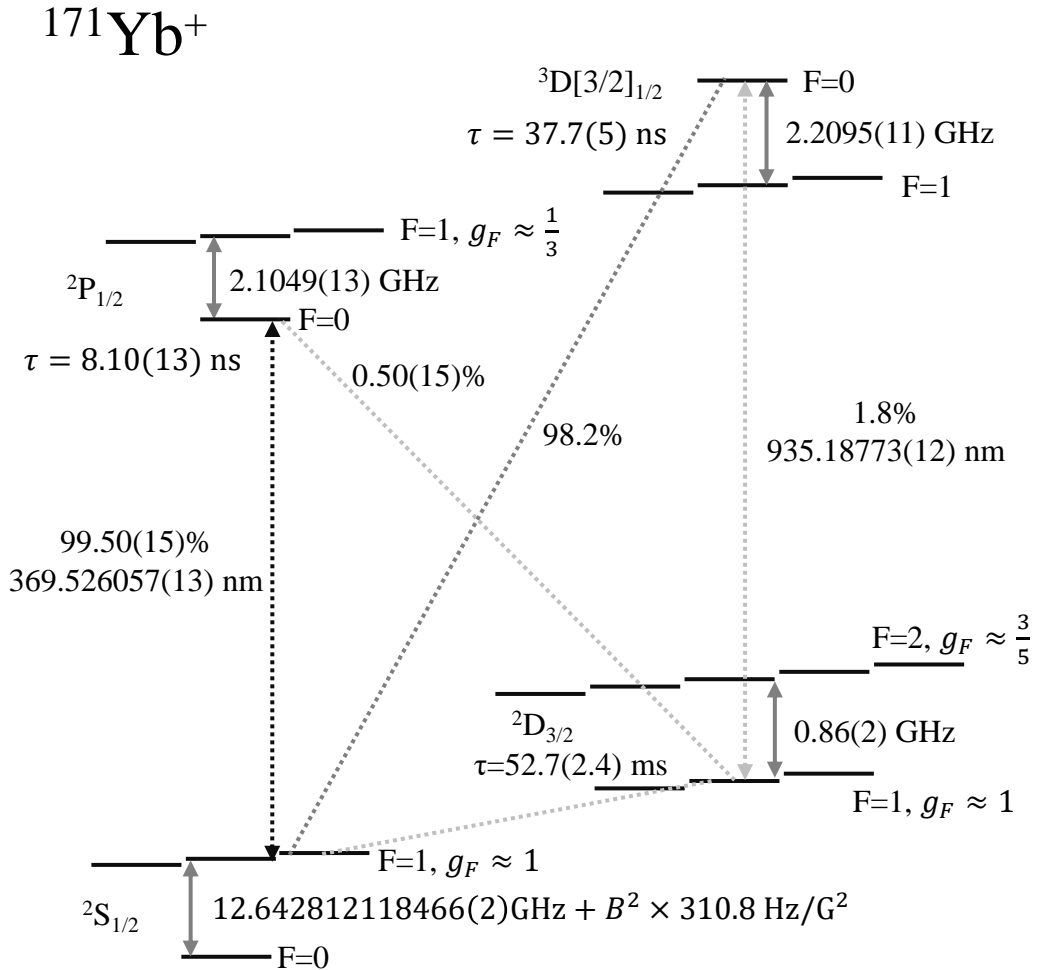


Figure 3.11: A Grotrian diagram of $^{171}\text{Yb}^+$ in similar fashion to Olmschenk et al[61]. Values for the $^2\text{S}_{1/2} \leftrightarrow ^2\text{P}_{1/2}$ and $^2\text{D}_{3/2} \leftrightarrow ^3\text{D}[3/2]_{3/2}$ resonances are derived from in-lab measurements of trapped ions (calibrated to a 780 nm Rubidium atomic reference). Other resonances and branching ratios are sourced from literature[60, 61, 62, 65, 115, 116, 117]. Landé-g factors, which can be used to calculate Zeeman shift, are calculated according to equation 3.33.

The $^2\text{S}_{1/2}$, $^2\text{P}_{1/2}$, $^3\text{D}[3/2]_{1/2}$ and $^2\text{D}_{3/2}$ states form a closed system that rarely leaks to any other states. Some ion trapping groups have observed the long lived $^2F_{7/2}$ state[118] populating sporadically and required a 638.6 nm[62, 119] or 760 nm[120] repump laser to bring population up to the short lived

$^1D[5/2]_{5/2}$ or $^1D[3/2]_{3/2}$ state and back into the cooling cycle. It is believed collisional events with background gas may contribute to the population of the $^2F_{7/2}$ state[121]. In our experience, we have not required such a repump laser, achieving trapping lifetimes of 2-12 hours.

Ytterbium-171 ions have become a popular species for quantum experiments for two main reasons. First is their long-lived addressable hyperfine $^2S_{1/2} F = 0 \leftrightarrow ^2S_{1/2} F = 1$ ground state clock transition. This transition is addressable with microwaves tuned near 12.6 GHz[65] and being a magnetic dipole transition that affects the nuclear spin, is very robust against the environment and has been shown to remain coherent experimentally for over one hour[122]. In terms of addressability and coherence, it makes a prime choice as a physical qubit. The second favourable characteristic of this species is its relatively simple closed cycle, fast fluorescing, 369.5 nm $^2S_{1/2} F = 1 \leftrightarrow ^2P_{1/2} F = 0$ transition, shown in figure 3.11 and specific couplings shown in figure 3.12. The transition uses the $F=1$ hyperfine qubit state as its ground state, and is split enough in energy from the $^2S_{1/2} F = 0 \& ^2P_{1/2} F = 1$ states, that state-selective fluorescence can be achieved and allows fast measurement of qubit state with low error rate[56]. It also offers a relatively simple structure to perform Doppler cooling and Raman sideband cooling.

3.5.1 The closed cycle transition

In similar fashion to how the excited state population of an optically driven electric dipole (equation 3.55) was solved by finding the steady state solution of its Lindblad master equation (equation 3.54), the excited state population of the closed cycle transition $6^2S_{1/2} F = 1 \leftrightarrow 6^2P_{1/2} F = 0$ has been solved[62, 63]. This solution is more complex because it must consider the three Zeeman sub-levels of the ground state with Zeeman shift δ_B between adjacent states. The solutions found by Berkeland et al[63] and Ejtemaei et

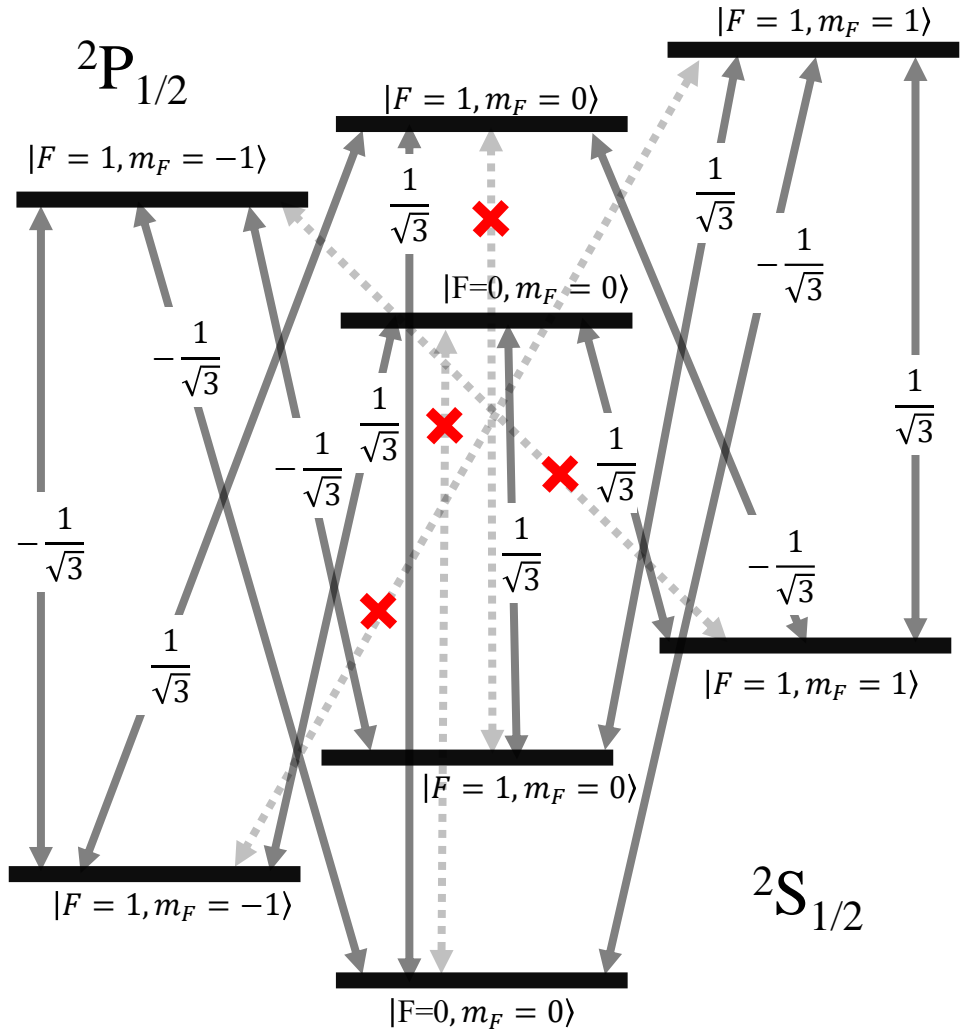


Figure 3.12: The coupling coefficients $\Omega_{reduced}/\Omega$, calculated as in appendix C with theory followed from Steck [96]. The four forbidden $^2S_{1/2} \leftrightarrow ^2P_{1/2}$ transitions are $|m_F = \pm 1\rangle \leftrightarrow |m_F = \mp 1\rangle$, $|F = 1, m_F = 0\rangle \leftrightarrow |F = 1, m_F = 0\rangle$ and $|F = 0\rangle \leftrightarrow |F = 0\rangle$.

al[62] are specifically for a driving optical field travelling perpendicular to the quantisation axis and linear polarisation with relative angle θ_{BE} between the quantisation axis and polarisation axis. Appropriate coupling coefficients are also considered as in figure 3.12. The solution given by Ejtemae et al[62] is

$$\mathcal{P}_{p0} = \frac{3}{4} \frac{\cos^2 \theta_{BE} \sin^2 \theta_{BE}}{1 + 3 \cos^2 \theta_{BE}} \frac{\frac{\Omega^2}{3}}{\Delta^2 + (\frac{\Gamma_{171}}{2})^2}, \quad (3.96)$$

where

$$\left(\frac{\Gamma_{171}}{2}\right)^2 = \left(\frac{\gamma}{2}\right)^2 + \frac{\Omega^2}{3} \cos^2 \theta_{BE} \frac{1 - 3 \cos^2 \theta_{BE}}{1 + 3 \cos^2 \theta_{BE}} + \frac{\cos^2 \theta_{BE}}{1 + 3 \cos^2 \theta_{BE}} \left(\frac{\Omega^4}{36\delta_B^2} + 4\delta_B^2\right). \quad (3.97)$$

Rabi rate has the same definition as equation 3.57 where the coupling coefficient is not factored into Ω . Compared to the solutions of a two-level atom, this transition has three extra notable phenomena:

1. Optical pumping caused by transition selectivity of the polarisation of the driving beam reduces fluorescence. The excited state population goes to zero when laser polarisation angle is parallel ($\theta_{BE} = 0$) or perpendicular ($\theta_{BE} = \pi/2$) relative to the quantisation axis. This is because at these angles, the laser can not address the Δm_F criteria of all three transitions simultaneously. When $\theta_{BE} = 0$ or π , the laser addresses π -transitions but not σ^\pm . When $\theta_{BE} = \pm\pi/2$, the opposite is true. This effect is described by the cosine and sine terms in equation 3.96. Plotting the \mathcal{P}_{p0} as a function of θ_{BE} shows these dips in population due to CPT (Figure 3.13.a). For low Rabi rate (s-parameter), the optimal angle for maximum population transfer is close to $\theta_{BE} \approx \arccos \frac{1}{\sqrt{3}}$ because at this angle, π and σ^\pm transitions are driven equally. The optimal angle edges closer to $\theta_{BE} \rightarrow \pi/2$ as laser intensity and therefore the Rabi rate is increased.
2. CPT can occur when the ground state population evolves into a configu-

ration where interference between the couplings of the Zeeman sub-levels to the excited state causes the net transfer to go to zero. Evolution into these states occurs at a rate proportional to the Rabi rate. The CPT effect can be counteracted by having a reasonably strong Zeeman shift (a magnetic field of a few Gauss) that evolves the phase of the Zeeman sub-levels at rate $m_F\delta_B$. The evolution of the phase of the Zeeman split states ruins the CPT dark state. The competition between the Rabi rate and Zeeman shift is described by the $\frac{\Omega^4}{36\delta_B^2}$ term in equation 3.97 and illustrated in figure 3.13.b. Excited state population begins to decrease due to CPT when $\Omega^4 > \frac{9\delta_B^2}{2}(3\gamma^2 + 12\Delta^2 + 8\delta_B^2)$ [62]. This behaviour can be understood[63] as the closed cycle transition pumping into dark states quicker than the Zeeman splitting can break them.

3. Line broadening occurs from the spread in Zeeman shifted ground states.

The ground state splitting caused by the Zeeman shift means the resonance moves blue (red) from ${}^2S_{1/2}, F = 1, m_F = 0$ resonance for the $m_F = +1(-1)$ state by $+(-)1.4$ MHz/G. This effect is described by the $4\delta_B^2$ term in equation 3.97. While increasing Zeeman shift helps break dark states formed by CPT, it can also adversely induce line broadening that reduces the excited state population and fluorescence of the atom (figure 3.13.c).

3.5.2 Off-resonant excitation and leakage

A mechanism equation 3.96 does not describe is the off-resonant excitation of the ${}^2P_{1/2}, F = 1$ state which can lead to decay into the ${}^2S_{1/2}, F = 0$ state. Figure 3.12 shows that each of the ${}^2S_{1/2}, F = 1$ Zeeman sub-levels couples to two of the ${}^2P_{1/2}, F = 1$ Zeeman sub-levels. A laser near-resonant to the ${}^2S_{1/2} F = 1 \leftrightarrow {}^2P_{1/2} F = 0$ transition will be red detuned by 2.1 GHz from the ${}^2S_{1/2} F = 1 \leftrightarrow {}^2P_{1/2} F = 1$ transition. This is large but not negligible such that excitation and spontaneous decay does occur on noticeable timescales

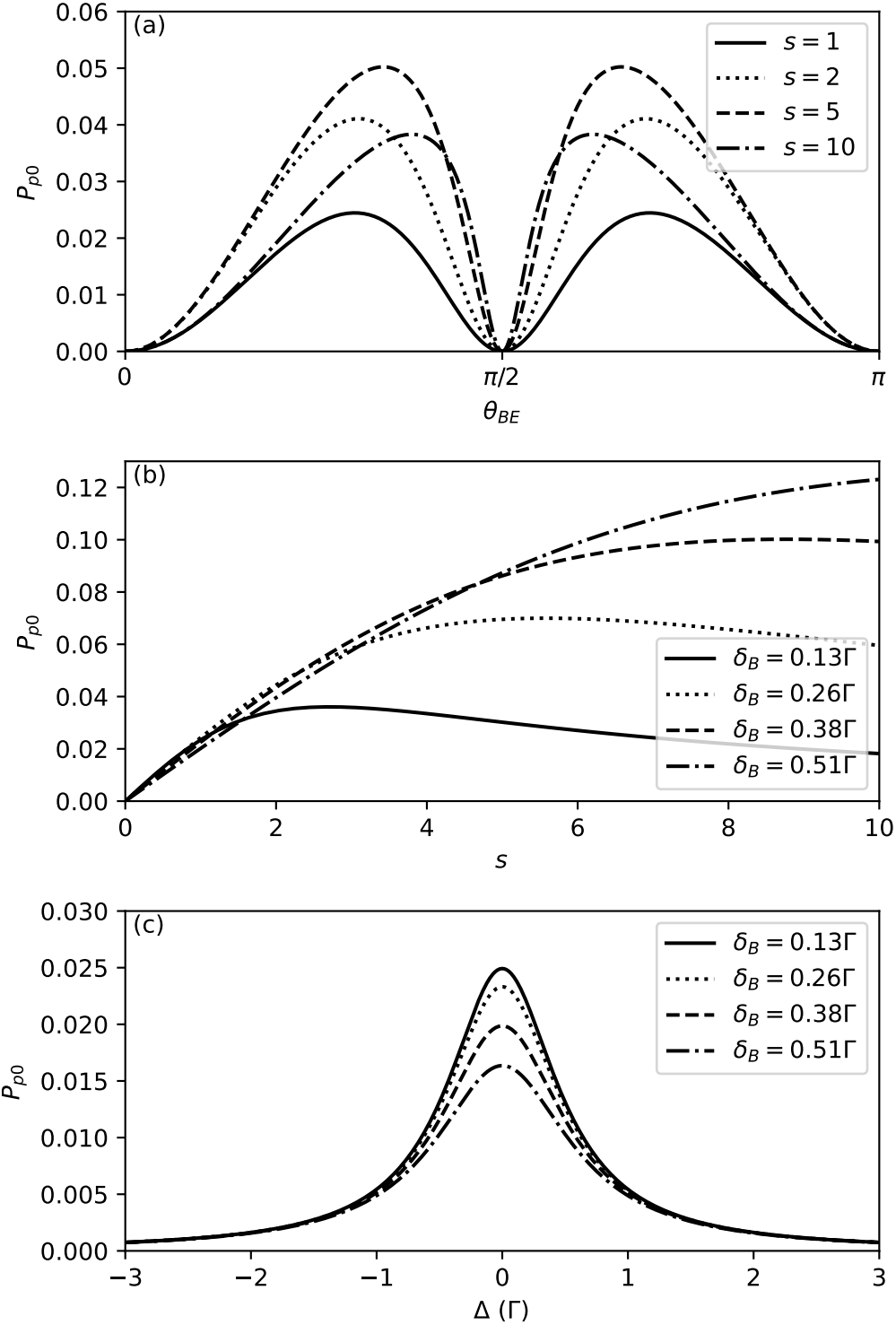


Figure 3.13: The excited state population (a) as a function of the relative angle of the laser polarisation to the quantisation axis θ_{BE} for different saturation parameters ($\Delta = -0.51\Gamma$, & $\delta_B = 0.18\Gamma$). The excited state population (b) as a function of the relative angle of the saturation parameter s for different Zeeman shifts ($\Delta = -0.51\Gamma$, & $\theta_{BE} = \arccos \sqrt{3^{-1}}$). The excited state population (c) as a function of detuning Δ for different Zeeman shifts ($s = 0.5$, & $\theta_{BE} = \arccos \sqrt{3^{-1}}$).

causing population to ‘leak’ out of the closed cycle transition. This creates a Λ system across the ground hyperfine states and $^2P_{1/2}$, $F = 1$ state where optical pumping can bring population into the $^2S_{1/2}$, $F = 0$ state. Ejtemae et al[62] approximate this leakage rate as

$$\gamma_{L,b} = \frac{2}{27} \Gamma \left(\frac{\Omega}{2\Delta_{p,HF}} \right)^2 (1 - \mathcal{P}_{p0}) \quad (3.98)$$

where $\Delta_{p,HF} = 2\pi \times 2.1049(13)$ GHz, the $^2P_{1/2}$ hyperfine splitting. The equation can be likened to the excited state population of equation 3.55 multiplied by the decay rate Γ in the regime where $(2\Delta_{p,HF})^2 \gg 2\Omega^2 + \Gamma^2$. The factor of $2/27$ comes from the $2/3$ branching ratio to $^2S_{1/2}$, $F = 1 \rightarrow ^2P_{1/2}$, $F = 1$, $1/3$ branching ratio of $^2P_{1/2}$, $F = 1 \rightarrow ^2S_{1/2}$, $F = 0$ and the $(1/\sqrt{3})^2$ coupling factor for the Rabi rate as in figure 3.12. The $1 - \mathcal{P}_{p0}$ factor accounts for the fact that leakage only occurs for population that is not already in the $^2P_{1/2}$ $F = 0$ state. This population can be calculated using equation 3.96.

Population in the $^2S_{1/2}$, $F = 0$ state can also off-resonantly excite into the $^2P_{1/2}$, $F = 1$ states and can decay into the $^2S_{1/2}$, $F = 0$ state. When driven by a laser near-resonant with the main cyclic transition, this occurs with a detuning of $\Delta_{s,HF} + \Delta_{p,HF} = 2\pi \times 14.7477(13)$ GHz. Ejtemae et al[62] approximate the rate of leakage as

$$\gamma_{L,d} \approx \frac{2}{9} \Gamma \left(\frac{\Omega}{2(\Delta_{s,HF} + \Delta_{p,HF})} \right)^2. \quad (3.99)$$

Similar to equation 3.98, the rate is approximated using a far-detuned case of equation 3.55, with scatter rate Γ . The factor $2/9$ comes from the $3/3$ branching of population transfer from $^2S_{1/2}$, $F = 0 \rightarrow ^2P_{1/2}$, $F = 1$, the $2/3$ branching of population from $^2P_{1/2}$, $F = 1 \rightarrow ^2S_{1/2}$ $F = 1$ and finally the coupling coefficient applied to Ω^2 , which is $(1/\sqrt{3})^2$. Unlike equation 3.98, the leakage rate is not affected by population in the other $^2P_{1/2}$, $F = 0$ state, because it has no coupling to the $^2S_{1/2}$, $F = 0$ state because of the angular

momentum selection rule for hyperfine dipole transitions, $F = 0 \nrightarrow F = 0$

3.6 Trapped ion qubit readout

Of particular interest to trapped ion quantum computing is being able to count photons to determine whether the ion is fluorescing or not. This fluorescence can be correlated to specific states and so can be used to read out trapped ion qubits. In $^{171}\text{Yb}^+$ for example, fluorescence of the 369.5 nm closed cycle transition (section 3.5.1) is evidence of the ion being in the $^2S_{1/2}$, $F = 1$ state prior to fluorescence, where the hyperfine ground state is also called the bright state. If the ion was in the $^2S_{1/2}$, $F = 0$ (dark) state, the same laser would not be resonant with any transitions and there would be no fluorescence to measure. A large portion of trapped ion qubit research was devoted to improving accuracy of this technique of trapped ion qubit readout[56, 62, 123].

The measurement of fluorescence for readout is performed by counting single photons with a detector. An ion that is driven by stable lasers such that it fluoresces at a constant rate will have Poissonian statistics when photons are counted over some time much longer than its decay time. Observing counts on time-scales of the decay time shows it is a single photon emitter[124]. Given the rate of photons emitted from $^{171}\text{Yb}^+$, $R = \Gamma\mathcal{P}_{p0}$ and the total detection efficiency of those photons η , the number of photons detected in a duration T would be on average,

$$\lambda = \eta\Gamma\mathcal{P}_{p0}T. \quad (3.100)$$

An actual single shot measurement of counts however is spread around this value and follows a Poisson distribution,

$$P(k, \lambda) = e^{-\lambda} \frac{\lambda^k}{k!} \quad (3.101)$$

where k is a specific number of counts in a readout, and $P(k)$ is the probability

of reading that number of counts. In absence of other sources of counts or change in fluorescence rate, the easiest way to determine if the ion is fluorescing is to consider detection of any number of counts above zero as meaning the ion is fluorescing. This is called the threshold method, because the counts are being compared to a threshold value (in this case, 1) to deem a bright state. This does have some error because an ion fluorescing with Poissonian statistics will also give zero counts with a probability of $P(0) = e^{-\lambda}$, but this error becomes negligible when $\lambda \gtrsim 10$.

This however is an ideal case. In reality, off-resonant excitation can change the hyperfine ground state state and cause the ion to randomly stop or start fluorescing (section 3.5.2) and other light sources as well as inherent detector noise can contribute to dark counts.

3.6.1 Dark counts

First, dark counts will be considered and off-resonant excitation will be ignored. Dark count rate R_D is mostly comprised of laser scatter and detector noise, and also follows a Poisson distribution. This means a count distribution from a dark ion will be a Poisson distribution with $\lambda_D = R_D T$. This can be compared against the count distribution for a bright ion $\lambda_B = (\eta \Gamma \mathcal{P}_{p0} + R_D)T$ as in the example given by figure 3.14.a, where $\lambda_D = 0.1$ and $\lambda_B = 10.1$. To discern the bright and dark state from a measurement of counts, it would be optimal to assume an ion is bright when 3 or more counts were measured on the detector, since this number of counts is more likely to come from a bright state. This conditional number of counts is called the threshold or discriminator count, n_t . This number can be optimally chosen by minimising the average of the bright and dark error in readout,

$$\epsilon(n_t) = \frac{1}{2} \left(\sum_{k=0}^{n_t-1} P(k, \lambda_B) + \sum_{k=n_t}^{\infty} P(k, \lambda_D) \right), \quad (3.102)$$

which is shown in figure 3.14.b.

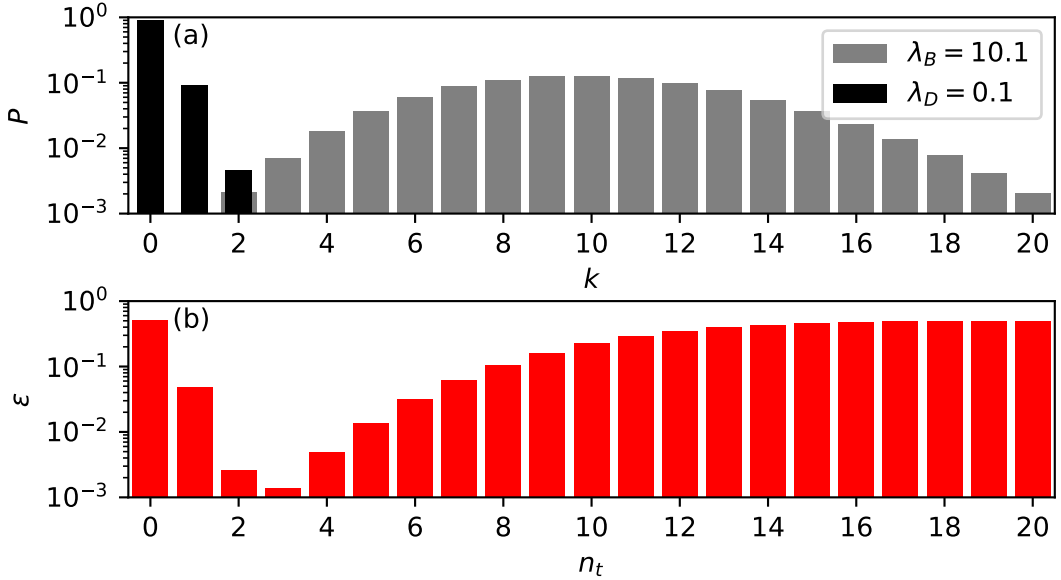


Figure 3.14: Two Poisson distributions (a) with $\lambda = 0.1$ (black) and $\lambda = 10.1$ (grey) that exemplify the count distribution of a trapped ion readout for a non-fluorescing (black) and fluorescing (grey) ion. The effect of off-resonant excitation and state mixing is not considered. The average error rate (b) of measuring state by using the threshold method as a function of threshold count is also illustrated where the optimal threshold count is 3.

3.6.2 State mixing

The next important consideration is off-resonant excitation of different hyperfine manifolds, which will mix the projected qubit states into one-another during readout. Void of any mixing, one could otherwise simply extend the duration of measurement to obtain a better fidelity. Wölk et al.[123] used Markov chains to better predict the state from a readout when the measured counts can be resolved in time. Solutions from their paper can also be used to estimate the change to the Poisson distribution incurred from off-resonant excitation. First considered is the bright to dark state off-resonant excitation and decay. An ion in the bright state has a rate of off-resonant excitation given by equation 3.98, which can be used to calculate the probability that the ion

off-resonantly excited and decayed to the dark state after duration t [123],

$$W_{B \rightarrow D}(t) = 1 - e^{-\gamma_{L,b} t}. \quad (3.103)$$

The compliment of this value, $W_{B \rightarrow B} = 1 - W_{B \rightarrow D}$ is the probability the ion did not flip state over that same time t . An important assumption is that the ion does not change state twice in this duration t , which is approximate when $\gamma_{L,b} t \ll 1$. It can then be said, the probability mass function (PMF)⁵ of the ion counts will only be a Poisson distribution when the ion remains bright over the entire measurement duration T . If the ion flips to the dark state at the unknown time t in T , then the expected counts will be reduced,

$$\lambda_{B \rightarrow D}(t) = R_B t + R_D T. \quad (3.104)$$

The value of t is random in each readout, but equation 3.103 gives the probability the flip will occur at time t , so the PMF for a bright ion can be calculated as

$$X_B(k, R_B, R_D, T) = W_{B \rightarrow B}(T)P(k, (R_B + R_D)T) + \int_0^T \frac{dW_{B \rightarrow D}}{dt} P(k, \lambda_{B \rightarrow D}(t))dt \quad (3.105)$$

where the second term considers the counts from an ion flipping from bright to dark at some unknown time t weighted against the probability of it flipping. The integral can be solved analytically (appendix B.1),

$$\begin{aligned} & \int_0^T \frac{dW_{B \rightarrow D}}{dt} P(k, \lambda_{B \rightarrow D}(t))dt \\ &= -\frac{\gamma_{L,b}}{R_B} e^{\frac{\gamma_{L,b}}{R_B} R_D T} \left(\frac{\gamma_{L,b}}{R_B} + 1 \right)^{-k-1} \frac{1}{k!} \left[\Gamma(k+1, (\frac{\gamma_{L,b}}{R_B} + 1)(R_B t + R_D T)) \right]_0^T, \end{aligned} \quad (3.106)$$

⁵A probability mass function is the discrete analog of a probability density function.

where

$$\Gamma(a, x) = \int_x^\infty t^{a-1} e^{-t} dt \quad (3.107)$$

is the upper incomplete Gamma function.

The PMF for the dark state is calculated similarly by using the probability of flipping from dark to bright,

$$W_{D \rightarrow B}(t) = 1 - e^{-\gamma_{L,d} t}, \quad (3.108)$$

and its compliment $W_{D \rightarrow D} = 1 - W_{D \rightarrow B}$. The expected counts will increase for a state flip (dark to bright) at time t

$$\lambda_{D \rightarrow B}(t) = R_B(T-t) + R_D T \quad (3.109)$$

where the PMF for the dark state is then,

$$X_D(k, R_B, R_D, T) = W_{D \rightarrow D}(T)P(k, R_D T) + \int_0^T \frac{dW_{D \rightarrow B}}{dt} P(k, \lambda_{D \rightarrow B}(t)) dt. \quad (3.110)$$

The integral's analytic solution is,

$$\begin{aligned} & \int_0^T \frac{dW_{D \rightarrow B}}{dt} P(k, \lambda_{D \rightarrow B}(t)) dt \\ &= \frac{\gamma_{L,d}}{R_B} e^{-\frac{\gamma_{L,d}}{R_B} (R_B + R_D)T} \left(1 - \frac{\gamma_{L,d}}{R_B}\right)^{-k-1} \\ & \times \frac{1}{k!} \left[\Gamma(k+1, (1 - \frac{\gamma_{L,d}}{R_B})((R_D + R_B)T - R_B t)) \right]_0^T. \end{aligned} \quad (3.111)$$

Figure 3.15 shows the difference between the count distribution with no state mixing during readout and state mixing considered with equations 3.105 and 3.110. The dark PMF skews towards higher counts as their is a probability the ion will turn bright and fluoresce more. The opposite is true of the bright PMF. The same method of calculating the average error and determining the optimal threshold count with equation 3.102 can be used.

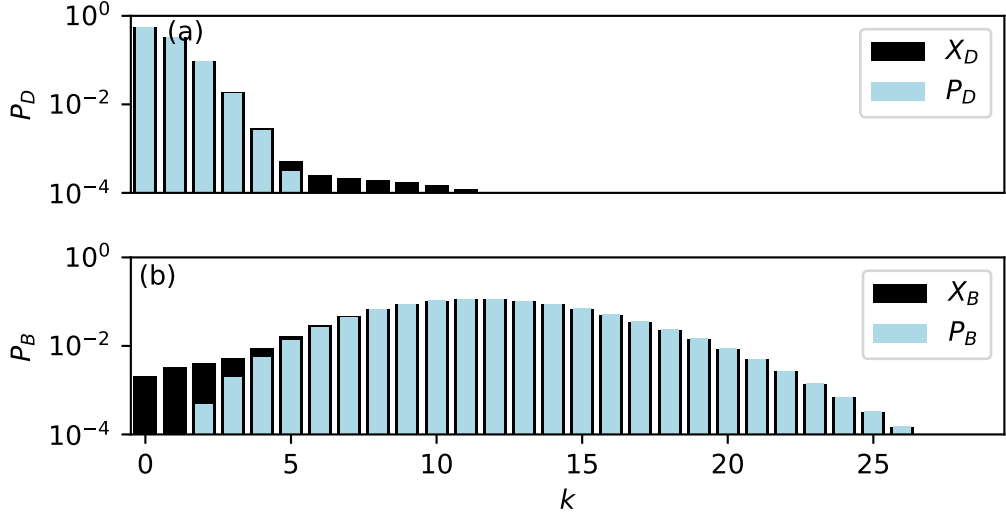


Figure 3.15: A comparison of dark and bright PMFs, when state mixing is (black) and is not considered (blue). The parameters used in this simulation are $s = 0.73$, $R_D = 1000c/s$, $\eta = 0.865\%$, $\Delta = -2\pi \times 10$ MHz, $\delta_B = 2\pi \times 3.5$ MHz and $T = 577$ μ s. The resultant state lifetimes are $\tau_B = 14.0$ ms and $\tau_D = 225$ ms.

3.6.3 Binomial proportion confidence interval

The measurement of a qubit by collapsing its population along its measurement axis is statistically equivalent to a Bernoulli trial, where the total number of trials n and the fraction of successes \hat{p} ($F=1$ measurements divided by total number of measurements) give some information about the true population of the bright and dark states. To approximate the success probability, the Wilson score interval[125] was used,

$$|\langle F = 1 \rangle|^2 \approx \frac{1}{1 + \frac{z^2}{n}} \left(\hat{p} + \frac{z^2}{2n} \right) \pm \frac{z}{1 + \frac{z^2}{n}} \sqrt{\frac{\hat{p}(1 - \hat{p})}{n} + \frac{z^2}{4n^2}} \quad (3.112)$$

where z is the number of standard deviations that the interval represents ($z=1$ is used for this thesis). The Wilson score interval is used because it is always in the range $0 \leq \langle F = 1 \rangle \leq 1$ and also it is simple to compute.

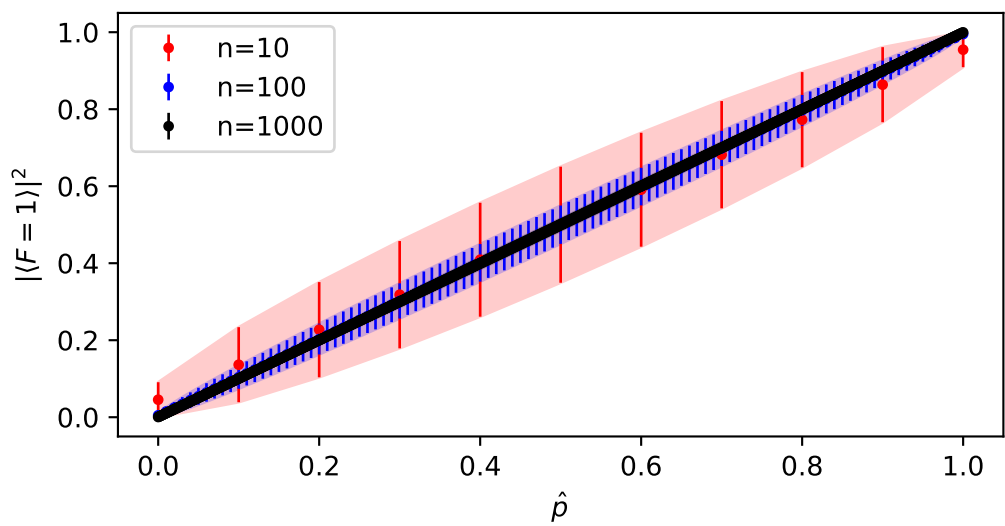


Figure 3.16: A plot of measured success probability \hat{p} versus confidence in success probability ($z=1$ is used meaning there is about a 68% chance that the true success probability is within the bounds). The uncertainty decreases with more trials. Most plots in this thesis use 100 trials per datapoint in experiment.

Chapter 4

Methods

This chapter will discuss the experiment hardware as well as the methods of measurement and analysis and how they were implemented. Ion trap systems require synchronized control of a diverse set of hardware systems. Careful attention needs to be paid to the timing, accuracy and stability of their control inputs to achieve good performance from an ion trap system. The systems involved in controlling an ion trap are:

- Frequency and intensity stabilised lasers (370 nm, 399 nm, 935 nm) for driving atomic transitions. Both frequency accuracy and stability are kept below 1 MHz. Typical laser power in the ion trap is $\sim 1 - 1000 \mu\text{W}$ and the 370 nm power is stabilized to $\sim 0.2 \mu\text{W}$ precision.
- Stable microwave sources to drive hyperfine transitions (12.6 GHz @ +32 dBm) and modulate lasers (2.105 GHz @ +26 dBm, 14.7 GHz @ +34 dBm & 3.07 GHz @ +10 dBm)
- RF voltages for creating trapping potentials (25 MHz @ $\sim 80 \text{ V}$) and laser modulation (180 MHz @ +33 dBm, 40 MHz @ +37 dBm)
- Precise DC voltages for generating appropriate electric fields at the ion ($\pm 20 \text{ V}$)
- Precise DC currents for generating magnetic fields at the ion ($\pm 3 \text{ A}$)

- Digital signals for synchronicity and communication between different pieces of hardware. Signal propagation and hardware response times can cause delay, usually on the order of nanoseconds, which have to be compensated for in certain experiments.

The ion trap control system has been developed and centered around a control computer using a high-level, purpose-built, Python-based control language, Artiq and Sinara hardware[126]. A Windfreak SynthHD[127] used as the 12.6 GHz microwave source and a Thorlabs PM100 powermeter are also connected via serial USB and controlled in the same Python scripts. Equipment is split physically across two separate areas to isolate high power laser systems from the user’s control computer and trap hardware.

4.1 Experiment hardware

4.1.1 Micro-fabricated surface electrode ion trap

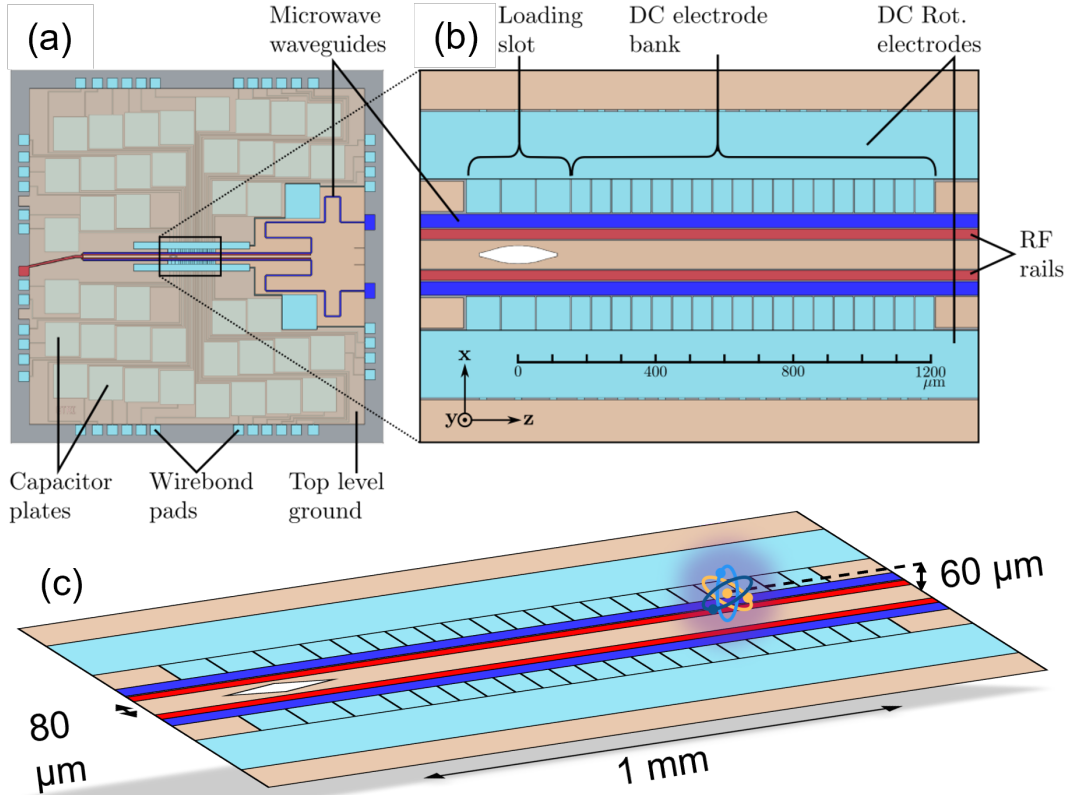


Figure 4.1: (a,b) A diagram of the GTRI trap, taken from the trap manual[128]. (a) shows the wider chip mainly populated by capacitors used to reduce RF noise on the trap electrodes. (b) shows the specific trap area with the Cartesian directions and scale along the shuttling axis. It also shows the ground electrodes (gold), RF electrodes (red), microwave wave-guides (blue) and DC electrodes (cyan). The loading slot (white) is the hole from where a neutral ytterbium beam enters perpendicular to the trap surface. (c) Isometric perspective showing scale and typical height of the ion above the trap surface.

A GTRI Microwave I surface-electrode ion trap[128] is the main ion trap used in this research (figure 4.1). It is a microfabricated planar surface trap with an $80 \mu\text{m}$ wide ground electrode and two $30 \mu\text{m}$ wide rf electrodes to each side of it. A grounding mesh situated far ($\gg 80 \mu\text{m}$) above the surface of the trap acts as the fourth electrode of the quadrupole linear ion trap. Outward from the RF rail electrodes are microwave rails that are used to radiate the ion with a 12.6 GHz magnetic field for driving the $^2S_{1/2} F = 0 \leftrightarrow F = 1$

transition in $^{171}\text{Yb}^+$. By altering the applied microwave's phase between the two rails, the magnetic field polarization at the ion can be changed within a 2D plane normal to the rail direction.

Approximately 100 μm from the centre rail are 42 DC electrodes spaced along the rails (30–50 μm long per segment) used for generating a DC trapping field along the z-direction. These are of similar function to end cap electrodes in typical quadrupole rod traps, but allow the creation and evolution of more complicated potentials, including ones to translate the ion substantial distances along the trap. The 42 electrodes are used to smoothly translate the DC potential along the rail axis (z-axis) which can move (shuttle) a trapped ion along inside the potential. Out from the 42 DC electrodes are two long DC electrodes used to compensate any stray electric field in the x-y plane.

DC source

To drive the 42+2 DC electrodes, twelve computer controlled NI PXI-4713 digital-to-analog converter (DAC) cards generate four DC voltages each within a range $\pm 10 \text{ V}$ which pass a doubling amplifier to $\pm 20 \text{ V}$. The 44 signals break out across $4 \times$ DB25 connectors and ribbon cables and pass into $4 \times \sim 67 \text{ kHz}$ (-3dB cutoff) single-pole low pass filters¹ before passing Accu-Glass 100220 DB25 feed-throughs to the chip trap. Electrode voltages are determined from a voltage look-up table calculated by the GTRI team and may be adjusted in experiment to compensate for stray electric fields. The main experiment computer uses a python-based graphical user interface (GUI) to select ion position, adjust compensation values, and perform shuttling. The Python script sends a 48-length array of values across an Ethernet connection to a separate computer that is connected to the DACs, and those values are applied to the twelve cards. As well as the 42+2 DC electrodes a 45th channel is used

¹The low pass filters have a +12 dB resonance at 1.65 MHz approximately 20 kHz wide. Above 1.65 MHz, the filter becomes double pole. This was likely a design flaw, as per communication with Jason Amini who was part of GTRI at the time.

for delivering a DC voltage to a piezo-controlled mirror that keeps incident lasers centred on the trapped ions as they are shuttled.

Microwave source

To drive the microwave lines, a 12.6 GHz microwave signal is sourced from a Windfreak SynthHD[127] dual channel microwave generator, which doubles a 6.3 GHz tone. The synth is connected via USB to the main experiment computer where serial communication is performed using the PyVISA python package and frequency and amplitude values can be changed directly within the Artiq dashboard GUI. The output of channel B of the synth is connected to two Hittite HMC547LC transistor-transistor logic (TTL)-controlled switches in series. The switches allow ~ 40 dB isolation individually and a measured 79 dB isolation combined. The TTL switch control is connected to a TTL output of the Sinara module. After the switches, the microwave signal passes into a Mini-Circuits ZVE-3W-183+ amplifier (+33 dB gain, 3 dB compression at +35 dBm out), and then an Analog Devices HMC1087F10 power amp (+10.5 dB gain, 3 dB compression at +37.5 dBm out). The signal finally passes through passive filtering, consisting of a DC block, PE8304 isolator and directional coupler and a band-pass filter to remove any half-tone remnant from the source. Approximately +33 dBm is passed into one of the trap microwave lines. A full schematic is shown in appendix D.

An important characteristic of the microwave source is its phase noise. If the microwave frequency fluctuates with some phase noise, the qubit phase also fluctuates in the rotating frame. The microwave source's phase noise was characterised using a HP 8593E with 1 Hz video bandwidth and 30 Hz resolution bandwidth. Its predicted effect on single qubit operations[110] was calculated according to equation 3.91 as shown in figure 4.2. In experiment for π -rotations typically performed in $1 - 5 \mu\text{s}$, the infidelity due to microwave phase noise is expected to be $\sim 2 \times 10^{-5}$.

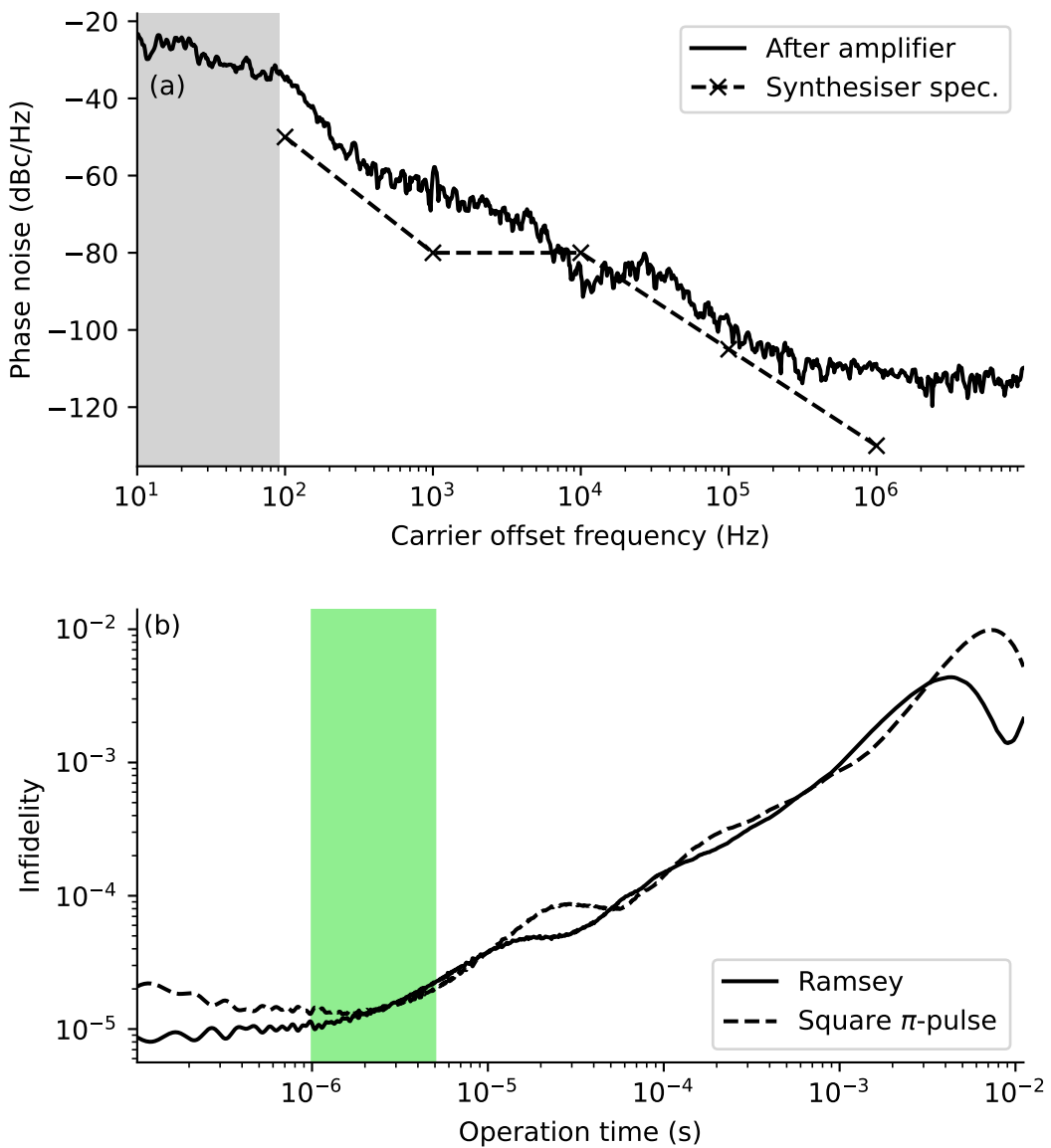


Figure 4.2: (a) Single-sideband phase-noise of the microwave signal going to the ion trap. Units of dBc/Hz represent logarithmic spectral density relative to the carrier. The grey area is where the resolution bandwidth of the spectrum analyzer ($f_{RBW} = 30$ Hz) may impinge on the measured phase noise ($3f_{RBW}$) as suggested by the spectrum analyser manual. The up-tick in phase noise near 30 kHz is likely caused by a phase-lock-loop used inside the synthesizer to maintain a stable resonance. (b) The corresponding infidelity when measuring a Ramsey envelope or a square π -pulse. The green band indicates typically achieved π -pulse durations in experiment. The calculation omits the phase noise component in the gray band.

Another important characteristic are the switching transients. The amplifier switch achieves a 10-90 rise time of 65 ns with an approximate error function profile. The fall time lasts 190 ns (10-90) with the same profile.

RF source

The trap RF delivered to the RF electrodes are sourced from a HP 8647A signal generator at 25.5 MHz and +5.4 dBm. This signal passes through a -30 dB attenuator and +40 dB RF amplifier. The attenuator was chosen so an RF amplitude that overdrives the amplifier or RF electrodes on the chip can never be selected from the signal generator. The output of the amplifier passes through a helical resonator, increasing its voltage and delivering RF to the electrodes with an amplitude of approximately 80 V. This is well below the maximum RF voltage of 250 V, at which dielectric breakdown can occur across electrode gaps, causing permanent damage to the trap.

4.1.2 Vacuum systems

Ion lifetime is increased by reducing the rate of collisions with background gas. Background gas can collide and knock trapped ions from the trap or can form chemical bonds with the ion[129], changing its atomic properties. To achieve this, the ion trap is housed within a Kimball Physics MCF600-SO200800 spherical octagon chamber pumped down to ultra-high vacuum pressures. The vacuum is maintained at a pressure of approximately 1×10^{-11} Torr (measured from the ion pump controller) by a Gamma Vacuum TiTan ion pump and 7 kV Gamma Vacuum small pump controller which draws a continuous 0.2 – 0.4 nA of current.

Windows are UV anti-reflection coated to allow efficient transmission of ion fluorescence and incident lasers, both with wavelength near 369.5 nm. Windows allow access back and forth along the z , $x + z$, $x - z$ and y (only upward) directions, relative to the trap principle axes (figure 4.1).

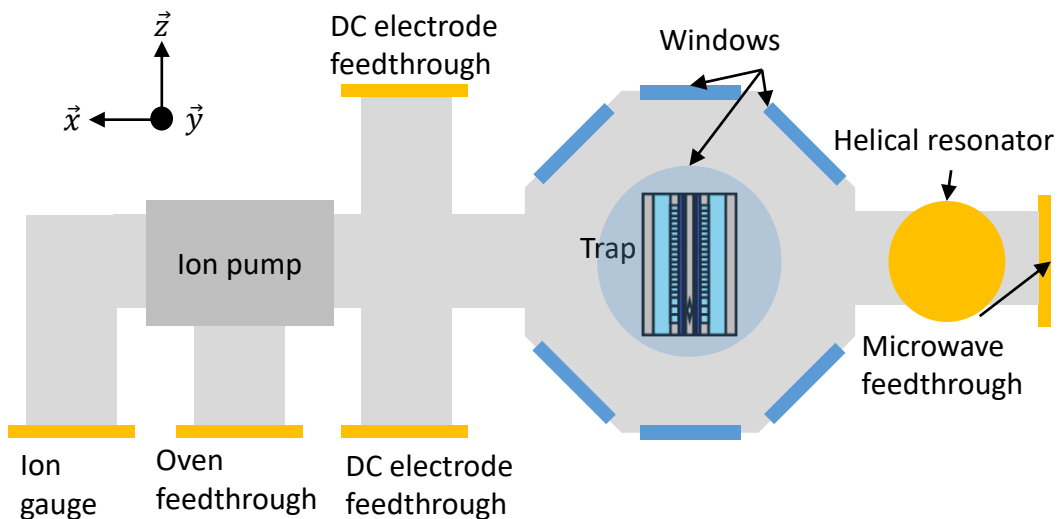


Figure 4.3: A diagram of the vacuum system used to house the ion trap. The ion trap is situated inside a spherical octagon vacuum chamber with 7 UV anti-reflection coated windows for laser access. Laser access directions are the z axis (up-down in figure), $x \pm z$ axes (both diagonals). The top window (out of the page) is used for fluorescence collection. Also shown are locations of the ion pump and DC, RF, oven and ion gauge feedthroughs.

4.1.3 Laser systems

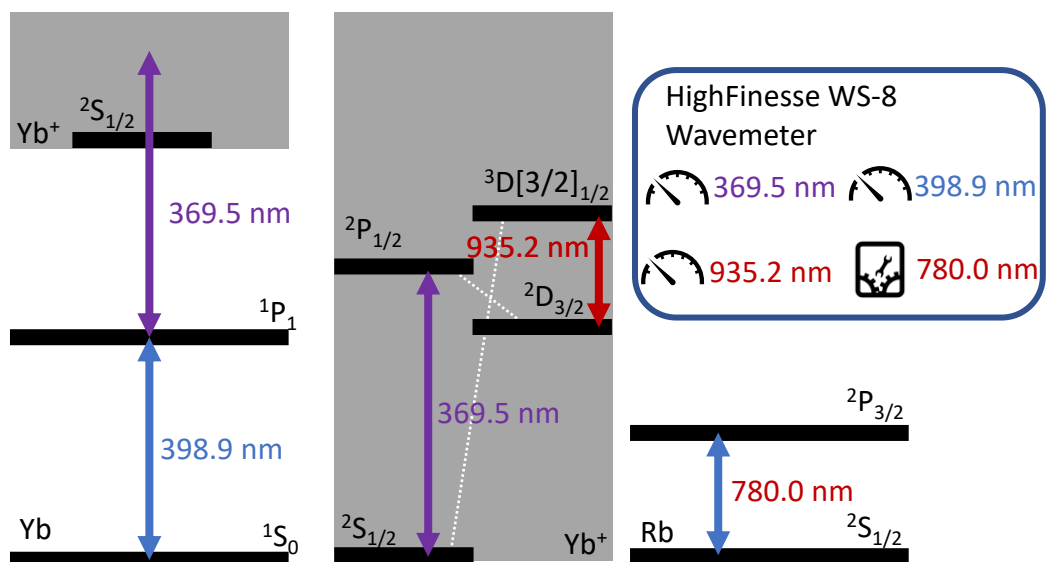


Figure 4.4: Grotrian diagrams of the atom transitions accessed by lasers used in experiment. The 780 nm Rubidium resonance is used to calibrate the wavemeter.

Ytterbium ions have a completely closed atomic system between only four states (figure 4.4), requiring only two lasers. The resonant wavelength of lasers

that drive these transitions are 369.5 nm and 935.2 nm. Besides these two lasers, a 398.9 nm laser is used loading the ion trap by ionizing neutral ytterbium and a 780.0 nm laser is locked to a Rubidium vapor cell to provide a frequency standard to which a HighFinesse WS-8 wavemeter is calibrated.

The 369.5 nm laser serves a few purposes:

- The second photon source in isotope selective 2-photon photo-ionisation explained in chapter 6
- The Doppler cooling beam for trapped ytterbium ions driving the strong $^2S_{1/2} \leftrightarrow ^2P_{1/2}$ transition
- Optical pumping into specific states in the $^2S_{1/2}$ hyperfine manifold in $^{171}\text{Yb}^+$
- When far detuned ($\Delta \gg \Gamma$) from the $^2S_{1/2} \leftrightarrow ^2P_{1/2}$, driving coherent Raman transitions

Doppler/pump beam

The Doppler limit in trapped ions is achieved when a weak Doppler beam is detuned from resonance by $\sim -\Gamma/2$ (if external heating is sufficiently low), or approximately -10 MHz for the $^2S_{1/2} \leftrightarrow ^2P_{1/2}$ transition. The laser's frequency stability must be much smaller than the transition linewidth to meet this condition. We derive this stable wavelength from a frequency doubled M2 SolTis, an ultra-narrow linewidth CW Ti:Sapphire laser whose etalon is locked to a HighFinesse WS-8 wavemeter referenced against an ultrastable Vescnt 780 nm laser locked to a Rubidium resonance using saturated absorption spectroscopy (SAS). The laser is pumped with a 532 nm 5W Coherent Verdi, and lasers at 739.1 nm. The laser is then sent through an M2 ECD-X second harmonic generation cavity and outputs a tuneable narrow linewidth (~ 300 kHz, stabilization loop noise limited) beam at 369.5 nm. The control loop is ~ 10 Hz, limited by the channel-switching and exposure time of the wavemeter.

To address the combinations of hyperfine split states in the $^2S_{1/2}$ and $^2P_{1/2}$ $F = 0$ and $F = 1$ states, Qubig EOMs resonant with 2.105 GHz (PM-Yb171+2.1G) and 14.748 GHz (EO-WG14.7M2-VIS) are used. When the EOMs are off, the beam is -10 MHz detuned from the $^2S_{1/2}$, $F = 1 \leftrightarrow ^2P_{1/2}$, $F = 0$ transition. The 2.105 GHz EOM produces sidebands with a modulation depth of 1.42 radians, reducing the carrier to 31% its original power and creating a first order blue sideband with 30% of the original carrier power, bridging the laser across the $^2S_{1/2}$, $F = 1 \leftrightarrow ^2P_{1/2}$, $F = 1$ resonance. Similarly, the 14.748 GHz EOM with a modulation depth of 0.42 radians reduces the carrier to 91% and produces a blue first order sideband with 4% the power of the carrier which addresses the $^2S_{1/2}$, $F = 0 \leftrightarrow ^2P_{1/2}$, $F = 1$ resonance. The $^2S_{1/2}$, $F = 0 \leftrightarrow ^2P_{1/2}$, $F = 0$ transition is forbidden so no 12.6 GHz EOM is used, however an EOMs at that half frequency has been used to generate the appropriate splitting for addressing the ground state hyperfine qubit using Raman beams[5].

For fast frequency and amplitude modulation of the laser, an AA Opto-Electronic MQ180-A0,2-UV AOM is used. The modulator is driven by a 2 W, 180 MHz RF source, with frequency modulation (FM), amplitude modulation (AM) and fast on/off switching. 50% of the laser light coupled into the AOM is diffracted into the +1 mode of the AOM by the generated RF acoustic waves. The $m = +1$ diffraction mode gains +180 MHz in frequency, making the diffracted light's frequency and amplitude directly controllable by the AOM's driving RF.

The diffracted beam is coupled to Thorlabs PM-S350-HP fibre optic cable, via a Thorlabs C671TME-A asphere, to deliver spatially pure single mode light to the ion trap. The light is collimated out of the fibre using an identical asphere. The beam is filtered via a linear polarising filter to project the laser light to a fixed polarisation. This is done because at high powers, polarisation modulation is induced inside the fibre. This light is then split via a non-

polarising beam splitter. Half the light is sent to a photodiode for power stabilisation while the other half is sent through a Conoptics 350-160 EOM, which allows fast control of laser polarisation via an analog control voltage input. The light is then combined co-propagating with other 398.9 nm and 935.2 nm lasers through dichroic optics. The lasers are focused on the trapping area using a 150 mm plano-convex UV-coated lens. The quality of the focused spot is most important for the 369.5 nm laser. This is because a well focused 369.5 nm beam helps avoid scattering on nearby trap surfaces which induces charging via the photo-electric effect. The photo-electric effect induces static charge on the trap electrodes which can inadvertently alter the electric field near the ion, inducing unwanted micro-motion.

Raman beams

The beams used for coherent Raman transitions are derived from a similar M2 SolTis CW Ti:Sapphire laser with an ECD-X frequency doubling module. The laser resonance is controlled by a feedback loop between the wavemeter that controls the etalon inside the SolTis. In experiments, the Raman laser is typically set to a few GHz red of the $^2S_{1/2} \leftrightarrow ^2P_{1/2}$ transition to avoid off-resonant excitation and spontaneous emission in the Raman excitation. The laser is split into the two Raman beams by a polarizing beam splitter (PBS) and the power in each arm is set by a half-wave plate (HWP) before the PBS. Each Raman beam passes through separate MQ180-A0,2-UV AOMs which are optimised for the $m = +1$ mode. C671TME-405 aspheres couple the beams into PM-S350-HP fibres that deliver the beams to the ion trap.

By using RF frequencies that are phase coherent, the frequency difference between the Raman beams can remain phase coherent relative to each other, even when the phase coherence of the laser is less coherent. This allows the resonance of the driven Raman transition to be much more stable than the laser linewidth ($\ll 300$ kHz).

935.2 nm repump laser

For the 935.2 nm repump laser, a Moglabs cateye external cavity diode laser (ECDL) laser is used. Instead of using a grating for frequency selection, like in typical narrow linewidth ECDLs, a cateye laser uses an intra-cavity rotatable narrow line filter. ~ 8 mW of the laser output is split into the wavemeter the rest is split (~ 15 mW each) between two IntraAction AOM-40 40 MHz AOMs. Light coupled into the first order mode of one of the AOMs. The AOM is driven by an RF source with a TTL-controlled switch. The switching allows fast control over the state of the ion, when the 369.5 nm laser is on and the 935.2 nm is off, the metastable $^2D_{3/2}$ state populates quickly (microseconds) due to the 1/200 branching ratio from the $^2P_{1/2}$ state. The diffracted AOM mode is coupled into Thorlabs 980HP fibre. This fibre is specified for single mode transmission between 980 and 1600 nm. For 935.2 nm light, the core likely supports more than the single TEM00 mode. Mode quality is not critical for repumping since the measured beam intensity at the ion is well beyond the saturation intensity required for repumping. 935.2 nm photons are not expected to have enough energy to induce noticeable charging on the trap surface, however photo-electric charging has been observed in wavelengths as long as 729 nm in ion traps[130].

4.1.4 Frequency references and laser stabilisation

To address the $^2S_{1/2} \leftrightarrow ^2P_{1/2}$ ($\Gamma = 2\pi \times 19.6$ MHz) and $^2D_{3/2} \leftrightarrow ^3D[3/2]_{1/2}$ ($\Gamma = 2\pi \times 4.2$ MHz) transitions, laser frequency accuracies need to be comparable to their linewidths over the duration of the experiment. Ideally, the stability of the laser frequencies are much less than the transition linewidths to avoid line-broadening from laser instability. A HighFinesse WS8-2 wavemeter is used for precise (<100 kHz) and accurate (2 MHz) measurement of the laser frequencies.

To mitigate drift that can lead to the 2 MHz innaccuracy, the waveme-

ter is calibrated to an atomic absolute optical frequency reference. The ^{87}Rb $^2S_{1/2} F = 2 \leftrightarrow ^2P_{3/2} F = (2, 3)$ cross-over resonance is used as the absolute frequency reference. The signal is obtained via saturated absorption spectroscopy and was chosen because it had the largest peak-to-peak error signal out of all ^{85}Rb and ^{87}Rb resonances observed. A Vescent D2-100 DBR laser is used to drive the 780 nm transition while a Vescent D2-210 Saturated Absorption Spectroscopy Module is used to acquire the spectroscopic features. The laser is locked using the error signal of the spectropic feature, which achieves locking with sub-100 kHz stability.

This 780 nm frequency reference is passed into an optical switch multiplexer (previously a home-made switch was used[131]) along with the other lasers used in experiment that goes to the wavemeter. Using a DAC and the wavemeter's software, a proportional-integral-derivative (PID) loop controls the frequency of the lasers used in experiment. The DAC sends voltages to laser controllers that can change the cavity length of the lasers. This allows the wavemeter PID to correct for laser frequency drift over a scannable range of several gigahertz for all lasers. All lasers locked using this method achieve standard deviations between 0.1-1 MHz, well within the natural linewidth of used transitions.

4.2 Control, measurement protocols, and analysis

4.2.1 Qubit readout parameter optimisation

In experiment the threshold readout method (section 3.6) was used to determine the $^2\text{S}_{1/2} F = 0 \leftrightarrow 1$ qubit state. Time-resolved fluorescence readout[123] was used for a period using photon arrival timing information from an ID Quantique ID800 time-tagger, but was later replaced in favor of the speed and simplicity of the threshold readout method. This state selective measurement

protocol required three experimentally chosen parameters,

1. readout duration
2. incident laser power
3. threshold number

The parameters were chosen to maximise readout fidelity. To quickly estimate these parameters, a model of qubit readout fidelity was optimised using parameters fitted from ion fluorescence saturation measurements.

Ion fluorescence saturation measurements

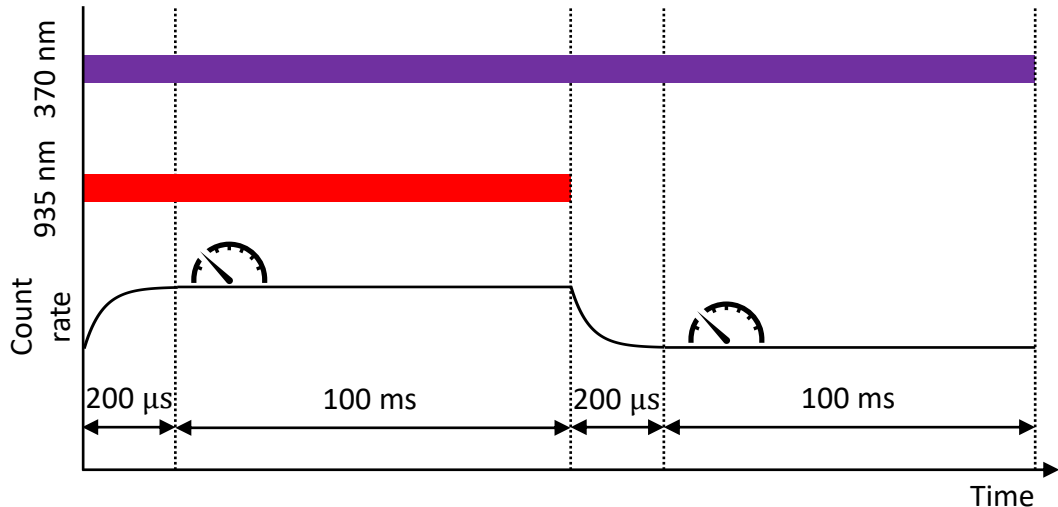


Figure 4.5: The background subtracted measurement protocol used to determine the ion's fluorescence rate. The ion is pumped into its cyclic fluorescing transition for $200 \mu\text{s}$ by switching on the 935 nm repump beam before photon counting for 100 ms. The ion is then pumped out of the cyclic transition into the metastable $^2D_{3/2}$ state for $200 \mu\text{s}$ by switching off the 935 nm repump via its AOM. The background count rate is then determined by photon counting for another 100 ms.

For this measurement, the system was initialised with the 369.5 nm Doppler cooling laser, its 14.7 GHz sidebands and the 935 nm repump laser turned on to facilitate continuous Doppler cooling. Then, the 369.5 nm laser power was stabilised using an algorithm that performs the function of the integral gain value in a PID controller.

Laser light was picked off via a beam sampler optic and sent to a photodiode. The photodiode current was transformed into a readable voltage using a trans-impedance amplifier and fast analog-to-digital converter (ADC). Photodiode voltage and laser power were calibrated beforehand, and found to be linear < 1 mW. The power stabilisation algorithm continually updated the amplitude of the RF signal sent to the laser beam's AOM, changing its power until the desired photodiode voltage was reached. The algorithm is expressed in pseudo-code in appendix C.3.

After the power was stabilised using a particular setpoint value, the ion fluorescence is measured for 100 ms to gain statistics on the rate of photo-electrons from an APD accounting for both the background count rate and ion fluorescence count rate (figure 4.5). The 935 nm laser's AOM's RF signal was then switched off with a TTL signal. After $200 \mu\text{s}$ (~ 6 1/e decay times), the atomic state is assumed to be in the long-lived $^2\text{D}_{3/2}$ state and the ion is dark. Photo-electrons were counted from the APD for a period of 100 ms to gain statistics on the background count rate, predominantly caused by laser scatter ($\sim 500 \text{ counts s}^{-1}\mu\text{W}^{-1}$) and detector dark counts ($\sim 100 \text{ counts/s}$). After this measurement, the 935 nm laser's AOM RF signal was switched back on and the ion was pumped back into the cyclic cooling transition after another $200 \mu\text{s}$. This pump-in time is much faster, 630(190) ns, than the pump out time since the decay from $^3\text{D}[3/2]_{1/2}$ to $^2\text{S}_{1/2}$ is $\sim 98.2\%$ (figure 3.11) compared to the 0.5% probability of the $^2\text{P}_{1/2}$ to $^2\text{D}_{3/2}$ decay.

This protocol was repeated over many different setpoint values to generate a trend of both ion fluorescence rate against laser power, as well as background scatter rate against power. Ion fluorescence rate was fitted to equation 3.96, where parameters δ_B , θ_{BE} and Δ were known. Equation 3.96 is scaled by $\eta_{\text{det}}\Gamma$, where total collection efficiency η_{det} was a free parameter. In equation 3.96, $\Omega = \Gamma\sqrt{P/2P_{\text{sat}}}$ where P was calibrated to the photodiode setpoints and P_{sat} is a free fitting parameter. With the two free parameters η_{det} and

P_{sat} , the ion count rate was fitted with sufficient accuracy (Figure 4.6). The background count rate is also fitted against laser power P to a linear function.

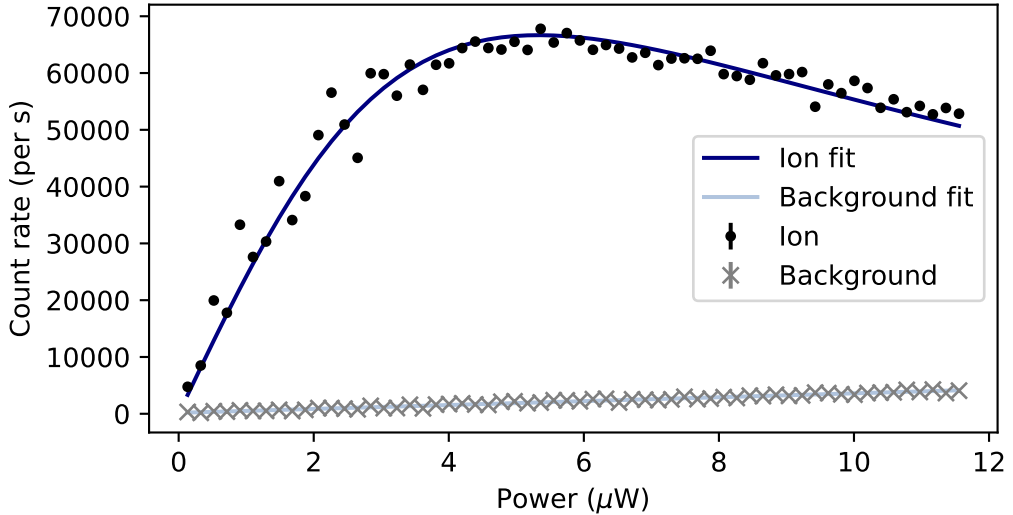


Figure 4.6: The measured fluorescence of an ion as a function of incident laser power using the saturation curve protocol. The measurement took approximately 20 seconds for the 120 datapoints. Fit parameters for this particular measurement were $\eta_{det} = 1.08\%$, $P_{sat} = 1.39 \mu\text{W}$, $m_{bkg} = 343 \text{ counts}\cdot\text{s}^{-1}\cdot\mu\text{W}^{-1}$ & $c_{bkg} = 166 \text{ counts/s}$.

With the resultant four fitted parameters, η_{det} , P_{sat} , m_{bkg} , c_{bkg} , a model of trapped ion qubit readout can be optimised for maximum readout fidelity (appendix C.1) with the free parameters, T_{read} , P & n_{thresh} . This is achieved by a parameter search that minimises single shot readout fidelity (equation 3.102) using the PMFs of bright and dark states (equations 3.105 and 3.110 respectively).

4.2.2 Single shot atomic state readout

Once optimal parameters have been determined, single shot readout can be performed by driving the Doppler cooling laser (no EOM sidebands) at the pre-determined power and duration while simultaneously counting fluorescent photons in the same period. Results of the readout of an $^2S_{1/2}$ $F = 0$ and $F = 1$ state are presented in figure 4.7 and are compared with the determined optimal readout from a saturation curve measurement. Fitted saturation curve

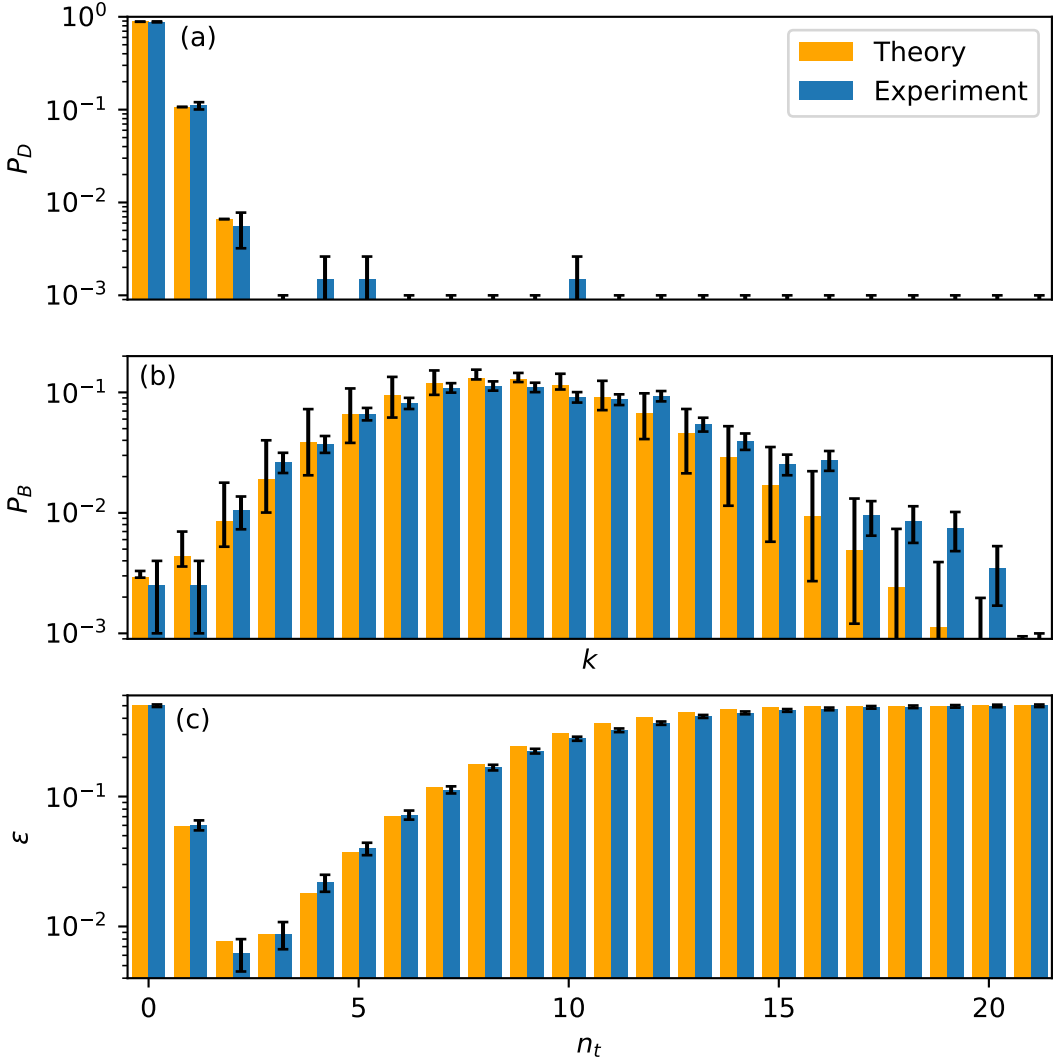


Figure 4.7: The PMFs of the (a) dark ${}^2S_{1/2} F = 0$ state and (b) bright ${}^2S_{1/2} F = 1$ state from a single shot readout (statistical error is from 1000 measurements per state). Theory corresponds to the optimal readout as determined by parameter optimisation using calibrations from the saturation curve fitting. There is good agreement between the P_D PMFs however the measured P_B PMF has a skew to the right from laser power uncertainty. Error bars on the theory plot account for the known laser power uncertainty. Readout error (c) compared shows ideal threshold number ($n_t = 2$) is in agreement between theory and experiment.

parameters were $\eta_{\text{det}} = 1.0\%$, $P_{\text{sat}} = 1.4 \mu\text{W}$ and background count fit was $R_D(P) = 274(7) (\text{s} \cdot \mu\text{W})^{-1}P + 60(50)\text{s}^{-1}$ and optimised readout parameters were $t_{\text{read}} = 313 \mu\text{s}$, $P = 1.2 \mu\text{W}$ and $n_t = 2$.

Figure 4.7.c shows agreement between theory and experiment for the optimal threshold number, however there is disagreement in the P_B distribution (figure 4.7.b). Even though the laser power is stabilized, this skew is likely from power calibration uncertainty $0.2 \mu\text{W}$ (16% relative uncertainty in the laser power for figure 4.7). Given the relative difference in the theoretical and experimental mean counts of the P_B PMF,

$$\frac{\sum_k k P_{B,\text{exp.}}(k) - \sum_k k P_{B,\text{theory}}(k)}{\sum_k k P_{B,\text{theory}}(k)} \approx \frac{9.3 - 8.7}{8.7} \approx 7\%, \quad (4.1)$$

this difference is reasonable given that the laser power uncertainty is higher and the fact that the experiment was performed under the saturation regime, where laser power and mean photon count will have approximately a linear relation.

4.2.3 Laser polarisation scan for optimising ion fluorescence

Steady state solutions (equation 3.96) for the fluorescing $^2S_{1/2} \leftrightarrow ^2P_{1/2}$ transition of $^{171}\text{Yb}^+$ [62, 63] predict polarisation dependency of the fluorescence rate. To determine the optimal laser polarisation in experiment for optically pumping on the π -transition ($\theta_{BE} = \frac{\pi}{2} \pm \frac{\pi}{2}$), the σ^\pm -transitions ($\theta_{BE} = \pm\pi/2$) or Doppler cooling and readout ($\theta_{BE} = \frac{\pi}{2} \pm \frac{\pi}{2} \pm \arccos \frac{1}{\sqrt{3}}$), a scan of ion fluorescence rate against laser polarisation is measured.

The measurement protocol consists of a control loop that scans through different voltages that control the polarisation angle of the incident Doppler beam via its EOM. A single measurement in the loop measures ion fluorescence rate by counting clicks on an APD incident with the ion's fluorescence

(figure 4.5). A count rate is determined by dividing the background subtracted counts by the measurement period (100 ms). Measurement durations of 100 ms were chosen because the shot noise is sufficiently low given count rates on the order of 10,000 counts/s are measured. This would correspond to ~ 1000 counts in a measurement which would have a shot noise standard deviation of $\sigma = \sqrt{1000} \sim 30$ counts.

Results of the polarisation scan (figure 4.8) show a reasonable fit to theory for a linearly polarised laser orthogonal to the external magnetic field direction. There is a discrepancy between theory and measurement that could be

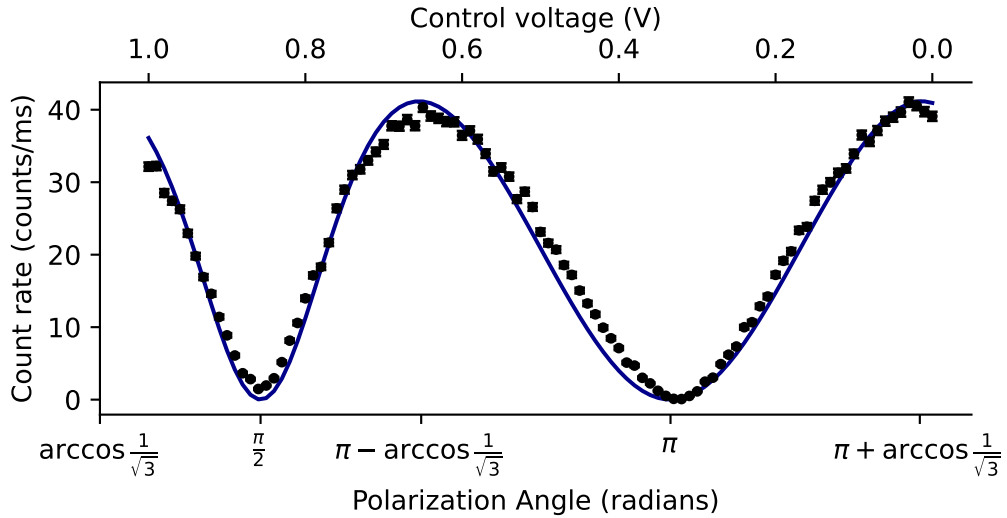


Figure 4.8: A scan of the ion fluorescence as a function of the laser polarisation angle relative to an external magnetic field. The curve fit uses equation 3.96 to find the relation between voltage applied and polarisation angle. Minima at $\pi/2$ and π correspond to the fluorescing laser only driving σ^\pm transitions and π transitions respectively. Maxima are at $\theta_{BE} = \pi \pm \arccos \frac{1}{\sqrt{3}}$.

due to the laser polarisation being slightly circular, which is not captured by the theoretical model. In experiment, where the π -transition is required for optically resetting the state (figure 4.10) in a Raman sideband cooling cycle (section 5), the voltage corresponding to the broad minimum in fluorescence is recorded and input into other experiment protocols. Similarly the sharp minimum corresponds to the σ^\pm dark state and can also be set for state preparation.

4.2.4 Optical pumping into ${}^2S_{1/2} F = 0$

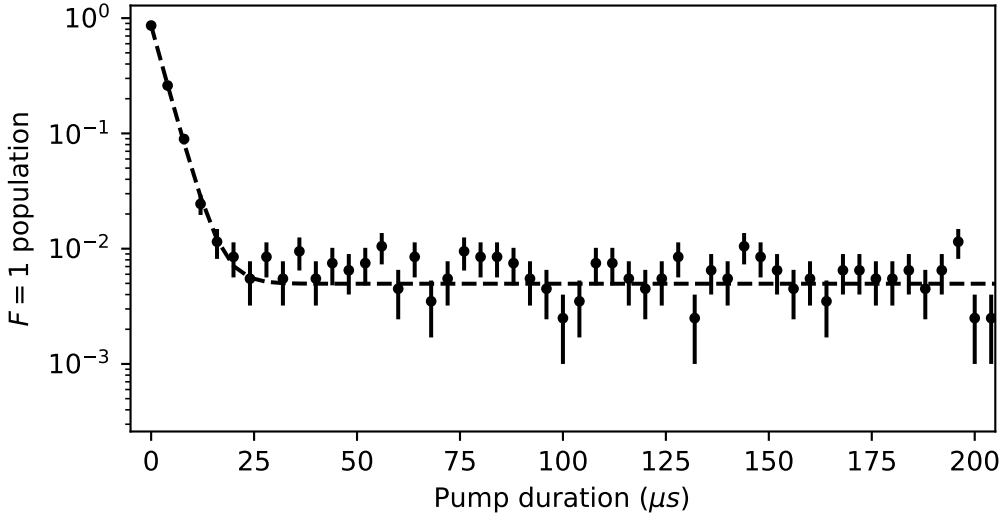


Figure 4.9: Measurement of the population of the ${}^2S_{1/2} F = 1$ manifold as a function of pumping duration. The asymptote is likely due to the noise floor of the state-selective readout method and not the limit of the optical pumping infidelity, which is expected to be of order 10^{-6} . The pump rate 1/e time constant was fit to $\tau = 3.33(9) \mu s$ and the readout infidelity asymptote was $\epsilon = 5(2) \times 10^{-3}$. Each data point represents the average of 1000 single shot measurements.

Most experiments using ${}^{171}\text{Yb}^+$ begin by initialising it to the ${}^2S_{1/2} F = 0$ state, because it is a single, energetically isolated state that is easy to prepare with high fidelity. This state forms a qubit with the ${}^2S_{1/2} F = 1 m_F = 0$ state that is first-order insensitive to external magnetic fields. It is prepared from the ${}^2S_{1/2} F = 1$ manifold by resonantly driving the ${}^2S_{1/2} F = 1 \leftrightarrow {}^2P_{1/2} F = 1$ transition which includes a decay channel to ${}^2S_{1/2} F = 0$. This state can be prepared to high fidelity because the energy separation between the nearest non-forbidden resonance and the resonance of the laser performing optical pumping is $\Delta = -2\pi \times 12.6$ GHz. The estimated preparation infidelity while optical pumping around $s_0 = 1$ will be

$$\epsilon_{\text{prep}} \approx \left(1 + \frac{s_0}{3}\right) \left(\frac{\Gamma}{2\Delta}\right)^2 \sim 8 \times 10^{-7} \quad (4.2)$$

In experiment, this state preparation is carried out by the Doppler cooling

beam phase modulated at 2.1 GHz. The EOM produces a blue sideband resonant with the optical pumping transition. Pump rate as well as the noise floor of measuring the $F = 1$ state are illustrated in figure 4.9.

This optical pumping technique is insensitive to the laser's polarisation, as long as the polarisation is not purely addressing σ^+ or σ^- transitions. Otherwise, the pump laser could unwantedly optically pump into the ${}^2S_{1/2}$, $F = 1$, $m_F = \pm 1$ states. This is never of concern since the Doppler beam is always linearly polarised.

4.2.5 Optical pumping into ${}^2S_{1/2}$ $F = 1$ Zeeman sub-levels

Typically, to prepare a fully populated Zeeman sub-level in the ${}^2S_{1/2}$ $F = 1$ hyperfine manifold, the $F = 0$ would be prepared by optically pumping the ${}^2S_{1/2}$ $F = 1 \leftrightarrow {}^2P_{1/2}$ $F = 1$ transition followed by a π -pulse using resonant microwaves to invert the population into the desired ${}^2S_{1/2}$ $F = 1$ Zeeman sub-level. The time needed to perform this method is $\sim 40 \mu\text{s}$. Most of this time is spent preparing the $F = 0$ state during optical pumping. This method is a two step process that requires extra control overhead compared to the following optical pumping technique.

All Zeeman sub-levels in the ${}^2S_{1/2}$ $F = 1$ manifold are coupled to ${}^2P_{1/2}$ $F = 0$ via an electric dipole transition (figure 3.12). By driving any two of the three transitions, the third un-driven ground state can be optically pumped into. This technique was used in our system using Doppler beams resonant with the ${}^2S_{1/2}$ $F = 1 \leftrightarrow {}^2P_{1/2}$ $F = 0$ transition and with appropriate polarisation to drive the desired states. Two different optical pumping schemes were used to drive population into the ${}^2S_{1/2}$ $F = 1$, $m_F = 0$ and $m_F = +1$ states.

Pumping to $F = 1, m_F = 0$

To prepare the $m_F = 0$ state, σ^+ and σ^- transitions must be driven, and no π transitions. This was achieved by rotating the 370 nm Doppler cooling laser's linear polarisation perpendicular to the external magnetic field using the Conoptics EOM. This linear polarisation drives an equal combination of the σ^\pm transitions since the electric field partially projects onto both electric dipole terms for the σ^\pm transitions,

$$\mathbf{d}_{\sigma^\pm} \cdot E_0 \hat{\mathbf{x}} = \frac{d_{\sigma^\pm}}{\sqrt{2}} (\hat{\mathbf{x}} \mp i \hat{\mathbf{y}}) \cdot E_0 \hat{\mathbf{x}} = \frac{d_{\sigma^\pm} E_0}{\sqrt{2}}. \quad (4.3)$$

The dark state generated by this technique is shown in figure 4.8 where $\theta_{BE} = \pi/2$.

Pumping to $F = 1, m_F = +1$

Preparing the $m_F = +1$ state can not be achieved with linearly polarised lasers alone². This is because linear polarisation will always contain equal (if not zero) components of σ^\pm couplings. Instead, a pure σ^+ transition was driven by aligning the external magnetic field along the direction of an incident laser with circular polarisation. This laser alone will on average pump population equally into the $m_F = 0$ & $+1$ states. To pump the population remaining in the $m_F = 0$ state, the Doppler cooling laser, which is perpendicular to the external magnetic field direction, has its polarisation rotated parallel to the magnetic field via the Conoptics EOM to drive only π transitions.

Fidelity of this technique is limited by the polarisation purity, alignment of the beams with respect to the external magnetic field, and the magnetic field direction stability. Fidelity was optimised by observing ion fluorescence on an electron-multiplying charge-coupled device (EMCCD) while tuning quarter-

²When Zeeman shift is weak s.t. resonances are unresolved within the transition linewidth. When the shift is strong, Zeeman states can be individually driven even with impure polarization.

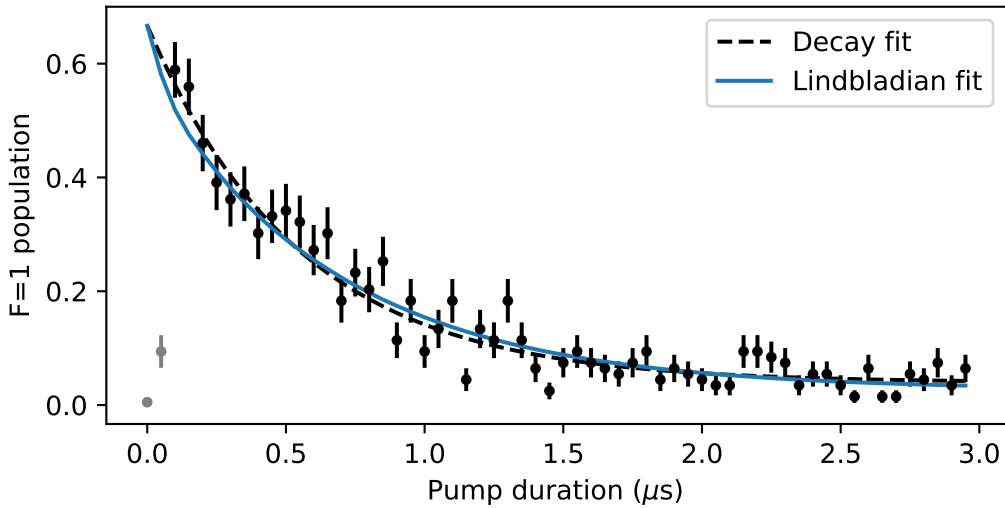


Figure 4.10: Measurement of the population of the $^2S_{1/2} F = 1$ manifold after a π -pulse is driven on the $^2S_{1/2} F = 0 \leftrightarrow F = 1, m_F = +1$ qubit as a function of pump laser pulse duration. The population is the compliment of the population that was in the $F = 1, m_F = +1$ state before the π pulse. Gray data points are unexplained artifacts, likely due the response time of the Conoptics EOM at short duration. The initial population is $\sim \frac{2}{3}$ since it begins in an even mix of the three Zeeman sub-levels of the $F = 1$ hyperfine manifold. Population is prepared with a fitted infidelity of 4(3)% into the $m_F = +1$ state. The fitted $1/e$ time constant was $0.55(9) \mu\text{s}$ corresponding to a pump rate of $0.015(2)\Gamma$. Individual Rabi rates of the 3 Zeeman sub-level transitions used in the Lindbladian simulation were $\Omega_\pi = 0.38\Gamma$ (measured), $\Omega_{\sigma+} = 0.14(1)\Gamma$ (fitted) and $\Omega_{\sigma-} = 0.025(11)\Gamma$ (fitted).

wave plates (QWPs) and HWPs as well as the current through Zeeman coils oriented perpendicular to the external magnetic field to fine-tune its co-alignment with the σ^+ -driving laser. Fluorescence measured on the EMCCD was minimised, which corresponds to the unwanted σ^- coupling being diminished. This method achieved a fidelity of 96(3)%.

To compare the pump rate performance to theory, the pumping scheme was simulated by numerically solving the appropriate Lindblad master equation. In experiment, the Rabi rate of the π -beam was estimated by taking a saturation curve with the laser polarisation set to 54.7° from the external magnetic field direction to give maximum fluorescence. The Rabi rate inferred for figure 4.10 was $\Omega_\pi = 0.38\Gamma$. Ω_{σ^+} beam could not easily be calibrated in the same way because the beam was coaxial with the external magnetic field, so it could never drive the cyclic fluorescing transition since it would always optically pump to a dark state. Its power however was measured at 2.4 μW with relative standard deviations of 0.5% over 3 seconds and 0.7% over 85 seconds. Performing a fit with the Lindbladian, $\Omega_{\sigma^+} = 0.14(1)\Gamma$ and $\Omega_{\sigma^-} = 0.025(11)\Gamma$ were found. This suggests there is a remaining polarisation impurity in either the π or σ^+ driving beam, since the σ^- coupling was not completely zero.

4.2.6 Qubit characterisation

The $|S, 0, 0\rangle \leftrightarrow |S, 1, 0\rangle$ and $|S, 0, 0\rangle \leftrightarrow |S, 1, 1\rangle$ qubits are probed using a combination of resonant microwaves for coherent operations as well as optical readout (section 4.2.2) for state collapse and measurement.

Rabi oscillation protocol

Once population is prepared into ${}^2S_{1/2} F = 0$, coherent operations on the ${}^2S_{1/2}$ hyperfine qubit can be performed. Three addressable magnetic dipole transitions exist between $F = 0$ and the 3 Zeeman sub-levels within $F = 1$.

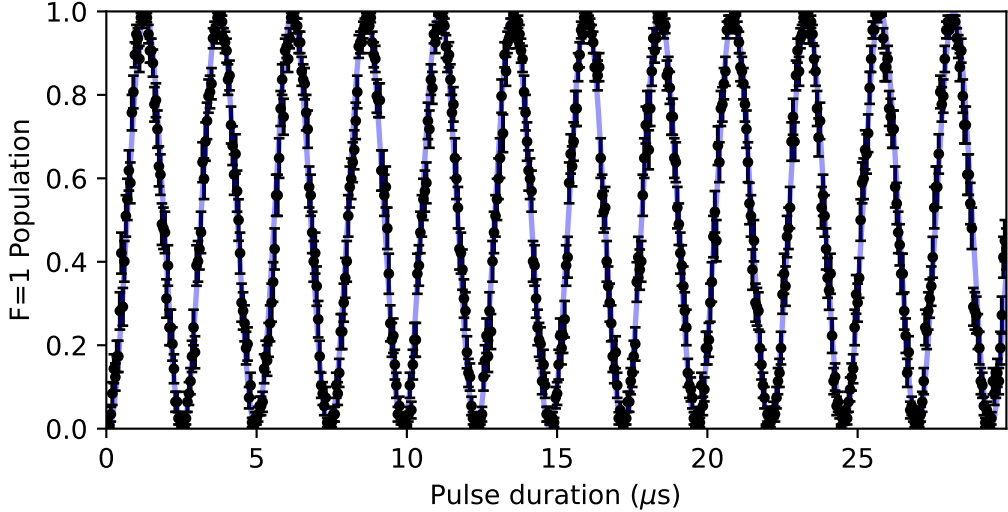


Figure 4.11: Rabi oscillations across the $^2S_{1/2} F = 0 \leftrightarrow ^2S_{1/2} F = 1 m_F = +1$ magnetic dipole transition. Error bars represent 1 standard deviation given by the statistical uncertainty of a binomial distribution given 100 measurements per data point. Fitted Rabi rate and amplitude are $2\pi \times 408.88(8)$ kHz and 99.64(15)% respectively.

Resonant microwaves are applied to the ion using the microwave system described in section 4.1.1. 370 nm lasers are switched off using AOMs while the microwaves are applied to prevent the weak quantum Zeno effect. Otherwise, the laser coupling to the $^2S_{1/2}$ states interrupts microwave driven Rabi oscillations[132]. After the microwave pulse, state selective measurement is performed, as explained in section 4.2.2.

By sweeping the duration of the resonant microwave over many measurements, Rabi oscillations can be recovered (figure 4.11). With the available +33 dBm from the microwave source, a π -pulse can be driven in a duration of $1.2229(2)\mu\text{s}$.

Microwave resonance protocol

The population inversion fidelity from a π -pulse is conditional on the frequency of the microwave source matching the atomic resonance (equation 3.47). To find the resonance of a transition, the microwave pulse duration was set to the π -pulse duration found from the previous Rabi oscillation protocol, then

a microwave frequency sweep is performed in a similar method. The sweep

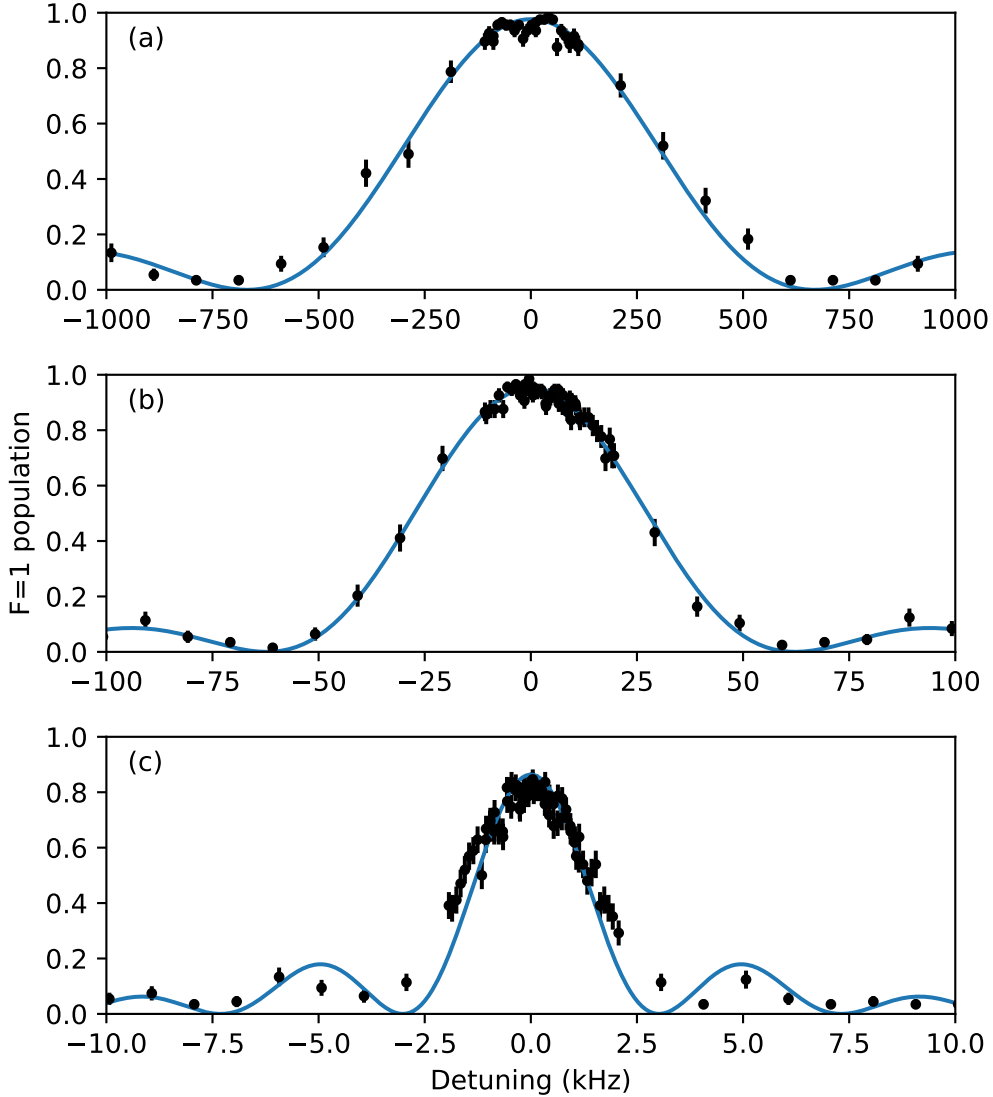


Figure 4.12: A sweep of the $^2S_{1/2} F = 0 \leftrightarrow ^2S_{1/2} F = 1 m_F = +1$ resonance at three different driving powers. The synthesizer's output power was set to (a) +5.4 dBm, (b) -20 dBm and (c) -40 dBm. The x-axis is centered around the fitted resonances, (a) $\omega_0=12.646296(5)$ GHz, (b) $12.6462985(3)$ GHz and (c) $12.64629903(3)$ GHz found by fitting equation 3.47. Fitted Rabi rates were (a) $\Omega_m = 2\pi \times 439(5)$ kHz, (b) $29.7(2)$ kHz and (c) $2.386(17)$ kHz. Fitting in the final plot is poor because coherence time is on the timescale of the probing pulse ($\sim 100 \mu\text{s}$).

of microwave frequency plots out a resonance peak which follows the equation for a coherent two-level atom driven by a field detuned by frequency Δ (equation 3.47). Line-broadening of this resonance scales with the driving field's intensity and increases the uncertainty in the resonance. This is evidenced

by the precision of fits quoted in figure 4.12. To obtain the most precise fit, microwave power is reduced to the point where π -pulse duration is of similar duration to the coherence time of the transition. Beyond this, the resonance peak drops and broadens due to decoherence.

Ramsey fringe protocol

The dephasing of the qubit can be measured by taking a Ramsey measurement. After preparing the qubit in its initial $|F = 0\rangle$ state, the qubit is rotated by near-resonant microwaves as close as possible to a 50-50 superposition. This is called a $\frac{\pi}{2}$ -pulse since it rotates the qubit along the polar angle of the Bloch sphere by $\frac{\pi}{2}$ radians. In practice this is achieved by first taking a Rabi curve as in figure 4.11 and finding the duration that is equal to half the duration for a π -pulse. After the qubit is rotated to an equal superposition, it is left to evolve and interact with the environment, as described in section 3.4.1. After this, a second $\frac{\pi}{2}$ -pulse will ideally rotate the qubit state back into $|F = 1\rangle$ if the environment did not change the qubit's phase. Finally, the qubit is measured. This process is repeated for different delays to find how the qubit phase evolves. This evolution can be expressed in terms of unitary operations of the Hamiltonian for a driven two level system (equation 3.48),

$$\hat{U}_I\left(\frac{\pi}{2\Omega}\right) = e^{i\frac{\pi}{4\Omega}(\Delta\hat{\sigma}_z + \Omega\hat{\sigma}_x)} = \hat{I} \cos\left(\frac{\pi\Omega'}{4\Omega}\right) + i\left(\frac{\Delta}{\Omega'}\hat{\sigma}_z + \frac{\Omega}{\Omega'}\hat{\sigma}_x\right) \sin\left(\frac{\pi\Omega'}{4\Omega}\right) \quad (4.4)$$

which approximates to a square-root-of-NOT-like-gate, $\frac{1}{\sqrt{2}}(\hat{I} + i\hat{\sigma}_x)$ when $\Delta \ll \Omega$. The unitary for free evolution in the rotating frame is

$$\hat{U}_0(T) = e^{i\frac{\Delta}{2}T\hat{\sigma}_z} = \hat{I} \cos\left(\frac{\Delta T}{2}\right) + i\hat{\sigma}_z \sin\left(\frac{\Delta T}{2}\right). \quad (4.5)$$

The excited state population after a probing the atom with a Ramsey protocol is then(see appendix B.3 for derivations),

$$|\langle e | \hat{U}_I(\pi/\Omega) \hat{U}_0(T) \hat{U}_I(\pi/\Omega) | g \rangle|^2 = \\ \left(\frac{2\Omega \sin(\frac{\pi\Omega'}{4\Omega})}{\Omega'} \right)^2 \left(\left(\frac{\Delta}{\Omega'} \sin \left(\frac{\pi\Omega'}{4\Omega} \right) \sin \left(\frac{\Delta T}{2} \right) \right)^2 - \frac{\Delta}{\Omega'} \sin \left(\frac{\pi\Omega'}{2\Omega} \right) \sin(\Delta T) + \left(\cos \left(\frac{\pi\Omega'}{4\Omega} \right) \cos \left(\frac{\Delta T}{2} \right) \right)^2 \right). \quad (4.6)$$

Figure 4.13 shows measured Ramsey fringes on both the $^2S_{1/2}$ $|F = 0, m_F = 0\rangle \leftrightarrow |F = 1, m_F = 0\rangle$ and $|F = 0, m_F = 0\rangle \leftrightarrow |F = 1, m_F = +1\rangle$ transitions. Using the theory for de-phasing in section 3.4.1 an envelope fit was produced for each measurement. Tonal noise at 50 Hz seems to dominate the de-phasing for the $|0, 0\rangle \leftrightarrow |1, 0\rangle$ qubit. This noise frequency is assumed in figure 4.13.a because of the drop in coherence near 10 ms and also because it is the dominant noise source in most labs because of the mains electricity operating at a fundamental tone of 50 Hz. The standard deviation in resonance produced by the mains noise is approximated to $\sigma_{\Delta\omega} = 2\pi \times 131(3)$ Hz or $\sigma_B = 84.8(1.9)$ mG in terms of external magnetic field strength standard deviation. This magnetic field is calculated using an approximation of the second-order sensitivity of $\delta_B = 2\pi \times 310.8$ Hz/G²[65] via a first-order taylor series to $2\delta_B B_0 = 2\pi \times 1.549$ kHz/G around the external magnetic field strength of $B_0 = 2.49137(2)$ G, as determined by the resonances of the microwave transitions. Using section 3.4.1 (equation 3.90), $T_2 = 4.72(13)$ ms is calculated, where $\langle e^{i\phi(T_2^*)} \rangle = e^{-1}$,

$$T_2 = \frac{2}{\omega_{noise}} \arcsin \left(\sqrt{\pi} \frac{\omega_{noise}}{\sigma_{\Delta\omega}} \right). \quad (4.7)$$

The Ramsey fringes of the $^2S_{1/2}$ $F = 0 \leftrightarrow F = 1$ $m_F = +1$ transition by comparison are much less coherent. This is because the energy of the $m_F = +1$ state has a much stronger dependence on external magnetic field

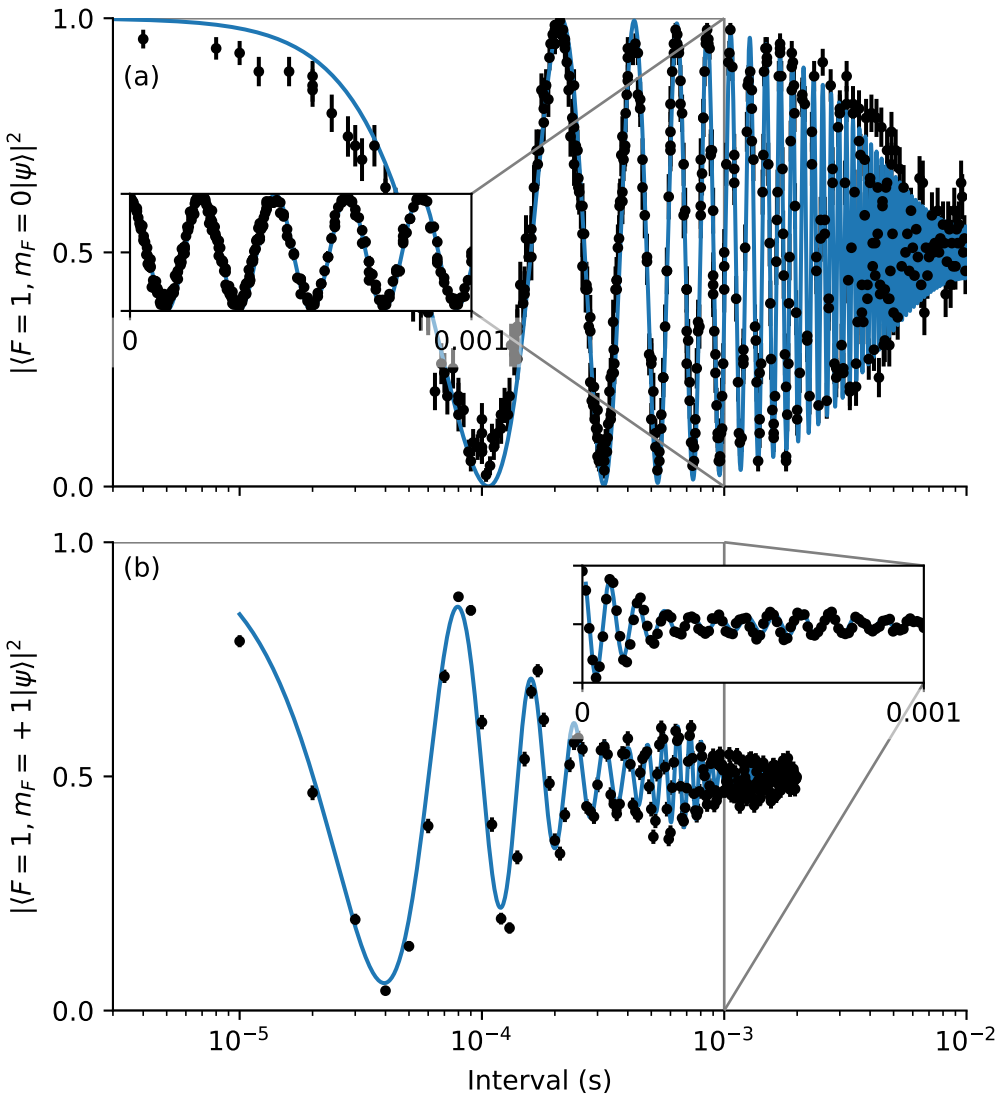


Figure 4.13: Ramsey interferometry of the (a) $|^2S_{1/2} \ F = 0, m_F = 0\rangle \leftrightarrow |F = 1 m_F = 0\rangle$ and (b) $|F = 0, m_F = 0\rangle \leftrightarrow |F = 1 m_F = +1\rangle$ qubits. Plots are logarithmic timescale with linear timescale 1 ms insets to show the timescale of both the interference fringes for (a) $\Delta/2\pi = 4.7054(11)$ kHz and (b) $\Delta/2\pi = 12.444(19)$ kHz, as well as the coherence times, (a) $T_2 = 4.72(13)$ ms and (b) $T_2 = 163(8)$ μ s.

strength ($g_J\mu_B/(2\hbar) = 1.4$ MHz/G) as determined by the Breit-Rabi formula (equation 3.31). The de-phasing envelope of figure 4.13.b fits well to a magnetic field noise power spectrum consisting of white noise with a power density of $\sqrt{\tilde{S}_0} = 27(7)$ $\mu\text{G}/\sqrt{\text{Hz}}$ and tonal noise resonant at 1.39(5) kHz with $\sigma_{\Delta\omega} = 1.98(11)$ mG standard deviation.

Investigations into the tonal noise of the magnetic field involved using the Zeeman coils and magnetic field sensors to measure the magnetic field noise spectrum around the trap. They found AC mains noise at its 50 Hz fundamental and trailing harmonics (150 Hz, 250 Hz, 350 Hz) but no signature tone near 1.39(5) kHz was ever found. It is likely then this magnetic field noise source is localised very close to the ion trap inside the vacuum chamber.

Another possibility is any DC biasing of the powerful microwaves may cause a change in the DC magnetic field direction during the Ramsey pulses. This would cause quantum beats in the Zeeman states because the quantization axis would be different between the microwave pulse and free evolution[133]. DC biasing may occur through rectification if the microwave line has any n-p-like junction.

Chapter 5

Raman Motional Sideband Cooling on Zeeman-split states

This chapter begins with my first author paper, J. Scarabel et al., “Raman Sideband Cooling $^{171}\text{Yb}^+$ Across Zeeman Sub-levels,” Front. Opt. + Laser Sci. 2021 (2021), Pap. JW7A.33, Nov. 2021, doi: 10.1364/FIO.2021.JW7A.33. I performed the experiment, wrote the entire paper and analysed all the data.

The rest of this chapter shows more results and explores a different Raman transition scheme that was implemented after the paper written.

Raman Sideband Cooling $^{171}\text{Yb}^+$ Across Zeeman Sub-levels

Jordan Scarabel,^{1,*} Kenji Shimizu,¹ Moji Ghadimi,¹ Mirko Lobino^{1,2} and Erik Streed^{1,3}

¹Centre for Quantum Dynamics, Griffith University, Nathan QLD 4111, Australia.

²Queensland Micro- and Nanotechnology Centre, Griffith University 4111, Australia.

³Institute for Glycomics, Griffith University, Southport 4215, Australia.

*jordan.scarabel@griffithuni.edu.au

Abstract: We implemented Raman sideband cooling in $^{171}\text{Yb}^+$ between weakly split Zeeman states rather than across the typical 12.6 GHz hyperfine splitting and infer sub-Doppler cooling from $\bar{n}_{x,y,z} = [29(2), 36(16), 16.2(5)]$ to $[0.07(7), 2.0(1.2), 5.6(2)]$. © 2021 The Author(s)

1. Introduction

Trapped ions are prepared in their motional ground state to reduce motion-induced errors in quantum operations [1]. The motional ground state can be prepared by either coherently driving Raman transitions with resolved motional sidebands [2], electromagnetically-induced transparency cooling [3] or sideband cooling on a narrow atomic transition [4]. Raman sideband cooling (RSC) $^{171}\text{Yb}^+$ has previously been reported using the 12.6 GHz $^2S_{1/2}$ hyperfine splitting as ground states in a 3-level Raman transition using a Raman transition derived an optical frequency comb [5] or electro-optic modulation [6], which can all be costly or technically difficult. However, a Raman transition across $^2S_{1/2} F = 1$ ground state Zeeman sub-levels can also be driven using only a single continuous wave laser and two acousto-optic modulators. RSC across Zeeman transitions has been achieved in even isotopes $^{138}\text{Ba}^+$ [7] and $^{40}\text{Ca}^+$ [8] but was not reported in $^{171}\text{Yb}^+$.

2. Methods

Here we achieve RSC across the $^2S_{1/2} F = 1$, $|m_F = 0\rangle \equiv |\downarrow\rangle \rightarrow |m_F = +1\rangle \equiv |\uparrow\rangle$ Zeeman splitting and $^2P_{1/2} |F = 0, m_F = 0\rangle \equiv |e\rangle$ excited state as in figure 1. Raman beams were detuned from resonance by -1 GHz and split by a few MHz using two 180 MHz acousto-optic modulators to bridge the Zeeman splitting $\delta_B = 2\pi \times 4.9$ MHz and motional mode frequencies $\omega_{x,y,z} = 2\pi \times [1.58, 1.33, 0.57]$ MHz. One laser was used for the two Raman beams and another for Doppler cooling and repumping, allowing flexibility in selecting Raman laser detuning.

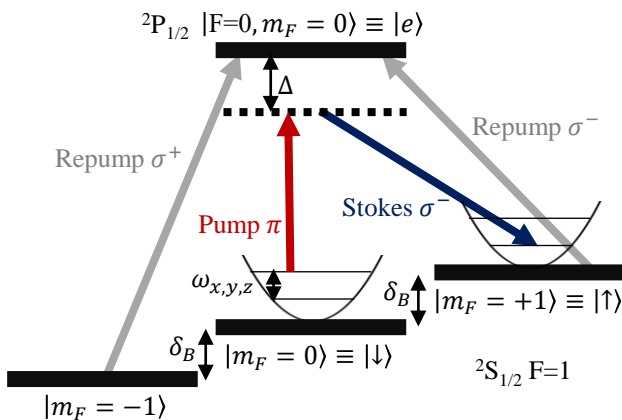


Fig. 1. State diagram of $^{171}\text{Yb}^+$ closed cycle system with narrow linewidth Raman and repump transitions.

To achieve RSC, the ion is first Doppler cooled then pumped to $|\downarrow\rangle$ by the σ^\pm repump beam (Fig 1). It is then driven by the Raman pump beam, linearly polarized parallel to the magnetic field, driving only π transitions to $|e\rangle$. The Raman transition is complete by the Stokes beam, linearly polarized perpendicular to the magnetic

field, driving σ^+ and σ^- transitions. The frequency of the Stokes beam is modulated throughout cooling so the σ^- transition switches between the resonances of the three (x, y, z) motional transitions that remove 1 quanta of motion. The Stokes σ^+ transition does not drive to $|m_F = -1\rangle$ because the Zeeman splitting makes it $2\delta_B$ detuned from resonance. The repump beam may also act as a Stokes beam during this process, but is not resonant with any states. The repump beam then pumps out any transferred population in $|\uparrow\rangle$ back to $|\downarrow\rangle$ by on-resonant scattering and the cooling cycle is repeated. The repump laser also has 14.7 GHz sidebands generated by an electro-optic modulator to repump any population that off-resonantly scatters to ${}^2S_{1/2} F=0 m_F=0$ back into the main cooling cycle.

After the cooling cycle, measurements are made by applying a Raman pulse and then transferring left-over population in $|\downarrow\rangle$ to ${}^2S_{1/2} F=0 m_F=0$ by a resonant microwave pulse. $|\downarrow\rangle$ and $|\uparrow\rangle$ can then be discriminated via state selective fluorescence using the Doppler cooling beam.

3. Results

Red side-bands of the Raman spectrum are suppressed after RSC (Fig. 2a) at frequencies $-\omega_{x,y,z}$. Rabi oscillation damping is also reduced on the center Raman transition after RSC (Fig. 2b). Simultaneous fits to the spectra and Rabi oscillations give thermal states with $\bar{n}_{x,y,z} = [29(2), 36(16), 16.2(5)]$ and $[0.07(7), 2.0(1.2), 5.6(2)]$ before and after RSC respectively. Also fitted are the Raman transition Rabi rate $2\pi \times 42.64(18)$ kHz and off-resonant scattering rate $2\pi \times 1.36(4)$ kHz. The Rabi rate during cooling is approximately 30 times faster than fitted because after cooling the Raman beam powers are reduced by a factor of 30 for the measurement pulse. Offset of population from $|\uparrow\rangle$ in figure 2a is attributed to off-resonant scattering.

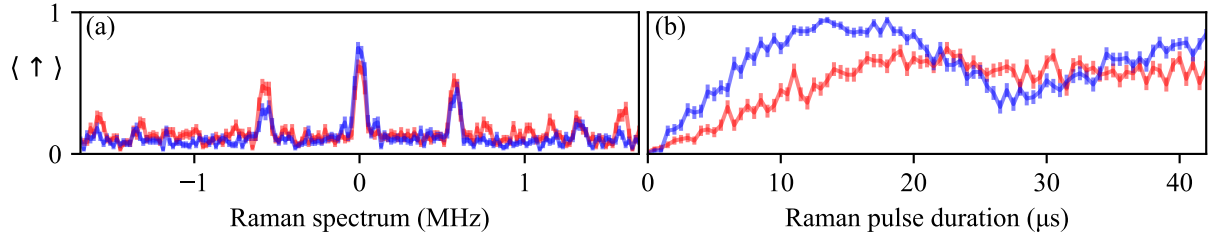


Fig. 2. Comparison of the Raman motion spectrum (a) and Rabi oscillations of the center resonance (b) with 0 ms (red) and 6 ms (blue) of RSC.

We demonstrate cooling beyond the Doppler limit via Raman sideband cooling on Zeeman split states in ${}^{171}\text{Yb}^+$. With a faster Rabi rate from higher intensity Raman beams and a secondary cooling phase with pulsed Raman transitions that do not compete with the reset beam, a lower motional quanta may be achieved.

References

1. F. Schmidt-Kaler et al. Realization of the Cirac-Zoller controlled-NOT quantum gate. *Nature*, 422(6930):408–411, mar 2003.
2. C. Monroe et al. Resolved-sideband Raman cooling of a bound atom to the 3D zero-point energy. *Physical Review Letters*, 75(22):4011–4014, nov 1995.
3. R. Lechner et al. Electromagnetically-induced-transparency ground-state cooling of long ion strings. *Physical Review A*, 93(5):053401, may 2016.
4. E. Peik et al. Sideband cooling of ions in radio-frequency traps. *Physical Review A - Atomic, Molecular, and Optical Physics*, 60(1):439–449, jul 1999.
5. D. Hayes et al. Entanglement of Atomic Qubits Using an Optical Frequency Comb. *Physical Review Letters*, 104(14):140501, apr 2010.
6. K. Kim et al. Quantum simulation of the transverse Ising model with trapped ions. *New Journal of Physics*, 13(10):105003, oct 2011.
7. C. M. Seck et al. Raman sideband cooling of a Ba + 138 ion using a Zeeman interval. *Physical Review A*, 93(5):053415, may 2016.
8. S. Webster. *Raman Sideband Cooling and Coherent Manipulation of Trapped Ions*. PhD thesis, University of Oxford, 2005.

5.1 Motivation

Raman sideband cooling across Zeeman-split states allows fine control of an ion's motion across a near-degenerate $^2S_{1/2}$ $F = 1$ Zeeman-shift-split qubit. Extracting optical work from an anti-Stokes style transition across the motional sidebands of the near-degenerate Zeeman-shift-split qubit will show that the process is energetically favourable and can perform above the Carnot limit.

A problem arises when attempting to drive degenerate states, where the heat engine efficiency would approach unity. Zeeman degenerate states require zero magnetic field to suppress Zeeman shift. In this case, magnetic field noise can dominate, and the quantisation axis of total angular momentum will drift in direction. The angular momentum of incident lasers then would not couple deterministically to the π , σ^+ & σ^- transitions and coherent transitions will not be able to be driven.

To avoid this, very weak magnetic fields of the order of 10^{-3} Gauss can suffice to define the quantisation axis and overcome magnetic field noise in a low noise system[134]. This bounds the efficiency of an otherwise fully efficient spin-heat engine by the Zeeman shift from the weak field. In the case of our system, a milliGauss field and an ion with harmonic frequency on the order of 10^6 Hz bounds the efficiency of the engine to $\lesssim 99.9\%$.

In $^{171}\text{Yb}^+$, the three Zeeman split states in the $^2S_{1/2}$ $F=1$ ground state have a Landé g-factor ≈ 1 and Zeeman shift 1.4 MHz/G proportional to the m_F quantum number of the Zeeman sub-level. An external magnetic field of the order of a few Gauss is used to minimise unwanted Zeeman broadening of the $^2S_{1/2} \leftrightarrow ^2P_{1/2}$ transition and simultaneously avoid coherent population trapping in dark states of the $^2S_{1/2}$ $F=1$ manifold during state selective fluorescence qubit readout. In future experiments, coherent population trapping at the required milli-Gauss levels can be avoided in Doppler cooling and qubit readout by modulating the laser polarization at rates proportional to the dipole transition Rabi rate[63].

5.2 Z-axis motion-coupled Raman transitions

The first attempt at Raman sideband cooling involved coupling solely to the trap's z-axis motional mode (figure 5.1.a). This mode is formed by the DC harmonic potential of the trap, which is aligned with the shuttling axis, which oscillated at $\omega_z = 2\pi \times 555$ kHz ($\omega_z = 2\pi \times 570$ kHz in later months as trap conditions changed).

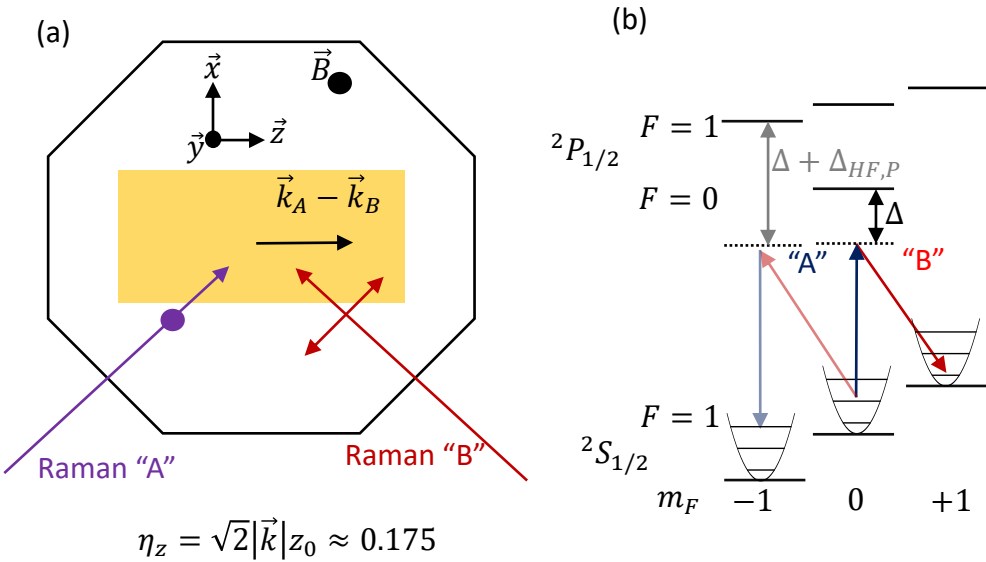


Figure 5.1: (a) Geometric configuration of Raman beams. Cartesian axes are mostly aligned to the trapping axes (x-y trap plane is slightly rotated by a few degrees). Magnetic field is aligned along \vec{y} . Raman A (pump) is linearly polarized parallel to the field and Raman B is linearly polarized orthogonal to the field. (b) Grotrian diagram of Raman excitation. The main Raman transition is $|S, 1, 0\rangle \leftrightarrow |S, 1, 1\rangle$ while a resonant weaker Raman transition is driven over $|S, 1, 0\rangle \leftrightarrow |S, 1, -1\rangle$.

The beam of Raman A enters the trap with a wave vector along the $\vec{k}_A = \frac{1}{\sqrt{2}}(\hat{x} + \hat{z})$ direction and Raman B with $\vec{k}_B = \frac{1}{\sqrt{2}}(\hat{x} - \hat{z})$. Using the quantum numbers $|l, F, m_F\rangle$ for naming states, the Raman transition is intended off-resonantly excite $|S, 1, 0\rangle \rightarrow |P, 0, 0\rangle$ via the Raman A beam and drive stimulated emission across $|P, 0, 0\rangle \rightarrow |S, 1, 1\rangle$ via the Raman B beam.

The difference in wave-vectors describes the effective wave vector of the Raman transition, $\vec{k}_A - \vec{k}_B = \sqrt{2}\frac{\omega_l}{c}\hat{z}$ and the direction of momentum transfer. This transfer couples almost completely to the z-axis of trapped ion motion.

Given $m = 171$ amu and $\omega_z = 2\pi \times 555$ kHz, the Lamb-Dicke parameter for the z-axis was $\eta_z \approx 0.179$. This coupling is quite strong, considering the Lamb-Dicke regime is achieved at temperatures $\bar{n}_z \ll \frac{1}{2}(\eta_z^{-2} - 1) \approx 15.2$ while the Doppler limit $\bar{n}_z \geq \frac{\Gamma}{2\omega_z} \approx 18.3$ is higher. The Lamb-Dicke approximation is not good in this regime and so the exact light-motion coupling will need to be used (equations 3.67) when beginning from a Doppler cooled motional state.

Another difficulty with this scheme (recognized only long after experiment) is there is a weaker but still driven coherent Raman resonance across the $|S, 1, 0\rangle \leftrightarrow |P, 1, -1\rangle \leftrightarrow |S, 1, -1\rangle$ states (figure 5.1.b). This is formed with the pump acting as the Stokes beam and vice versa. The result is a more complicated effective 5-level system that simultaneously drives both resonances out of $|S, 1, 0\rangle$. This transition is weaker because it has an extra detuning from the laser equal to $\Delta_{HF,P}$. Its motional resonances are also of opposite sign such that it weakly heats the ion when attempting Raman sideband cooling.

Simulations performed using five ($|S, 1, -1\rangle$, $|S, 1, 0\rangle$, $|S, 1, 1\rangle$, $|P, 1, 0\rangle$ and $|P, 1, -1\rangle$) and eight (adding $|S, 0, 0\rangle$, $|P, 1, 0\rangle$ and $|P, 1, 1\rangle$) states showed deviating results after one coherent Raman oscillation. The eight level simulation includes the effect of the Raman beams coupling off-resonantly to other $^2P_{1/2}$ states and the σ^+ component of the Stokes beam generating other coherent Raman transitions detuned by $2\delta_B$. From full Lindbladian simulations of this Raman excitation (appendix B.4), an empirical trend was found that the unwanted $|S, 1, 0\rangle \leftrightarrow |P, 1, -1\rangle \leftrightarrow |S, 1, -1\rangle$ Raman transition contributes

$$\frac{|\langle S, 1, -1 \rangle|^2}{|\langle S, 1, -1 \rangle|^2 + |\langle S, 1, 1 \rangle|^2} \approx \frac{\Delta^2}{(\Delta + \Delta_{HF,P})^2 + \Delta^2} \quad (5.1)$$

fractional population to the measured excited state. This fraction is important later for estimating the final temperature of the ion from measured Raman spectra after Raman sideband cooling. The unwanted Raman transition had the same Rabi rate as the intended transition and it increased the Raman transition's effective Rabi rate over the rate expected using the the 2-level

adiabatic approximation. The empirically found trend (see appendix B.4 for plots of these trends) is

$$\Omega_R \approx \frac{\Omega_S \Omega_P}{2} \sqrt{\frac{1}{\Delta^2} + \frac{1}{(\Delta + \Delta_{HF,P})^2}}. \quad (5.2)$$

5.2.1 Experiment protocol and results

In experiment, Raman excitation measurements were performed following the protocol in figure 5.2.

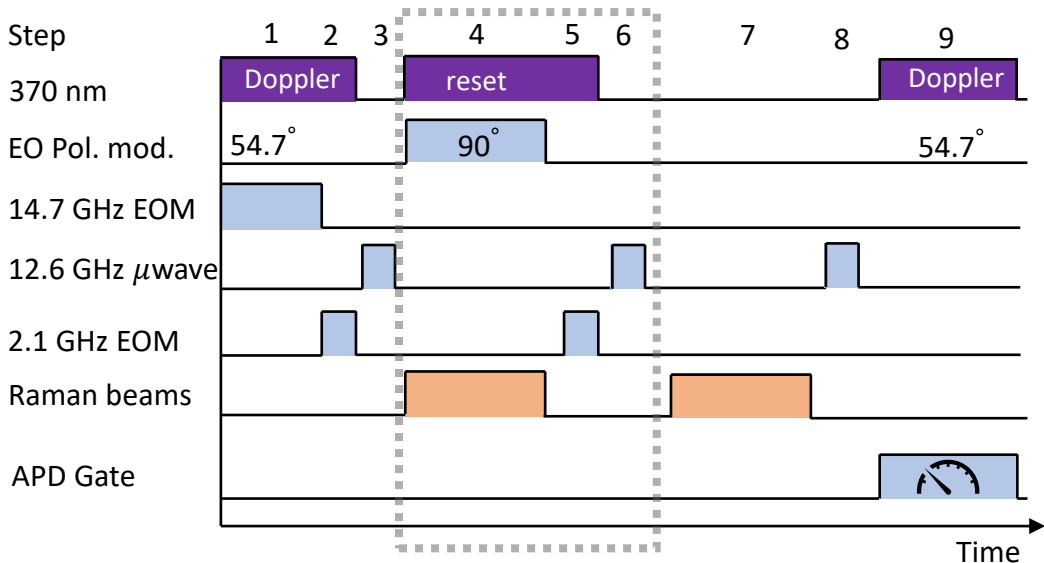


Figure 5.2: Switching pattern of the protocol used to perform Raman sideband cooling.

1. The ion is Doppler cooled to prepare it to a low but non-zero motional state in each trapping axis.
2. 2.1 GHz sidebands are driven on the Doppler laser to prepare the qubit in state ${}^2S_{1/2} F = 0$.
3. Microwaves resonant with the ${}^2S_{1/2} F = 0 \leftrightarrow F = 1 m_F = 0$ transition are driven to flip the state.
4. The Ramam beams are pulsed on a $n \rightarrow n - 1$ transition while the Doppler laser with polarization set to drive σ^\pm transitions pulses out of

phase with the Raman beams to reset the Raman transition when the ion projects to the excited Raman state.

5. Repeat of step 2.
6. Repeat of step 3.
7. The Raman transition is driven to probe a particular motional Raman transition.
8. The qubit is measured via state selective fluorescence. Steps 4-6 are not performed if Raman sideband cooling is not being performed.

It involves the same state preparation, microwave excitation and single shot qubit state readout methods as described in chapter 4. There are two extra Raman methods used in steps 4 (Continuous Raman sideband cooling) and 7 (probing a Raman transition) of figure 5.2.

Measurements of the Raman spectrum and Rabi oscillations on the $|n\rangle \leftrightarrow |n - 1\rangle$ motional resonance are shown in figure 5.3.

Spectrum characteristics

As predicted by the high Lamb-Dicke parameter and low motional resonance, the motion coupling is outside of the Lamb-Dicke regime, evidenced by the strong couplings to the $k = \pm 2$ and ± 3 resonances ($f = \pm 1.11$ MHz and ± 1.68 MHz) in the Raman spectra (figure 5.3.a). Typically such a Raman spectrum would be a good indicator of the approximate temperature of the ion, however as predicted by the Lindbladian simulations, there is a non-negligible coupling to the opposite motional resonance ($|n\rangle \rightarrow |n - (-k)\rangle$) such that the spectrum appears more symmetric than for a pure motion coupled Raman spectrum.

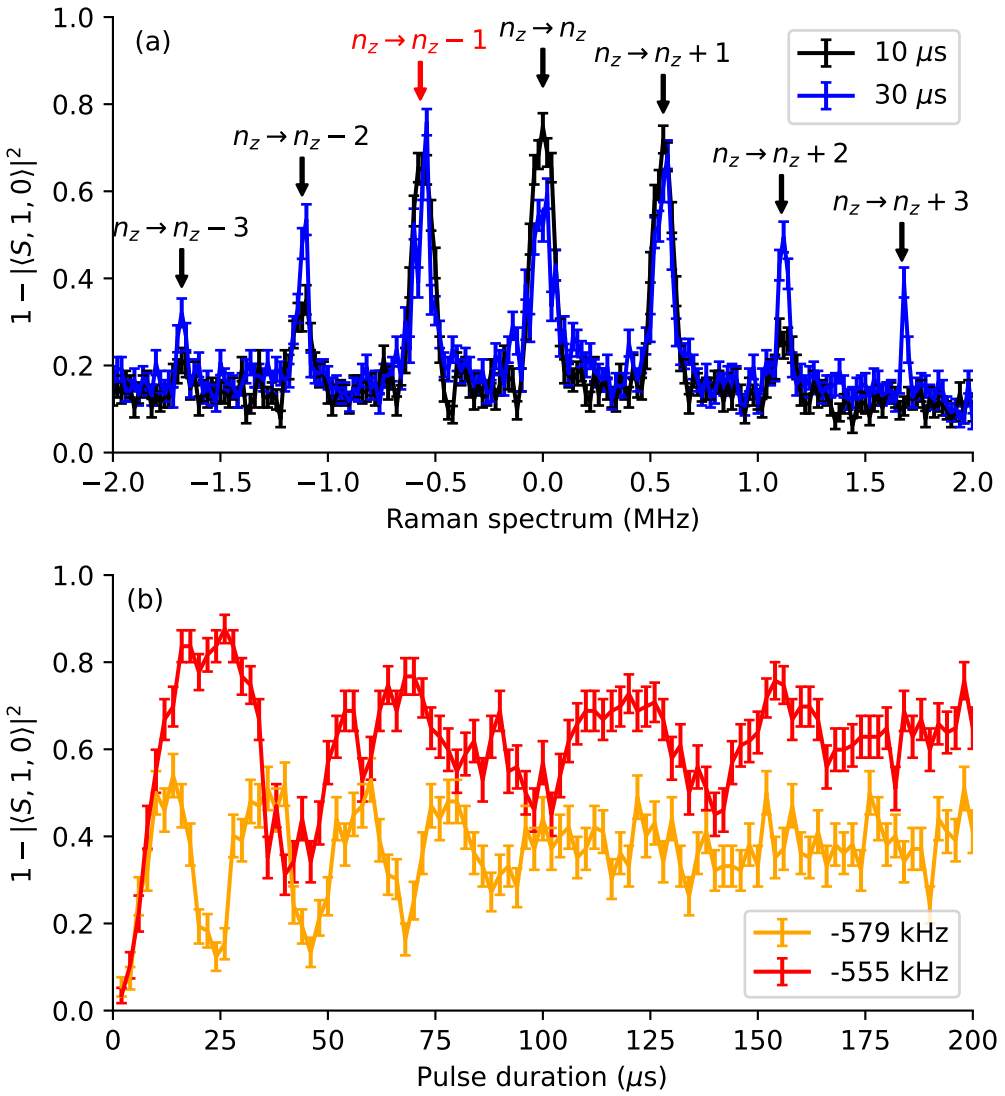


Figure 5.3: (a) Scan of the Raman spectrum with motional sidebands across the $^2S_{1/2} F = 1 m_F = 0 \rightarrow +1$ Zeeman sub-levels at two different probe durations (legend). Raman A and B powers were $13.7(3)$ μ W and $48.1(4)$ μ W respectively with $\Delta = -4.64$ GHz. (b) A pulse duration scan on the $|n\rangle \rightarrow |n-1\rangle$ transitions with two slightly different tunings (legend). The complex dynamics of the oscillation is from the spread in populated motional modes (section 3.3.2) and off-resonant spontaneous emission causing decoherence. Raman A and B powers were $27.3(4)$ μ W and $95.8(6)$ μ W respectively and $\Delta = -10$ GHz.

Rabi oscillation characteristics

Rabi oscillations in figure 5.3.b show the coherent but still complex Rabi oscillation dynamics expected from the strong light-motion coupling. When the Raman beams are tuned -579 kHz from the centre resonance, the transition is slightly detuned from the $|n\rangle \rightarrow |n-1\rangle$ transition such that the maximum excited state population is reduced as expected from the dynamics of the Rabi model (equation 3.47).

Off-resonant scattering off $|P, 0, 0\rangle$ equally populates $|S, 1, -1\rangle$, $|S, 1, 0\rangle$ & $|S, 1, 1\rangle$. It is observed in figure 5.3.a as a population offset from zero in the spectra and as a slight trend towards $2/3$ in figure 5.3.b. This is because the quantum state readout technique measures the combined population of $|S, 0, 0\rangle$, $|S, 1, -1\rangle$ and $|S, 1, 1\rangle$ which will trend to a total population of $2/3$ in a steady state where the $|S, 1\rangle$ Zeeman sub-levels become equally and fully populated.

Checking the Rabi rate

The set powers for the Raman beams were chosen in accordance with saturation powers determined by fits to saturation curves taken with the Raman beams close to resonance with $^{174}\text{Yb}^+$ ions¹. Saturation powers of $0.9135(5)$ μW and $1.61(4)$ μW were fitted for Raman A and B beams respectively following the steady state solutions found by Ejtemae et al.[62, Eqs. 9 & 10]. Ejtemae's solution accounts for laser polarisation, Zeeman broadening and the Clebsch Gordon coefficients of the $^2S_{1/2} \leftrightarrow ^2P_{1/2}$ transition in $^{174}\text{Yb}^+$, unlike the simple two level optical Bloch equation. These saturation powers would correspond to Gaussian waists $w_A = 34$ μm and $w_B = 45$ μm given equation 3.58 and

$$I = \frac{2P}{\pi w_0^2}. \quad (5.3)$$

¹Saturation curves using $^{171}\text{Yb}^+$ ions were not performed because a separate re-pump laser 14.7 GHz blue tuned from the S-P resonance would have been required.

Measured waists² were $w_A = 26 \mu\text{m}$ and $w_B = 57 \mu\text{m}$. Discrepancy is likely from the ion or beam profiler not being exactly at the focal plane, and/or the ion not being directly in the centre of the Raman beams since the trap surface is comparably close ($\Delta y = 60 \mu\text{m}$) and the beams induce large unwanted scattering if positioned too close.

The Raman transition Rabi rates can be approximated according to the estimated saturation powers and equation 3.76, $\Omega_R = 2\pi \times 153.9(12) \text{ kHz}$. Since the Raman transitions have a strong Lamb-Dicke parameter in the z-direction and are resonant with the $\Delta n_z = -1$ transition, the Rabi rate will be reduced and is dependent on the motional state.

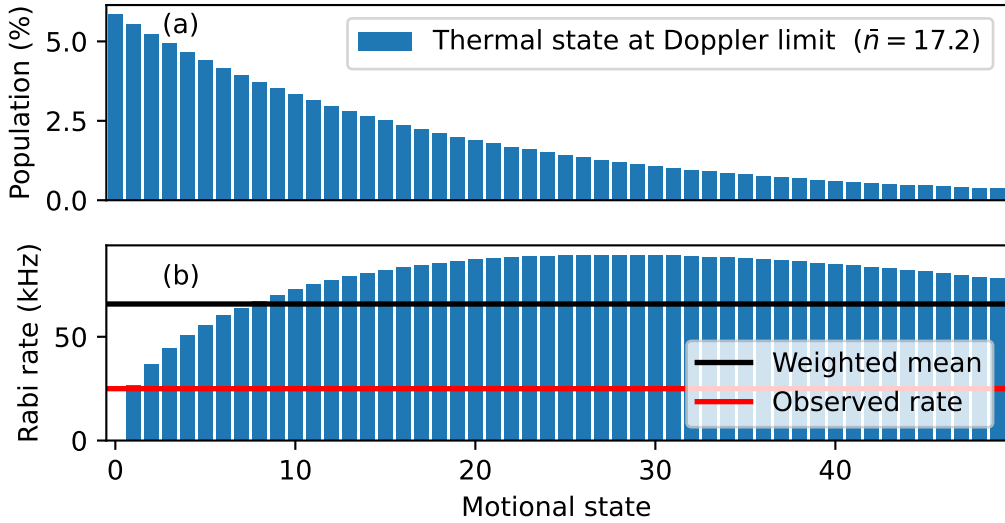


Figure 5.4: (a) Population distribution of a thermal state at the motional Doppler limit for the ion in the z-axis. Corresponding expected Rabi rates given $\Omega_R = 2\pi \times 153.9(12) \text{ kHz}$ and motional couplings according to equation 3.67. The Rabi rates are weighted against the thermal distribution in (a) to give the weighted mean (65.8(5) kHz). The observed rate ($\sim 25 \text{ kHz}$) corresponds to the inverse of the oscillation period in figure 5.3.b (red -555 kHz line).

Figure 5.4 shows the expected thermal state and corresponding Rabi rates for each motional eigenstate being driven on the $k = -1$ transition. The on-resonant $n \rightarrow n - 1$ Raman transition (red line in figure 5.3.b) is equivalent to a summation of the individual Rabi oscillations of each of the eigenstates.

²The geometric mean of x and y waist radii were used.

It has an observed oscillation of ~ 25 kHz (red line in figure 5.4.b). This is around the expected Rabi rate for the $n=0$ motional eigenstate but is $2.6\times$ slower than the weighted mean of all the Rabi rates (weighted against the thermal state at the Doppler limit). The weighted mean is only meant as a rough indication of what Rabi rate to expect.

5.3 Reconfiguration for 3D addressability

To address not only the z modes, but the x and y modes as well, the Raman beams needed to be geometrically reconfigured. The Raman B beam was re-positioned incident on the ion with wave-vector $\vec{k}_B = \frac{2\pi}{\sqrt{2}\lambda}(-\hat{x} - \hat{z})$. This creates a total Raman transition wave-vector $\vec{k} = \vec{k}_A - \vec{k}_B = \sqrt{2}\frac{2\pi}{\lambda}(\hat{x} + \hat{z})$.

The axes of the secular motion differ from the geometric trap structure with a rotation in the x-y plane. This rotation of the secular modes is performed via the trap DC electrodes to induce stronger coupling between the incident lasers and the y-direction secular mode. Without this rotation, the Lamb-Dicke parameter would be near-zero ($\eta_y = \vec{k} \cdot \hat{y}y_0 \approx 0$) and the ion would experience negligible Doppler cooling, reducing trapping lifetime from instability in that axis. A rotation of the secular axes reduces the x and increases the y Lamb-Dicke parameters,

$$\begin{aligned}\eta_x &= \sqrt{2} \cos(\theta) \frac{2\pi x_0}{\lambda} \\ \eta_y &= \sqrt{2} \sin(\theta) \frac{2\pi y_0}{\lambda}.\end{aligned}\tag{5.4}$$

This rotation is applied via the DC rotation electrodes in figure 4.1 with approximately 1 V on each but of opposite polarity. The rotation angle would be similar 25 degrees like its earlier trap design[135]. Determining a more accurate value would require a 3D simulation of the electric field generated by electrodes. The estimated Lamb-Dicke parameters from these values are $\eta_x = 0.094$ and $\eta_y = 0.048$. The Lamb-Dicke regime in terms of motional quanta would then be $\bar{n}_x \ll 56$ and $\bar{n}_y \ll 220$ which is hot compared to the Doppler limits of each axis, $\bar{n}_x \geq 6.2$ and $\bar{n}_y \geq 7.4$.

5.3.1 3D Raman sideband cooling

Raman sideband cooling was performed by alternating the Raman lasers and σ^\pm reset beam. The Raman B beam was modulated between the resonances of the (-1,0,0), (0,-1,0), (0,0,-1) x-y-z transitions in an x-y-z-x-y-z... order. The x, y and z transitions were driven for 36 μs , 104 μs and 20 μs respectively with 1.2 μs between each pulse where the σ^\pm beam would pulse and reset the atomic state to $|S, 1, 0\rangle$. The reasoning was to drive the transitions for durations roughly inversely proportional to the Lamb-Dicke parameters, the main scaling of the strength of the transitions.

The Raman transition's Rabi rate was approximately $\Omega_R/2\pi \sim 1.02(4)$ MHz, 30 \times larger than the Raman coupling during probing for readout, $\Omega_R/2\pi = 33.9(1.3)$ kHz (fitted). The expected readout Rabi rate was $\Omega_R/2\pi = 101(4)$ kHz given experimentally measured saturation parameters ($P_{sat,A} = 0.72(3)$ μW and $P_{sat,B} = 2.22(13)$ μW) of the Raman beams using $^{174}\text{Yb}^+$ and equation 5.2. The power of the Raman beams were set to $3P_{sat}$ for readout and $90P_{sat}$ for the cooling phase³.

The observed rate is 3 \times slower than the expected rate. This is close to the factor of 2.6 found in the ratio of expected and measured Rabi rates of the Raman transitions purely along the z-axis (section 5.2.1). It is suspected this systematic error is coming from the fitting of saturation parameters for the Raman beams. This could be because of changes in the trapping conditions between $^{171}\text{Yb}^+$ and $^{174}\text{Yb}^+$.

The results as presented in the paper at the beginning of this chapter are re-analysed with a method that extracts a better temperature fit to the motional spectra. The fit of figure 5.5 involves calculating the individual Rabi oscillations of all combinations of the x, y and z motional states. 90 states were simulated for each of the three modes, totalling to 729,000 combinations of initial states for each motional transition. All motion was approximated as

³For saturation parameter s , the power of Raman beam B was set to $2sP_{sat,B}$ because only half its power is polarized to drive σ^- transitions.

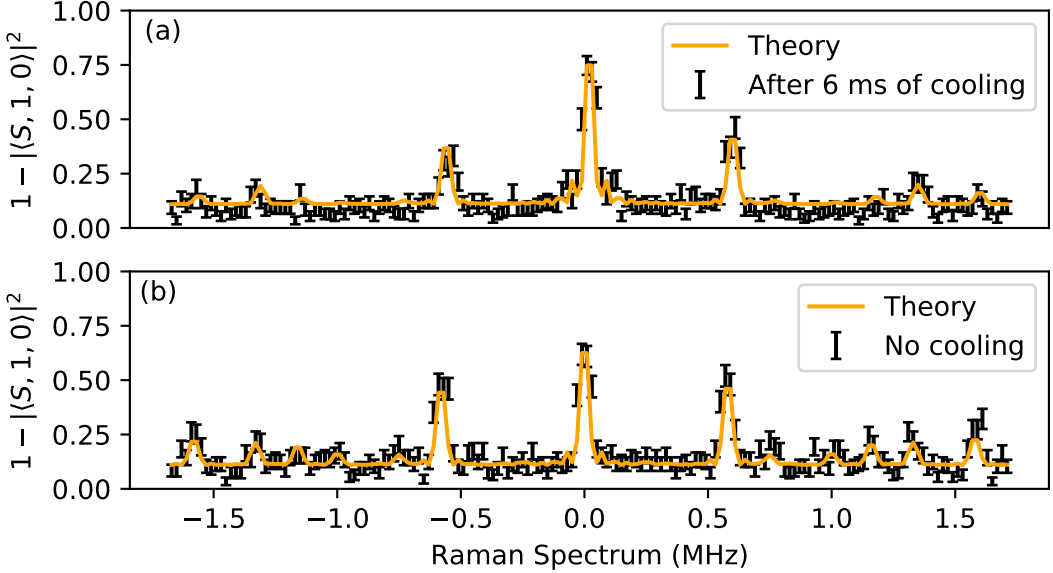


Figure 5.5: (a) A Raman spectrum taken after 6 ms of modulating the Raman beam between the three resonances of the motional modes that remove 1 quanta of motion. (b) Takes the same measurement except does not perform Raman sideband cooling. Measurements are performed as in figure 5.2. Statistics are gained from 100 single shot measurements per data point.

thermal and \bar{n}_x , \bar{n}_y , & \bar{n}_z were left as fitting parameters.

Since the thermal states contain no off-diagonal terms, population of the excited states of each initial state weighted by its probability of being populated could be added without consideration of any interference effect. Since motional modes were well resolved, it is also a valid approximation to say that the resonances of the different motional transitions could also be added without needing to consider the interference of overlapping resonances. For the fit in figure 5.5, only resonances within a 2 MHz range that would change motional states by one quanta⁴ were calculated to reduce the amount of computation required (see appendix C.4). The population transfer equation becomes,

$$P(\Delta) = \sum_{k_x} \sum_{k_y} \sum_{k_z} \sum_{n_x=0}^{89} \sum_{n_y=0}^{89} \sum_{n_z=0}^{89} \frac{\Omega_{\{n,k\}_{\{x,y,z\}}}^2}{\Omega_{\{n,k\}_{\{x,y,z\}}}^2 + \Delta_{k_{\{x,y,z\}}}^2} \times \dots \sin^2 \left(\frac{1}{2} \sqrt{\Omega_{\{n,k\}_{\{x,y,z\}}}^2 + \Delta_{k_{\{x,y,z\}}}^2} T \right) \quad (5.5)$$

⁴Transitions where the z mode changed by two quanta were included because its strength was not negligible.

where the Rabi rates

$$\Omega_{\{n,k\}_{\{x,y,z\}}} = A_{n_x \rightarrow n_x + k_x} A_{n_y \rightarrow n_y + k_y} A_{n_z \rightarrow n_z + k_z} \Omega_R \quad (5.6)$$

are calculated according to the terms in equation 3.67 and the detunings

$$\Delta_{k_{\{x,y,z\}}} = \Delta - k_x \omega_x - k_y \omega_y - k_z \omega_z \quad (5.7)$$

are according to equation 3.81. To account for the opposite heating transition that is simultaneously driven, the result is scaled down by equation 5.1 and the opposite resonances ($k_i \rightarrow -k_i$) are also calculated and added to the solution (scaled down by the compliment of equation 5.1). Given $21(\times 2)$ resonances, the 6 iterative summations total to 30,618,000 individual population transfers to calculate. A time-wise envelope is applied to the final excited state population to approximate the effect of spontaneous emission on the Raman transition's excited state,

$$P_{env}(P) = e^{-T/\tau} P - \frac{2}{3}(1 - e^{-T/\tau}). \quad (5.8)$$

It approaches a population of $2/3$ in the steady state. The three mean quanta of the motional modes, the Raman transition's base Rabi rate Ω_R and the off-resonant scatter rate τ are left as fitting parameters.

The model does not account for any T_2 decoherence. A model was made that uses the solution of the optical Bloch equations with transverse decay. An algebraic solver was used to find the eigenvalues and eigenvectors of the coupled ODEs, then the coefficients required for the initial condition $\langle \sigma_z(0) \rangle = -1$ were calculated to find the analytic solution. A solution with a length of ~ 100 values could be calculated in $\sim 20 \mu s$ using a just-in-time compiler[136]. This method was still too slow (~ 10 mins per plot) to use in the fitting function, which typically requires hundreds of iterations (blowing out to day-long time-

scales).

Both the T_2 time of the $|S, 0, 0\rangle \leftrightarrow |S, 1, 1\rangle$ transition (figure 4.13) as well as the time to heat the motional state by 1 quanta (table 5.2) were both on the order of hundreds of microseconds, longer than the 20 μs pulse duration. Not simulating the T_2 decoherence is not expected to change the fit majorly.

The results of the fit of the motional quanta are given in table 5.1 and the fitting curve is shown in figure 5.5. The fits are supported by Rabi oscillations

	\bar{n}_x	\bar{n}_y	\bar{n}_z
No cooling	12(3)	80(90)*	14(2)
6 ms cooling	1.9(16)	16(8)	5.2(11)
Doppler limit	5.7	6.9	16.4

Table 5.1: Fitted expectation values of the number operator of the motional modes given assuming a thermal distribution for all. *The temperature of the y-mode could not be reliably fit, likely because of its weak signal and being the least coupled mode to the Raman beams.

measured right after each of the spectrum scans. The Rabi oscillations when cooled and not cooled are compared against plots of the theory with the exact same parameters fitted for the spectrums.

Estimating cooling/heating rate

The average cooling rate across 6 ms can be estimated by taking the change in fitted motional quanta in table 5.1 over their difference in cooling time,

$$\frac{\Delta \bar{n}}{\Delta t} = [-3.4(11), -20(30), -2.9(8)] \frac{\text{quanta}_{[x,y,z]}}{\text{ms}}. \quad (5.9)$$

This value alone does not give much information about the heating rate or performance of the scheme used. The performance of the Raman sideband cooling scheme is estimated by calculating the temperature dependent cooling rate (figure 5.7). Equation 5.5 was used to simulate the population transfer⁵ of the three cooling transitions. The model predicts that cooling rate of the

⁵proportional to the change in motional quanta.

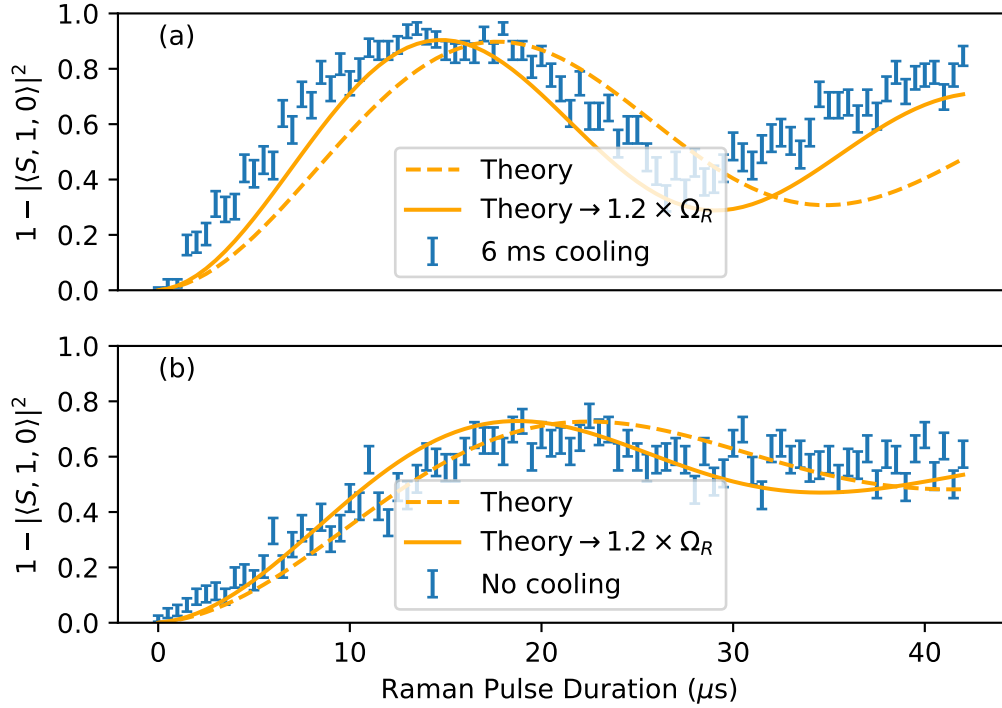


Figure 5.6: Rabi oscillations observed on the $k_{[x,y,z]} = [0, 0, 0]$ transition after (a) and before (b) Raman sideband cooling. The dashed fit line is the exact same parameters found from fitting to the spectra in figure 5.5. The solid fit line is those same parameters again but with the Raman transition's effective Rabi rate scaled by a factor of 1.2 ($\Omega_R/2\pi \rightarrow 40.6(16)$ kHz).

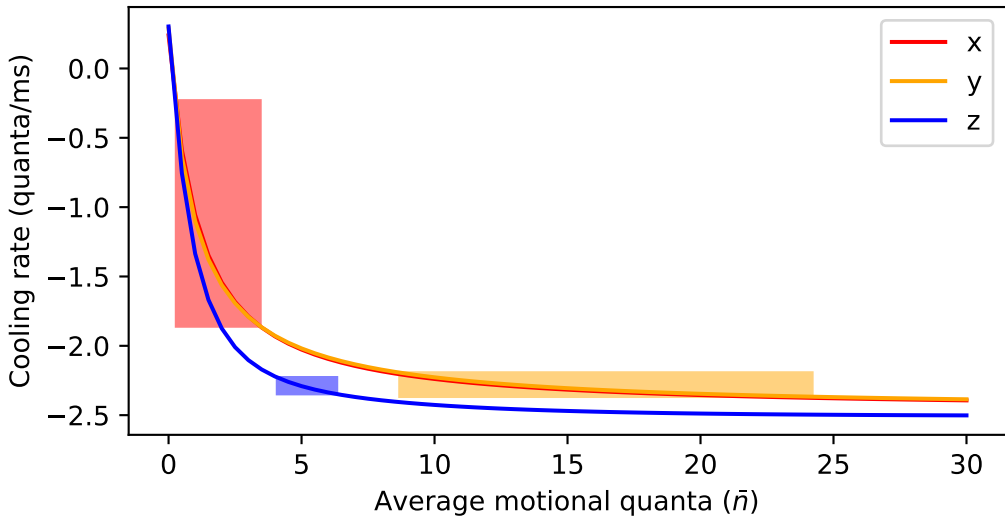


Figure 5.7: The temperature of each mode \bar{n}_i is plotted against an estimated cooling rate for the experiment. The horizontal of the filled boxes represents the fitted temperature of the ion from table 5.1 with ± 1 standard deviation, while the vertical of the boxes are the estimated cooling rate within that temperature range.

scheme goes to zero at $\bar{n} = 0.14 - 0.16$. This is where the weaker heating transition becomes equal in strength to the cooling transition. Assuming they are in a steady state after the experimentally performed 6 ms of Raman sideband cooling, there would be an equal and opposite heating rate counteracting the cooling rate. Table 5.2 gives these heating rates for each of the modes. In

Mode	$\Delta\bar{n}/\Delta t$ (quanta/ms)	$\omega_i S_E(\omega_i)$ ($\times 10^{-4} \text{V}^2/\text{m}^2$)
x	1.0(8)	5(4)
y	2.28(9)*	7.4(3)*
z	2.29(6)	1.42(4)

Table 5.2: $\Delta\bar{n}/\Delta t$ is the heating/cooling rate of each of the motional modes in the Raman sideband cooling scheme assuming the motion is in a steady state. $\omega_i S_E(\omega_i)$ is an estimate of the electric field noise spectrum that would produce this heating rate. It is scaled by ω_i to produce a quantity that is comparable across different secular frequencies. *The y-values are likely a poor estimate because of the weak coupling of the Raman beams to the y-mode.

terms of electric field noise spectral density at the ion's frequency, multiplied by the frequency⁶,

$$\omega_i S_E(\omega_i) = \omega_i \frac{4m}{e^2} \hbar \omega_i \frac{d\bar{n}}{dt}, \quad (5.10)$$

the estimated electric field variance is slightly lower but of the same magnitude as Tungsten surface-electrodes traps with similar ion-electrode distances($60 \mu\text{m}$)[124, 137]. This is good agreement considering another study showed electric field noise can span many orders of magnitude in surface traps of similar ion-electrode distance[138].

5.4 Reconfiguration for more pure transitions

The configuration used for cooling posed a problem with its weak coupling to transitions that transferred motional quanta opposite to the desired direction. A new scheme was chosen addressing the $|S, 1, 1\rangle \leftrightarrow |P, 0, 0\rangle \leftrightarrow |S, 1, -1\rangle$ transition (figure 5.8). This transition spans two quanta of angular momentum,

⁶This is done to remove the 1/f dependence of the spectral noise and make noise values comparable across traps of different secular frequencies[137]

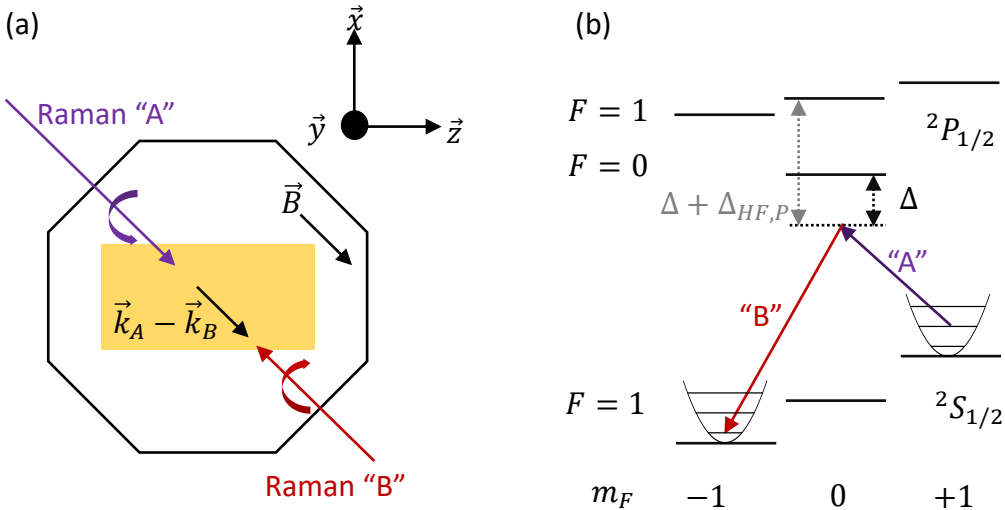


Figure 5.8: (a) Geometric configuration of Raman laser beams, their polarisations and the external magnetic field at the ion. (b) Grotrian diagram of the Raman transition, addressing $|S, 1, 1\rangle \leftrightarrow |S, 1, -1\rangle$ ground states.

so $|S, 1, 0\rangle$ is not unintentionally driven into. This method allowed cleaner transfer of population in the Zeeman states and avoided quantum beats from interference of unwanted transitions unlike the previous method (figure 5.9). A simulation of all 8 states in the $^2S_{1/2}$ & $^2P_{1/2}$ orbitals (see appendix B.4) shows how the new method also transfers more population to the target state since the $m_F = 0$ state is not being populated (figure 5.9).

One downside of this configuration is that the Raman coupling strength decreases more with Δ than the previous method. A secondary Raman coupling, $|S, 1, 1\rangle \leftrightarrow |P, 1, 0\rangle \leftrightarrow |S, 1, -1\rangle$, has opposite sign due to Clebsch-Gordon coefficients, causing considerable interference between the $|P, 0, 0\rangle$ and $|P, 1, 0\rangle$ excited states when $\Delta \gg \Delta_{HF,P}$ (see appendix B.5). This was only figured out after experiment but was observed when the Raman coupling got unexpectedly weak when larger detunings ($\Delta = -10\text{ GHz}$) were tried. The transitions, however, are expected to constructively interfere when the Raman beams are tuned in between the $^2P_{1/2}$ hyperfine states, the optimal detuning being $\Delta = +\Delta_{P,HF}/2$, equally far apart from both states.

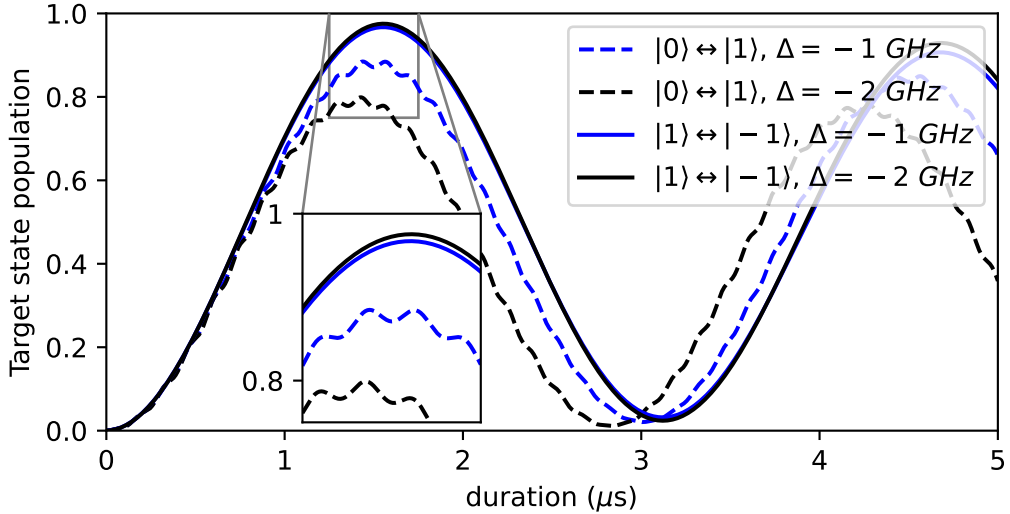


Figure 5.9: Full 8-level Lindbladian coherent Raman transition simulation of the two different addressing schemes (dashed lines, $|0\rangle \leftrightarrow |1\rangle$) and (solid lines, $|1\rangle \leftrightarrow |-1\rangle$). The $|0\rangle \leftrightarrow |1\rangle$ scheme performs worse because of an extra resonant Raman transition via the intermediary $^2P_{1/2} F=1 m_F=-1$ state which coherently drives population also to $^2S_{1/2} F=1 m_F=-1$. Raman beam intensities were chosen to give similar Rabi rates.

5.4.1 Setup

The magnetic field needed to be re-aligned along the $-\vec{x} + \vec{z}$ direction. The pre-existing current coil on the $\vec{x} - \vec{z}$ side chamber window was intended to cancel out external fields and was not strong enough to produce Gauss-level fields. A new copper coil (~ 250 loops, 70 mm diameter, 18 AWG with insulating enamel) that produced $1.298(7)$ G/A was attached to the $-\vec{x} + \vec{z}$ side chamber window. It produced a 2.5 G field at the ion when supplied with 1.92 A and 2.98 V ($R=1.55\ \Omega$).

Also, a new optical setup for the Raman pump (Raman A) beam needed to be set up along the $-\vec{x} + \vec{z}$ direction with circular polarization to purely address σ^- transitions (figure 5.10). A co-propagating σ^+ on-resonant beam was also set up to optically pump the ion to $|S, 1, 1\rangle$ ⁷.

⁷Along with the main Doppler cooling beam whose polarization is rotated to address π -transitions (section 4.2.5).

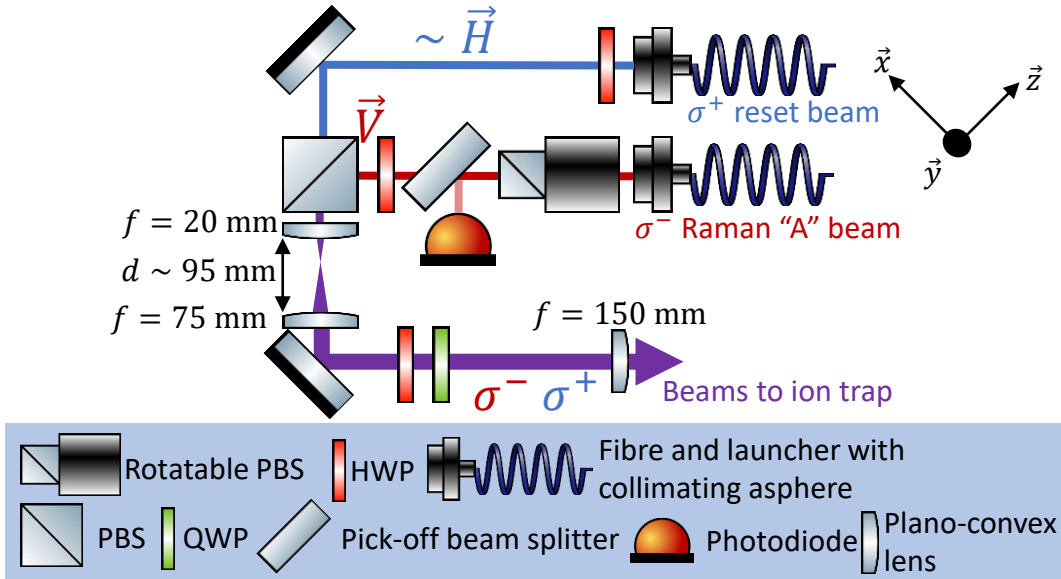


Figure 5.10: A near resonant σ^+ reset beam and far detuned σ^- Raman beam combine and co-propagate at a PBS. A photodiode was set up before the PBS to servo the Raman beam laser power. The beam is magnified $3.75\times$ so that when it is focused by a $f=150$ mm plano-convex lens, the waist is of similar length to the $60\ \mu\text{m}$ height of the ion above the surface trap. The combined beams with orthogonal polarization are retarded by a pair of QWPs and HWPs to generate orthogonal circularly polarized beams that co-propagate with the external magnetic field experienced by the ion.

5.4.2 Power instability

The new scheme was tested by performing Rabi flops on the $k = (0, 0, 0)$ transition and spectrum scans at a fixed pulse duration. It was found early on that the new Raman pump beam's power stability was poor in an averaging time of around 6 ms (figure 5.11). The power noise was characterised along the signal path and found to originate as polarization modulation in the panda-core fibre used to deliver the beam to the trap. Other fibres were tried and the polarization was optimized for minimal noise but the noise would drift in and out over minute timescales.

The laser power instability problem (figure 5.11) was later solved by speeding up the laser power stabilization loop. It was changed from a software defined integral-controller (Appendix C.3) to a proportional-integral controller that runs directly between the ADC (which reads the photodiode voltage) and the direct digital synthesis (DDS) tone generator (which sends an AM RF

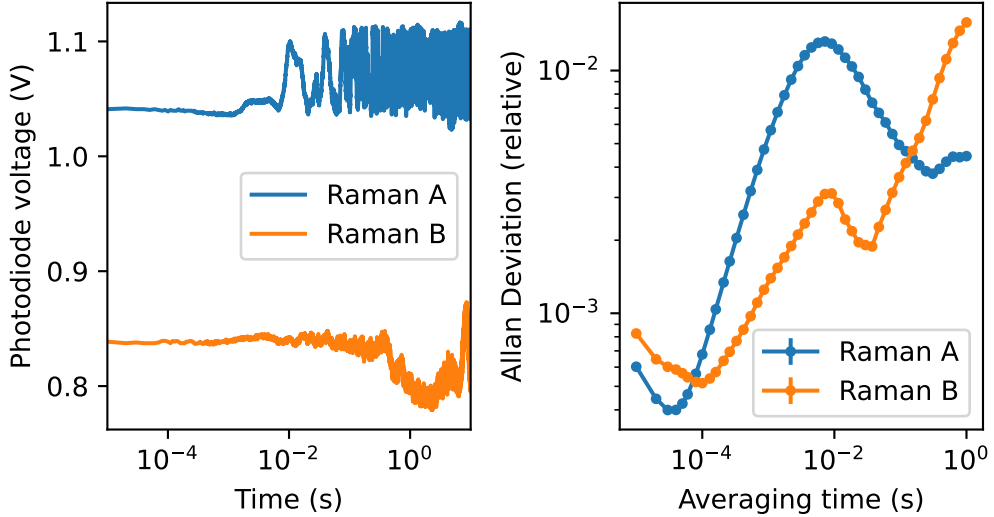


Figure 5.11: (a) Photodiode (with 100 kHz bandwidth Thorlabs AMP120 transimpedance amplifiers) voltage traces of the Raman beams with no locking in log-scale to show on what timescale noise appears. (b) Allan deviation of the same traces over ten seconds of data at a 100 kHz sampling rate.

tone to the AOM for power stabilisation) to allow for a much faster locking bandwidth (> 100 kHz, limited by the trans-impedance amplifier bandwidth). The power instability reduced from a measured relative instability of 3% when unlocked (10 ms timescales) to 0.09% when stabilized.

While the laser power instability was unsolved, the Rabi oscillations were too noisy to extract any meaningful information from. Spectral scans however still showed resonances clearly, so a study of resonance shifts from changes in trap RF strength and light shift was conducted.

5.4.3 Motional resonances and trap strength

In the experiment, stable trapping can only be achieved over a certain operating range of the trapping RF voltage/power. When the RF power is too low ($V_0 \sim 40$ V), the q_y parameter decreases and trapping in the y-axis becomes unstable as the a-q parameters approach the negative stability boundary of figure 3.1. When the power is too high ($V_0 \sim 250$ V), the RF electrodes approach their breakdown voltage where arcing can damage the trap electrodes.

Figure 5.12 shows measurements made of the ion's motional resonances at different RF powers. Figure 5.12.b was taken with the RF source set at +5.4 dBm and figure 5.12.c at +4.9 dBm on the same day. A 200:1 capacitive divider is connected to the output of the coil so that the trap RF output could be monitored. The peak to peak monitor voltage at +5.4 dBm and +4.9 dBm were 700(4) mV and 664(4) mV respectively, which corresponds to approximate trap RF amplitudes of 70.0(4) V and 66.4(4) V respectively. The oscilloscope used to measure these voltages would alter the conversion ratio because of its load, so these values are only rough estimates. The amplitude V_0 of the driving trap voltage $V(t) = V_0 \sin \Omega_{RF} t$ can be related to the secular frequencies by manipulating equation 3.17 into

$$V_0 = \frac{\Omega_{RF} m R^2}{q} \sqrt{\omega_x^2 + \omega_y^2 + \omega_z^2} \quad (5.11)$$

where $R = 142 \mu\text{m}$ [128] is a length related to the spacing of the RF electrodes in the GTRI trap, which also already accounts for the difference in geometry of surface electrode traps and quadrupole rod traps. Figures 5.12.b and c have determined voltages of $V_b = 77.24(4)$ V and $V_c = 72.66(3)$ V respectively. These determined voltages are in line with estimates taken from the capacitive divider monitor. The power difference $10 \log_{10}(V_b^2/V_c^2) = 0.531(3)$ dB is close to the 0.5 dB difference of the change in source power. The 0.031(3) dB discrepancy may be caused by change in thermal conditions of the helical resonator. Figure 5.12.a was also taken at 5.4 dBm source power but 134 days later. Calculation of the apparent drift in power shows the RF power at trap increased by 1.22(5) dB, likely thermal/mechanical drift in the helical resonator.

The three spectra of figure 5.12 were fitted to a Lorentzian peak model that used the three secular frequencies as free parameters, and fitted the combination resonances ($\omega_{x,y,z} = k_x \omega_x + k_y \omega_y + k_z \omega_z$). This model was used and not a full quantum simulation, because the Hilbert space of the atomic states

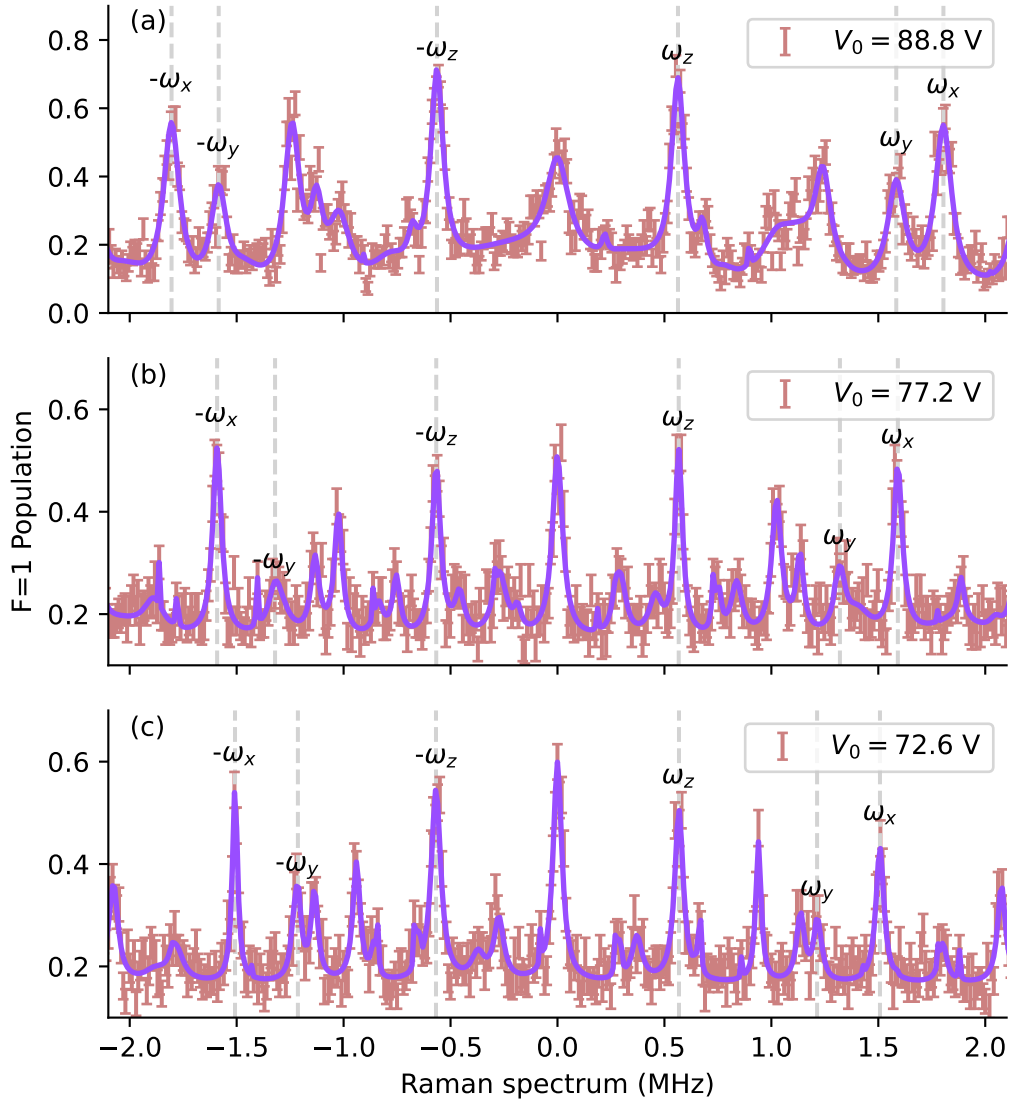


Figure 5.12: 3-D motional Raman spectra of $^{171}\text{Yb}^+$ after Doppler cooling. ω_x and ω_y resonances vary between the three plots. (b) and (c) were taken on the same day (3rd June 2021) varying the RF source power from (b) +5.4 dBm to (c) +4.9 dBm. (a) was measured 134 days later (15th October 2021) at +5.4 dBm, however helical resonator conditions appear to have changed the RF power received by the trap compared to (b). V_0 voltages in the legend are calculated according to equation 5.11. Notice the ω_z secular frequencies from the DC trapping potential did not change. Other peaks are combination resonances of the secular frequencies ($\pm\omega_x \pm \omega_z$, $\pm 2\omega_z$, etc.).

and 3 harmonic oscillators is impractical to compute. The Lorentzian model is a good approximation in the regime where the spectroscopic peaks are well resolved and the transitions are not overdriven ($\Omega_R T \lesssim \pi$).

Figure 5.13 shows how the fitted parameters vary with V_0 and comparing

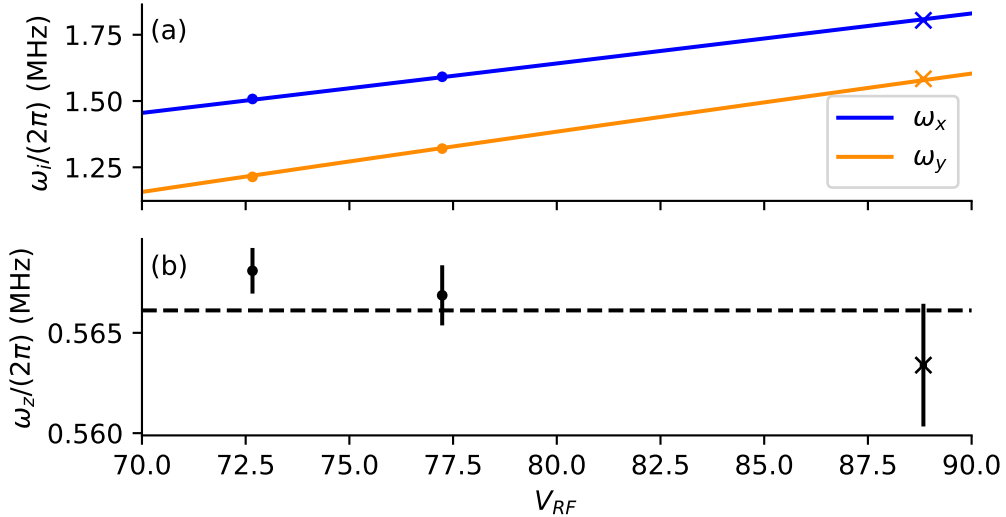


Figure 5.13: (a) ω_x and ω_y fits from the spectra in figure 5.12. ·'s are used for data taken on the 3rd of June 2021 and ×'s are used for data taken on the 15th of October 2021. The theory curves (equation 3.17) for (a) agree well with measurements. (b) secular frequency ω_z is expected to remain constant, and does over the two measurements taken on the same day (to within fitting uncertainty) but appears to have drifted between the measurements taken 134 days apart. The mean value (dashed line) was used for calculation of the theory line in (a).

with the trends of theory. Figure 5.14 also shows the determined a and q parameters for these spectra which contextualises the trap conditions in terms of the a - q stability region. The a -parameter is small because of the ± 20 V limit on the DAC, and the DC degeneracy breaking field means the difference between a_x and a_y is of the same order.

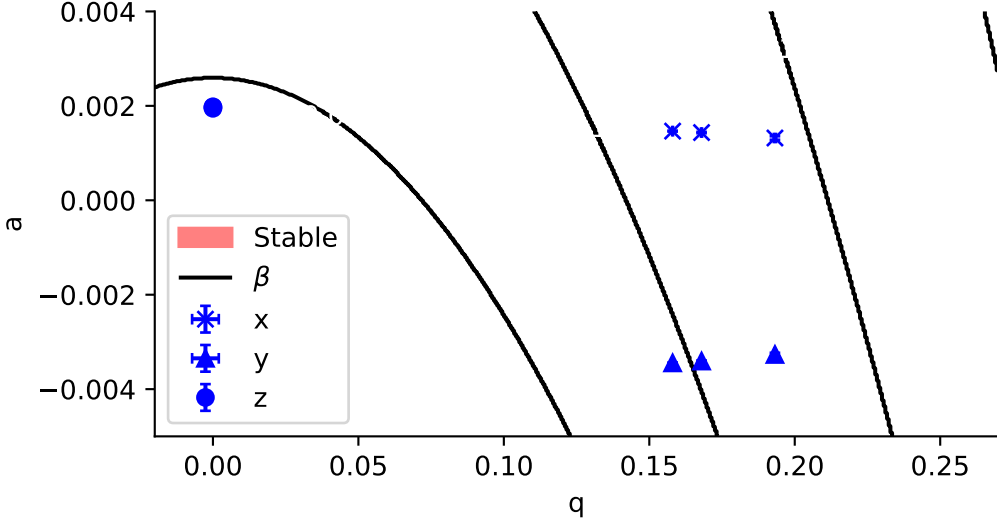


Figure 5.14: Experimentally determined a and q parameters for a trapped $^{171}\text{Yb}^+$ ion given fitted secular frequencies and known RF frequencies. The three points for each mode correspond to the three spectra in figure 5.12. $q_{x,y}$ increases approximately linearly with V_{RF} (72.66(3) V, 77.24(4) V, 88.84(9) V). The difference in a_z is small ($\sim 10^{-5}$) and the three points are superimposed on each other. Uncertainty propagated from the spectral fits is smaller than the marker size.

Light-shift measurement

Light-shift in Raman transition resonances according to equation 3.77 scales quadratically with Rabi rate of each Raman beam and therefore linearly with power. To test this, the Raman beam powers were calibrated and stabilized to laser light picked off and sent to photodiodes during measurements of resonances. The Raman beams' powers were set over three scans to $10\mu\text{W}$, $20\mu\text{W}$ and $30\mu\text{W}$ each while keeping the other beam's power constant (Figures 5.15.a-c). A measurable shift in the entire spectrum was observed in the scans, where the observed light-shift was in opposite directions for each beam (Figure 5.15.d). According to equation B.19, the light-shift scales with laser power P as

$$\frac{d\Delta_R}{dP} = \pm \frac{\Gamma^2}{24P_{sat}} \left(\frac{1}{\Delta} + \frac{1}{\Delta + \Delta_{HF,P}} \right). \quad (5.12)$$

The detuning was kept constant in scans at $\Delta = -1$ GHz and the fitted P_{sat} values were $P_{sat,A} = 5.5(3) \mu\text{W}$ and $P_{sat,B} = 2.31(7) \mu\text{W}$.

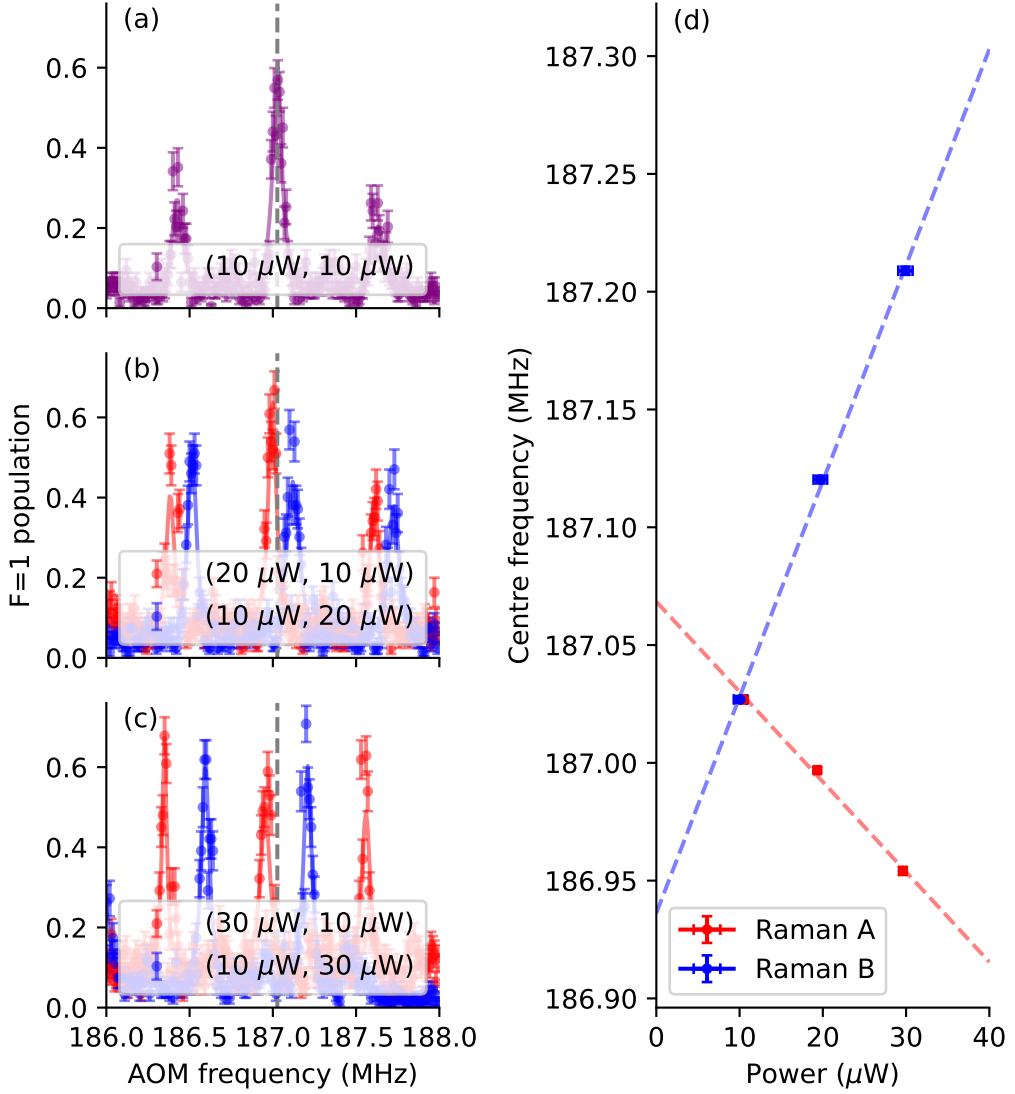


Figure 5.15: Measured Raman spectra (a-c) with varying power in each Raman beam. Light shift moves the entire spectra dependent on the power in each Raman beam. Raman A and B light shift (d) is $-3.8(2)$ kHz/ μW and $9.2(3)$ kHz/ μW respectively. From these values, the saturation power for each Raman beam is determined as $P_{sat,A} = 5.5(3)$ μW and $P_{sat,B} = 2.31(7)$ μW according to equation B.19.

5.4.4 Zero light-shift resonance

By tuning the frequency of the two Raman beams exactly between the resonances of the two hyperfine $^2P_{1/2}$ states ($\Delta = +\Delta_{HF,P}/2$), light-shift induced by unequal Raman beam couplings goes to zero (equation B.19). Line broadening from Raman beam power instability becomes negligible and was tested by taking Raman spectra where the pump beam was set to $10 \mu\text{W}$ and the Stokes beam was set to 10 and $20 \mu\text{W}$. The fitted light shift was $250 \pm 260 \text{ Hz}/\mu\text{W}$, which agrees with the theory's estimate of zero. Also, the frequency shift between the two Raman beams to drive the centre resonance, $f_{AOM,Stokes} - f_{AOM,pump} = 7.1485(14) \text{ MHz}$ was equal to twice the Zeeman shift $2\delta_B = 7.158(14) \text{ MHz}$ as measured by finding the difference in microwave resonance between the clock transition ($|S,0,0\rangle \leftrightarrow |S,1,0\rangle$) and the $|S,0,0\rangle \leftrightarrow |S,1,+1\rangle$ transition. This aligns exactly with theory and also supports that there is no light shift.

5.4.5 Raman Sideband Cooling

Section 5.3.1 showed Raman sideband cooling using the less pure excitation scheme. Raman sideband cooling was re-attempted with the new scheme (figure 5.8) at the zero light-shift detuning. Using the same Raman sideband cooling protocol as in section 5.3.1, the $n_z \rightarrow n_z - 1$ transition was pulsed for $16 \mu\text{s}$ with $20 \mu\text{W}$ of power used for each of the Raman beams. The cooling pulse is followed by a reset pulse (see table 5.3) and repeated 100 times in a pulse train. Pulse trains take less than 2 ms and after probing and finding the population transfer of the red (p_{rsb}) and blue (p_{bsb}) z-motion sidebands of the Raman spectrum (figure 5.16), the mean motional quanta could be estimated[38, 69].

$$\bar{n} = \frac{p_{rsb}}{p_{bsb} - p_{rsb}} \quad (5.13)$$

Equation 5.13 is only true if the motional eigenstates follow a thermal distri-

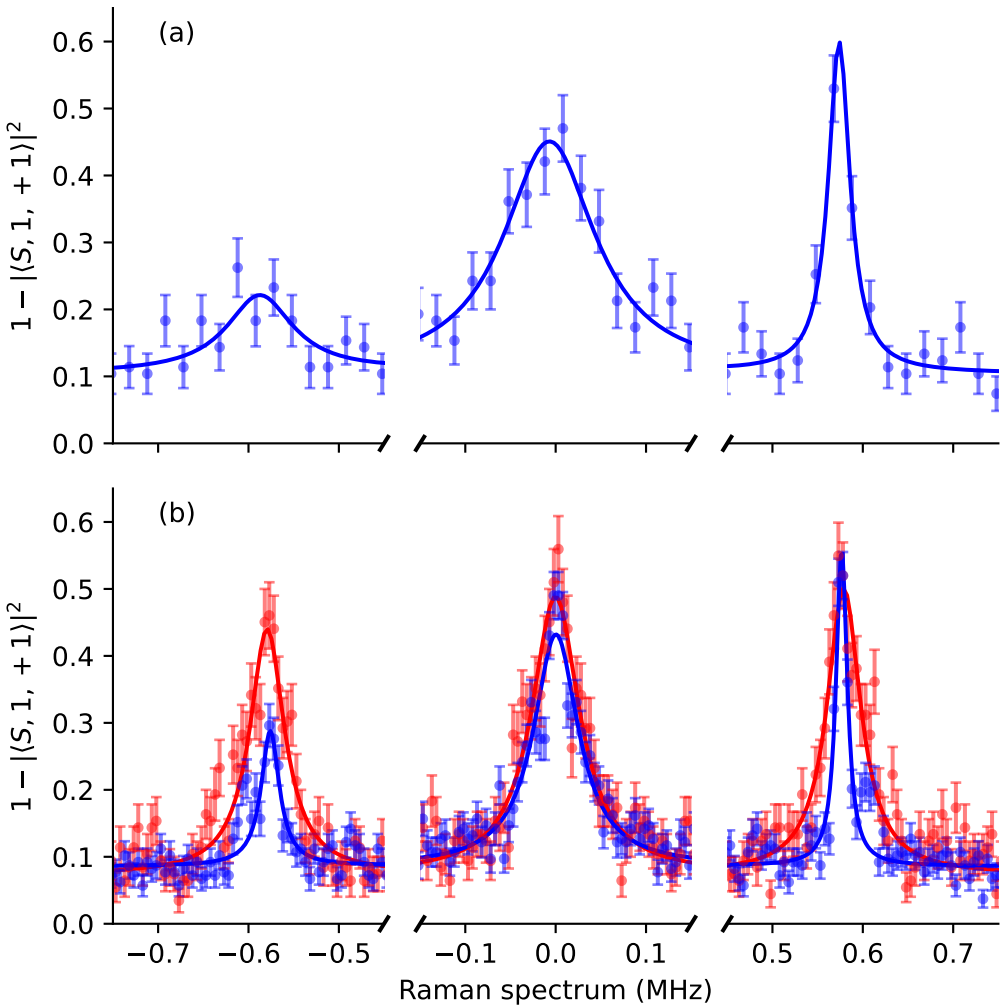


Figure 5.16: Raman sideband cooling on the z-axis motional mode ($\omega_z/2\pi = 576.3(6)$ kHz). (a) The best Raman sideband cooling results were $\bar{n}_z = 0.30(13)$. (b) Another Raman sideband cooling attempt (blue) with different experimental parameters (table 5.3) shows more scan detail. The inferred temperature was higher $\bar{n}_z = 0.74(17)$ and the spectrum is compared against another spectrum under the same conditions but with the ion only Doppler cooled. Other weaker combination resonances exist in the spectrum but are ignored in the fitting.

	Figure 5.16.a	Figure 5.16.b
Probe pulse duration (μs)	30	50
Repetitions per point	100	200
Sweep interval (kHz)	20	5
Probe pulse powers (μW)	20	10
Reset pulse duration (μs)	4	3
Cooling-to-reset dead time (μs)	2	0.5

Table 5.3: A list of parameters that were modified between the two Raman sideband cooled spectra of figure 5.16.

bution (equation 3.26).

5.5 Conclusions

A new Raman sideband cooling scheme was demonstrated achieving cooling in a singular motional mode down to $\bar{n}_z = 0.30(13)$ or $T = 22(4) \mu\text{K}$, where the ultimate ground state temperature of that mode was $13.83(1) \mu\text{K}$, limited by the zero-point energy. The scheme requires low power since the detuning is relatively close ($\sim 50\Gamma$) to the $^2P_{1/2}$ state and is also precise since it is driven at a detuning where light shift goes to zero.

Raman sideband cooling between ground Zeeman states of an $I = 1/2$ trapped ion offers a less complex alternative to previously demonstrated schemes[3, 5, 4, 20, 2]. It is a useful technique in surface electrode traps that are prone to charging from UV lasers since only $20 \mu\text{W}$ was needed of each Raman beam to cool the ion close to its ground state. Simulations show population transfer upwards of 95% can be achieved (limited by off-resonant scattering), which is not suitable for quantum computing applications but is suitable for Raman sideband cooling and research demonstrations that may require a cheap or lower power means of driving coherent Raman transitions.

Chapter 6

Enhanced Spectroscopy

Techniques with Ytterbium

This chapter primarily consists of a published paper I second authored, V. Blūms et al., “Laser stabilization to neutral Yb in a discharge with polarization-enhanced frequency modulation spectroscopy,” Rev. Sci. Instrum., vol. 91, no. 12, p. 123002, Dec. 2020, doi: 10.1063/5.0019252. I expand on the difference between polarisation spectroscopy (PS) and POLEAS spectroscopic techniques and perform a more in-depth analysis of the laser frequency stability measurements shown in the paper.

Laser stabilization to neutral Yb in a discharge with polarization-enhanced frequency modulation spectroscopy

Cite as: Rev. Sci. Instrum. 91, 123002 (2020); doi: 10.1063/5.0019252

Submitted: 7 July 2020 • Accepted: 22 November 2020 •

Published Online: 11 December 2020



Valdis Blūms,¹ Jordan Scarabel,¹ Kenji Shimizu,¹ Moji Ghadimi,¹ Steven C. Connell,¹ Sylvi Händel,¹ Benjamin G. Norton,¹ Elizabeth M. Bridge,¹ David Kielpinski,¹ Mirko Lobino,^{1,2} and Erik W. Streed^{1,3,a)}

AFFILIATIONS

¹Centre for Quantum Dynamics, Griffith University, Brisbane, Queensland 4111, Australia

²Queensland Micro- and Nanotechnology Centre, Griffith University, Brisbane, QLD 4111, Australia

³Institute for Glycomics, Griffith University, Gold Coast, QLD 4222, Australia

^{a)}Author to whom correspondence should be addressed: e.streed@griffith.edu.au

ABSTRACT

Isotope selective optical excitation of atoms is important for experiments with neutral atoms, metrology, and work with trapped ions, including quantum information processing. Polarization-enhanced absorption spectroscopy is used to frequency stabilize a tunable external cavity laser diode system at 398.9 nm for isotope selective photoionization of neutral Yb atoms. This spectroscopy technique is used to measure isotope resolved dispersive features from transitions within a see-through configuration ytterbium hollow-cathode discharge lamp. This Doppler-free dichroic polarization spectroscopy is realized by retro-reflecting a laser beam through the discharge and analyzing the polarization dependent absorption with balanced detection. The spectroscopy signal is recovered using lock-in detection of frequency modulation induced by current modulation of the external cavity laser diode. Here, we show an order of magnitude improvement in the long-term stability using polarization-enhanced absorption spectroscopy of Yb compared to polarization spectroscopy.

Published under license by AIP Publishing. <https://doi.org/10.1063/5.0019252>

I. INTRODUCTION

The 398.9 nm $^1S_0 \leftrightarrow ^1P_1$ transition is commonly used in both Yb and Yb⁺ atomic physics experiments due to its large dipole moment and accessibility with low-cost laser diodes. For neutral Yb, this transition allows for faster cooling and a broader velocity capture range of atoms than the narrower 555.8 nm $^1S_0 \leftrightarrow ^3P_1$ transition, eliminating the need for a Zeeman slower,¹ while still being suitable for sub-Doppler cooling.² For generating Yb⁺ ions, the 398.9 nm transition provides a well-resolved isotope selective excitation step in the ionization process, which is frequently completed by continuum ionization by the Yb⁺ UV cooling laser at 369.5 nm. This approach is more economical and accessible than using an isotope-enriched Yb source combined with non-isotope selective electron impact ionization.³

Frequency-stable lasers, tunable to within a few MHz of an atomic resonance, are now a standard tool for precision atomic

physics experiments.^{4–8} Common approaches to frequency stabilize a CW laser include interfering it with a stabilized optical frequency comb^{4,9} as well as using a Fabry-Pérot transfer cavity^{7,8,10,11} or commercial Fizeau-interferometer-based wavemeter^{12,13} to transfer the frequency stability from one laser wavelength to another. All of these options require an existing stable frequency reference, which can result in a greater cost, greater complexity, or potentially lower robustness over directly stabilizing the laser frequency to the desired atomic frequency standard. As an alternative vacuum, isolated Fabry-Pérot cavities with drifts of 80 Hz/s¹⁴ and -1.02 MHz/day¹⁵ have been shown to be sufficient for atomic physics experiments without the need for regular stabilization to an absolute frequency standard.

Numerous spectroscopy techniques have been reported,¹⁶ primarily using atomic or molecular vapor cells.¹⁷ Traditional vapor cells are not suitable for low vapor pressure/high boiling point elements including ytterbium. At room temperature, Yb has a vapor

pressure 11 orders of magnitude lower than cesium or rubidium. Increasing the temperature to produce comparable pressures results in Yb reacting chemically with the glass windows of a vapor cell. Efforts have been made to design and build vapor cells for elements including strontium and ytterbium,^{18,19} however, there are no commercially available options. A reliable and cost-effective alternative to stabilize a UV laser is using atoms produced in the discharge of a hollow-cathode lamp (HCL). First demonstrated in 1970,²⁰ laser stabilization to a discharge has been extended to various atomic species, including neutral ytterbium,²¹ erbium,^{22–24} dysprosium,²⁵ chromium,²⁶ and strontium.²⁷ Several spectroscopy techniques using Yb have been reported in an atomic oven²⁸ or a discharge lamp including modulation transfer spectroscopy (MTS),²⁹ which uses non-linear four-wave mixing as well as dichroic atomic vapor laser locking (DAVLL).^{21,30} In addition, other experiments with hollow cathode lamps have utilized polarization spectroscopy (PS) to measure sub-Doppler features for both neutral and ionized Yb, which are stable with respect to frequency.^{31,32} The ability to swap between probing dichroism and laser-induced birefringence in a discharge by changing the analysis optics has been reported.³³

Here, we demonstrate the use of polarization-enhanced absorption spectroscopy (POLEAS)³⁴ to probe the dichroism of a Yb transition. When compared to PS, POLEAS has a locking frequency stability at least ten times less sensitive to polarization drift, aided by the different analysis optics while still providing a larger signal-to-noise ratio (SNR) than Doppler-free saturation absorption spectroscopy (D-F SAS).^{35,36} POLEAS is also cheaper than MTS for this near UV transition, as it can be achieved without extra components for creating sidebands on a sub-400 nm laser beam. This is the first time this type of spectroscopy has been used on ytterbium in a discharge lamp and swapping from PS to POLEAS requires minimal changes to a spectroscopy system.

II. PRINCIPLE OF THE TECHNIQUE

A key aspect of many high precision spectroscopy techniques is the ability to produce well-resolved, stable dispersive features suitable for incorporation into a frequency stabilization servo loop. Many of these spectroscopy techniques modulate the laser light, which results in a change of the response of the atomic system, such that the obtained signal from probing the sample can be passed through a lock-in amplifier to obtain a sharp and stable error signal feature.

In its most elementary form, D-F SAS comprises a pump beam and a counter-propagating probe beam. The nonlinear interaction between the counter-propagating beams enables the tighter constraints in this spectroscopy technique, restricting the atom interaction with both beams simultaneously to a particular velocity class, resulting in a Doppler-free spectroscopy signal. The probe beam changes properties (amplitude and polarization) as it passes through a sample and gets sent to an analysis setup. The presence of the on-resonant pump beam saturates the transition and reduces the change in probe beam properties. The pump beam modulation is sent to a lock-in amplifier as a reference signal and is mixed with the signal obtained from the probe beam after the analysis setup. Due to the beams being counter propagating, assuming perfect

overlap, the end signal is free from the heterogeneous first order Doppler broadening.

Figure 1 shows a generic setup for both PS and POLEAS along with the expected output signals after lock-in detection. The setup for PS and POLEAS is similar in pump and probe beam polarizations; however, they differ in the analysis optics. A circularly polarized pump beam is sent through the sample (for convention, let us call this σ^R). The counter propagating probe light is linearly polarized, which is also an equal superposition of σ^R and σ^L . The pump beam saturates the transition for the counter propagating σ^L light. This uses the same counter-propagating beam technique as D-F SAS, and thus, the Doppler broadened spread in the resonant frequency of the transition can be ignored. For a two-level atomic transition, the probe light experiences a change in its properties explained by the complex absorption coefficient, which, when broken into its real and imaginary parts, is³⁷

$$\text{Re}(\alpha) = \alpha_0 \frac{\gamma^2}{\gamma'^2 + (\omega_0 - \omega)^2} \quad (1)$$

and

$$\text{Im}(\alpha) = -\alpha_0 \frac{\gamma(\omega_0 - \omega)}{\gamma'^2 + (\omega_0 - \omega)^2}, \quad (2)$$

where

$$\gamma' = \gamma\sqrt{1 + s_0} \quad (3)$$

and

$$s_0 = \frac{I}{I_{\text{sat}}} = \frac{3I\lambda^3\tau}{\pi hc}. \quad (4)$$

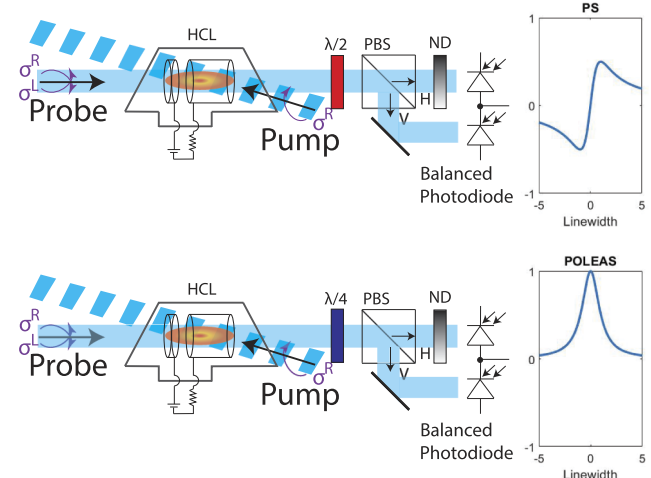


FIG. 1. The top optical setup probes laser-induced birefringence and is commonly referred to as PS. The bottom optical setup probes dichroism and is referred to as POLEAS. The only difference between these two schematics is the wave plate used before the analysis optics, shown in red and blue. The right of each optical setup is a theoretical example of a spectroscopy feature, calculated from Eqs. (1) and (2) with $s_0 = 0$ for feature clarity. For PS, $\text{Im}(\alpha)/\alpha_0$ is plotted. For POLEAS, $\text{Re}(\alpha)/\alpha_0$ is plotted. HCL—hollow-cathode lamp, PBS—polarizing beam splitter, ND—variable neutral density filter, H—horizontal polarization, and V—vertical polarization.

Here, α_0 is the linear resonant absorption coefficient ($s_0 = 0$), s_0 is the dimensionless on-resonance saturation parameter, ω is the laser frequency, ω_0 is the transition resonant frequency, γ is the natural transition linewidth, and γ' is the power-broadened linewidth. Equations (1) and (2) are similar to the Kramers–Kronig dispersion relations obtained when looking at the real and imaginary parts of the complex refractive index.¹⁷ The analysis optics are set up such that, for PS, the real part of the complex absorption coefficient is suppressed and, for POLEAS, the imaginary part is suppressed. The reason for this is as follows.

For PS, without an atomic sample, the probe beam is set to a linear polarization such that equal amounts of both σ^R and σ^L light go to both detectors for analysis. In this case, the polarization controlling $\lambda/2$ wave plate in the probe arm can be before or after the sample. When probing the sample, the change in absorption is fed into both detectors equally and is filtered out when taking the difference between detectors. However, the σ^R light and σ^L light experience circular dichroism proportional to the difference in absorption coefficients $\Delta\alpha = \text{Im}(\alpha)^{+,L} - \text{Im}(\alpha)^{-,R}$. This, as well as the change in amplitude between the σ^R and σ^L light, changes the probe beam polarization after the lamp to be slightly elliptical. For a frequency blue shifted from resonance, this ellipticity sends more light toward one detector, and when the frequency is red shifted from resonance, more light is sent to the other detector. This produces the dispersive spectroscopy locking signal. This setup is highly sensitive to polarization fluctuations of the probe beam and any fluctuation of the $\lambda/2$ wave plate from temperature, as the resulting changes to the spectroscopy signal appear similar to that caused by changes in the laser frequency.

For POLEAS, without an atomic sample, the probe beam is again set to a linear polarization such that equal amounts of both σ^R and σ^L light go to both detectors. However, by placing a $\lambda/4$ wave plate after the sample, all of the σ^R light can be sent to one detector, while all of the σ^L light is sent to the other detector. The difference in the amount of light at each detector is determined by the complex absorption coefficients for the σ^R and σ^L light through the sample, where $\text{Re}(\alpha)$ dominates in the end feature. The effects from $\text{Im}(\alpha)$ are suppressed as this spectroscopy is first order insensitive to polarization fluctuations of the probe beam from induced circular dichroism, or from temperature shifts of the $\lambda/4$ wave plate. In the compressed form of POLEAS, the probe beam is a retroreflected portion of the pump beam. The Doppler-free absorption profile obtained from this spectroscopy is then converted into a suitable locking signal through frequency modulation of the laser.^{38–40}

III. YTTERBIUM SPECTROSCOPY

Ytterbium has a relatively straightforward lower energy level structure with optically accessible transitions that are suitable for laser cooling in both neutral and ionized Yb^+ atomic physics experiments. Ytterbium has seven naturally occurring isotopes with atomic mass units and abundances shown in Table I. Here, we considered the two most abundant isotopes (^{174}Yb , ^{172}Yb) as well as ^{171}Yb that is frequently used for quantum information processing (QIP).

^{174}Yb and ^{172}Yb have a simpler energy level structure compared to ^{171}Yb because the ground-state nuclear spin is zero for even

TABLE I. Yb isotopes and their naturally occurring abundances.

Yb isotope	Precise atomic mass ⁴¹	Abundance (%) ^{42,43}
168		0.1232(4)
170	169.934 767 241(18)	2.982(6)
171	170.936 331 514(19)	14.086(20)
172	171.936 386 655(18)	21.686(19)
173	172.938 216 213(18)	16.103(9)
174	173.938 867 539(18)	32.025(12)
176	175.942 574 702(22)	12.995(1.3)

isotopes and 1/2 for ^{171}Yb . This nuclear spin of 1/2, which interacts with the electron spin, splits the energy levels and results in a hyperfine structure in ^{171}Yb (see Fig. 2). For $^{171}\text{Yb}^+$, this hyperfine splitting of the ground state is 12.64 GHz,^{44,45} which provides long lived microwave accessible states for QIP.^{47,48} This hyperfine splitting also provides a single $F = 0$ ground state, which is ideal for optical ion clocks used in metrology.⁴⁹ The simpler energy level structure in the even isotopes makes them useful for studying fundamental physics problems, such as observing the shadow of a single ion⁵⁰ or sensing sub-attoneutron forces in three dimensions,⁵¹ with minimal parameters and relaxes the requirements on needed equipment. This also makes them useful when setting up a new experiment for QIP applications.⁵²

Table II and Fig. 3 provide detailed information on the $^1\text{S}_0 \leftrightarrow ^1\text{P}_1$ transition around 398.9 nm for the different isotopes with respect to the transition frequency in ^{174}Yb . Table II lists the isotope specific shift in the resonant frequency, and in Fig. 3, we estimate the potential isotopic purity of ion formation from a natural abundance source based on the excitation probabilities as a function of laser detuning.

The ionization purity f_i (Fig. 3) is calculated for a given laser frequency ω from the relative scattering rate for a particular isotope Γ_i vs the total scattering rate from a natural abundance distribution,

$$f_i(\omega) = \frac{\Gamma_i(\omega)}{\sum_n \Gamma_n(\omega)}. \quad (5)$$

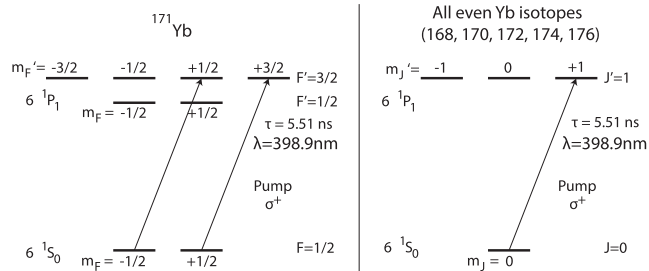


FIG. 2. Relevant energy levels for the Yb isotopes producing prominent spectroscopy features suitable for laser stabilization. Excited state lifetime $\tau = 5.51$ ns calculated from Ref. 54. The transitions shown with arrows are saturated via the pump beam, dependent on the magnetic field direction. A more complete energy level structure can be found from Ref. 31. For ^{171}Yb , the $^1\text{S}_0$ ground-state m_F levels are split by the nuclear spin, while the excited $^1\text{P}_1$ state m_F levels are split by the electronic and nuclear magnetic dipole interactions.

TABLE II. Yb isotopes and their 398.9 nm $^1S_0 \leftrightarrow ^1P_1$ transition frequency shifts.⁴⁶

Yb isotope	Hyperfine level	Isotope shift (MHz) ^a
168		1887.400(50)
170		1192.393(66)
171	(F' = 1/2)	1153.696(61)
171	(F' = 3/2)	832.436(50)
173	(F' = 7/2)	587.986(56)
172		533.309(53)
173	(F' = 3/2)	515.975(200)
174		0
173	(F' = 5/2)	-253.418(50)
176		-509.310(50)

^aRelative to ^{174}Yb .

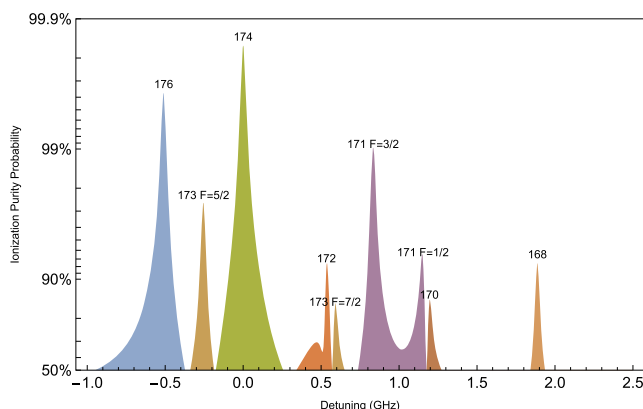


FIG. 3. Isotope ionization purity rates of neutral Yb on the 398.9 nm $^1S_0 \leftrightarrow ^1P_1$ transition for a natural abundance source as a function of detuning. The plot is for a collimated laser beam perpendicular to a dilute collimated atomic beam (zero Doppler broadening), in the low laser intensity limit with no optical pumping. Detunings are with respect to the transition frequency in ^{174}Yb . Note that for ^{171}Yb , exciting the F = 3/2 transition provides the largest probability of only exciting that isotope.

For isotopes 171 and 173 with nuclear spin $I \neq 0$, the scattering rate is the sum across all transitions with a weighting factor h_j based on the spin multiplicity,

$$\Gamma_i(\omega) = \sum_j h_j \frac{\gamma_{S_0}/2}{1 + s_0 + 4(\omega_j - \omega)^2 \gamma^{-2}}. \quad (6)$$

IV. EXPERIMENTAL METHODS AND RESULTS

Three setups were tested for obtaining Yb spectroscopy. The simplest one utilized an in-house assembled external-cavity diode laser (ECDL), shown in Fig. 4. In this setup, the 398.9 nm laser system consists of an ECDL on a temperature stabilized base. The UV laser diode (Nichia Corporation LD-0397-0030-1) has a free running wavelength of 397.9 nm, tuned to 398.9 nm by optical feedback from a Littrow configuration 3600 groove/mm holographic grating

(Thorlabs GH13-36U). The diode is driven with a combination of direct current and current modulation. The direct current ranges from 41.41 mA to 43.10 mA for day to day use. This provides a total ECDL output power of 11 mW after the grating. The modulation depth is estimated as 1.25 MHz/ μA from measurements using a wavemeter. A peak-to-peak modulation depth of 25 MHz was used at a modulation rate of 50 kHz. The beam out of the laser diode is collimated using an asphere (Thorlabs C671TME-A), providing an elliptical beam with Gaussian $1/e^2$ diameters of 1.89(1) mm in the horizontal direction and 0.51(1) mm in the vertical direction. To prevent unwanted back reflections into the diode, modulating the laser frequency or amplitude, we use an optical isolator (Conoptics 711C-1) with 80% transmission in the forward direction and 37 dB isolation in the reverse direction. The 9 mW beam out of the isolator gets split on a polarizing beam splitter (PBS) cube where 2 mW of light is sent to an ion-trap experiment via a polarization maintaining optical fiber. The remaining 7 mW of light is turned circularly polarized, using a $\lambda/4$ wave plate, and sent through a DC hollow-cathode lamp backfilled with Ne buffer gas (Hamamatsu L2783-70NE-Yb) operating at a supply current of 1.2 mA and a voltage of 140 V. The choice of buffer gas species is not critical for neutral atom spectroscopy; however, it does have a substantial impact on the in-lamp ion population.³⁰ The estimated pressure broadening from neon gas colliding with neutral ytterbium is not present in the literature and was estimated as 7 MHz/Torr at room temperature. This value was calculated from a hard sphere model for collisions and using the covalent radii of the two atoms.

The complete drive circuitry for this lamp is shown in Fig. 4, with the DC power supply operating in the current limited mode. The lamp is housed in a die-cast aluminum container with no

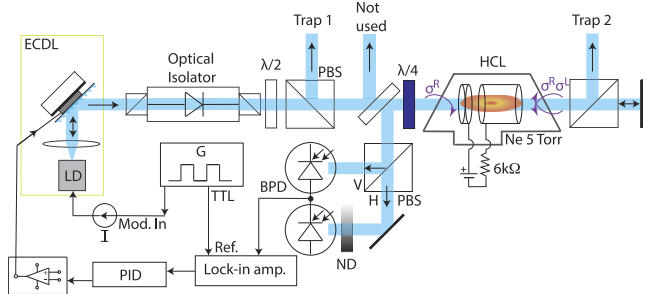


FIG. 4. Optical setup for spectroscopy using the in-house external-cavity diode laser (ECDL). The ECDL provides a total output power of 9 mW after the optical isolator. Part of the light from the ECDL is picked off before the spectroscopy and fiber coupled to a 2D RF Paul trap (trap 1). The spectroscopy is realized in a hollow-cathode lamp (HCL), and the absorption signal is recorded on a differential photodiode (BPD). After the HCL, the beam passes through a PBS where the reflected component is sent out of the setup and sent to a 3D RF Paul trap (trap 2). Also shown are the electronics to generate the error signal, which is fed back into the laser, and the electronic circuit used for controlling the HCL. The electric potential between the HCL anode and cathode results in neutral, excited, and ionized Ne buffer gas atoms. Ne⁺ ions bombard the Yb cathode, sputtering neutral Yb through the lamp.⁵³ The second optical setup replaced the ECDL with a Moglabs laser system and fiber coupled 3.54(1) mW into the setup before the optical isolator. The third optical setup replaced the Moglabs laser with an M Squared SolsTiS plus ECD-X laser system and fiber coupled 8.26(1) mW into the setup before the optical isolator.

external magnetic fields applied and designed for optical access at both sides with windows at a 10° angle to deflect back reflections. It comprises a ring cathode of length 19 mm and bore diameter 3 mm. The collimated beam exits the hollow cathode lamp and passes through a PBS, where the reflected portion of the beam is sent to a second ion-trap experiment. The transmitted portion of the beam is then retroreflected through the discharge, and $\lambda/4$ wave plate, before a fraction of that light is picked off using a glass blank and sent for analysis. This light is split on a PBS and sent to a balanced pair of photodiodes. In order to precisely balance the photocurrents, we use a variable neutral density filter (ND) to balance the optical power. The difference in the detector's measured current is amplified, providing an absorption signal on a flat background. A Newport 2107-FS-M balanced photoreceiver was used for spectroscopy and locking stability measurements. It has a measured conversion gain of $88.3(5)$ mV/ μ W and a bandwidth of 10 MHz.

To further amplify the POLEAS signal, as well as to turn it into a zero-crossing locking signal by taking its derivative, we frequency modulated the laser through its drive current. The laser was modulated at a frequency of 20 kHz, with the modulation depth optimized for the largest signal-to-noise ratio without reducing feature details. Any change in the laser power from drive current modulation was filtered out of the spectroscopy signal through the balanced photodiodes. For lock-in detection, we used a Stanford Research Systems' SR510 lock-in amplifier, with a sensitivity of 1 mV/V and a post low-pass filter time of 0.1 s. In Fig. 5(c), the resulting signal out of the lock-in amplifier is shown. Changing the lamp current then changed the peak-to-peak height of the spectroscopy features. As described in Ref. 31 for the case of PS of Yb in a discharge, the size (slope) of the features increases linearly with lamp current until a tipping point is reached, measured to be 0.8 mA for these laser settings. At higher lamp currents, the absorption attenuates the probe beam reducing the signal size. The lamp current at 0.8 mA is optimized to provide the largest spectroscopy feature for ^{174}Yb , which coincides with the largest peak-to-peak slope for stabilizing the laser frequency. Once obtained for a particular laser system, the lamp current does not need to be changed and the feature sizes become stable.

The second setup provided similar results using a more expensive, off-the-shelf, Moglabs 399 nm laser (Littrow Desmo) and controller (DLC102HC). This setup contained a second optical isolator with an additional 88% transmission and 49 dB isolation. The 398.9 nm light from this laser source was fed into the system of Fig. 4, replacing the ECDL, through a polarization maintaining fiber. The collimated-laser power of the pump beam before the HCL was 2.56(1) mW, with Gaussian $1/e^2$ diameters of 0.26(1) mm in the horizontal direction and 0.24(2) mm in the vertical direction. The diode operating current, as seen on the front display panel, was 54.78 mA, where the lasing threshold was 41.24 mA. The current modulation amplitude for frequency modulation was 1.5 mA. The Moglabs internal dip-switches from 1 to 16 were set to 0101 1000 0000 0000, where 0 and 1 represent the off and on states, respectively. This allowed a feed-forward bias of the ECDL grating piezo-voltage to diode current for a longer mode-hop free tuning range. This ratio can be measured as voltages on Ch A and Ch B of the Moglabs controller, with the channel outputs set to measure the frequency and current, respectively. This ratio of

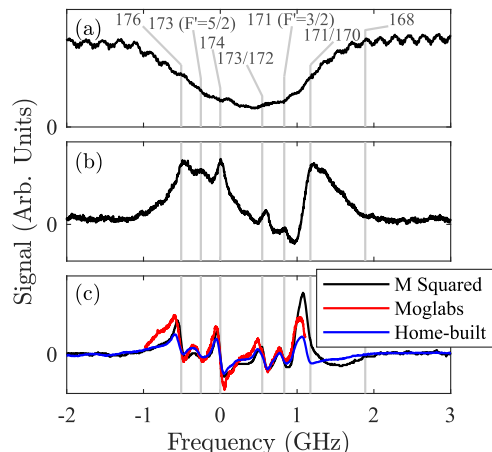


FIG. 5. Laser induced spectra of neutral Yb, with the frequency axes referenced to the 174 isotope resonance. (a) Absorption signal of the discharge before lock-in detection on the differential photodiode. (b) Laser induced resonance spectra of neutral Yb. (c) Differential photodiode signal after lock-in detection using three different lasers. Assignments of isotope resonances using Table II are shown in gray.

frequency/current was 7.1 to 1. The spectroscopy trace from this laser source is also shown in Fig. 5(c). For this trace, the best results were obtained with a lamp current of 1.4 mA and the dual photodiodes were turned off to reduce the power supply noise. The spectroscopy signal was sent into the current input of the lock-in amplifier, with sensitivity set to 2 mV/V and a low pass filter time constant of 10 ms.

The third, and most expensive, setup used an off-the-shelf M Squared lasers' SolsTiS plus ECD-X system. This laser again provided similar results to the home-built ECDL, where the spectroscopy trace for this laser is also shown in Fig. 5(c). The lock-in settings used for this laser are as follows: sensitivity 5 mV/V, low pass filter time constant 3 ms, and modulation rate 8.52 kHz. A modulation depth of 3 MHz was used. For this laser source, Fig. 5(a) shows the raw absorption signal observed on the positive balanced photodiode. Etalon fringes were evident in this scan. The etalon fringe period and size were consistent with a cavity of 80 cm and 2% reflection. This distance is that between the laser emission asphere and retro-reflecting mirror after the HCL. The irises 20 cm separate from either side of the HCL were close to 1 mm diameter, and a 0.5 ND filter was placed before the retro-reflecting mirror. These optics helped reduce etalon effects in the system. An optical isolator was not implemented for this scan due to spatial constraints. Figure 5(b) shows the POLEAS spectrum corrected for etalon fringes by subtracting a background signal, generated by turning off the HCL power supply.

The natural linewidth for the 398.9 nm $^1\text{S}_0 \leftrightarrow ^1\text{P}_1$ transition is $\gamma = 2\pi \times 28.9$ MHz.⁵⁴ However, the feature sizes in Fig. 5(b) are close to an order of magnitude larger ($\gamma = 2\pi \times 280$ MHz). The dominant mechanisms for the broadened linewidth are pressure broadening and power broadening. The pressure broadening is estimated to be 36 MHz by a hard sphere model of gas using the covalent radii of neon and ytterbium. The pressure broadened linewidth is then

~65 MHz. The saturation parameter is then approximated, given a probe power of 50(13) μW and a spot size of 0.0421(9) mm^2 as $s_0 = 0.9(2)$. The power broadened linewidth is then estimated as 89(5) MHz, which is an underestimate of the observed linewidth. It is likely that the hard sphere model of pressure broadening is underestimating the collisional cross section of neon and ytterbium since the valence electron of ytterbium is in an excited, large P-orbital. A pressure broadening of 40 MHz/Torr for excited ytterbium colliding with neon would better explain the observed linewidth as in Fig. 5. A comparable pressure broadening of 70 MHz/Torr is seen in He–Ne laser transitions.⁵⁵ The Doppler broadening is approximated to be on the order of 1 MHz given a small angle of acceptance through the irises (5 mrad) around the HCL. This approximated Doppler broadening is less than that previously reported in spectroscopy measurements.^{31,56}

In order to achieve the optimal laser frequency stabilization for a given laser source, we investigated the signal-to-noise ratio (SNR) of POLEAS and PS in terms of pump beam saturation through the lamp. For an operating lamp current of 1.2 mA, the laser intensity from the home-built ECDL was varied with a half-wave plate and PBS, while the beam size and lamp current were kept constant. The signal was defined as the peak-to-peak difference in the voltage of the POLEAS and PS ^{174}Yb spectroscopy features. SNR was defined as the peak-to-peak signal size divided by the root-mean-square noise of the signal when the laser was not in resonance with a spectroscopic feature. In Fig. 6(a), it can be seen that for our given lamp current, the absorption of a beam, through the lamp, saturates at high intensities. In Fig. 6(b), it can be seen that for low intensities, the SNR of POLEAS increases linearly with increased pump beam saturation. This is consistent with creating a larger difference in the absorption coefficient between σ^+ and σ^- transitions.

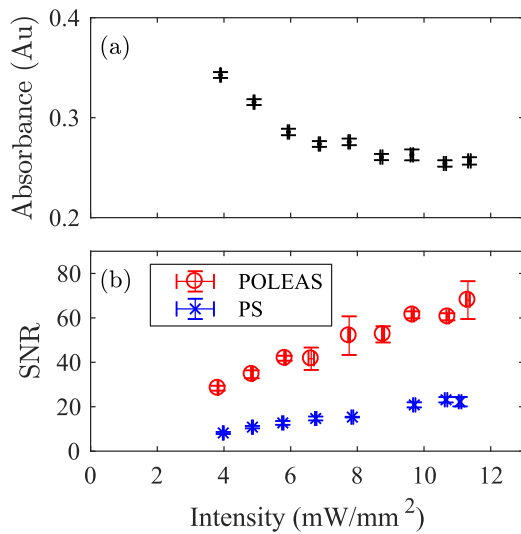


FIG. 6. Circularly polarized single pass absorbance and signal-to-noise ratio (SNR) of the differential POLEAS and PS signal. Intensity axis set to pump beam intensity before entering the HCL. (a) Pump beam saturation curve. (b) SNR of the prominent ^{174}Yb spectroscopy feature, calculated as the ratio of the signal V_{pp} to noise V_{rms} . Both the signal and noise increased linearly in this intensity regime.

A similar trend is seen for PS. POLEAS has three times the SNR of PS over the range of intensities shown. The dominant noise source after lock-in detection is likely laser intensity noise because the rms noise was measured to increase with laser intensity. The signal size grows linearly with higher input pump beam intensities in this low intensity regime. Using the high-powered SOLSTIS ECD-X laser and a different photoreceiver, the SNR peaks at 645(161) for an intensity of 120(10) mW/mm^2 because of signal saturation. Above this pump beam intensity, the noise on the signal increases, even when using an attenuated return probe beam. The large uncertainty in

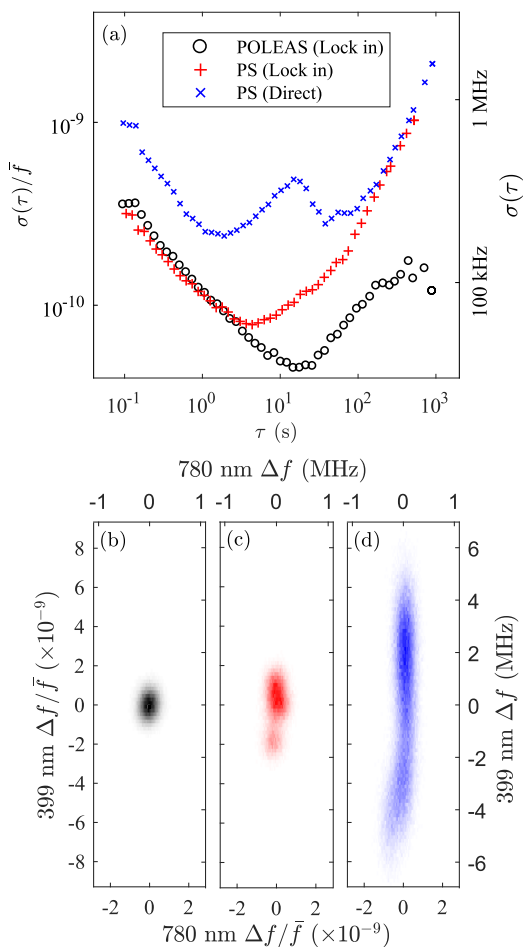


FIG. 7. Frequency fluctuation of the stabilized home-built laser, when locked using different spectroscopy techniques, (a) as a function of averaging time τ . Fractional frequency fluctuation [Allan deviation $\sigma(\tau)$] scale bar on the left. Absolute frequency fluctuations on the right. The results are from 1 h (POLEAS), 35 min (PS lock in), and 1 h (PS direct) measurements. The lock-in settings are as follows: sensitivity 500 $\mu\text{V/V}$, integration time 3 ms, and modulation rate 50 kHz. The $\sigma(\tau)$ uncertainty is smaller than the marker size. The covariance plots show the 399 nm laser frequency difference from mean while locked using: (b) POLEAS, (c) PS lock in, and (d) PS direct and their relation to the difference from mean of a locked Vescent 780 nm laser and rubidium spectroscopy module. The fractional frequency difference scale is shown on the bottom and left. The absolute frequency difference scale is shown on the top and right.

measurement is due to polarization drift from coupling high intensity light into the polarization maintaining fiber. This was a worse system configuration compared to the more stable free space source of light from the home-built ECDL.

The lock-in amplified signal of the ytterbium-174 POLEAS feature is used as an error signal for a locking loop. The signal is sent to a proportional-integral-derivative (PID), which sends its output to a piezo connected to the grating of the ECDL. This locking method is compared against the stabilizing method of PS by modifying the optics in the spectroscopy system. To switch our setup in Fig. 4 to PS, the quarter wave plate is moved to the left of the pickoff, and a half wave plate is put in its place, in front of the HCL. Both the direct signal of PS and the lock-in amplified signal of PS were used as error signals in locking loops. Measurements involving the lock-in amplifier were taken with identical settings: 500 μ V/V sensitivity, 50 kHz modulation rate, 3 ms integration time, and 25 MHz modulation depth. Drift measurements were made of these laser stabilizing systems using a High Finesse WS8-2 wavemeter. These measurements are compared against measurements of a reference Vescnt D2-100-DBR 780 nm laser locked via PS to a D2-110 rubidium spectroscopy module. This reference laser reliably exhibits a sub-100 kHz stability. Measurements of the 399 nm laser take 12 ms of integration. A wavemeter switch then takes 12 ms to multiplex from the 399 nm laser to the 780 nm laser. The 780 nm laser also then takes 12 ms of integration time and 12 ms of switching time. The total measurement period is 48 ms and is repeated in measurement runs of 1 h (POLEAS lock-in amplified), 35 min (PS lock-in amplified), and 1 h (PS direct signal). From the Allan deviation graph shown in Fig. 7, we observe that POLEAS locking has a similar short term frequency instability to PS when taking the lock-in amplified signal. In long-term timescales, the instability diverges with POLEAS being approximately an order of magnitude more stable at 10^3 s of averaging time. Figure 7 shows the covariance between the two locked lasers measured on the wavemeter. Their covariance shows minimal wavemeter drift over the course of measurements. We have previously taken comparable Allan deviation measurements locking to a wavemeter as Ref. 57; however, these do not show long-term instability since they are measured and stabilized off the same instrument.

Even with these drifts, we observe that during the 3600 s measurement time, the maximum Allan deviation was \sim 300 kHz, which is well within the 28.9 MHz linewidth of the atomic transition, and this is in line with our observations that the laser lock is sufficient to allow us to drive the transition and selectively photoionize the different isotopes of ytterbium.

V. CONCLUSIONS

In summary, we have successfully demonstrated the POLEAS locking technique with neutral Yb atoms in a hollow cathode discharge lamp for stabilizing a 398.9 nm laser to the $^1S_0 \leftrightarrow ^1P_1$ transition of several Yb isotopes.

For narrow-linewidth applications such as ultra-cold Bose-Einstein condensates, this technique may require an external modulator to prevent the sidebands from interfering with the laser beam delivered to the experiment. The locking bandwidth of this method is limited by the 1 ms integration time of the lock-in amplifier.

A greater locking bandwidth (into the acoustic regime) could be achieved with a faster lock-in amplifier.

This locking technique has shown to provide the necessary frequency stability to reliably photoionize the selected isotope of ytterbium from a naturally abundant source. Furthermore, the frequency stability measured would be sufficient for laser decelerating Yb atoms in a Zeeman slower for experiments utilizing neutral Yb. By using commercially available equipment and a simple optical setup, our approach significantly simplifies that taken compared to designing and building a Yb vapor cell or transfer cavity. We present this as a simple, robust solution for frequency stabilizing the 398.9 nm laser for atomic physics experiments using Yb atoms and Yb⁺ ions.

ACKNOWLEDGMENTS

This research was financially supported by the Griffith University Research Infrastructure Program, the Griffith Sciences equipment scheme, and the Australian Research Council Discovery (Grant No. DP130101613) and Linkage (Grant No. LP180100096) Projects. E.W.S., M.L., and D.K. were supported by the Australian Research Council Future Fellowships (Grant Nos. FT130100472, FT180100055, and FT110100513). V.B., J.S., K.S., and S.C.C. were supported by the Australian Government Research Training Program Scholarship.

DATA AVAILABILITY

The data that support the findings of this study are available from the corresponding author upon reasonable request.

REFERENCES

- ¹ U. D. Rapol, A. Krishna, A. Wasan, and V. Natarajan, *Eur. Phys. J. D* **29**, 409–414 (2004).
- ² N. Kostylev, E. Ivanov, M. E. Tobar, and J. J. McFerran, *J. Opt. Soc. Am. B* **31**(7), 1614–1620 (2014).
- ³ V. Enders, Ph. Courteille, R. Huesmann, L. S. Ma, W. Neuhauser, R. Blatt, and P. E. Toschek, *Europhys. Lett.* **24**(5), 325–331 (1993).
- ⁴ T. W. Hänsch, *Rev. Mod. Phys.* **78**, 1297 (2006).
- ⁵ E. A. Cornell and C. E. Wieman, *Rev. Mod. Phys.* **74**(3), 875–893 (2002).
- ⁶ Y. Takasu, K. Maki, K. Komori, T. Takano, K. Honda, M. Kumakura, T. Yabuzaki, and Y. Takahashi, *Phys. Rev. Lett.* **91**, 040404 (2003).
- ⁷ J. J. McLoughlin, A. H. Nizamani, J. D. Siversen, R. C. Sterling, M. D. Hughes, B. Lekitsch, B. Stein, S. Weidt, and W. K. Hensinger, *Phys. Rev. A* **83**(1), 013406 (2011).
- ⁸ F. Rohde, M. Almendros, C. Schuck, J. Huwer, M. Hennrich, and J. Eschner, *J. Phys. B: At., Mol. Opt. Phys.* **43**, 115401 (2010).
- ⁹ X. Shao, H. Han, Y. Su, H. Wang, Z. Zhang, S. Fang, G. Chang, and Z. Wei, in *IEEE Conference on Lasers and Electro-Optics* (IEEE, 2019), pp. 1–2.
- ¹⁰ W. Z. Zhao, J. E. Simsarian, L. A. Orozco, and G. D. Sprouse, *Rev. Sci. Instrum.* **69**(11), 3737–3740 (1998).
- ¹¹ K. Möhle, E. V. Kovalchuk, K. Döringshoff, M. Nagel, and A. Peters, *Appl. Phys. B* **111**, 223–231 (2013).
- ¹² K. Saleh, J. Millo, A. Didier, Y. Kersalé, and C. Lacroûte, *Appl. Opt.* **54**, 9446 (2015).
- ¹³ L. Couturier, I. Nosske, F. Hu, C. Tan, C. Qiao, Y. H. Jiang, P. Chen, and M. Weidmüller, *Rev. Sci. Instrum.* **89**, 043103 (2018).
- ¹⁴ M. Kumph, Ph.D. dissertation (University of Innsbruck, 2015).

- ¹⁵J. de Hond, N. Cisternas, G. Lochead, and N. J. van Druten, *Appl. Opt.* **56**, 5436–5443 (2017).
- ¹⁶J. L. Hall, *Rev. Mod. Phys.* **78**, 1279–1295 (2006).
- ¹⁷W. Demtroeder, *Laser Spectroscopy* (Springer, 2003).
- ¹⁸E. M. Bridge, J. Millen, C. S. Adams, and M. P. A. Jones, *Rev. Sci. Instrum.* **80**, 013101 (2009).
- ¹⁹A. Jayakumar, B. Plotkin-Swing, A. O. Jamison, and S. Gupta, *Rev. Sci. Instrum.* **86**, 073115 (2015).
- ²⁰M. Skolnick, *IEEE J. Quantum Electron.* **6**, 139 (1970).
- ²¹J. I. Kim, C. Y. Park, J. Y. Yeom, E. B. Kim, and T. H. Yoon, *Opt. Lett.* **28**(4), 245–247 (2003).
- ²²J. Ang'ong'a and B. Gadway, *J. Phys. B: At., Mol. Opt. Phys.* **51**, 045003 (2018).
- ²³H. Brammer, J. Ulitzsch, R. Bourouis, and M. Weitz, *Appl. Phys. B* **106**, 405–408 (2012).
- ²⁴A. Frisch, K. Aikawa, M. Mark, and F. Ferlaino, *Phys. Rev. A* **88**, 032508 (2013).
- ²⁵M. Schmitt, M.Sc. thesis, University of Stuttgart, 2012.
- ²⁶A. Greiner, J. Sebastian, P. Rehme, A. Aghajani-Talesh, A. Griesmaier, and T. Pfau, *J. Phys. B: At., Mol. Opt. Phys.* **40**, F77–F84 (2007).
- ²⁷Y. Hayakawa, T. Sato, C. Watanabe, T. Aoki, and Y. Torii, *Appl. Opt.* **57**, 1450–1454 (2018).
- ²⁸A. H. Nizamani, J. J. McLoughlin, and W. K. Hensinger, *Phys. Rev. A* **82**, 043408 (2010).
- ²⁹W.-L. Wang and X.-Y. Xu, *Chin. Phys. Lett.* **28**, 033202 (2011).
- ³⁰E. W. Streed, T. J. Weinhold, and D. Kielpinski, *Appl. Phys. Lett.* **93**, 071103 (2008).
- ³¹S. Zhu, T. Chen, X. Li, and Y. Wang, *J. Opt. Soc. Am. B* **31**, 2302–2309 (2014).
- ³²M. W. Lee, M. C. Jarratt, C. Marciniak, and M. J. Biercuk, *Opt. Express* **22**, 7210–7221 (2014).
- ³³B. Smeets, R. C. M. Bosch, P. Van Der Straten, E. Te Sligte, R. E. Scholten, H. C. W. Beijerinck, and K. A. H. Van Leeuwen, *Appl. Phys. B* **76**, 815–819 (2003).
- ³⁴P. D. Kunz, T. P. Heavner, and S. R. Jefferts, *Appl. Opt.* **52**, 8048–8053 (2013).
- ³⁵S. Haroche and F. Hartmann, *Phys. Rev. A* **6**, 1280–1300 (1972).
- ³⁶C. Y. Park and T. H. Yoon, *Jpn. J. Appl. Phys., Part 2* **42**(7A), L754–L756 (2003).
- ³⁷P. Meystre and M. Sargent, *Elements of Quantum Optics* (Springer, 2007).
- ³⁸G. C. Bjorklund, *Opt. Lett.* **5**, 15–17 (1980).
- ³⁹S. Kobayashi, Y. Yamamoto, M. Ito, and T. Kimura, *IEEE J. Quantum Electron.* **18**(4), 582–595 (1982).
- ⁴⁰W. Lenth, *Opt. Lett.* **8**(11), 575–577 (1983).
- ⁴¹R. Rana, M. Höcker, and E. G. Myers, *Phys. Rev. A* **86**(5), 050502 (2012).
- ⁴²J. R. de Laeter and N. Lukic, *Int. J. Mass Spectrom.* **252**(3), 222–227 (2006).
- ⁴³J. Meija, T. B. Coplen, M. Berglund, W. A. Brand, P. De Bièvre, M. Gröning, N. E. Holden, J. Irrgeher, R. D. Loss, T. Walczyk, and T. Prohaska, *Pure Appl. Chem.* **88**(3), 293–306 (2016).
- ⁴⁴P. T. H. Fisk, M. J. Sellars, M. A. Lawn, and G. Coles, *IEEE Trans. Ultrason. Ferroelectr. Freq.* **44**(2), 344–354 (1997).
- ⁴⁵R. Blatt, H. Schnatz, and G. Werth, *Z. Phys. A* **312**(3), 143–147 (1983).
- ⁴⁶D. Das, S. Barthwal, A. Banerjee, and V. Natarajan, *Phys. Rev. A* **72**(3), 032506 (2005).
- ⁴⁷Y. Wang, M. Um, J. Zhang, S. An, M. Lyu, J.-N. Zhang, L.-M. Duan, D. Yum, and K. Kim, *Nat. Photonics* **11**, 646–650 (2017).
- ⁴⁸S. Olmschenk, K. C. Younge, D. L. Moehring, D. N. Matsukevich, P. Maunz, and C. Monroe, *Phys. Rev. A* **76**(5), 052314 (2007).
- ⁴⁹N. Huntemann, C. Sanner, B. Lipphardt, C. Tamm, and E. Peik, *Phys. Rev. Lett.* **116**, 063001 (2016).
- ⁵⁰E. W. Streed, A. Jechow, B. G. Norton, and D. Kielpinski, *Nat. Commun.* **3**, 933 (2012).
- ⁵¹V. Blüm, M. Piotrowski, M. I. Hussain, B. G. Norton, S. C. Connell, S. Gensemer, M. Lobino, and E. W. Streed, *Sci. Adv.* **4**(3), eaao4453 (2018).
- ⁵²M. Ghadimi, V. Blüm, B. G. Norton, P. M. Fisher, S. C. Connell, J. M. Amini, C. Volin, H. Hayden, C.-S. Pai, D. Kielpinski, M. Lobino, and E. W. Streed, *npj Quantum Inf.* **3**, 4 (2017).
- ⁵³P. Hannaford, *Contemp. Phys.* **24**(3), 251–270 (1983).
- ⁵⁴P.-Y. Zhao, Z.-X. Xiong, J. Liang, L.-X. He, and B.-L. Lu, *Chin. Phys. Lett.* **25**(10), 3631–3634 (2008).
- ⁵⁵A. E. Siegman, *Lasers* (University Science Books, Sausalito, CA, 1986).
- ⁵⁶D. F. Kimball, *Collisional Perturbation of States in Atomic Ytterbium* (University of California at Berkeley, 1998).
- ⁵⁷M. Ghadimi, E. M. Bridge, J. Scarabel, S. Connell, K. Shimizu, E. Streed, and M. Lobino, *Appl. Opt.* **59**, 5136–5141 (2020).

To load the ion trap used in this research, a ytterbium source with a natural isotope abundance near the trap RF node is heated to produce an atomic beam passing through the that node. The neutral ytterbium is excited from its ground 1S_0 state to 1P_0 via a resonant laser near 398.9 nm[139] that is narrow and stable enough to excite a particular isotope's resonance. The excited valence electron is then given further energy by a 369.5 nm laser and photo-ionized from the atom. The newly created positively charged ion in the trapping node is then Doppler cooled by the same 369.5 nm laser. The 398.9 nm laser was locked to the spectroscopic lines of a separate source of neutral ytterbium to meet the resonance condition for $^1S_0 \leftrightarrow ^1P_0$ excitation of specific isotopes. This is possible because for ytterbium, on this transition, the resonance separation between isotopes is of order 100 MHz while the transition natural linewidth is $\Gamma/(2\pi) = 28.9$ MHz[140].

Vapour cells are often used in atomic spectroscopy where the atomic sample exists in a vapour form. A problem with spectroscopy of neutral ytterbium is its very low vapour pressure at room temperature $P_{Yb}(298 K) = 2.9(8) \times 10^{-18}$ Torr or $9(3) \times 10^{-2}$ atoms/cm³[141] compared to other samples such as neutral Rubidium $P_{Rb}(298 K) = 1.0 \times 10^{-6}$ Torr or 3.2×10^{10} atoms/cm³[142], which are commonly used in vapour cells.

Instead, hollow cathode lamps (HCLs) avoid these problems. In our experiment, a neon buffer gas¹ at 5 Torr is ionized in the strong electric field between electrodes at a 300 V potential in the lamp. The neon ions accelerate and hit the cathode sputtering off ytterbium. This ytterbium is then optically accessible because of the geometric design of the electrodes allowing a laser to pass through the region of released ytterbium.

The $^1S_0 \leftrightarrow ^1P_0$ spectral feature is strong owing to the fast decaying excited state ($\tau = \Gamma^{-1} = 5.51$ ns[140]). The natural abundance of ytterbium isotopes leads to many comparably strong spectral features within a bandwidth of less

¹Neon buffer gas is used because its sputtering also releases ytterbium ions which can also be spectroscopically detected.

than 3 GHz (Table 6.1).

Isotope	Abundance (%)	Isotope Shift (MHz)	1P_0 F number
168	0.1232(4)	1887.400(50)	-
170	2.982(6)	1192.393(66)	-
171	14.086(20)	1153.696(61)	1/2
		832.436(50)	3/2
172	21.686(19)	533.309(53)	-
173	16.103(9)	515.975(200)	3/2
		-253.418(50)	5/2
		587.986(56)	7/2
174	32.025(12)	0	-
176	12.995(1)	-509.310(50)	-

Table 6.1: Quantities for the isotope abundance[112] and detuning [143] from the $^1S_0 \leftrightarrow ^1P_0$ resonant frequency of ^{174}Yb .

6.1 Polarization Spectroscopy

The average separation in resonance of the ytterbium isotopes ($\sigma_f = 213$ MHz) is of the same order as the Doppler broadening of the transitions at room temperature $\sigma_D = \lambda^{-1} \sqrt{\frac{k_B T}{m}} \approx 303$ MHz which is enough to wash away isotope-specific features. To avoid Doppler broadening, velocity-selective excitation techniques are used.

A popular method is polarization spectroscopy[144, 145, 146] using counter-propagating beams separated by a fixed frequency interval (usually 0 Hz by using the same laser). An incident near-/on-resonant beam, circularly polarized (say RHC), pumps a sizeable population of the ytterbium gas to an excited state. Only atoms whose $^1S_0 \leftrightarrow ^1P_0$ resonance (account for Doppler shift) match the laser's frequency are pumped (to within the transition linewidth). A counter-propagating probe beam to the pump beam, usually the retro-reflected pump beam itself, is then made incident on the partially excited sample. The probe beam is made to have a superposition of both RHC and LHC polarized light in the form of a linearly polarized beam. If the probe beam is of the same frequency as the pump beam, only atoms with no Doppler shift will experience the both beams at the same frequency. A sample excited by the pump

beam will appear partially transparent to the LHC component of the probe beam, since the pump beam has an identical angular momentum transfer condition and is saturating those transitions. The RHC component of the probe interacts with the sample stronger than the LHC component and so relative measurements of phase retardation through the sample can be made. This phase shift is proportional to the difference in refractive index, given by the solution to the phase shift of an electric field interacting with an ensemble of damped electric dipole harmonic oscillators[96],

$$\Delta n(\Delta) = \frac{Ne^2}{4\omega m_e \varepsilon_0} \frac{\Delta}{\Delta^2 + (\gamma/2)^2}, \quad (6.1)$$

where Δ is the difference between the electric field and the resonator's frequency. N represents the number density of the sample. Also derived from the same model[96] is the attenuation coefficient, equation 6.2, which can describe how much light is absorbed,

$$a(\Delta) = \frac{Ne^2}{m\varepsilon_0 c \gamma} \frac{(\gamma/2)^2}{\Delta^2 + (\gamma/2)^2}. \quad (6.2)$$

This model describes a single resonance (two level system). The phase shift of a certain polarization of light from an initial horizontal beam can be shown to produce a dispersive feature when sent through a half wave plate and PBS cube using Jones calculus. Begin with the vector for a horizontal beam,

$$\vec{H} = \begin{pmatrix} 1 \\ 0 \end{pmatrix} = \sqrt{1/2}(\vec{L} + \vec{R}) = \frac{1}{2} \begin{pmatrix} 1 \\ -i \end{pmatrix} + \frac{1}{2} \begin{pmatrix} 1 \\ i \end{pmatrix} \quad (6.3)$$

and apply a phase shift $e^{-i\phi} = e^{-i\Delta n L/\lambda}$ and attenuation $e^{-\alpha} = e^{-aL}$ (L is the sample interaction length with the beam and λ is the beam wavelength), to

the right circular component

$$\hat{A} = \frac{e^{-(i\phi+\alpha)}}{2} \begin{pmatrix} 1 & i \\ -i & 1 \end{pmatrix} + \frac{1}{2} \begin{pmatrix} 1 & -i \\ i & 1 \end{pmatrix}. \quad (6.4)$$

It is assumed the LHC component is completely pumped and so does not interact with the probe. $\hat{A}\vec{H}$ represents the polarization of the probe after interaction with the atomic sample. Afterwards, the probe interacts with a half-wave plate with its fast axis at an angle $\pi/8$ radians from horizontal

$$\hat{M}_{HWP}(\pi/8) = \sqrt{1/2} \begin{pmatrix} 1 & 1 \\ 1 & -1 \end{pmatrix}. \quad (6.5)$$

The polarization is then equivalent to,

$$\vec{O} = \hat{M}_{HWP}(\pi/8)\hat{A}\vec{H} = \frac{1}{2\sqrt{2}} \begin{pmatrix} (1+i) + (1-i)e^{-(\alpha+i\phi)} \\ (1-i) + (1+i)e^{-(\alpha+i\phi)} \end{pmatrix} \quad (6.6)$$

and the difference in power out of each arm of the PBS, as detected on a differential photodiode is then proportional to

$$|\vec{O} \cdot \vec{V}|^2 - |\vec{O} \cdot \vec{H}|^2 = e^{-\alpha} \sin(\phi), \quad (6.7)$$

which for small ϕ and α is approximately $(1-\alpha)\phi = \Delta n \frac{L}{\lambda} (1 - La)$ and a trend proportional to equation 6.1 is recovered. Note, the effect of the absorbed \vec{R} polarized light is negligible when $aL \ll 1$, because the absorbed \vec{R} light is split equally across both detectors, cancelling out any difference. It would only attenuate the dispersive signal towards resonance slightly.

6.2 Polarisation enhanced absorption spectroscopy

Another way to analyze the probe beam is to use a quarter wave plate with its fast axis $\pi/4$ radians from the horizontal instead of a half wave plate. Instead of rotating the beam polarization 45 degrees and analyzing the phase difference of the RHC and LHC components, the quarter wave plate projects the RHC and LHC components into \vec{H} and \vec{V} polarizations. The quarter wave plate's Jones matrix is

$$\hat{M}_{QWP}(\pi/4) = \frac{1}{2} \begin{pmatrix} 1+i & 1-i \\ 1-i & 1+i \end{pmatrix} \quad (6.8)$$

and the Jones vector output after the quarter wave plate would be,

$$\vec{O} = \hat{M}_{QWP}(\pi/4) \hat{A} \vec{H} = \frac{1}{2} \begin{pmatrix} 1+i \\ e^{-(\alpha+i\phi)}(1-i) \end{pmatrix}. \quad (6.9)$$

The difference in power after a PBS as detected on a differential photodiode would be

$$|\vec{O} \cdot \vec{V}|^2 - |\vec{O} \cdot \vec{H}|^2 = \frac{1}{2}(e^{-2\alpha} - 1) \quad (6.10)$$

where for small α , the result approximates to $(1/2)(1 - (2\alpha - 1)) = -\alpha = -La$. Unlike polarization spectroscopy, there are no terms involving ϕ and so the POLEAS signal is independent of the change in phase induced by the atomic sample.

In experiment, POLEAS and PS were implemented to lock a laser's frequency to the spectroscopic lines of ytterbium. The system was mainly used in POLEAS mode (figure 6.1.a) and was modified as in figure 6.1.b to measure the locking performance of PS.

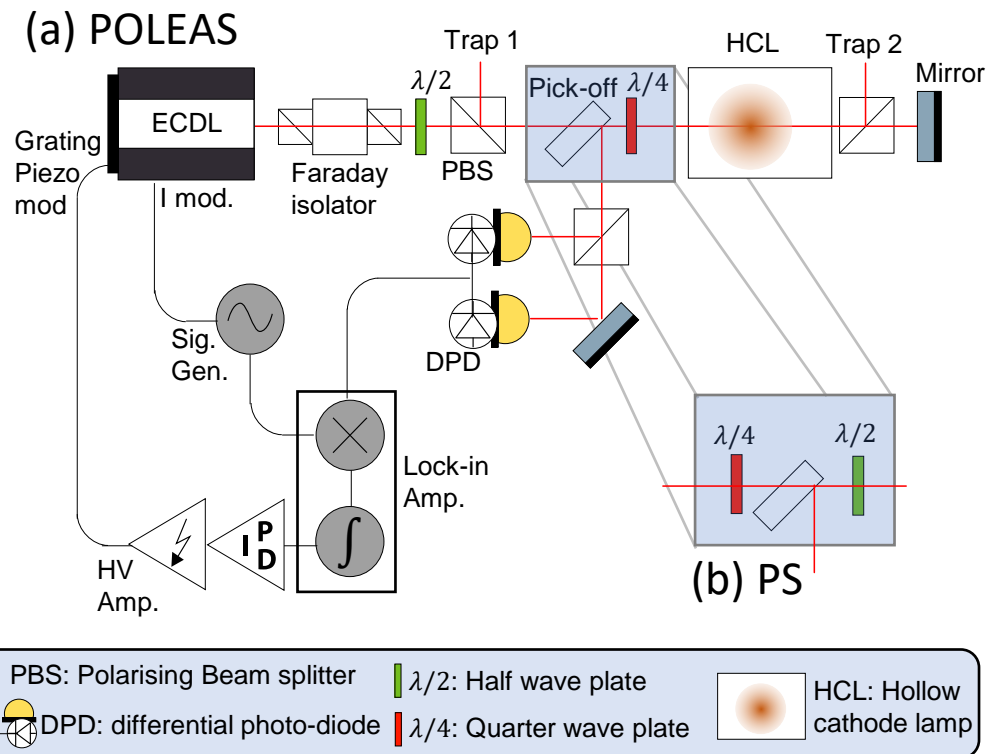


Figure 6.1: (a) The optical setup used to lock a 399 nm laser to the spectroscopic signal of Yb^+ using POLEAS. (b) The modified optical setup to produce a PS signal by moving the QWP to before the pick-off and replacing it with a HWP.

6.3 Stability analysis

Locking performance was measured in terms of absolute laser frequency stability. A common problem in precision measurement is knowing if instability is from a sample or the measuring device itself. When determining the frequency stability of the 399 nm laser using different locking techniques, this problem arose when considering the long-term stability of the HighFinesse WS8-2 wavemeter used for measuring laser frequency. Also, single-shot resolution of the wave-meter is quoted to 100 kHz by the manufacturer[147] which puts a lower bound on the Allan deviation at $100 \text{ kHz}/\sqrt{N}$ for N measurements (assuming Gaussian noise).

To assess the stability of the wave-meter over the measurement period, an independent frequency reference, a Rubidium-locked 780 nm laser was measured in between 399 nm frequency measurements. If the wave-meter drifts, there would appear to be a correlation in the change in frequencies of the 399 nm and 780 nm frequencies. These drifts can be identified by calculating the co-variance matrix of the fractional frequencies $F(t)$ of the lasers

$$F(t) = \frac{f(t) - \langle f(t) \rangle}{\langle f(t) \rangle}. \quad (6.11)$$

Measurements of the two lasers frequencies are performed by alternating the input of the wavemeter between each laser, where a full measure cycle of both lasers together takes 48 ms. For the POLEAS and PS locking techniques that used the lock-in amplifier, the lasers were continuously measured for 1 hour. For PS with no lock-in amplifier, the frequencies were measured for 38 minutes, limited by the lock stability.

To confirm there was no large measurement drift of the wavemeter over the measurement runs, a covariance plot (2D histogram) of the measurements of the lasers was made (figure 6.2). Calculation of the covariance matrix of the lasers gives values for the variance along the diagonals as well as a measure of

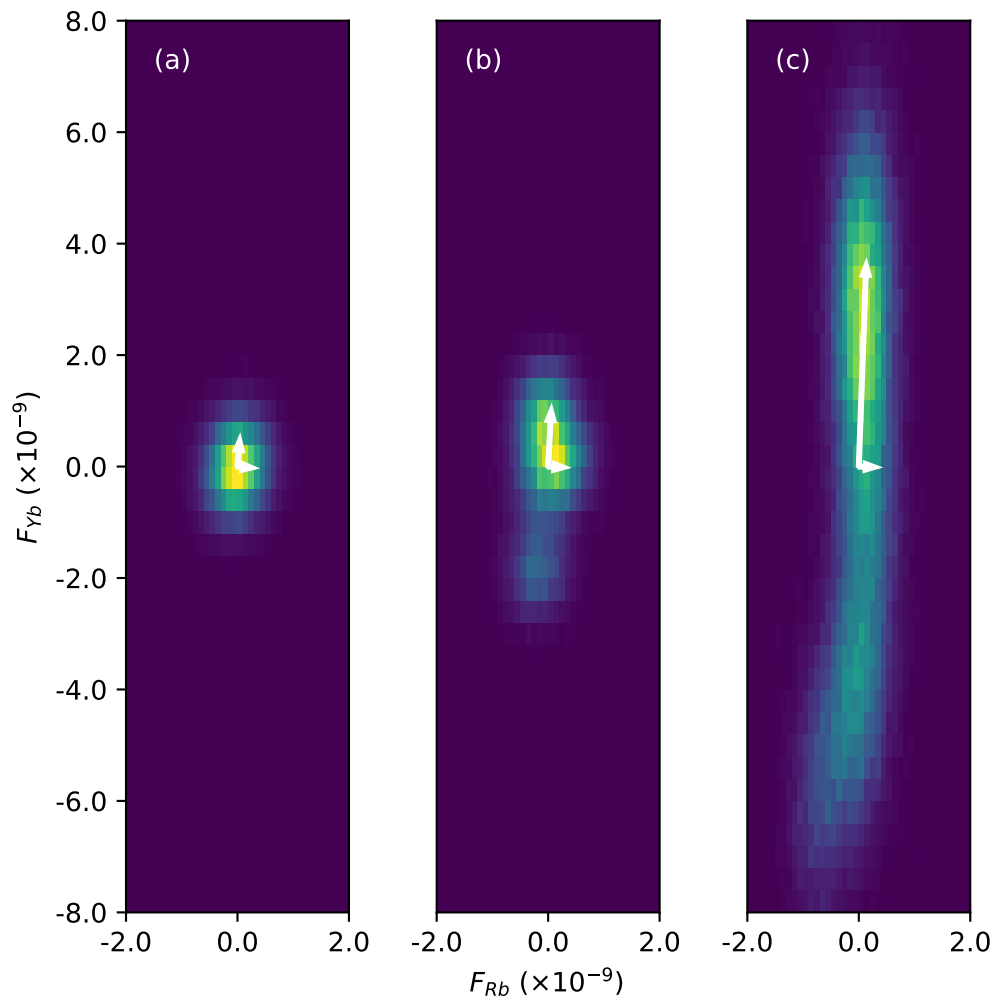


Figure 6.2: Simultaneous frequency measurements of the 399 nm ytterbium-locked and 780 nm rubidium-locked lasers when the 399 nm is locked via (a) lock-in amplified POLEAS, (b) lock-in amplified PS and (c) raw PS. Vectors are eigenvectors of the co-variance plot scaled by the square-root of the eigenvalues. These correspond to the orthogonal axes in an equivalent bi-variate normal distribution. The misalignment from the measurement axes suggests the frequency of the two lasers have some correlation, measuring instrument artifact or otherwise.

correlation along the anti-diagonals.

Each term of the covariance matrix is calculated according to

$$\sigma_{i,j}^2 = \frac{1}{T} \int_0^T F_i(t)F_j(t)dt \quad (6.12)$$

where i and j are indexes for the lasers used. Diagonal terms of the matrix equate simply to the variance of the individual frequencies of the lasers, while off-diagonal terms relate to the covariance between lasers. The correlation between two lasers frequencies,

$$\text{corr}_{i,j} = \frac{\sigma_{i,j}^2}{\sigma_{i,i}\sigma_{j,j}} \quad (6.13)$$

is a number ranging [-1, 1]. 0 represents no correlation between the two time series of laser frequencies while 1(-1) represents perfect (anti-)correlation. Given the two lasers were independently locked, any correlation in their frequency can be assumed to be measurement error from the wavemeter or shared noise from the environment.

In table 6.2 the correlation between the two locked lasers appears to increase with increased instability in the 399 nm laser frequency. This behaviour is likely from imperfect isolation between wavemeter channels, where leaking 399 nm light is skewing the 780 nm frequency measurement. The correlation is unlikely from an external environmental dependence like pressure or temperature because the correlation number would have stayed constant and not scaled with the 399 nm deviation.

Method	σ_{399}	σ_{780}	$\text{corr}_{399,780}$
POLEAS (Lock-in)	5.4×10^{-10}	3.4×10^{-10}	0.083
PS (Lock-in)	1.1×10^{-9}	3.6×10^{-10}	0.15
PS	3.7×10^{-9}	3.9×10^{-10}	0.34

Table 6.2: Standard deviation of the frequency data of the locked lasers for each locking method.

6.3.1 Allan Deviations of stabilized laser frequency

This analysis so far assumes the 780 nm laser itself does not drift. To assess this claim, a tripod of stability can be formed where relative measurements between:

1. The 399 nm laser and 780 nm reference laser,
2. The wave-meter and 399 nm laser,
3. The 780 nm reference laser and wave-meter,

can determine if one of the three devices are deviating more or less compared to the others. To assess the stability of the devices over time, Allan deviations between each of the pairs of devices can be made. Allan deviations of the frequency measurements between the wavemeter and lasers are straightforward to calculate. Allan deviation of the 399 nm laser frequency referenced off the 780 nm laser frequency requires calibrating the 399 nm laser frequency post-measurement according to the 780 nm laser frequency. By changing the stored 780 nm reference frequency in the wavemeter software, it was found the wavemeter software's calibration protocol was:

1. Measure the calibration laser frequency f_c .
2. If the frequency is within a reasonable range of the reference frequency stored in the computer's memory, calculate the ratio to the f_r/f_c .
3. Re-calibrate the wavemeter by scaling all measured frequencies from now on by $\times f_r/f_c$.

This calibration method was copied to calibrate the measured 399 nm frequencies post-measurement using the simultaneously measured 780 nm frequencies. Figure 6.3 then shows Allan deviation plots of the 3 devices relative to each other. The commercial rubidium-locked 780 nm laser measured via the wavemeter has the lowest Allan deviation except for in a time-band between 5-30 seconds where the ytterbium locked 399 nm laser measured via

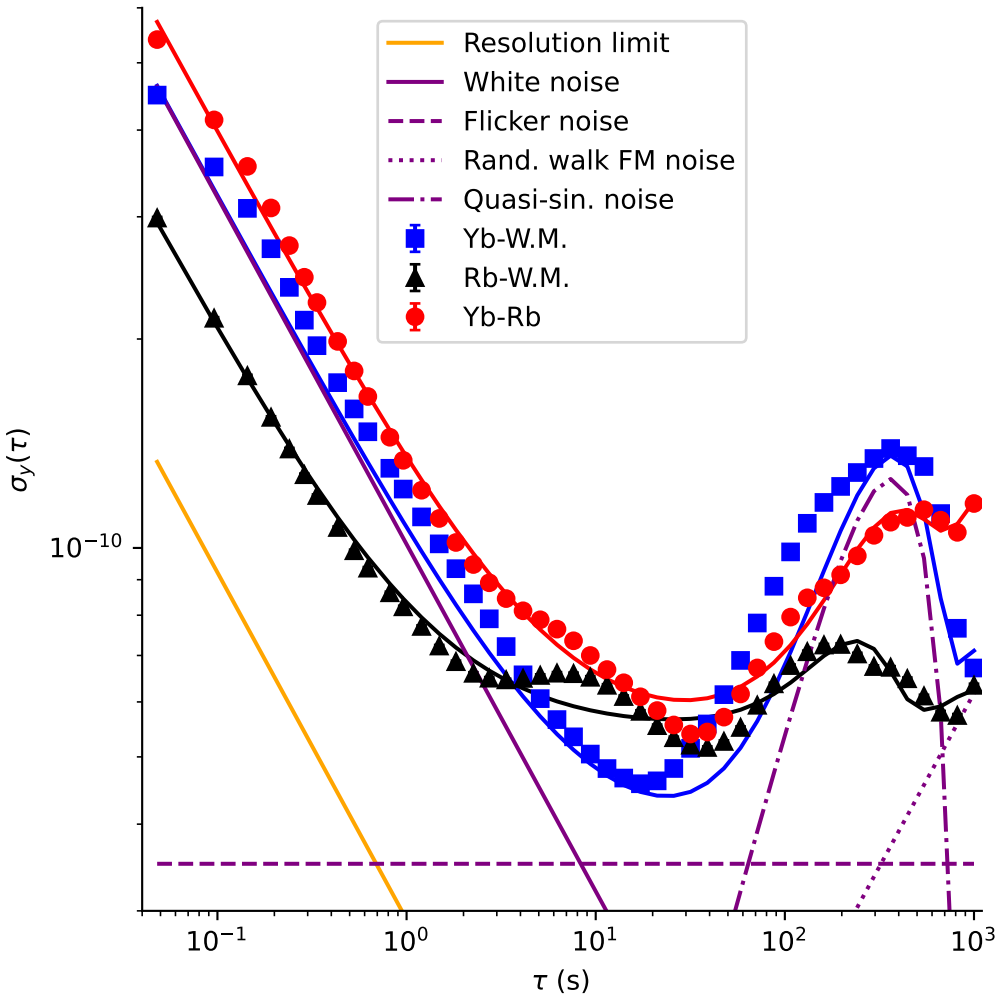


Figure 6.3: Allan deviation plots for: (Blue square) The frequency of a 399 nm laser locked to a Yb spectroscopic line using POLEAS measured off a wavemeter. (Black triangle) The frequency of a 780 nm laser locked to a Rb spectroscopic line using PS. (Red circle) The frequency of the 399 nm laser measured off a wavemeter but calibrated to the simultaneously measured 780 nm frequency.

the wavemeter has lower Allan deviation. At long timescales (> 30 s), the 399 nm laser calibrated against the 780 nm laser performs slightly better than being calibrated off the wavemeter alone (although measurements are within each other's standard deviation). This suggests wavemeter drift may dominate on timescales > 30 s compared to 780 nm frequency drift, and the wavemeter may be optimally re-calibrated in other experiments roughly every 30 seconds. The Allan deviations can be well described using four types of noise,

1. White noise which dominates at short timescales. It has a power noise spectrum that is spectrally flat and amplitude h_0 . In Allan deviations, it appears as a $\sqrt{\tau}^{-1}$ trend at short timescales.
2. Flicker noise has a power spectrum that scales as f^{-1} and amplitude h_{-1} . In Allan deviations, it appears as a noise floor independent of τ .
3. Random walk frequency modulation (drift) which dominates at long timescales. Random walk frequency modulation has a power noise spectrum that scales as f^{-2} and amplitude h_{-2} . In Allan deviations, it appears as a $\sqrt{\tau}$ trend at long timescales.
4. Quasi-sinusoidal noise[148] which occurs at a single frequency f_q and appears sinusoidal in Allan deviation plots with maxima at $\tau = (2N + 1)/2f_q$ and amplitude h_s that drops off as τ^{-1} .

The equation relating the noise to the Allan deviation is[149]

$$\sigma_y(\tau) \approx \sqrt{\frac{h_0}{2\tau} + 2 \ln(2)h_{-1} + \pi^2 \frac{2\tau h_{-2}}{3} + 2h_s \frac{\sin(\pi\tau f_q)^4}{(\pi f_q \tau)^2}}. \quad (6.14)$$

The sinusoidal term can be found by applying a Dirac delta function noise spectrum to the equation for Allan variance in the limit where measurement period approaches zero[148, Eq. 2]. From fits to this model of Allan deviation (table 6.3), white frequency modulation power coefficient $\sqrt{h_0}$ in units of

fractional-frequency-deviation-root-averaging-time (\sqrt{s}) is lowest for the commercial Rubidium locked laser which is likely because it has a faster locking bandwidth (~ 100 kHz) compared to the 399 nm POLEAS lock (~ 100 Hz).

	$\sqrt{h_0} (10^{-10} \sqrt{s})$	$\sqrt{h_{-1}} (10^{-11})$	$\sqrt{h_{-2}} (\frac{10^{-12}}{\sqrt{s}})$	$\sqrt{h_s} (10^{-10})$
Yb-W.M.	1.43(5)	3.0(4)	0.76(20)	1.23(12)
Rb-W.M.	0.896(7)	4.62(8)	0.35(7)	0.46(3)
Yb-Rb	1.8(2)	4.3(1.4)	1.9(5)	0.75(7)

Table 6.3: Power coefficients for power-law frequency noise fitted to the Allan deviation plots.

The quasi-sinusoidal noise has repetition rates of 1.02(8) mHz, 1.59(11) mHz and 1.03(10) mHz for the Yb-W.M., Rb-W.M. and Yb-Rb datasets respectively. This 1000 second timescale is suggestive of air-conditioner cycle noise, where they change cycle every 10 to 15 minutes, which could alter the pressure and temperature in the lab. The reduction in Allan deviation of the Yb-Rb pair compared to Yb-W.M. suggests the two atomic references share long timescale common mode noise which is suppressed when they are measured relative each other.

In summary, our POLEAS laser locking scheme offers laser stability on par with a commercial system that uses PS to lock a 780 nm laser to a spectral line in a Rubidium vapour cell. Stability of the referencing wavemeter is confirmed via simultaneous measurement of the ultra-stable 780 nm Rb reference confirming long-term stability down to sub- 10^{-10} fractional frequencies at $\tau = 1000$ s timescales.

Chapter 7

Conclusion

7.1 Achievements

This thesis presents the first demonstration of Raman sideband transitions in hyperfine trapped ions across Zeeman sub-levels. It also demonstrates motional spectroscopy and Raman sideband cooling using this method.

This thesis also presents all necessary hardware and measurement protocols implemented and refined over my candidature period to achieve fast and high fidelity single qubit operations using a $^{171}\text{Yb}^+$ trapped ion hyperfine qubit. The system was developed from one initially designed around trapping $^{174}\text{Yb}^+$ isotopes which lacked the infrastructure to perform single-shot readout and all necessary hyperfine qubit operations. A simple method of parameter estimation was developed for high-fidelity trapped ion qubit readout using a single saturation curve measurement. The simplicity of this method allows it to be scaled using CCDs and applied to large ion chains.

Also presented is the improvement in the spectroscopy of a HCL ytterbium sample via POLEAS. Comparisons of stability to the technique of PS were made using a wavemeter and an independent reference laser stabilized to the 780 nm spectroscopic signal of rubidium.

7.2 Outlook

The technique of addressing motional sidebands across Zeeman-split states will aid in the characterization of spin-heat quantum engines based off spin-motion coupling in near-degenerate spin-states. Future work will explore the viability of different atomic species for trapped ions and spin baths to optimize the performance of a spin-heat engine. It may also look at the application of EIT cooling for optical work extraction. This will likely involve greater theoretical support as well as a new system that will allow simultaneously an ion trap and a magneto-optical trap (MOT).

The next natural progression in terms of the current trapped ion system is the co-trapping of two $^{171}\text{Yb}^+$ ions simultaneously. In the current GTRI trap, this will require better understanding of the electric fields and wave-tables used to generate the trapping potential in the z-axis of the trap. This would enable the study of two-qubit operations as well as the extension of the readout protocol to CCDs.

A statement of contribution to co-authored published papers included in the thesis.

This statement is relevant only for candidates submitting full copies of co-authored papers in chapters of their thesis.

This statement is to be included at the beginning of each relevant chapter – if the chapter includes more than one published paper, the statement and set of signatures should be included for each paper. For assistance in establishing whether a statement is required, please see the published papers requirements diagram (PDF 73k).

state of contribution word doc

Appendix A

Other publications

Copies of authored publications during candidature related to the thesis topic are attached below.

- Multichannel optomechanical switch and locking system for wavemeters.
Published to Applied Optics in June 2020.
- Ion-Photonic Frequency Qubit Correlations for Quantum Networks. Published to Journal of Physics B: Atomic, Molecular and Optical Physics October 2021
- Ultrafast coherent excitation of an Ytterbium ion with single laser pulses.
Published to Applied Physics Letters in November 2021
- Dynamic compensation of stray electric fields in an ion trap using machine learning and adaptive algorithm. Published to Scientific Reports May 2022



Multichannel optomechanical switch and locking system for wavemeters

MOJI GHADIMI,^{1,*} ELIZABETH M. BRIDGE,¹ JORDAN SCARABEL,¹ STEVEN CONNELL,¹ KENJI SHIMIZU,¹ ERIK STREED,^{1,2} AND MIRKO LOBINO^{1,3}

¹Centre for Quantum Dynamics, Griffith University, Nathan QLD 4111, Australia

²Institute for Glycomics, Griffith University, Southport QLD 4215, Australia

³Queensland Micro- and Nanotechnology Centre, Griffith University, Nathan QLD 4111, Australia

*Corresponding author: m.ghadimi@griffith.edu.au

Received 20 February 2020; revised 17 May 2020; accepted 18 May 2020; posted 19 May 2020 (Doc. ID 390881); published 5 June 2020

Here we present a cost-effective multichannel optomechanical switch and software proportional–integral–derivative (PID) controller system for locking multiple lasers to a single-channel commercial wavemeter. The switch is based on a rotating cylinder that selectively transmits one laser beam at a time to the wavemeter. The wavelength is read by the computer, and an error signal is output to the lasers to correct wavelength drifts every millisecond. We use this system to stabilize 740 nm (subsequently frequency doubled to 370 nm), 399 nm, and 935 nm lasers for trapping and cooling different isotopes of a Yb⁺ ion. We characterize the frequency stability of the three lasers by using a second, more precise, commercial wavemeter. We also characterize the absolute frequency stability of the 740 nm laser using the fluorescence drift rate of a trapped ¹⁷⁴Yb⁺ ion. For the 740 nm laser we demonstrate an Allan deviation σ_y of 3×10^{-10} (at 20 s integration time), equivalent to sub-200 kHz stability. © 2020 Optical Society of America

<https://doi.org/10.1364/AO.390881>

1. INTRODUCTION

Atomic physics covers a range of applications including quantum computing [1–4], quantum simulation [5,6], quantum frequency metrology [7], and tests of fundamental physics. The majority of these experiments rely heavily on laser systems, frequency stabilized to an atomic reference, for optical cooling [8], trapping, and manipulating the electronic state of the atoms or ions being used as the quantum system. Traditionally, the laser frequency would be locked to an atomic reference signal [9,10], or more recently, a stabilized optical reference cavity [11,12]. The difficulty with these locking systems is the limited availability of atomic lines at the desired frequencies or the drift associated with optical reference cavities [13]. Both approaches can only operate over a narrow design wavelength range. A relatively new alternative is to use wavemeters based on Fizeau interferometers [14–18]. These state-of-the-art wavemeters can achieve submegahertz (MHz) level precision, making them suitable for stabilizing the majority of laser systems in atomic physics experiments. They have the advantage that they are broadband, enabling the laser to be stabilized to any desired wavelength in their operating range (e.g., 400 to 1100 nm for the HighFinesse WSU series), and with an appropriate optical switch they can become multichannel, allowing the concurrent stabilization of multiple laser systems at different wavelengths [14].

Similar to the optical reference cavities, the wavemeter is not inherently stable and is subject to drift, but due to the broadband nature and multichannel capabilities they can be easily stabilized to a master laser system, stabilized to an absolute frequency reference, operating anywhere within its wavelength range. This effectively transfers the stability of the master laser system to any desired wavelength within the operating range of the wavemeter. This is similar to the case of stabilizing a mode-locked laser using frequency-domain stabilization, in that the base frequency reference can be in the microwave or RF regime [19,20].

An optical switch is required to allow the concurrent stabilization of multiple laser systems with one wavemeter. Commercial optical switches along with locking software are available to perform this task, but they are costly, limiting their availability to many laboratories.

Here we present a low-cost optomechanical four-channel switch and four-channel locking software that is used with a commercial HighFinesse WSU-30 wavemeter to simultaneously lock multiple laser wavelengths. Unlike the commercial switch that can only be used with the expensive, top-of-the-range wavemeters, this system can work with any wavemeter that provides an accessible electrical or digital signal. It has no bandwidth limitation and perfect extinction. Theoretically, it

can have near 100% transmission; however, in our setup the transmission is 25% (see Section 2.A).

The design can readily be changed to accommodate more than four lasers by adding more openings to the cylinder and additional optics for overlapping the beams.

We use lasers at wavelengths of 399 nm, 740 nm (frequency doubled to 370 nm), and 935 nm for photo-ionizing, cooling, and trapping of $^{174}\text{Yb}^+$ or $^{171}\text{Yb}^+$ ions for quantum physics experiments. We characterize the frequency stability of the three locked laser systems using a second, higher-resolution HighFinesse wavemeter. We also measure the absolute frequency fluctuations of the 740 nm laser using the fluorescence fluctuations of a $^{174}\text{Yb}^+$ ion as an absolute atomic reference.

The mechanical switch does the job of alternating between the lasers with a duration of a few milliseconds (dependent on the rotation speed). Since the lasers are mechanically blocked, when one laser is on, the others are perfectly extinguished. The four-channel software interprets the different readings from the wavemeter and compares them with the desired frequency of each laser and uses digital-to-analog converter (DAC) devices to apply the necessary voltage to correct the frequency of that particular laser. The large difference between the wavelengths allows us to perform the separation of signals in software without the need for additional synchronization information. All the material required to replicate the system, including a 3D design of the cylinder and the LabVIEW software, is available for download at <https://github.com/Moji131/Wavemeter-Switch-PID-Labview>.

2. EXPERIMENTAL SETUP

A schematic of our experimental setup is shown in Fig. 1. We use three lasers for trapping and cooling of a single $^{174}\text{Yb}^+$ ion. Initially, a MOGLabs 399 nm diode laser is used for isotopically selective excitation of a neutral ^{174}Yb atom from its ground state to the $^2P_{1/2}$ state. From this state, we use 370 nm laser light to ionize the atom (see Ref. [21] for energy level details). We use a M Squared SolsTiS Ti-sapphire laser with wavelength of 740 nm and a ECD-X second-harmonic generation (SHG) box to generate this 370 nm light. The same laser is then used for Doppler cooling of the ion. The cooling transition of the ion is nearly closed; however, with a probability of 0.5% per cycle, the ion may decay into the long-lived $^2D_{3/2}$ state. To prevent an interruption of the cooling process, we use a MOGLabs 935 nm diode laser to return the ion to the $^2S_{1/2}$ state via the $^3D[3/2]_{1/2}$ state [21].

We use a HighFinesse WSU-30 wavemeter, and our software-locking system to lock the wavelengths of the 740, 935, and 399 nm lasers. When trapping the $^{174}\text{Yb}^+$ ion, the wavemeter is recalibrated to a Thorlabs HRS015 stabilized He–Ne laser ($\Delta\nu \approx 2$ MHz) every 10 s. In order to lock the lasers, a small portion of the power of each laser is coupled into single-mode optical fibers. These single-mode fibers take the light to a small breadboard that contains the mechanical switch and the optics shown in Fig. 2 to overlap the beams such that they are all coupled into a single single-mode 830 nm optical fiber. This fiber delivers the light to the wavemeter as shown in Fig. 1. The mechanical switch ensures that only one laser is delivered to the wavemeter at a time; the full details of the switch are discussed in

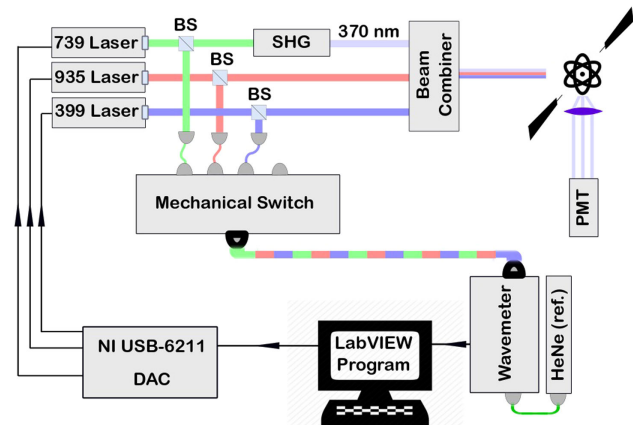


Fig. 1. Schematic of the experiment for trapping and cooling a $^{174}\text{Yb}^+$ or $^{171}\text{Yb}^+$ ion (BS, beam splitter; SHG, second-harmonic generation; PMT, photomultiplier tube). Three beam splitters couple a fraction of the laser light into three single-mode optical fibers that go to the mechanical switch (see Fig. 2 for details of the switch), which delivers the beams one at a time into an 830 nm single-mode fiber that goes to the wavemeter. A LabVIEW program is used to read the wavemeter output and “lock” the laser wavelengths. To mitigate long-term drift of the wavemeter, it is automatically recalibrated to a reference He–Ne laser every 10 s.

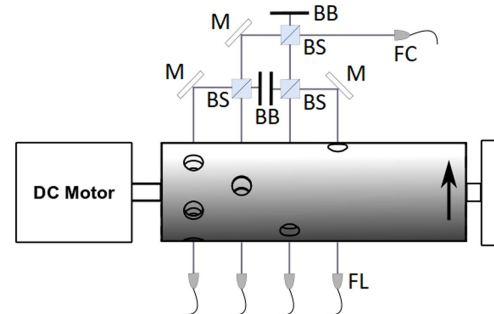


Fig. 2. Schematic of the mechanical switch and optical layout (M, mirror; BS, beam splitter; BB, beam block; FL, fiber launcher; FC, fiber coupler). The lasers are delivered using single-mode optical fibers specific to each laser. Rotation of the cylinder allows one laser to pass at a time. Lasers are overlapped using three broadband 50:50 beam splitter cubes and are coupled into a Thorlabs P1-830A-FC-2 fiber, which is single mode for 830 to 980 nm and few mode for shorter wavelengths. This fiber delivers the alternating beams to the wavemeter.

Section 2.A. The output of the wavemeter is read by a LabVIEW program that uses four separate software PID controllers to generate feedback signals, via a DAC, that go to the control electronics of the lasers. Details of the program are discussed in Section 2.B. We were able to trap and cool either a $^{174}\text{Yb}^+$ or a $^{171}\text{Yb}^+$ ion using this wavemeter, switch, and locking system, and the stability of the lasers is discussed in Section 3.

A. Mechanical Switch

The main design considerations for the mechanical switch were that it needed to switch between multiple laser beams, letting

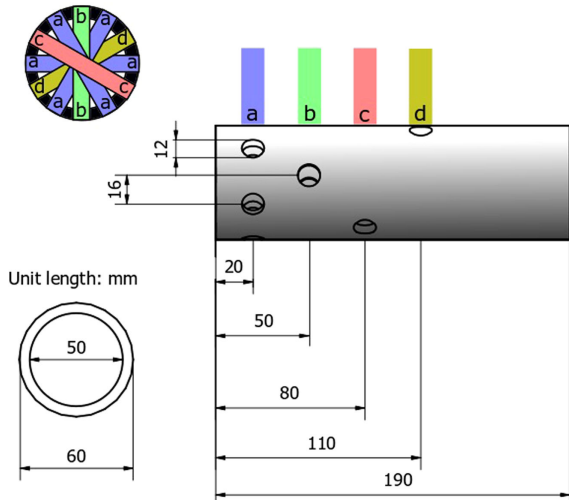


Fig. 3. Design of the cylinder used for the switching. Three pairs of holes on the left-hand end of the cylinder allow the primary laser to pass six times a turn, whereas the other three lasers are allowed to pass twice per turn. The top left image illustrates the duty cycle attributed to each laser: “a” sections represent the primary laser with three pairs of holes, and “b,” “c,” and “d” represent the secondary lasers with one pair of holes each. The black sections indicate where no lasers are passing.

only one beam through at a time; that it be easy to build; and that it provide a cost-effective alternative to commercially available fiber switches. The main body of the switch is a rotating Delrin cylinder that has apertures positioned to allow four laser beams through, one at a time. The schematic of the cylinder is shown in Fig. 3. The main cylinder is 60 mm in diameter and 190 mm in length. Six pairs of 12 mm diameter holes run radially through the cylinder, positioned around its circumference with an azimuthal distance of 16 mm between hole centers. Three of these pairs of holes are used for the primary laser input (“a” channels in Fig. 3); the remaining three pairs are spaced along the length of the cylinder and are used for three other laser inputs. In our experiments, the cooling laser has higher stability requirements than the other two lasers, so we chose to have multiple sets of holes for the primary input beam in order to allocate a higher proportion of the wavemeter read and feedback time to this laser system.

A 24 V Unite MY6812 Brush DC Motor is used to rotate the cylinder. By applying 15 V to this motor, we reach the speed of one revolution per 30 ms (2000 RPM). At this speed, the “on” time for each pair of holes is approximately 2 ms, with a duty cycle of 37.5% for the primary beam and 12.5% for each of the other three beams. The dark time between two “on” times is 0.66 ms. During each half-turn, the primary input beam will be delivered to the wavemeter 3 times, and the others three beams are each delivered once.

Four single-mode fibers are used to deliver the laser beams to the mechanical switch. In our setup, we used Thorlabs P1-630A-FC-2 single-mode fiber for the 740 nm laser, Thorlabs PM-S350-HP fiber for the 399 nm laser, and Thorlabs SM800-5.6-125 fiber for the 935 nm laser. After the cylinder, three broadband 50:50 beam-splitter cubes (Thorlabs BS010, $\lambda = 400 - 700$ nm) are used to overlap the beams, which are

then coupled into a Thorlabs P1-830A-FC-2 fiber and delivered to the wavemeter. This last fiber is single mode for 830 to 980 nm and few mode for shorter wavelengths. Approximately 75% of the power of each input beam is lost due to combining the beams using the 50:50 beam splitters. A more efficient but less versatile approach would be to use carefully chosen dichroic mirrors to overlap the beams. A schematic of the switching system is shown in Fig. 2.

B. Locking Software

In order to lock the lasers to the desired frequency, we developed a LabVIEW program to interpret the wavemeter output and feedback to each of the laser controllers. The input to this program is the wavemeter output, which will either be the frequency of the incident laser or no reading if there is no incident laser at that time. On the LabVIEW front panel, the user can specify a set frequency for the laser to lock to and an active frequency window for each of the four channels. If the reading from the wavemeter is within the active window of one of the channels, it will be treated as an input for that channel, compared to the set point, and passed through the PID servo for that channel. The PID output value is passed to one of the National Instruments USB-6211 DACs, which generates the control voltage to feed back to the laser controller. For all the lasers, cavity length is used as the tuning mechanism.

When the wavemeter reading is outside the range of a particular channel, the channel remains temporarily inactive and the output voltage retains its current value until a new reading in that active window is available. The user must ensure that the active frequency windows do not overlap and that each initial laser frequency is inside the active locking window to enable the servo to start the locking process. Future improvements would include ordering to allow for multiplexing nearby wavelengths so long as they were not on neighboring channels.

On the LabVIEW front panel, each channel has a graph to display the deviation of the laser frequency in MHz from its set point; this assists the user in identifying if the laser is suitably locked and if the PID parameters are set appropriately. We have added the option for assigning two preset lock frequencies for all channels and buttons to easily toggle between them. We use this option to easily switch between the laser frequencies required for trapping two different isotopes of Yb (usually $^{171}\text{Yb}^+$ and $^{174}\text{Yb}^+$).

3. RESULTS

A. Absolute Frequency Instability Measurements

To characterize the absolute instability of the frequency of the 740 nm laser, we monitored the fluctuations in the ion fluorescence rate during the steady-state cooling process. The ion fluorescence rate is dependent on the detuning of the laser frequency from the resonance of the cooling transition. For $^{174}\text{Yb}^+$, the natural full width at half-maximum (FWHM) of the profile is 20 MHz. In our experiment, the FWHM is approximately 40 MHz due to power broadening and the ion’s micro-motion as a result of stray electric fields in the trapping region. Figure 4 shows the graph of ion fluorescence count rate versus laser detuning from the ion resonance close to the

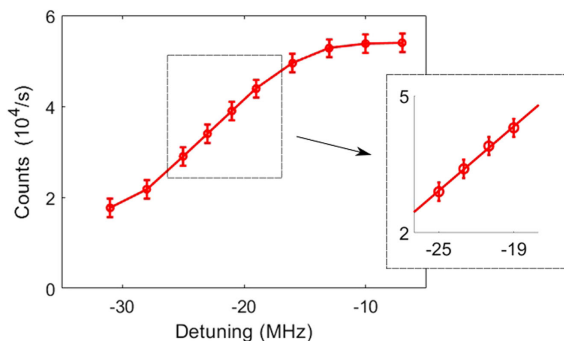


Fig. 4. Measured ion fluorescence counts versus detuning of a 370 nm laser from the resonance of the cooling transition of a $^{174}\text{Yb}^+$ ion. The curve is almost linear near -22 MHz detuning. Inset: a linear fit with MATLAB to the points near -22 MHz shows a slope of 2.3×10^3 counts/s/MHz with $1 - \sigma$ error of 20 counts/s/MHz. This slope is used to convert fluorescence counts to frequency deviation of the 370 nm laser, and the result is halved to infer the frequency deviations of the 740 nm laser.

half-maximum point of the curve; the line shape approximates a straight line, where the fluorescence rate is linearly proportional to the detuning. For the frequency instability measurements, the laser is locked to -22 MHz detuning. We use an AA Opto Electronic MQ180-A0,2-UV acousto-optic modulator to tune the detuning from -19 to -25 MHz to calibrate the linear correlation between ion count rate and laser frequency. The inset in Fig. 4 shows the linear fit. The linear fit has slope of 2.3×10^3 counts/s/MHz with $1 - \sigma$ error of ± 20 counts/s/MHz.

We lock the laser frequency to this half-maximum value (detuning = -22 MHz) so that changes in the ion fluorescence rate are linearly proportional to frequency deviations of the laser lock. We record the ion fluorescence for 500 s, convert this to frequency fluctuations, and calculate the Allan deviation [22]

$$\sigma_y(\tau) = \sqrt{\frac{1}{2(M-1)} \sum_{i=1}^{M-1} (\bar{y}_{i+1} - \bar{y}_i)^2}, \quad (1)$$

where $y_i = \frac{v_i - v}{v}$ is the i th of M fractional frequency values averaged over the measurement (sampling) interval τ . Here v_i is the i th frequency measurement (averaged over the sampling interval) and v is the nominal frequency.

The result of this measurement is shown in Fig. 5(a). We repeat the measurement with the mechanical switch disabled so that the laser is continuously measured by the wavemeter, and we show that in the same Fig. 5(a). We see the fractional frequency deviations are below 2×10^{-9} at all measurement times for both scenarios; this corresponds to frequency deviations of 800 kHz at the 740 nm locking wavelength, which will be equivalent to 1.6 MHz deviations after the frequency-doubling process to the ultraviolet. After 1 s of averaging time, both data sets show frequency deviations of < 200 kHz at the locking wavelength. The plots show there is very little difference between the scenario where the wavemeter is constantly measuring the frequency (switching disabled) and the one where it is measuring for 2 ms of every 5 ms (switching enabled). This suggests the switching is not adversely affecting the lock stability. It

is important to note that during all the instability measurements in this paper, recalibration to the reference He–Ne laser was kept off; this is to prevent the wavemeter from recalibrating during the measurement, which would show up as a frequency jump in the data. The wavemeter will experience some drift during the measurement time, but this is small due to the wavemeter being housed in a temperature-controlled environment.

B. Relative Frequency Instability Measurements

Due to the lack of available closed cycling transitions for the ion at 399 nm and 935 nm, we were not able to characterize the absolute frequency instability of these lasers. Instead we used a second wavemeter to characterize their frequency instability. This second wavemeter (Angstrom WS8-2 from HighFinesse GmbH, Germany) has a measurement resolution of 200 kHz and accuracy of 2 MHz. The locked laser to be measured is delivered to the WS8-2 via a single-mode optical fiber. The fiber was connected through the commercial HighFineess switch, but switching was disabled, and only this particular port was being measured. The automatic recalibration to the He–Ne laser was switched off during the measurements.

To test this measurement scheme, we started by making a measurement of the frequency instability of the locked 740 nm laser relative to the second wavemeter. The resulting Allan deviation is shown in Fig. 5(b). We see that the laser instability looks to follow the same trend as for the absolute fractional frequency instability measurement: it starts at $\sim 2 \times 10^{-9}$ and reduces to a minimum of a few 10^{-10} after 10 s. It also confirms that the instability does not differ significantly between having the switch enabled or disabled. This measurement is noisier than using the ion, and we attribute this to the relative drift of the two wavemeters, which are not recalibrated to the reference He–Ne laser during the measurement and so are drifting relative to each other. The fact that the plots in Figs. 5(a) and 5(b) are broadly similar means that this is an appropriate way to characterize the frequency instability of the 399 nm and 935 nm lasers.

The results for characterizing the frequency instability of the locked 399 nm and 935 nm lasers are shown in Figs. 5(c) and 5(d), respectively. We see that when the mechanical switch is disabled, and the wavemeter is continually measuring and feeding back to that laser, the fractional frequency instability follows the same trend as the 740 nm laser. At short measurement times the instability is ~ 2 to 3×10^{-9} , and after 10 s averaging time it reaches $\sim 2 \times 10^{-10}$. For both laser systems we see that enabling the mechanical switch, so that the wavemeter can lock multiple lasers, increases the instability of the locks. We observe that the 399 nm laser lock fluctuates around a fractional frequency instability of 2×10^{-9} , which corresponds to frequency deviations of ~ 1.5 MHz. The 935 nm laser fractional frequency instability stays below a maximum of 9×10^{-9} , which is equivalent to 3 MHz frequency deviations from the lock point. This stability is good enough for trapping Yb ions. An important observation is that the lock instability of the 399 nm and 935 nm lasers increases when the mechanical switch is enabled, but the stability of the 740 nm laser remains constant. The switch channel for the 740 nm laser beam has extra sets of holes, which means the wavelength of this laser is measured 3 times as often as the other lasers, and this appears to significantly help with the lock

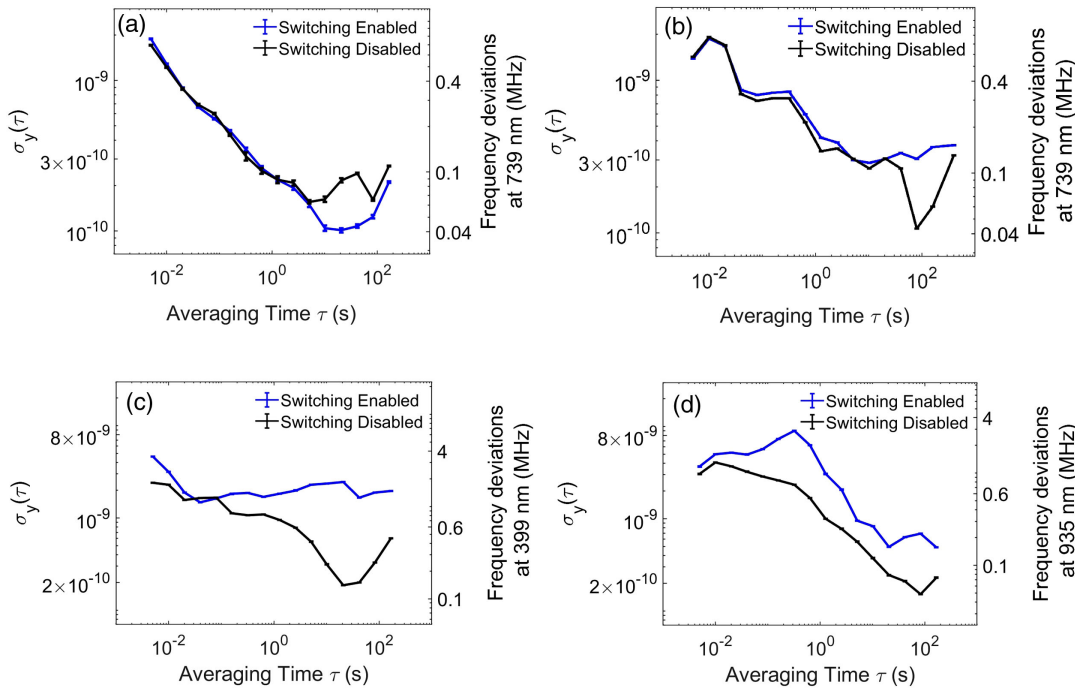


Fig. 5. Allan deviation measurements. (a) 740 nm laser: The frequency deviations are inferred from the fluctuations in the fluorescence count rate of the ion. Fractional frequency deviations remain below 2×10^{-9} at all measurement times. There is little difference between the results when the switch is enabled or disabled. (b) 740 nm laser: The frequency deviations are measured by a second wavemeter. The Allan deviation is broadly similar to that in (a) and shows little difference between the scenarios when the switch is enabled or disabled. (c) 399 nm laser: When the switch is enabled, the instability increases but remains good enough for our application. (d) 935 nm laser: Similar to (c), when the switch is enabled, the instability increases but remains good enough for our experiments. The main difference between the locking of these lasers and the 740 nm laser is that they are sampled only 2 times a cycle while the 740 nm laser is sampled 6 times a cycle.

performance for this particular laser. If we needed better stability from the other lasers, we could look at modifying the switch design to allow for more measurement time of these two lasers.

4. CONCLUSION

We have presented a multichannel optomechanical switch for use with a commercial wavemeter to allow multiple lasers to be locked to one wavemeter. We developed a LabVIEW program to read the multiple laser frequencies from the wavemeter and feed back to the corresponding laser. We successfully used the system to lock three lasers to trap and cool a single $^{174}\text{Yb}^+$ ion and a $^{171}\text{Yb}^+$ ion. We characterized the frequency instability of the locked cooling laser using the fluorescence of the ion and showed that it reaches a fractional frequency instability of a few 10^{-10} . The frequency instability of the other two lasers were characterized by a second wavemeter with higher frequency resolution, and the fractional instability remained below 9×10^{-9} for all measurement times.

During the tests, center frequency instability of the main cooling laser remained within 1 MHz, which is much smaller than the 20 MHz natural linewidth of the transitions. The instability of the two other lasers also remained within the acceptable range of a few MHz. This shows the suitability of using a Fizeau wavelength meter and our mechanical switch for locking the lasers required to trap and cool ions or atoms in atomic physics experiments. This system can replace complicated and more costly atomic spectroscopy or Fabry–Perot

cavity locking setups specific to each laser system. For absolute accuracy, the wavemeter needs to be regularly calibrated to a calibrated and stabilized laser, but this can be easily achieved with a commercial stabilized He–Ne laser, which we find to be a simple and cost-effective solution.

Funding. Griffith University; Australian Research Council (FT180100055, LP180100096M); Australian Government Research Training Program Scholarship.

Disclosures. The authors declare no conflicts of interest.

REFERENCES

1. M. Saffman, "Quantum computing with atomic qubits and Rydberg interactions: progress and challenges," *J. Phys. B* **49**, 202001 (2016).
2. H. Haffner, C. Roos, and R. Blatt, "Quantum computing with trapped ions," *Phys. Rep.* **469**, 155–203 (2008).
3. J. Benhelm, G. Kirchmair, C. F. Roos, and R. Blatt, "Towards fault-tolerant quantum computing with trapped ions," *Nat. Phys.* **4**, 463–466 (2008).
4. C. Monroe and J. Kim, "Scaling the ion trap quantum processor," *Science* **339**, 1164–1169 (2013).
5. B. P. Lanyon, C. Hempel, D. Nigg, M. Müller, R. Gerritsma, F. Zähringer, P. Schindler, J. T. Barreiro, M. Rambach, G. Kirchmair, M. Hennrich, P. Zoller, R. Blatt, and C. F. Roos, "Universal digital quantum simulation with trapped ions," *Science* **334**, 57–61 (2011).
6. M. Safronova, D. Budker, D. DeMille, D. F. J. Kimball, A. Derevianko, and C. W. Clark, "Laser cooling of trapped Yb^+ ," *Rev. Mod. Phys.* **90**, 025008 (2018).

7. A. D. Ludlow, M. M. Boyd, J. Ye, E. Peik, and P. Schmidt, "Optical atomic clocks," *Rev. Mod. Phys.* **87**, 637 (2015).
8. J. Metcalf and P. V. der Straten, *Laser Cooling and Trapping of Neutral Atoms* (Wiley, 2007).
9. D.-Q. Su, T.-F. Meng, Z.-H. Ji, J.-P. Yuan, Y.-T. Zhao, L.-T. Xiao, and S.-T. Jia, "Application of sub-Doppler DAVLL to laser frequency stabilization in atomic cesium," *Appl. Opt.* **53**, 7011–7016 (2014).
10. G. C. Bjorklund, M. D. Levenson, W. Lenth, and C. Ortiz, "Frequency modulation (FM) spectroscopy," *Appl. Phys. B* **32**, 145–152 (1983).
11. T. Kessler, C. Hagemann, C. Grebing, T. Legero, U. Sterr, F. Riehle, M. J. Martin, L. Chen, and J. Ye, "A sub-40-MHz-linewidth laser based on a silicon single-crystal optical cavity," *Nat. Photonics* **6**, 687 (2012).
12. A. A. Tonyushkin, A. D. Light, and M. D. D. Rosa, "Phase-locked scanning interferometer for frequency stabilization of multiple lasers," *Rev. Sci. Instrum.* **78**, 123103 (2007).
13. J. Alnis, A. Matveev, N. Kolachevsky, T. Udem, and T. W. Hänsch, "Subhertz linewidth diode lasers by stabilization to vibrationally and thermally compensated ultralow-expansion glass Fabry-Pérot cavities," *Phys. Rev. A* **77**, 053809 (2008).
14. L. Couturier, I. Nosske, F. Hu, C. Tan, C. Qiao, Y. H. Jiang, P. Chen, and M. Weidemuller, "Laser frequency stabilization using a commercial wavelength meter," *Rev. Sci. Instrum.* **89**, 043103 (2018).
15. K. Saleh, J. Millo, A. Didier, Y. Kersalé, and C. Lacroûte, "Frequency stability of a wavelength meter and applications to laser frequency stabilization," *Appl. Opt.* **54**, 9446–9449 (2015).
16. S. Saakyan, V. Sautenkov, E. Vilshanskaya, V. Vasilev, B. Zelener, and B. Zelener, "Frequency control of tunable lasers using a frequency-calibrated I-meter in an experiment on preparation of Rydberg atoms in a magneto-optical trap," *Quantum Electron.* **45**, 828–832 (2015).
17. G. P. Barwood, P. Gill, G. Huang, and H. A. Klein, "Automatic laser control for a 88Sr+ optical frequency standard," *Meas. Sci. Technol.* **23**, 055201 (2012).
18. S. Kobtsev, S. Kandrushin, and A. Potekhin, "Long-term frequency stabilization of a continuous-wave tunable laser with the help of a precision wavelengthmeter," *Appl. Opt.* **46**, 5840–5843 (2007).
19. H. R. Telle, G. Steinmeyer, A. E. Dunlop, J. Stenger, D. H. Sutter, and U. Keller, "Carrier-envelope offset phase control: a novel concept for absolute optical frequency measurement and ultrashort pulse generation," *Appl. Phys. B* **69**, 327–332 (1999).
20. D. J. Jones, S. A. Diddams, J. K. Ranka, A. Stentz, R. S. Windeler, J. L. Hall, and S. T. Cundiff, "Carrier-envelope phase control of femtosecond mode-locked lasers and direct optical frequency synthesis," *Science* **288**, 635–639 (2000).
21. H. A. Klein, A. S. Bell, G. P. Barwood, and P. Gill, "Laser cooling of trapped Yb+," *Appl. Phys. B* **50**, 13–17 (1990).
22. W. Riley and D. A. Howe, *Handbook of Frequency Stability Analysis* (NIST, 2008).

Ion–photonic frequency qubit correlations for quantum networks

Steven C Connell¹, Jordan Scarabel¹, Elizabeth M Bridge¹, Kenji Shimizu¹, Valdis Blūms¹, Mojtaba Ghadimi¹, Mirko Lobino^{1,2} and Erik W Streed^{1,3,*}

¹ Centre for Quantum Dynamics, Griffith University, Brisbane, QLD 4111, Australia

² Queensland Micro and Nanotechnology Centre, Griffith University, Brisbane, QLD 4111, Australia

³ Institute for Glycomics, Griffith University, Gold Coast, QLD 4222, Australia

E-mail: e.streed@griffith.edu.au

Received 6 September 2021, revised 19 September 2021

Accepted for publication 23 September 2021

Published 11 October 2021



Abstract

Efficiently scaling quantum networks to long ranges requires local processing nodes to perform basic computation and communication tasks. Trapped ions have demonstrated all the properties required for the construction of such a node, storing quantum information for up to 12 min, implementing deterministic high fidelity logic operations on one and two qubits, and ion–photon coupling. While most ions suitable for quantum computing emit photons in visible to near ultraviolet (UV) frequency ranges poorly suited to long-distance fibre optical based networking, recent experiments in frequency conversion provide a technological solution by shifting the photons to frequencies in the telecom band with lower attenuation for fused silica fibres. Encoding qubits in frequency rather than polarization makes them more robust against decoherence from thermal or mechanical noise due to the conservation of energy. To date, ion–photonic frequency qubit entanglement has not been directly shown. Here we demonstrate a frequency encoding ion–photon entanglement protocol in $^{171}\text{Yb}^+$ with correlations equivalent to 92.4(8)% fidelity using a purpose-built UV hyperfine spectrometer. The same robustness against decoherence precludes our passive optical setup from rotating photonic qubits to unconditionally demonstrate entanglement, however it is sufficient to allow us to benchmark the quality of ion–UV photon correlations prior to frequency conversion to the telecom band.

Keywords: quantum networking, trapped ion, quantum communication, frequency qubit

(Some figures may appear in colour only in the online journal)

1. Background

Quantum networks [1] are the key infrastructure for the long-range distribution of quantum information through the sharing of entanglement between distant locations. Such a network would enable a range of applications including quantum key distribution [2], distributed quantum computing [3], and blind

quantum computing [4]. The main challenge preventing the sharing of quantum information over long distances is transmission losses. For a quantum state, these losses cannot be compensated via amplification as in classical communication networks but their long-range effects can be mitigated using more complex protocols.

The quantum repeater architecture [5] is a communications protocol which achieves long-distance communication by dividing the communication channel into shorter, lower-loss segments connected by nodes capable of storing quantum information and performing entanglement swapping [6]. Satellite based quantum communication provides a contrasting

* Author to whom any correspondence should be addressed.

 Original content from this work may be used under the terms of the [Creative Commons Attribution 4.0 licence](#). Any further distribution of this work must maintain attribution to the author(s) and the title of the work, journal citation and DOI.

single segment architecture which has also been demonstrated over distances >1000 km [7, 8], however requires clear lines of sight.

Trapped ions have implemented all the key functionalities of a quantum network node including local quantum information processing [9–11], coupling of ion fluorescence into single mode fibres [12, 13], remote entanglement [14], and frequency conversion of single photons to the infrared telecom band [15–18]. At the local node trapped ions can store quantum states for >10 min [9], realise high fidelity one and two qubit gates [10], and achieve deterministic ion–ion entanglement [11]. High efficiency single ion fluorescence collection has been demonstrated in free space with bulk optics [12] while efficient single mode ion–fibre coupling has been demonstrated using a surface chip trap with integrated optics [13] as well as direct coupling into a fibre with a fibre based Fabry–Perot [19].

Optical frequency conversion in nonlinear crystals has been used to interface the fixed fluorescence frequencies from ion qubits in the visible and ultraviolet (UV) with photonic qubits in the infrared telecom spectral region [15–18] where fused silica fibres exhibit extremely low losses.

Independent of the choice of hardware used in the network node, photons are the best candidate to be the courier for the transmission of quantum information. It is likely that these photons will be transmitted through optical fibres similar to the ones currently used for conventional optical telecommunications. While polarization is the most common type of encoding basis used for experiments with photonic qubits, real-world optical fibre networks has shown that this degree of freedom is substantially more susceptible to decoherence from environmental noise sources including vibrations, temperature fluctuations, and stress birefringence. These all would require active stabilisation [20] for practical transmission over long distances, with a substantial increase in complexity and potential fundamental noised based limits on fidelity.

A more robust encoding basis for the photonic qubit is frequency. By mapping the qubit state directly on the energy of the photon, entanglement swapping can be performed on a nonpolarizing beam splitter [11] without the need for active stabilisation of the fibre polarisation [21] or the substantial losses in passive schemes [22].

However, manipulation of a photonic frequency qubit requires the use of active optical components, such as amplitude or phase modulators, instead of passive optical components including waveplates and polarizing beam splitters [23, 24]. Only recently has fully arbitrary control of frequency qubits been demonstrated [25].

Ion–ion entanglement mediated by frequency photonic qubit [11], and ion–photonic polarization qubit [26, 27] have been shown, but no direct measurement of ion–photonic frequency qubit correlations and entanglement has yet been measured. Characterizing the performance of the ion–frequency qubit state correlations and entanglement is essential for benchmarking a quantum network with arbitrary topology that uses this type of encoding and has applications in memory-assisted quantum communication [28].

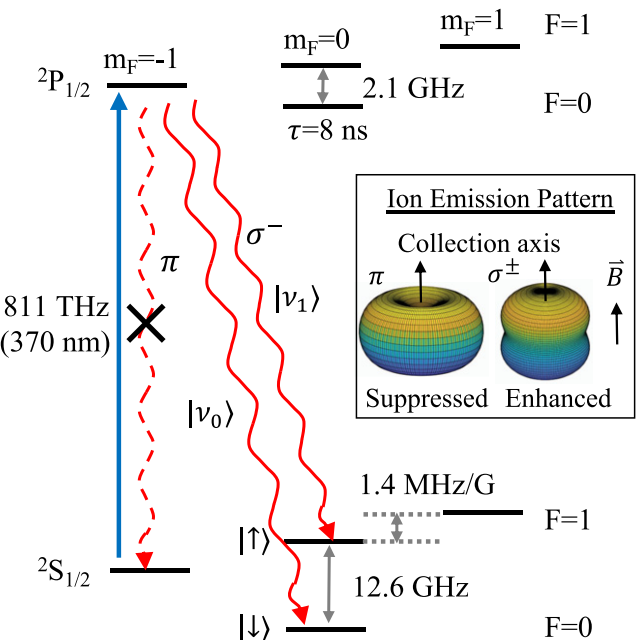


Figure 1. Relevant energy structure and transitions in $^{171}\text{Yb}^+$ which indicate the qubit states for the ion, the frequency qubit of the photon, and the optical pulse used to excite the ion (blue arrow). The decay paths are represented by the red arrows. In the experiments light from the π decay transition (crossed in the figure) is suppressed due to the collection geometry.

Here we implement a protocol for the generation of ion–photon frequency entanglement and measure the correlations between ground state hyperfine levels of a single $^{171}\text{Yb}^+$ ion and the energy state of the emitted UV photon. For this purpose, we built a UV spectrometer with a maximum theoretical resolution of 1.73 GHz (FWHM), capable of clearly resolving the 12.6 GHz separation of the photonic frequency states. While entanglement could not be verified in our set-up, since it cannot implement arbitrary single qubit gate operations on the frequency degree of freedom of the photon, we demonstrated ion–photon correlations with a fidelity of 92.4(8)%.

2. Ion–photon entanglement protocol

In a proposed architecture, trapped ion quantum networks [29] will link distant quantum nodes via optical fibres carrying photonic qubits. The first stage of entanglement swapping can be implemented using only photons and probabilistic Bell measurements. Subsequently, each quantum node, hosting a number of ions dependent on the topology of the network, will perform deterministic single qubit gates, entanglement swapping, and error correction. Telecom band photons can be interfaced with trapped ions using frequency conversion in nonlinear crystals [15–18].

For our experiments we use $^{171}\text{Yb}^+$ because of its long-lived hyperfine ground states, relatively simple electronic structure, and fast cycling transition for quick readout [30]. A simplified energy level structure for $^{171}\text{Yb}^+$ is shown in figure 1 with the ion qubit states $| \uparrow \rangle = ^2\text{S}_{1/2}, | F = 1, m_F = 0 \rangle$

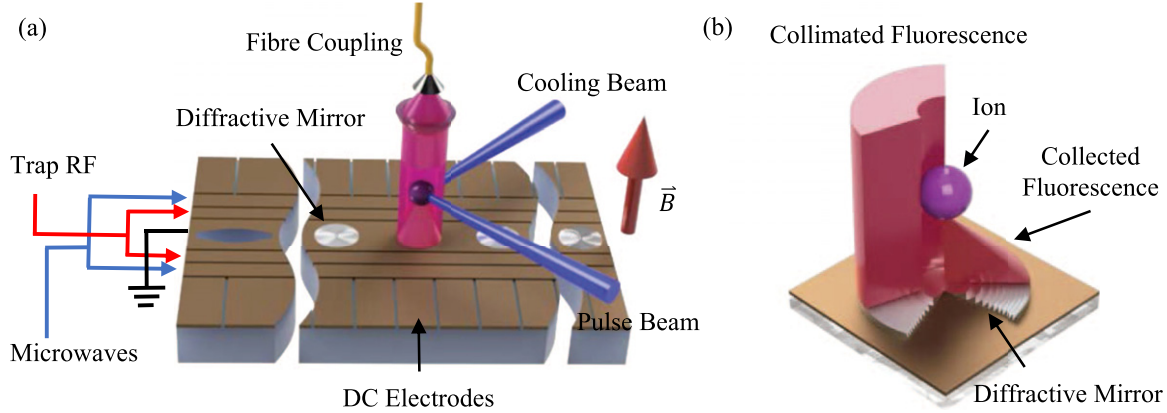


Figure 2. (a) Schematic of the trapping set-up. Cooling and pulsed excitation beams are perpendicular to each other. The DC electrodes allows shuttling of the ion along the trap. The magnetic field \vec{B} is perpendicular to the trap's surface and defines the ion's quantization axis. (b) Image of the diffractive mirror on the trap's surface. A cross section is shown for the collection of emitted ion light and for the resulting collimated light.

and $|\downarrow\rangle = ^2\text{S}_{1/2} |0, 0\rangle$, and the photonic qubit states, $|\nu_0\rangle$ and $|\nu_1\rangle$, which are separated by 12.6 GHz.

For the ion–photon entanglement protocol [31] we begin by optically pumping the $^{171}\text{Yb}^+$ ion into $^2\text{S}_{1/2} |0, 0\rangle$ and then transferring population into $^2\text{S}_{1/2} |1, -1\rangle$ with a microwave π -pulse at 12.6 GHz. The ion is then excited into the $^2\text{P}_{1/2} |1, -1\rangle$ state via a π transition driven by a short, linearly polarized, resonant laser pulse. From this state the ion can spontaneously decay via three different paths shown in figure 1. With the appropriate orientation of the quantization axis and fluorescence collection geometry, the spontaneously emitted photons from the π transition are not emitted in the collection direction and hence are geometrically suppressed.

After decay, the ion–photon system is in the state $(|\uparrow, \nu_1\rangle + e^{i\phi} |\downarrow, \nu_0\rangle)/\sqrt{2}$ where the state of the ion is entangled with the frequency of the photon. Measurements in the logic basis show the correlation between the states of the two sub-systems, but measurement in at least one other basis is necessary to unconditionally prove entanglement. While arbitrary rotations of the ion qubit with microwaves is straightforward to realise, this is much more difficult to achieve for photonic frequency qubits as it would require high-efficiency active microwave components to change the photon's energy. Our set-up currently is not capable of implementing single qubit rotations on frequency photonic qubit and thus can only be used to verify correlations.

3. Experimental setup

Individual $^{171}\text{Yb}^+$ ions are confined above a micro-fabricated surface trap [32] shown in figure 2(a). The trap design includes several integrated diffractive mirrors for collection of the ion fluorescence and coupling the light into a single mode optical fibre [13]. Ions are produced from a neutral Yb beam via isotope selective two-photon photoionization [33]. They are trapped at the electric field node generated 60 μm above the trap surface from two RF rails and shuttled along the trap by varying the voltages on 48 segmented DC electrodes (see

figure 2(a)). The DC electrodes are independently controlled and are used to shuttle the ion over the top of the different diffractive mirrors.

Figure 2(a) shows the geometry of the ion trap, together with the cooling beam, pulsed excitation beam, magnetic field used to define the quantization axis, and the photon collection path. Doppler cooling is performed by having the cooling laser light nearly resonant with the $^2\text{S}_{1/2} F = 1 \leftrightarrow ^2\text{P}_{1/2} F = 0$ transition with a 14.7 GHz repumping sideband generated by an EOM (Qubig: PM-Yb+_14.7) to clear off resonant scattering into $^2\text{S}_{1/2} F = 0$, the light has a linear polarization roughly 54.7° from the quantization axis to prevent unwanted coherent population trapping during cooling [34]. Omitted for clarity is a 935 nm repumping laser co-linear with the cooling beam to clear the meta-stable $^2\text{D}_{3/2}$ states and the 399 nm photoionization laser.

The diffractive mirrors etched into the central ground rail have dimensions of $80 \mu\text{m} \times 127 \mu\text{m}$, covering 13.3% of the total fluorescence solid angle. The mirror used for our experiment has a focal length of 60 μm (corresponding to an average NA of 0.68), generating a collimated beam from the ion's fluorescence (see figure 2(b)). The fluorescence passes through $\lambda/4$ and $\lambda/2$ waveplates angled so the σ^- photonic qubits are transmitted through a polarizing beamsplitter. During cooling and state readout fluorescence from σ^+ transition decays on $^2\text{P}_{1/2} |F = 0, m_F = 0\rangle \rightarrow ^2\text{S}_{1/2} |F = 1, m_F = -1\rangle$ is reflected by this beamsplitter and is directed onto an avalanche photodiode (APD) (laser components: COUNT-100B) for detection. The transmitted photonic qubit fluorescence is coupled into a single mode polarization maintaining fibre (Thorlabs: PM-S350-HP) via a mode-matching telescope reaching an overall ion to fibre coupling efficiency of 2.7(3)%.

From the fibre, the photon frequency is then measured using the UV hyperfine spectrometer (figure 3). After the fibre an $f = 4.02 \text{ mm}$ aspheric lens (Thorlabs: C671TME) collimates the beam and sends it to an expanding telescope made of a second $f = 4.02 \text{ mm}$ asphere and a 75 mm diameter, $f = 500 \text{ mm}$ plano-convex lens (Thorlabs: LA4246-UV). After

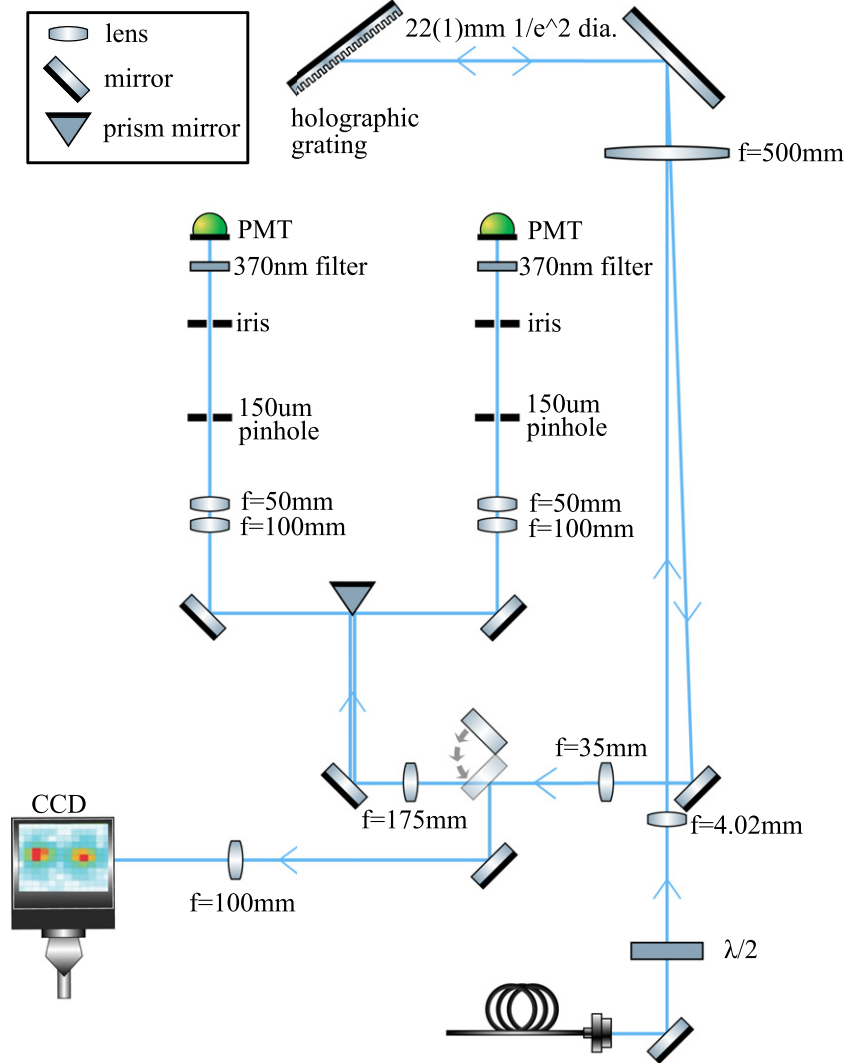


Figure 3. Diffraction grating spectrometer set-up. Ion light is inserted in the bottom of the image and is collimated with an asphere. Light is expanded with a telescope and hits the holographic grating in Littrow configuration where it is reflected on a slightly different trajectory. This light is picked off for detection, either to a CCD or to a mirrored prism which separates the two frequencies of light to be incident on two PMTs.

these optics, light is sent to the key component of this apparatus, a 128 mm × 102 mm Richardson holographic grating with 4320 lines/mm. The grating is operated in a near Littrow configuration at an angle of 59°. The reflected beam is slightly offset from the input path so it can be picked off using a D shaped mirror and sent along the detection path. A flip mirror is used to send the ion light to either a camera set-up, for beam profiling and diagnostics, or a mirrored knife edge type prism (Thor-Labs: MRAK25-F01) to separate the two qubit frequencies for detection. After the mirrored prism, the two frequency beams are focused through 150 μm pinholes and detected on photomultiplier tubes (PMT) (Hamamatsu: H10682-210) which are otherwise protected from background light by 370 nm line filters (Semrock Brightline: FF01-370/10-25). Pulses from both detectors are counted using a time to digital converter (ID Quantique: id800-TDC).

For the experiment we adjusted the position of the first 4.02 mm asphere so that a 22(1) mm diameter beam reaches the

500 mm lens. This third lens is then moved in order to produce a collimated beam that is then reflected by the grating. This configuration has a resolving power of around $\mathcal{R} = \Delta\nu/\nu \sim 95\,000$, with roughly that many lines of the grating illuminated.

We characterised the spectrometer by measuring its losses and the spot separation between two laser frequencies corresponding to $|\nu_1\rangle$ and $|\nu_0\rangle$, centred around 369.5 nm (811.3 THz), and separated by 12.6 GHz. Figure 4 shows the two spots measured by an EMCCD camera (Andor: Luca-S 658M), the spot $1/e^2$ diameters, 47.4(4) μm and 46.6(4) μm, and a spot separation of 3.5(2) radii. Theoretically, the field-mode overlap of these two Gaussian beams is <0.34% corresponding to a maximum estimated fidelity of >99.66%, but sending attenuated laser light to the two PMTs, we measured a detection fidelity of 98.0(6)% for $|\nu_0\rangle$ and 97.2(4)% for $|\nu_1\rangle$. The spectrometer system's overall quantum efficiency, from fibre to detector, is 3.7(5)%. This number accounts for 79(2)% coupling efficiency into a single mode optical fibre, 25(3)%

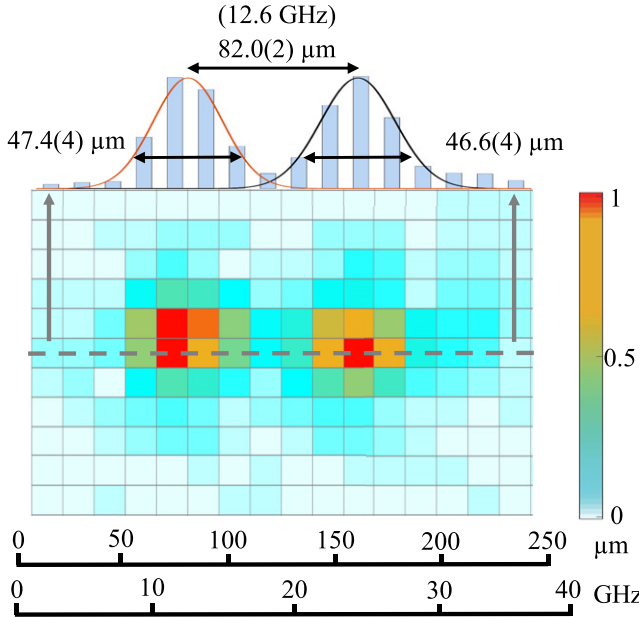


Figure 4. Spectrometer spot separation of laser photons with 12.6 GHz frequency difference. The spots are 47.4(4) μm and 46.6(4) μm $1/e^2$ diameter with a separation of 82.0(2) μm , corresponding to 3.5(2) $1/e^2$ radii and a resolution of 3.6(2) GHz. The image was taken with a 1 s exposure.

grating efficiency and losses in the set-up optics, and 19% PMT quantum efficiency.

4. Results

For our experiment we followed the protocol described in section 2 and reference [11]. Initially the ion is prepared in state $|\downarrow\rangle$ via optical pumping for 10 μs by the cooling laser, modulated by a 2.1 GHz EOM (Qubig: PM-Yb+_2.1), resonant with the $^2\text{S}_{1/2} |1, -1 0 + 1\rangle \leftrightarrow ^2\text{P}_{1/2} |0, 0\rangle$ and $^2\text{P}_{1/2} |1, -1 0 + 1\rangle$ transitions. Subsequently a 17 μs microwave π -pulse at 12.637 855 GHz transfers the population from $|\downarrow\rangle$ to $^2\text{S}_{1/2} |1, -1\rangle$ with 91(4)% fidelity. The lower than ideal fidelity is due to magnetic field drift of ~ 7 mG resulting in a 9(2) kHz detuning of the microwave from resonance.

The ion is then optically excited from $^2\text{S}_{1/2} |1, -1\rangle$ to $^2\text{P}_{1/2} |1, -1\rangle$ by a linearly polarized pulse (see figures 1 and 2(a)). The pulse is created from a CW laser by an AOM (AAoptics MQ180-A0,2-UV) which generates a 51 ns optical pulse. From the state $^2\text{P}_{1/2} |1, -1\rangle$, the ion decays to the ground state with a spontaneous lifetime of 8.1 ns and emits a single photon at 369.5 nm. Using a Lindbladian describing the system in figure 1 we find the probability the ion excites and decays into $|\uparrow, \nu_1\rangle$ or $|\downarrow, \nu_0\rangle$ after a pulse is estimated as 11.6(4)% for either state.

The ion fluorescence is collimated by the diffractive mirror on the chip trap surface, covering a solid angle of 14.3% on the σ transition, and collected in a direction parallel to the magnetic field axis (see figures 2(a) and (b)). This configuration minimizes the light collected from the π decay channel into

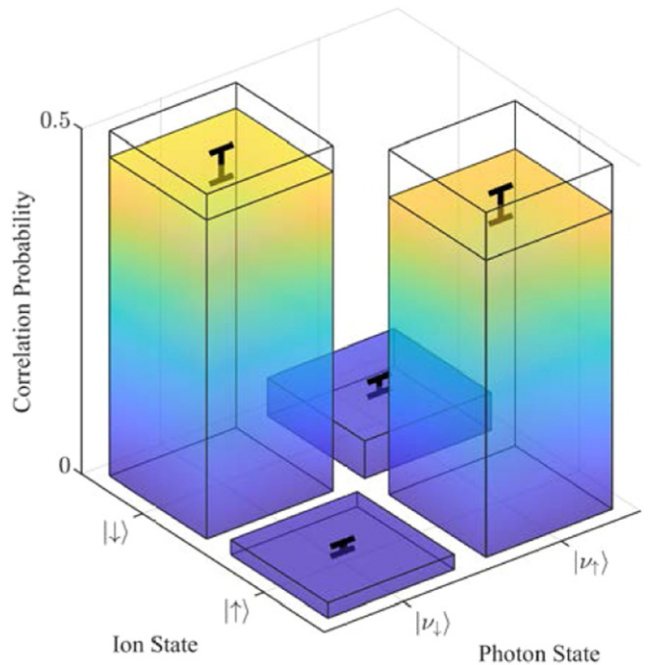


Figure 5. Ion photon correlations. Wire frames indicate ideal outcome. For a $|\nu_0\rangle$ photon we get 95.2(7)% and for a $|\nu_1\rangle$ photon we get 89.6(10)% fidelity. Data corresponds to 2006 counts out of 14 883 327 experimental runs.

$^2\text{S}_{1/2} |1, -1\rangle$, which is also partially filtered out by a polarizer, and optimizes the collection of light from the σ^- decay into $|\uparrow\rangle$ and $|\downarrow\rangle$. As a result of this decay an entangled state is generated between the ion and the photon. The emitted circularly polarized single photons are rotated to linear polarization with a quarter wave plate, sent through a polarizing beam splitter cube to spatially separate them from photons with a different polarization, and coupled into a single mode fibre. The fibre is connected to the UV hyperfine spectrometer and the photon frequency states, $|\nu_1\rangle$ and $|\nu_0\rangle$, are spatially separated to be read out on separate PMTs (see figure 3) with a 200 ns time gate.

The ion state is read out by shining the cooling laser without any sidebands from the EOMs, for 1.38 ms and measuring the arrival times of fluorescence counts on a third ‘readout’ APD. Using the state selective detection method outlined in [35], the trapped ion qubit state was determined with an approximate readout fidelity of 95.5% for $|\uparrow\rangle$ and 97.3% for $|\downarrow\rangle$. Fidelity in all cases is defined as the inner product overlap between the expected and actual states in an orthogonal basis as per the density matrix based approach of [11].

We ran this protocol over 5 h and 50 min in 10 min blocks with each run taking 1411 μs . From these runs we detected a total of 2006 signal photons on the spectrometer. For each successful click from the signal photons, the ion qubit state was also recorded and the ion–photon qubit correlation fidelity is calculated. The coincidence detection probability per shot for our system is 0.013(3)%, measured over 14 883 327 runs. This probability comes from a 91(4)% state preparation fidelity, the 11.6(4)% probability of generating a photon from the excitation pulse, a 2.7(3)% probability of collecting the photon into

the fibre and the 3.7(5)% efficiency of the spectrometer set-up. Combined, the expected coincidence detection probability per shot is in agreement at 0.011(2)%.

The correlations between the states of the ion and the signal photon are shown in figure 5. For the $|\downarrow, \nu_0\rangle$ state fidelity is 95.2(7)% and $|\uparrow, \nu_1\rangle$ state fidelity is 89.6(10)% while the average fidelity of the correlation matrix is 92.4(8)%. The asymmetry in fidelity is mainly due to higher rate of incorrect photon readout of the $|\nu_1\rangle$ photon. The main sources of infidelity are trapped ion qubit hyperfine state readout at approximately 3.6%, and spot separation in the diffraction grating spectrometer at 2.4(5)% (see figure 4).

5. Conclusions

We demonstrate ion–photonic frequency qubit correlations with a 92.4(8)% average fidelity. Measurements were performed with a high-resolution spectrometer for characterizing frequency encoded photonic qubits. This is an important result for the development of an ion-based quantum network which use more robust frequency encoding. The next step would be to demonstrate quantum frequency conversion of our photonic qubit and show that correlations are preserved after frequency conversion. These are key first steps towards developing quantum repeater architecture for photonic qubits in a fibre optic network. For comparison ion–photonic polarisation qubit correlations have been demonstrated at 90.1% from a fibre integrated Fabry–Perot [19] and could reasonably approach that from more experimentally mature systems such as the 98.2% fidelity observed with a fibre-coupled HALO lens [15].

Several improvements could be made to the current system for improving its efficiency and fidelity. State preparation and optical pulse fidelity can be improved to near unity by shaping our microwave pulse (by using a BB1 protocol [32] for example) and using an EOM for switching the optical pulse duration to below the excited lifetime of 8.1 ns. Readout could be improved towards the 99.93% fidelity for $^{171}\text{Yb}^+$ observed in 11 μs demonstrated by [30] with improved detector performance. Once we have our single photon generation protocol optimized, we can send ion fluorescence directly to the grating, negating the fibre coupling and attenuation losses. The grating performance can be improved with larger optics which will allow us to get a diffraction limited spot without loss of efficiency, so the grating efficiency will be the ideal diffraction efficiency of 55% with correct polarization and the fidelity will be <99.9%. By making these changes we expect to achieve a fidelity of 99.1% and achieve a bit rate of 34 Hz for successful trials without considering detector quantum efficiency.

Acknowledgments

This research was financially supported by the Griffith University Research Infrastructure Program, the Griffith Sciences equipment scheme, Australian Research Council Linkage Project (LP180100096). ML was supported by Australian Research Council Future Fellowships (FT180100055), VB,

JS, KS, and SC were supported by the Australian Government Research Training Program Scholarship.

Data availability statement

The data that support the findings of this study are available upon reasonable request from the authors.

ORCID iDs

Mirko Lobino  <https://orcid.org/0000-0001-8091-8951>
Erik W Streed  <https://orcid.org/0000-0001-6234-4560>

References

- [1] Kimble H J 2008 *Nature* **453** 1023–30
- [2] Bunandar D *et al* 2018 *Phys. Rev. X* **8** 021009
- [3] Cuomo D, Caleffi M and Cacciapuoti A S 2020 *IET Quantum Commun.* **1** 3–8
- [4] Fitzsimons J F 2017 *npj Quantum Inf.* **3** 23
- [5] Sangouard N, Simon C, de Riedmatten H and Gisin N 2011 *Rev. Mod. Phys.* **83** 33–80
- [6] Yuan Z-S, Chen Y-A, Zhao B, Chen S, Schmiedmayer J and Pan J-W 2008 *Nature* **454** 1098–101
- [7] Yin J *et al* 2020 *Nature* **582** 501–5
- [8] Yin J *et al* 2017 *Science* **356** 1140–4
- [9] Wang Y, Um M, Zhang J, An S, Lyu M, Zhang J-N, Duan L-M, Yum D and Kim K 2017 *Nat. Photon.* **11** 646–50
- [10] Ballance C, Harty T, Linke N, Sepiol M and Lucas D 2016 *Phys. Rev. Lett.* **117** 060504
- [11] Moehring D L, Maunz P, Olmschenk S, Younge K C, Matsukevich D N, Duan L-M and Monroe C 2007 *Nature* **449** 68–71
- [12] Maiwald R, Golla A, Fischer M, Bader M, Heugel S, Chalopin B, Sondermann M and Leuchs G 2012 *Phys. Rev. A* **86** 043431
- [13] Ghadimi M *et al* 2017 *npj Quantum Inf.* **3** 4
- [14] Maunz P, Moehring D L, Olmschenk S, Younge K C, Matsukevich D N and Monroe C 2007 *Nat. Phys.* **3** 538–41
- [15] Bock M, Eich P, Kucera S, Kreis M, Lenhard A, Becher C and Eschner J 2018 *Nat. Commun.* **9** 1998
- [16] Kasture S, Lenzini F, Haylock B, Boes A, Mitchell A, Streed E W and Lobino M 2016 *J. Opt.* **18** 104007
- [17] Krutyanskiy V, Meraner M, Schupp J and Lanyon B P 2017 *Appl. Phys. B* **123** 228
- [18] Krutyanskiy V, Meraner M, Schupp J, Krcmarsky V, Hainzer H and Lanyon B P 2019 *npj Quantum Inf.* **5** 72
- [19] Kobel P, Breyer M and Köhl M 2021 *npj Quantum Inf.* **7** 6
- [20] Sun Q-C *et al* 2016 *Nat. Photon.* **10** 671–5
- [21] Xiang Z H, Huwer J, Stevenson R M, Skiba-Szymanska J, Ward M B, Farrer I, Ritchie D A and Shields A J 2019 *Sci. Rep.* **9** 4111
- [22] Wengerowsky S *et al* 2020 *npj Quantum Inf.* **6** 7
- [23] Lu H-H, Lukens J M, Williams B P, Imany P, Peters N A, Weiner A M and Lougovski P 2019 *npj Quantum Inf.* **5** 24
- [24] Clemmen S, Farsi A, Ramelow S and Gaeta A L 2016 *Phys. Rev. Lett.* **117** 223601
- [25] Lu H-H, Simmerman E M, Lougovski P, Weiner A M and Lukens J M 2020 *Phys. Rev. Lett.* **125** 120503
- [26] Blinov B B, Moehring D L, Duan L M and Monroe C 2004 *Nature* **428** 153–7
- [27] Crocker C, Lichtman M, Sosnova K, Carter A, Scarano S and Monroe C 2019 *Opt. Express* **27** 28143
- [28] Bhaskar M K *et al* 2020 *Nature* **580** 60–4

- [29] Sangouard N, Dubessy R and Simon C 2009 *Phys. Rev. A* **79** 042340
- [30] Crain S, Cahall C, Vrijen G, Wollman E E, Shaw M D, Verma V B, Nam S W and Kim J 2019 *Commun. Phys.* **2** 97
- [31] Moehring D L, Madsen M J, Younge K C, Kohn, Jr. R N, Maunz P, Duan L-M, Monroe C and Blinov B B 2007 *J. Opt. Soc. Am. B* **24** 300
- [32] Shappert C M et al 2013 *New J. Phys.* **15** 083053
- [33] Blüms V et al 2020 *Rev. Sci. Instrum.* **91** 123002
- [34] Ejtemaei S, Thomas R and Haljan P C 2010 *Phys. Rev. A* **82** 063419
- [35] Wölk S, Piltz C, Sriarunothai T and Wunderlich C 2015 *J. Phys. B: At. Mol. Opt. Phys.* **48** 075101

Ultrafast coherent excitation of an ytterbium ion with single laser pulses

Cite as: Appl. Phys. Lett. **119**, 214003 (2021); doi:10.1063/5.0073136

Submitted: 28 September 2021 · Accepted: 9 November 2021 ·

Published Online: 23 November 2021



View Online



Export Citation



CrossMark

Kenji Shimizu,¹ Jordan Scarabel,¹ Elizabeth Bridge,² Steven Connell,¹ Moji Chadimi,¹ Ben Haylock,¹ Mahmood Irtiza Hussain,^{3,4} Erik Streed,^{1,5} and Mirko Lobino^{1,6,a)}

AFFILIATIONS

¹Centre for Quantum Dynamics, Griffith University, Brisbane, Queensland 4111, Australia

²Australian Research Council Centre of Excellence for Engineered Quantum Systems, School of Mathematics and Physics, University of Queensland, St. Lucia, Queensland 4072, Australia

³Institute for Quantum Optics and Quantum Information (IQOQI), Austrian Academy of Sciences, Innsbruck 6020, Austria

⁴Institute for Experimental Physics, University of Innsbruck, Innsbruck 6020, Austria

⁵Institute for Glycomics, Griffith University, Gold Coast, Queensland 4222, Australia

⁶Queensland Micro and Nanotechnology Centre, Griffith University, Brisbane, Queensland 4111, Australia

^{a)}Author to whom correspondence should be addressed: m.lobino@griffith.edu.au

ABSTRACT

Experimental realizations of two qubit entangling gates with trapped ions typically rely on addressing spectroscopically resolved motional sidebands, limiting gate speed to the secular frequency. Fast entangling gates using ultrafast pulsed lasers overcome this speed limit. This approach is based on state-dependent photon recoil kicks from a sequence of counter-propagating, resonant, ultrafast pulse pairs, which can allow sub-microsecond gate speeds. Here, we demonstrate a key component of the ultrafast gate protocol, the coherent excitation of a $^{171}\text{Yb}^+$ ion across the $^2\text{S}_{1/2}$ - $^2\text{P}_{1/2}$ transition with a single near-resonant short optical pulse at 369.53 nm. We achieve a maximum population transfer of 94(1)% using a picosecond pulsed laser that can be tuned across the $^2\text{S}_{1/2}$ - $^2\text{P}_{1/2}$ transition and 42.5(9)% with 190(7) GHz detuning.

Published under an exclusive license by AIP Publishing. <https://doi.org/10.1063/5.0073136>

Trapped-ion qubits are a leading candidate for the realization of a full-scale quantum computer because of their long coherence time, deterministic gates and readout, and their potential for scalability.^{1,2} High fidelity two-qubit gates have been demonstrated on this platform^{3–5} with a speed on the order of few microseconds. This is because most two-qubit gates^{6,7} are performed in the Lamb-Dicke regime via the excitation of single motional sidebands, tying the gate duration to the period of the secular motion of the ions typically on the order of microseconds. These gate protocols^{6,7} require near ground state motional cooling and for some also individual laser addressability for each ion.⁶ Furthermore, the speed limit set by secular motion worsens for ion crystals since the frequency of the collective motional modes decreases with the number of ions and crosstalk between modes can reduce the gate fidelity.⁸

In 2003, García-Ripoll *et al.*⁹ proposed a scheme for a sub-microsecond two-qubit gate that does not require individual ion-laser addressability or ground state motional cooling. The scheme operates by driving the ions' optical transition with counter-propagating, resonant, ultrafast π -pulses that excite and then de-excite the ion. The

pulse pairs are polarized to deterministically result in either a momentum kick of $2 \ h \ k$ or no momentum kick, depending on the internal qubit state of the ion. The sequence of $2 \ h \ k$ kicks generates closed state-dependent trajectories of the ions through their phase-space, where they all go back to their initial motional and qubit states at the end of the protocol.¹⁰ Pairs of qubits undergo a phase shift from the state-dependent kicks (SDKs), only if they are both in a particular state, resulting in a two-qubit phase gate.^{10,11}

Other protocols have been used to realize single ion gates at a rate faster than the secular motion¹² and one-qubit spin-motion entanglement.¹³ One of these two-qubit gate protocols¹⁴ uses amplitude-shaped Raman pulses to drive the motion of the ions along trajectories in phase-space so that the gate operation becomes insensitive to the optical phase of the pulses. Although this approach achieved a gate time of $1.6 \ \mu\text{s}$ with a fidelity of 99.8%, it only works in the Lamb-Dicke regime. Another gate protocol¹⁵ demonstrated the generation of an entangled Bell state using a sequence of ten sets of eight pairs of counter-propagating Raman pulses to apply the SDKs. While this method does not require confinement of ions to within the

Lamb-Dicke regime, the entangled state fidelity of 76% was limited by the individual fidelity of each SDK, because of micro-motion and the fact that the eight pulse pairs generate only a good approximation of an ideal SDK.¹³

Implementation of the fast gate protocol^{9–11} using resonant pulses is at the stage where suitable ultrafast laser sources have been realized for calcium,¹⁶ ytterbium,¹⁷ and cadmium¹⁸ ions, and demonstration of coherent excitation of ⁴⁰Ca⁺ and ¹¹¹Cd⁺ ions has been reported.^{18,19} Coherent excitation of a single ¹⁷¹Yb⁺ ion with a pulsed laser was reported;²⁰ however, the pulse area was only 0.05π . Here, we show the coherent excitation of a ¹⁷¹Yb⁺ ion along the ²S_{1/2} → ²P_{1/2} transition using a single resonant π -pulse. Using picosecond pulses, which are much shorter than the 8.12(2) ns lifetime²¹ of the excited state, we achieve a population inversion of 94(1)% when the laser is near resonance and 42.5(9)% with 190(7) GHz detuning. We compared our results with the semi-classical two-level atom theory and found good agreement with our temporal and spectral laser parameters.

A single ¹⁷¹Yb⁺ ion is trapped and Doppler cooled in a quadrupole Paul trap formed by two tungsten needles driven by the radio frequency high voltage at 18.810 MHz [see Fig. 1(a)]. The ion is cooled by a CW laser, which is red-detuned by 10 MHz from the ²S_{1/2} F = 1 ↔ ²P_{1/2} F = 0 transition²² and repumped from the ²S_{1/2} F = 0 dark state with light from 14.7 GHz sidebands generated by a Qubig PM-Yb171+ + 14.7M2 electro-optic modulator (EOM). The ion's fluorescence is collected by a 0.64 numerical aperture (NA) binary phase Fresnel lens, located on top of the ion but inside a vacuum chamber, and measured with a photo-multiplier tube (PMT) mounted above the chamber. An additional 935 nm laser with 3.07 GHz sidebands generated by diode current modulation repumps the atom out of the metastable ²D_{3/2} state. Details of the trap geometry can be found in Ref. 23.

The laser used for coherent excitation of the ion is a home-built system¹⁷ that uses a telecom band femtosecond fiber laser as the master oscillator. The oscillator wavelength is centered at 1564 nm, and the repetition rate is frequency stabilized at 300.000000 MHz. Femtosecond pulses are used to generate supercontinuum in a highly nonlinear fiber, where a portion around 1108.6 nm is selected with three chirped fiber Bragg grating (CFBG) mirror stages and amplified. Second harmonic generation (SHG) in a periodically poled stoichiometric lithium tantalate (PPSLT) crystal produces radiation around 554 nm. Sum frequency generation between the SHG and 1108.6 nm beam in a LiB₃O₅ (LBO) crystal produces laser pulses around $\lambda = 369.52$ nm. A maximum average power of 100 mW in the UV is generated, which can be frequency tuned around the ²S_{1/2} ↔ ²P_{1/2} transition [Fig. 1(c)] by adjusting the temperatures of the CFBGs and the PPSLT crystal independently. The final pulse is near transform limited with a duration of ~ 1 ps.

During experiment, the UV pulse spectrum is monitored by a high resolution spectrometer²⁴ built around a custom Newport Richardson diffraction grating mirror with 4320 grooves/mm and dimensions of 128×102 mm² [see Fig. 1(b)]. The optically magnified pulsed laser illuminates the diffraction grating mirror in the Littrow configuration, where the laser is diffracted on a slightly different trajectory and then sent to a CCD camera. The spectrometer has a resolution of 3.6(2) GHz around 370 nm and was calibrated against the cooling laser. For the ion excitation, a collimated beam of 1.88 mm waist and a beam quality factor M² of 2.7 are focused down to a waist of 8.5 μ m with a lens of 50 mm focal. We relay that spot size on the ion with a 75 mm focal length relay lens setup [Fig. 1(a)].

Coherent excitation measurements are performed with a four step protocol of 289 μ s duration repeated every 426.66 μ s. First, the ion is Doppler cooled for 40 μ s and then optically pumped to the ²S_{1/2} F = 0 state for 20 μ s by applying 2.1 GHz sidebands to the

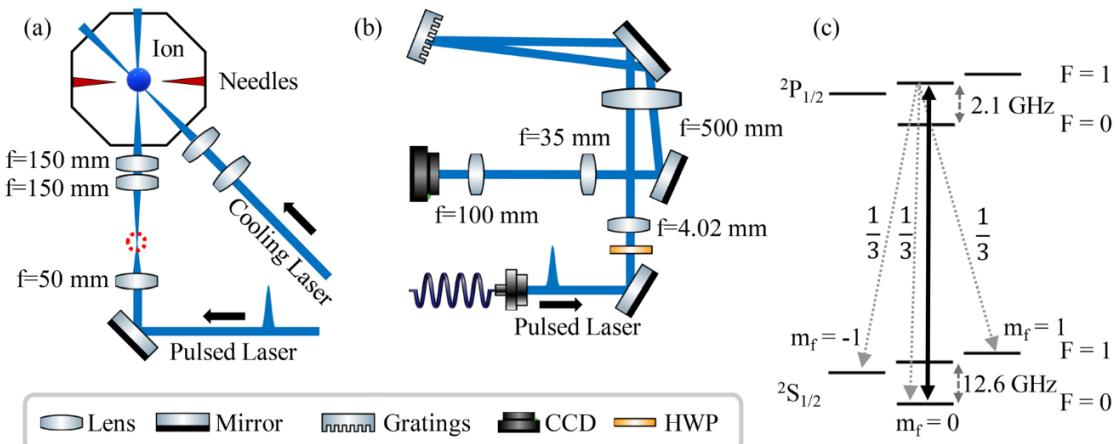


FIG. 1. (a) The pulsed laser and the cooling laser are focused onto an ion in a vacuum chamber using the illustrated optics. Due to geometric limitations, we use an f-2f lens configuration where a focused spot outside the chamber (indicated with a red dotted circle) can be replicated at the ion inside the chamber with a relay of two $f = 150$ mm lenses. (b) The pulsed laser was spectrally analyzed with a diffraction grating spectrometer setup. The light coming from a fiber is collimated with a $f = 4.02$ mm aspheric lens, expanded by a telescope with magnification $M = 124$, and sent to a holographic grating. The reflected pulses are slightly offset from the input path so they can be picked off using a D-shaped mirror and measured by a CCD camera. (c) The ²S_{1/2}–²P_{1/2} energy level diagram shows blue arrows illustrating the transition of the pulsed laser is resonant with. The pulsed laser has linear polarization parallel to an external magnetic field, so it can excite ions prepared in the ²S_{1/2} F = 0 state only to the ²P_{1/2} F = 1, $m_F = 0$ state via a π -transition. Dotted arrows show the spontaneous emission paths.

cooling beam generated by a QUBIG PM-Yb171+_.21G EOM. The ion is then excited with a single laser pulse and left to decay to the ground state for $2\ \mu\text{s}$ [Fig. 1(c)]. This is much longer than the 8.12(2) ns lifetime of the excited state.²¹ After excitation, the ion can decay into the states $^2\text{S}_{1/2}\ F = 1\ m_F = \pm 1$ and $^2\text{S}_{1/2}\ F = 0$ with a probability of 1/3 each. Read-out via state selective fluorescence²⁵ is performed with the Doppler beam for 227 μs .²⁷ If the ion was excited by the single pulse and had spontaneously decayed, the ion's atomic state will be in the $^2\text{S}_{1/2}\ F = 1$ manifold with a probability of 2/3 [Fig. 1(c)] and be bright during state readout. We measure the probability of single pulse excitation as a function of the pulse energy. For each value of the pulse energy, we repeat the protocol approximately 68 500 times to build up statistics for the probability of excitation into the $^2\text{P}_{1/2}$ state. The count statistics are fitted to two complementary weighted probability mass functions²⁶ that describe the bright and dark count distributions. The weight of the bright component is our estimate of the $^2\text{S}_{1/2}\ F = 1$ manifold population. The population measurement of the $^2\text{S}_{1/2}\ F = 1$ manifold is scaled by 3/2 to account for the $^2\text{P}_{1/2}\ F = 1$ branching ratio. The results are shown in Fig. 2, including the measurements performed with a laser detuning of 190(7) GHz. The maximum population transfer is 94(1)% for the on-resonance case and 42.5(9)% with detuning.

During the acquisition, which took a total of 65 min, the laser spectrum was measured every 10 s from the high resolution spectrometer

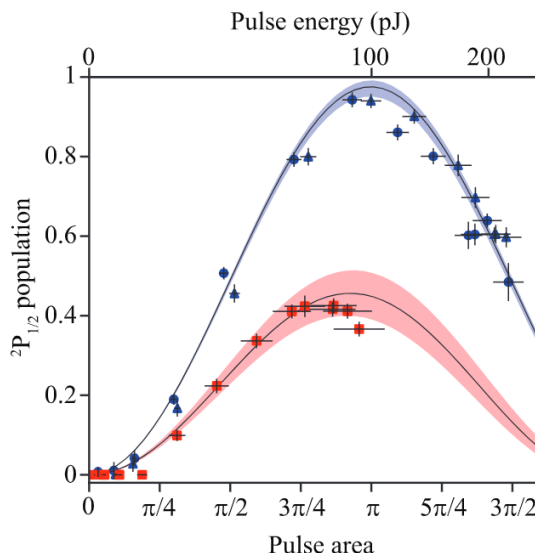


FIG. 2. Excitation probability of the ion to $^2\text{P}_{1/2}$ with single pulses as a function of the pulse area $\Theta = \Omega_{\text{eff}} \times t_{\text{eff}}$ (lower axis) and the pulse energy (upper axis). Blue data points represent on-resonant excitation measurements, where triangles and then circles are two consecutively taken sets of data. Red data points are off-resonant excitation measurements also taken with the same ion. The solid lines are a one-parameter theoretical fit of Eq. (1) using values of detuning and pulse duration from the spectral measurements. The blue curve corresponds to a laser detuning of 33(7) GHz and $t_{\text{eff}} = 2.36(1)$ ps, while the one in red is for 190(7) GHz detuning and $t_{\text{eff}} = 2.25(2)$ ps. The error bars on the experimental data represent two standard errors for horizontal and vertical axes, where the main source of the horizontal error is from fluctuations in the pulse intensity on the ion. The vertical error bar is from population parameter estimation in fitting measurements' statistical distributions. The theoretical curves have confidence bands of two standard deviations. The main sources of error are from pulse duration and laser detuning.

[see Fig. 1(b)]. Figure 3 shows the average of the measured spectra for the on-resonance and detuned case. Both curves are fitted with a Gaussian function from which we find detunings -33(7) GHz and -190(7) GHz from the $^2\text{S}_{1/2}\ F = 1 \rightarrow ^2\text{P}_{1/2}\ F = 0$ transition for the on-resonant and detuned excitation, respectively.

The experimental data shown in Fig. 2 are fitted with the equation for rectangular pulse excitation

$$P_{\text{ex}} = \frac{\Omega_{\text{eff}}^2}{\Omega_{\text{eff}}^2 + \Delta^2} \sin^2 \frac{1}{2} t_{\text{eff}} \sqrt{\Omega_{\text{eff}}^2 + \Delta^2}, \quad (1)$$

where Δ is the detuning measured from the spectrometer, t_{eff} is the effective pulse duration, and Ω_{eff} is the effective Rabi frequency. Because Ω_{eff} is proportional to the square root of the pulse energy, we estimated its value from the PMT counts due to the pulsed laser background scattering C_{sc} . We defined $\Omega_{\text{eff}} = \alpha \sqrt{C_{\text{sc}}}$ and obtained the value of α from the fitting of the experimental points in Fig. 2 with Eq. (1). The theoretical lines in Fig. 2 are obtained using the values of detuning and pulse duration obtained from the spectrometer data with α being the only fitting parameter.

The pulse duration was calculated from the spectra of Fig. 3, giving a $1/e^2$ field duration of 0.941(4) ps for the on-resonance and 0.896(9) ps for the detuned case. These pulse durations are in good agreement with the 0.88(5) ps measured independently with a Michelson interferometer.²⁷ These values are multiplied by $\sqrt{2\pi}$ in order to get the equivalent square pulse area, corresponding to an effective pulse duration $t_{\text{eff}} = 2.36(1)$ ps for the on-resonance case and $t_{\text{eff}} = 2.25(2)$ ps for the off resonance one.

From the on-resonance fitting curve shown in Fig. 2, we estimate a Rabi frequency for the maximum population transfer $\Omega_{\text{eff}} = 1.24(2) \times 10^{12}$ rad/s. This value is compared with a theoretical estimation obtained from

$$\Omega_{\text{th}} = C \Gamma \sqrt{\frac{I_p}{2 I_s}}, \quad (2)$$

where $\Gamma = 2\pi \times 19.6$ MHz is the natural linewidth of the $^2\text{S}_{1/2} - ^2\text{P}_{1/2}$ transition in $^{171}\text{Yb}^+$, $C = 1/\sqrt{3}$ is the Clebsch–Gordan coefficient,

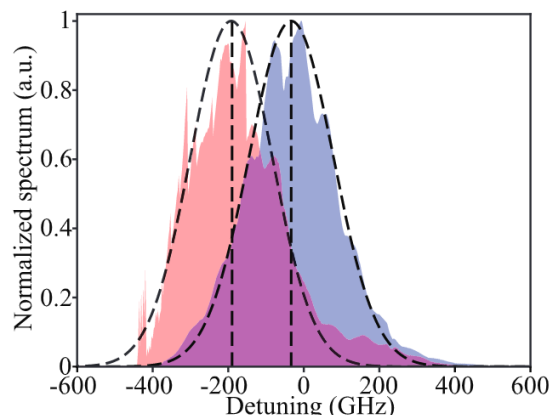


FIG. 3. Averaged frequency spectrum on-resonance (blue) and off resonance (red). The black dashed lines show the Gaussian fit of the spectra and their center frequencies.

$I_s = 508 \text{ W/m}^2$ is the saturation intensity, and I_p is the peak intensity of the pulsed laser. For a consistent comparison, we assume that our pulses are square with a duration $t_p = \sqrt{\pi} \times 0.941(4) \text{ ps} = 1.667(7) \text{ ps}$, and the peak intensity I_p is given by

$$I_p = \frac{2E}{\pi w_0^2 t_p} = 458(9) \times 10^9 \text{ W/m}^2, \quad (3)$$

where $E = 0.0867(17) \text{ nJ}$ is the measured energy of a pulse and $w_0 = 8.5 \mu\text{m}$ is the beam waist at the ion location. With these numbers, we estimate a theoretical Rabi frequency $\Omega_{\text{th}} = 1.510(15) \times 10^{12} \text{ rad/s}$, which is in good agreement with the value obtained from our measurements.

In conclusion, we have experimentally demonstrated ultrafast coherent excitation of $^{171}\text{Yb}^+$ in an ion trap with single laser pulses. We show a maximum population transfer of 94(1)% , mainly limited by the 33(7) GHz detuning of our pulsed laser, which can be compensated with more precise tuning of the CFBG temperature or with an active feedback on the laser source that uses continuous measurements of the high resolution diffraction grating spectrometer. The next step will be splitting the pulses from the laser for creating a pair of counter-propagating π -pulses and illuminate the ion also from the opposite window of the vacuum chamber to implement the SDKs and later demonstrate a fast entangling gate.

We thank Dr. Valdis Blüms for helpful discussions and comments. This research was financially supported by the Griffith University Research Infrastructure Program, the Griffith Sciences equipment scheme, and the Australian Research Council Linkage project (No. LP180100096M). M.L. was supported by the Australian Research Council Future Fellowship (No. FT180100055), and J.S., S.C., and K.S. were supported by the Australian Government Research Training Program Scholarship.

AUTHOR DECLARATION

Conflict of Interest

The authors have no conflicts to disclose.

DATA AVAILABILITY

The data that support the findings of this study are available from the corresponding author upon reasonable request.

REFERENCES

- ¹C. D. Bruzewicz, J. Chiaverini, R. McConnell, and J. M. Sage, *Appl. Phys. Rev.* **6**, 021314 (2019).
- ²A. Bermudez, X. Xu, R. Nigmatullin, J. O’Gorman, V. Negnevitsky, P. Schindler, T. Monz, U. G. Poschinger, C. Hempel, J. Home, F. Schmidt-Kaler, M. Bieruk, R. Blatt, S. Benjamin, and M. Müller, *Phys. Rev. X* **7**, 041061 (2017).
- ³F. Schmidt-Kaler, H. Häffner, M. Riebe, S. Gulde, G. P. T. Lancaster, T. Deuschle, C. Becher, C. F. Roos, J. Eschner, and R. Blatt, *Nature* **422**, 408 (2003).
- ⁴J. P. Gaebler, T. R. Tan, Y. Lin, Y. Wan, R. Bowler, A. C. Keith, S. Glancy, K. Coakley, E. Knill, D. Leibfried, and D. J. Wineland, *Phys. Rev. Lett.* **117**, 060505 (2016).
- ⁵C. J. Ballance, T. P. Harty, N. M. Linke, M. A. Sepiol, and D. M. Lucas, *Phys. Rev. Lett.* **117**, 060504 (2016).
- ⁶J. I. Cirac and P. Zoller, *Phys. Rev. Lett.* **74**, 4091 (1995).
- ⁷K. Mølmer and A. Sørensen, *Phys. Rev. Lett.* **82**, 1835 (1999).
- ⁸C. Monroe and J. Kim, *Science* **339**, 1164 (2013).
- ⁹J. J. García-Ripoll, P. Zoller, and J. I. Cirac, *Phys. Rev. Lett.* **91**, 157901 (2003).
- ¹⁰C. D. B. Bentley, A. R. R. Carvalho, and J. J. Hope, *New J. Phys.* **17**, 103025 (2015).
- ¹¹C. D. B. Bentley, A. R. R. Carvalho, D. Kielpinski, and J. J. Hope, *New J. Phys.* **15**, 043006 (2013).
- ¹²W. C. Campbell, J. Mizrahi, Q. Quraishi, C. Senko, D. Hayes, D. Hucul, D. N. Matsukevich, P. Maunz, and C. Monroe, *Phys. Rev. Lett.* **105**, 090502 (2010).
- ¹³J. Mizrahi, C. Senko, B. Neyenhuis, K. G. Johnson, W. C. Campbell, C. W. S. Conover, and C. Monroe, *Phys. Rev. Lett.* **110**, 203001 (2013).
- ¹⁴V. M. Schäfer, C. J. Ballance, K. Thirumalai, L. J. Stephenson, T. G. Ballance, A. M. Steane, and D. M. Lucas, *Nature* **555**, 75 (2018).
- ¹⁵J. D. Wong-Campos, S. A. Moses, K. G. Johnson, and C. Monroe, *Phys. Rev. Lett.* **119**, 230501 (2017).
- ¹⁶M. I. Hussain, D. Heinrich, M. Guevara-Bertsch, E. Torrontegui, J. García-Ripoll, C. Roos, and R. Blatt, *Phys. Rev. Appl.* **15**, 024054 (2021).
- ¹⁷M. I. Hussain, M. J. Petrasunas, C. D. B. Bentley, R. L. Taylor, A. R. R. Carvalho, J. J. Hope, E. W. Streed, M. Lobino, and D. Kielpinski, *Opt. Express* **24**, 16638 (2016).
- ¹⁸M. J. Madsen, D. L. Moehring, P. Maunz, R. N. Kohn, L.-M. Duan, and C. Monroe, *Phys. Rev. Lett.* **97**, 040505 (2006).
- ¹⁹D. Heinrich, M. Guggemos, M. Guevara-Bertsch, M. I. Hussain, C. F. Roos, and R. Blatt, *New J. Phys.* **21**, 073017 (2019).
- ²⁰C. Roman, A. Ransford, M. Ip, and W. C. Campbell, *New J. Phys.* **22**, 073038 (2020).
- ²¹S. Olmschenk, D. Hayes, D. N. Matsukevich, P. Maunz, D. L. Moehring, K. C. Younge, and C. Monroe, *Phys. Rev. A* **80**, 022502 (2009).
- ²²M. Ghadimi, E. M. Bridge, J. Scarabel, S. Connell, K. Shimizu, E. Streed, and M. Lobino, *Appl. Opt.* **59**, 5136 (2020).
- ²³V. Blüms, M. Piotrowski, M. I. Hussain, B. G. Norton, S. C. Connell, S. Gensemer, M. Lobino, and E. W. Streed, *Sci. Adv.* **4**, eaao4453 (2018).
- ²⁴S. C. Connell, J. Scarabel, E. M. Bridge, K. Shimizu, V. Blüms, M. Ghadimi, M. Lobino, and E. W. Streed, “Ion-photon frequency qubit correlations for quantum networks,” [arXiv:2104.05189 \[quant-ph\]](https://arxiv.org/abs/2104.05189) (2021).
- ²⁵S. Ejtemaei, R. Thomas, and P. C. Haljan, *Phys. Rev. A* **82**, 063419 (2010).
- ²⁶S. Wölk, C. Piltz, T. Sriarunothai, and C. Wunderlich, *J. Phys. B: At., Mol. Opt. Phys.* **48**, 075101 (2015).
- ²⁷A. Levchenko, D. Batani, and V. Zvorykin, *AIP Conf. Proc.* **827**, 182 (2006).



OPEN

Dynamic compensation of stray electric fields in an ion trap using machine learning and adaptive algorithm

Moji Ghadimi¹✉, Alexander Zappacosta¹, Jordan Scarabel¹, Kenji Shimizu¹, Erik W. Streed^{1,2} & Mirko Lobino^{1,3}

Surface ion traps are among the most promising technologies for scaling up quantum computing machines, but their complicated multi-electrode geometry can make some tasks, including compensation for stray electric fields, challenging both at the level of modeling and of practical implementation. Here we demonstrate the compensation of stray electric fields using a gradient descent algorithm and a machine learning technique, which trained a deep learning network. We show automated dynamical compensation tested against induced electric charging from UV laser light hitting the chip trap surface. The results show improvement in compensation using gradient descent and the machine learner over manual compensation. This improvement is inferred from an increase of the fluorescence rate of 78% and 96% respectively, for a trapped $^{171}\text{Yb}^+$ ion driven by a laser tuned to -7.8 MHz of the $^2\text{S}_{1/2} \leftrightarrow ^2\text{P}_{1/2}$ Doppler cooling transition at 369.5 nm .

Trapped ions are one of the most promising candidates for implementing scalable quantum information processing^{1–4}. Traditionally macroscopic rod traps were used for electrically trapping laser cooled ions. These Paul traps have a deep potential well that enables the trapping of multiple ions in a chain, but their distant electrodes lack the fine spatial control of electric fields necessary to efficiently split and combine small ion crystals⁵. One of the proposed architectures for scaling up the number of trapped ions in a quantum processor is the use of microfabricated surface chip traps with multiple DC electrodes that are able to manipulate multiple ions individually^{6–10}.

In these chip traps the ions are confined to a potential formed by the node of an oscillating RF electric field in two dimensions while a DC field generated from multiple electrodes provides a finely spatially adjustable potential in the third dimension. It is well-known in Paul trapping that stray DC electric fields push the ion off the RF node and induce micromotion that degrades or outright prevents effective confinement and laser-cooling¹¹. The solution to this problem is to use the DC electrodes to generate an opposite DC electric field that compensates for these stray fields⁹.

Micromotion amplitude can be measured and dealt with in multiple ways^{9,12–15}. Most of the conventional methods are time consuming and can only be done manually. A simple and quick proxy, that is only applicable to small amounts of micromotion, is to measure the ion's fluorescence under laser cooling near the Doppler limit. In fact for low magnitudes of micromotion, if a laser is red-detuned near the natural linewidth of the atom, the ion fluorescence rate increases as the micromotion amplitude decreases (see “Experimental setup” section and Fig. 2a). While stray electric fields can be readily compensated in simple fixed trap geometries¹⁶, this task becomes more challenging for multi-electrode designs¹⁷ and in proximity of surfaces which are vulnerable to laser induced charging¹⁸.

Automation, optimization, and machine learning have been used to improve different manual tasks in atom and ion traps^{19–21} and they are also useful tools for optimizing the individual electrode voltages which generate the trapping electric field. In this work we show how the voltages of an array of electrodes in a surface chip trap can be optimized using a fully automated, machine learning driven process to minimize micromotion and maximize fluorescence. The chip trap in our experiment has 44 segmented DC electrodes and 2 RF rails, as shown in Fig. 1. The trap incorporates nearly aberration free diffractive mirrors directly fabricated onto the

¹Center for Quantum Dynamics, Griffith University, Nathan, QLD, Australia. ²Institute for Glycomics, Griffith University, Southport, QLD, Australia. ³Queensland Micro Nanotechnology Centre, Nathan, QLD, Australia. ✉email: moji131@gmail.com

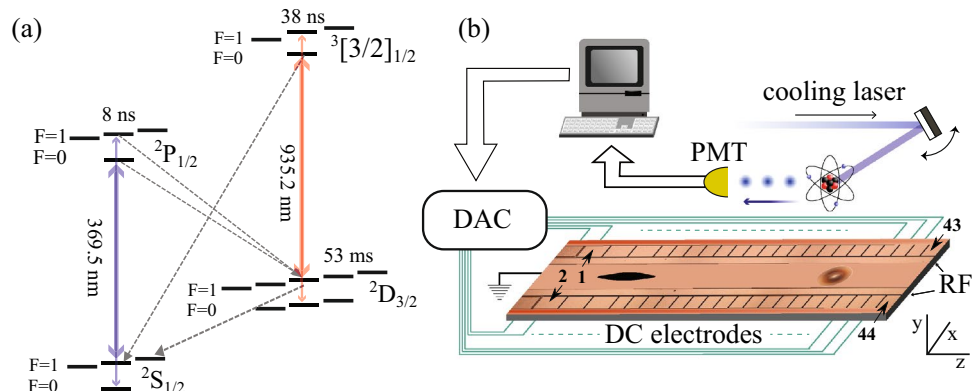


Figure 1. (a) Transitions for laser cooling $^{171}\text{Yb}^+$. The ion is laser cooled on the nearly closed 369.5 nm $^2\text{S}_{1/2}$, $F = 1$ to $^2\text{P}_{1/2}$, $F = 0$ transition. The small amount of off-resonant scattering into the $^2\text{S}_{1/2}$, $F = 0$ state is repumped with a 14.7 GHz sideband on the primary cooling laser. Decays from $^2\text{P}_{1/2}$ can also populate the $^2\text{D}_{3/2}$ level, which are repumped using a 935 nm laser. (b) Schematics of the ion trap chip and the optimization devices. RF and DC electrodes are used to trap the ion and shuttle it above the diffracting mirror that collects photons from the ion and sends it to photo multiplier tube (PMT). The PMT counts are processed by the optimiser and DC electrode voltages and cooling laser position are updated using a digital to analogue converter (DAC).

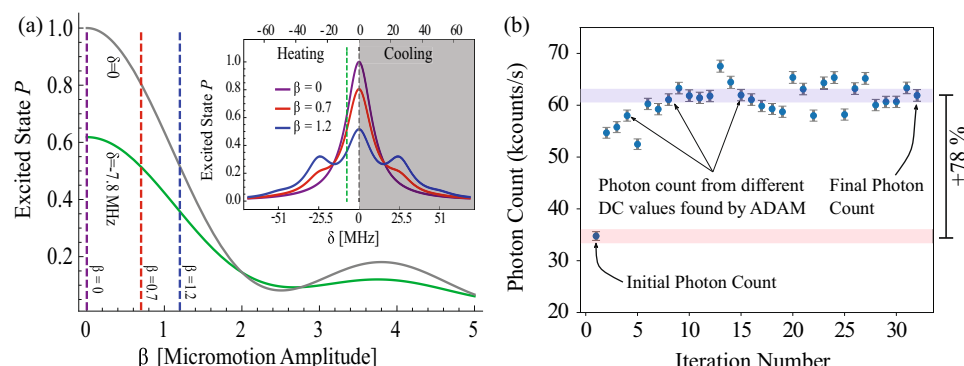


Figure 2. (a) Ideal micromotion broadening of the transition fluorescence in a two-level system as a function of the micromotion amplitude [β] and laser detuning (δ) in the low intensity limit (Eq. 1). For our 370 nm transition the fluorescence rate is proportional to the $^2\text{P}_{1/2}$ excited state population. The laser frequency detuning $\delta = -7.8$ MHz, the natural linewidth $\gamma = 20$ MHz and the RF trap drive frequency $\Omega = 25.5$ MHz. Heating/cooling dynamics are neglected. Our optimizations occur in the low beta (< 1) limit. (b) The photon count improvement using ADAM starting from manually optimized voltage set weights. This graph demonstrates a $78 \pm 1\%$ improvement in ion fluorescence. The error bars are a combination of the readout error of the PMT and peak to peak variations in the photon count whilst not optimizing. The background photon count here is 1184 ± 34 counts/s.

central ground electrode for efficient fluorescence collection from the ion²². A Gradient descent (ADAM²³) and a machine learning algorithm (MLOOP²⁰) were compared on the basis of the versatility and time taken to find the optimal compensation and highest fluorescence rate of the ion. These methods were applied to a trapped $^{171}\text{Yb}^+$ ion and compared to a manual optimization performed by an experienced operator.

With ADAM we were able to improve the fluorescence by 78% starting from voltages already optimized by manual adjustment, while MLOOP achieved a 96% improvement. Subsequently we tested the versatility and adaption of this procedure by deliberately charging the trap with UV light to drop the fluorescence rate by around 35% and compensating back to the optimal with ADAM. This was not tested on MLOOP as it was observed to be quite sensitive to the noise in the fluorescence signal and did not make a solid candidate for final optimization of the artificially charged trap.

Experimental setup

The ion trap used in these experiments and described in^{22,24}, consists of a planar rectangular chip of $1400 \mu\text{m}$ length and $800 \mu\text{m}$ width. It has a set of aluminum electrodes patterned on top and is schematically shown in Fig. 1. The ion is trapped $60 \mu\text{m}$ above the surface, between the two RF electrode rails that extend for the full length of chip, and 44 DC electrodes on the sides. The DC electrodes are used for creating a reconfigurable

trapping potential along the length of the trap, compensating stray electric fields, and enabling ion crystals merging, separation, and shuttling.

An atomic oven underneath one end of the trap generates a beam of neutral Yb atoms which passes through a slit in the chip. The ^{171}Yb is first excited by an isotopically selective 399 nm laser²⁵, and subsequently non-resonantly ionized by a 369.5 nm laser. The ion is then Doppler cooled using the same 369.5 nm laser tuned nearly resonant with $^2\text{S}_{1/2} \text{F} = 1 \leftrightarrow ^2\text{P}_{1/2} \text{F} = 0$ transition. To efficiently cool the ion in both x and y directions, the RF axis of the trap is slightly tilted and therefore the horizontal cooling laser has a component along both nearly horizontal x-axis and nearly vertical y-axis. Occasionally off-resonant scattering from the $^2\text{P}_{1/2} \text{F} = 1$ state will populate the dark $^2\text{S}_{1/2} \text{F} = 0$ ground state, which is repumped by a small amount of light from a 14.7 GHz sideband added to the primary 369.5 nm cooling laser. There is also a probability of 0.5% for the atom to decay from the $^2\text{P}_{1/2}$ into the meta-stable $^2\text{D}_{3/2}$ state. In this case a 935 nm laser repumps the ions back into the cooling cycle. Figure 1a depicts the cooling and repumping transitions.

After initial trapping near the oven slit region, the ion is shuttled along the length of the trap by properly controlling the voltages of the array of DC electrodes with a 12-bit National Instruments PXI-6713 DAQ (output doubled to $+/-20\text{V}$ with 10 mV resolution). For our experiments, the ion was shuttled above the surface of an integrated diffracting micro-mirror patterned on the ground electrode with a focal length of $60\ \mu\text{m}$, equal to the height of the ion above the trap, to improve fluorescence collection and coupling into a single mode fiber²².

For efficient Doppler cooling and subsequent quantum information processing experiments, it is important to minimize any micromotion induced by stray electric fields. This is done by tuning the voltages of the DC electrodes so that they generate an opposing electric field that compensates for the stray fields. To manually compensate stray electric fields in the RF confinement plane xy (see Fig. 1), it is not practical to individually tune all the 44 DC electrodes. We instead use two voltage sets (array of DC voltages for individual electrodes) which were calculated for generating an electric field of 100 V/m in the x (horizontal) and y (vertical) directions. Electrode voltages of -1 to $+1\text{V}$ for the x direction and -2 to $+2\text{V}$ for the y direction are needed to create electric field of 100 V/m at the location of the ion. These sets of voltages are multiplied by arbitrary weights w_x and w_y to compensate arbitrary fields in the RF trapping plane. In practice this process has imperfections and cannot fully compensate for the stray electric fields¹⁷. Instead, individual electrodes need to be tuned independently for optimal compensation. This optimum compensation is position dependent and there might be multiple solutions for a multi-electrode trap.

Two other DC voltage sets are used and their relative weights tuned: a harmonic voltage set, and RF plane trap axis rotation voltage set. The former creates a harmonic potential to trap the ion in different locations along the chip length, while the latter rotates the trap's secular confinement axes to lift the degeneracy and improve cooling²⁶.

We infer the magnitude of the stray electric field from the fluorescence rate of the ion when the cooling laser is red-detuned near half its natural linewidth for optimal cooling. When driving an ideal cold two-level atom with this laser, the fluorescence is proportional to the population of excited state, P_e , that can be calculated from the optical Bloch equation²⁷. The relationship between P_e and the strength of the stray electric field is given by¹⁵:

$$P_e(\beta) = C \sum_{m=-\infty}^{\infty} \frac{J_m^2(\beta)}{\left(\frac{\delta_L}{\gamma} + m \frac{\Omega}{\gamma} \right)^2 + \frac{1}{4}} \quad (1)$$

where J_m is the m_{th} order Bessel function of the first kind, $\delta_L = \omega_{\text{atom}} - \omega_{\text{laser}}$ is the laser frequency detuning, γ is the natural linewidth and Ω is the RF trap frequency. The amount of micromotion is embedded in the dimensionless parameter β which accounts for the dimensionless measure of the ion's coherently driven motion from the stray electric fields and RF phase imbalances (AC micromotion)¹⁵. C depends on the strength of the coupling between the levels that is a constant here since we keep laser intensity and direction fixed. Figure 2a shows a graph of $P_e(\beta)/P_e(0)$ as a function of β . The graph shows that at our detuning ($-7.8\ \text{MHz}$) the population decreases monotonically as β increases if β is less than 2.5. For larger β micromotion induced local maxima arise that prevent inferring the magnitude of micromotion from fluorescence rate. Since our operating regime is below this threshold, we can use the change in fluorescence rate to detect the change in magnitude of the stray electric field.

Results

A gradient descent algorithm (ADAM) and a deep learning network (MLOOP) were tested for compensating stray fields in different working regimes. The source code used for the experiments is available in²⁸. The software controlled the voltages using the PXI-6713 DAQ and read the fluorescence counts from a photo-multiplier-tube (PMT) through a time tagging counter (IDQ id800). All software was written in python and interfaced with the DAQ hardware using the library NI-DAQmx Python. A total of 44 DC electrodes and the horizontal position of the cooling laser were tuned by the program, resulting in a total of 45 input parameters.

Gradient descent optimizer. The first compensation test was performed by ADAM gradient descent algorithm. This is a first order optimizer that uses the biased first and second order moments of the gradient to update the inputs of an objective function, and was chosen for its fast convergence, versatility in multiple dimensions and tolerance to noise²³. Our goal was to maximize the fluorescence of the ion which was described by a function $f(\vec{\alpha})$, where $\vec{\alpha} = (\alpha_1, \alpha_2, \alpha_3, \dots, \alpha_{45})$ represents the array of parameters to be optimized. To find the optimal $\vec{\alpha}$, the algorithm needs to know the values of the partial derivatives for all input parameters. Because we do not have an analytic expression for $f(\vec{\alpha})$, the values of its derivatives were estimated from experimental measurements by sequentially changing each input α_i , and reading the associated change in fluorescence f . This data were used as inputs to ADAM for finding the optimal $\vec{\alpha}$ which maximized f .

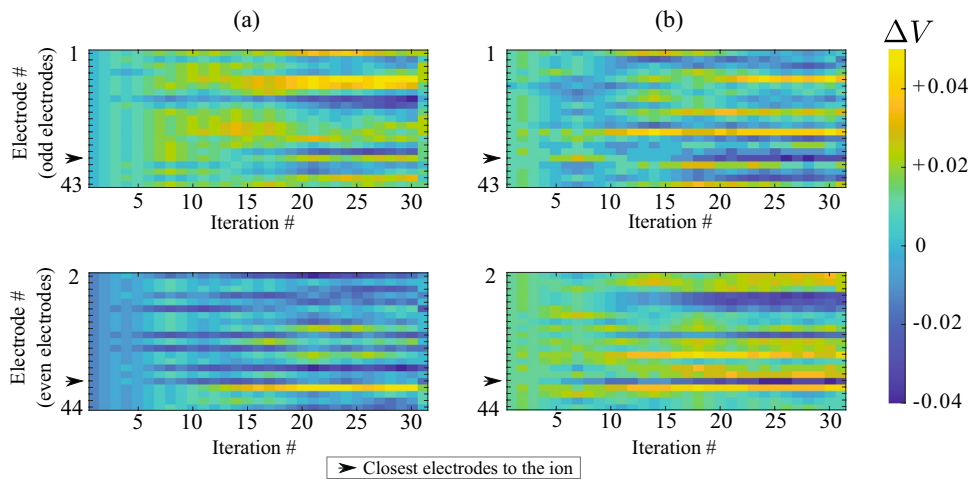


Figure 3. Voltage deviation from the original starting point during optimization with ADAM. (a) uncharged trap (“Gradient descent optimizer” section). (b) During UV charging (“Testing under poor trap conditions”). Top graphs show odd electrode numbers corresponding to top DC electrodes in Fig. 1b and the bottom graphs show the even electrode numbers. The values were determined by subtracting the voltage at each iteration by the starting voltage $\Delta V = V_n - V_0$. Changes can be seen in almost all the electrodes of the trap.

Before running the automated compensation, we manually adjusted the 4 weights of the voltage sets used for compensation described in the previous section. We also tried to run ADAM to optimize these 4 parameters but the increase in fluorescence was limited to 6%. After manual compensation, we ran ADAM on all 45 inputs with the algorithm parameters given in the source code²⁸. Each iteration took 12 s, where 9.8 s were the photon readout (0.1 s×2 readouts per parameter plus 2×0.1 s readouts at the beginning and end of the iteration), and the rest of the time was the gradient computation. If the photon count reduced by more than 40% of its initial value, the algorithm terminated and applied the previously found optimum. This acted as the safety net for the program, ensuring the ion was not lost while optimizing the 45 inputs. We need this safety net because if the ion is heated past the capture range for the used cooling detuning, it will be ejected from the trap. In our implementation of the algorithm we removed the reduction in the step size of the optimization algorithm as iterations progressed. This step reduction, which is present in the standard version of ADAM, is not ideal when stray fields change with time since the optimal values of the voltages also drift in time. The removal caused some fluctuations in the photon readout near the optimal settings. Adding to these fluctuations, other sources of noise, such as wavemeter laser locking³², and mechanical drift in the trap environment, resulted in daily photon count variations of around 5%. Fluctuation in laser power was not a concern here since the power of the cooling laser was stabilized. Despite these fluctuations, and the fact that stray fields change every day, the algorithm demonstrated an increase in fluorescence collection up to $78 \pm 1\%$ (Fig. 2b) when starting from a manually optimized configuration in less than 10 iterations, or 120 s.

The ADAM algorithm was fast and reliable (the ion was never lost during optimization), even in extremely volatile conditions like having time-dependent charging and stray electric field buildup. Figure 3a shows a colourmap of the voltages and laser position adjustments, where most of the improvement came from adding the same voltage to all DC electrodes indicating that the ion was not at optimal height. The volatility of the ion-trap environment causes the fluorescence rate to oscillate around the optimal point. To get the best value, instead of using the values of the final iteration, the software saved all voltage combinations and applied the setting with the highest photon count after all iterations were finished. Despite picking the best value it can be seen in Fig. 2b that the fluorescence for some iterations during the optimization are higher than the final point selected by the software. This is because when the settings are changed, the ion fluorescence rate may transiently increase and subsequently stabilize to a slightly lower value for the same voltage settings.

Deep learning network for the ion trap. The second algorithm tested was a deep learning network using the python based optimization and experimental control package MLOOP²⁰. MLOOP uses Differential Evolution³³ for exploring and sampling data. The blue points in Fig. 4a corresponds to these samples and it can be seen that even at the end of optimization, they can have non-optimum fluorescence rates. MLOOP also trains a neural network using the data collected by Differential Evolution and creates an approximate model of the experimental system. It then uses this model to predict an optimum point. The red points in Fig. 4a shows the optimum points predicted by the neural network model. It can be seen that this section starts later than Differential Evolution, as it requires some data for initial neural network training, and gradually finds the optimum and stays near it. For training of the neural network, the inbuilt ADAM optimizer is used to minimize the cost function. The sampling in MLOOP does not require a gradient calculation which greatly improves the sampling time. Even though the sampling is fast, training the network to find an optimal point requires a minimum of 100 samples and that makes MLOOP slower than ADAM. With our settings for MLOOP, each iteration took 0.7 s on average and therefore 700 s was needed to take 1000 samples shown in Fig. 4a.

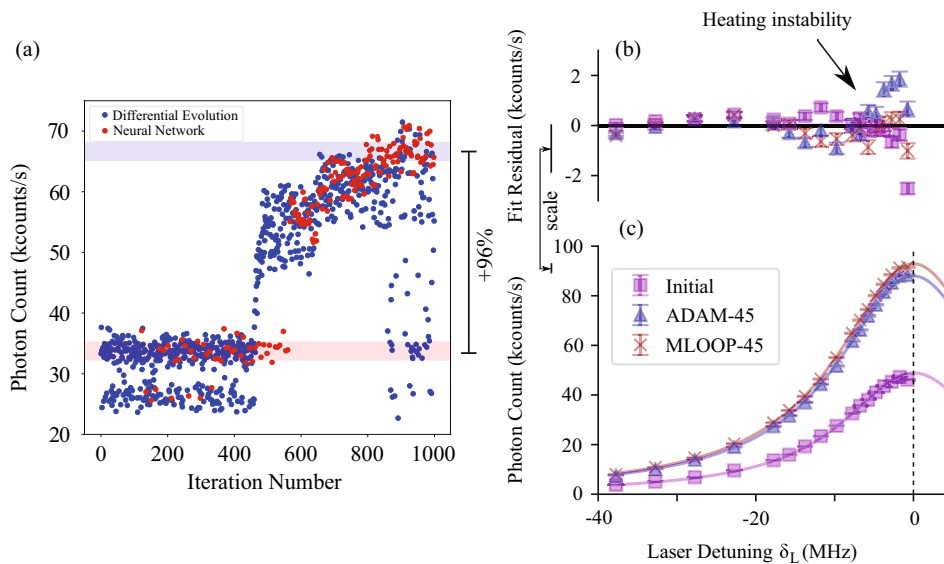


Figure 4. (a) MLOOP deep learning network. Differential Evolution explores the input space (blue points) and the neural network creates a model of the data and predicts an optimum (red points). Maximum photon count of the neural network points is $96 \pm 1\%$ higher than manual optimization. Differential Evolution continues to explore the input space and has varied photon counts. The beginning point for the process (found by manually adjusting the 4 voltage set weights) was at 33700 counts/s and the highest photon count found by the neural network was at 66200 counts/s. (b) and (c) Fluorescence versus laser frequency detuning from the resonance for initial setting and after different optimizations. It can be seen from that the experimental values are very close to the theoretical Lorentzian fit^{29–31}. This shows the heating is low before and after optimization and therefore the change in fluorescence can be used to infer the change in heating. Deviation from the theory near the resonance shown in (b) is a sign of small heating instability.

In our test the neural network in MLOOP had 5 layers with 45 nodes each, all with Gaussian error correction. The neural network structure (number of layers and cells) was manually optimized and tested on a 45-dimensional positive definite quadratic function before being used for the experiment. Once the ion was trapped, positioned above the integrated mirror²², and photon counts were read, the program started sampling 100 different voltage combinations around its initial point. Then, the network started training on the initial data and making predictions for the voltages that maximise fluorescence. Since the ion trap setup is very sensitive to changes in the electric field, the voltages were set to move a maximum of 1% of their previous value in each iteration to reduce the chance of losing the ion. As a step size value could not be explicitly defined, this percentage was chosen to make the changes similar to the step size used for ADAM.

A small percentage of our initial trials with the maximum change of a few percent (instead of 1%) led to an unstable ion during the parameter search sequence. This is because MLOOP is a global optimizer and can set the voltages to values far from the stable starting point. Since the ion trap is a complicated system that can only be modelled for a specific range of configurations, moving away from these settings can lead to unpredictable and usually unstable behavior. MLOOP also has an in-built mechanism that handles function noise using a predefined expected uncertainty. We set this uncertainty to the peak-to-peak noise of the photon readout when no optimization was running.

Since MLOOP is a global optimizer it was able to find optimum points different from the points found by ADAM. For trials where low numbers of initial training data points were used, these configurations proved to be unstable and in most cases resulted in the loss of the ion. Unstable states were also observed occasionally if the optimizer was run for too long. With moderate-size training sets, MLOOP was able to find voltage settings with fluorescence rates similar or higher than optimum points found by ADAM as shown in Fig. 4a. Considering the long duration of the MLOOP iteration sequence and the possibility of finding unstable settings in volatile conditions, the test of optimization with induced changing stray fields (“Testing under poor trap conditions”) was only performed with the ADAM optimizer as the gradient based search method proved to be more robust against fluctuations in the ion environment.

To test the effectiveness of the protocols, the saturation power, P_{sat} , was measured before and after the optimization process. The P_{sat} is the laser power at which the fluorescence rate of a two-level system is half the fluorescence at infinite laser power. We also measured the overall detection efficiency η , the fraction of emitted photons which resulted in detection events. Table 1 shows P_{sat} decreased (ion photon absorption was improved) using both ADAM and MLOOP. The detection efficiency was approximately the same for all runs as expected.

Another test was done by measuring fluorescence versus laser detuning before and after optimization. Figure 4b shows that the measured values follows the expected Lorentzian profile^{29–31} and associated linewidth before and after optimization. This indicates that the initial micromotion magnitude β was sufficiently small for fluorescence to be a good optimization proxy. Clear increase in fluorescence can be seen after optimizing 44

	P_{sat} (μW)	η (%)	Bkg (1/s)
Initial	4.11(1)	0.971(2)	1184(34)
ADAM-45	1.86(1)	0.938(1)	1227(35)
MLOOP-45	1.86(1)	0.989(1)	1291(35)

Table 1. Saturation power (P_{sat}), detection efficiency (η) and average background count rate (Bkg) before and after optimization with different methods. P_{sat} and η values are calculated by fitting the theoretical formula for Fluorescence Rate versus Laser Power to the experimental data^{29–31}. A clear drop in saturation power is observed after ADAM and MLOOP optimization of individual electrodes indicating a reduction of the micromotion.

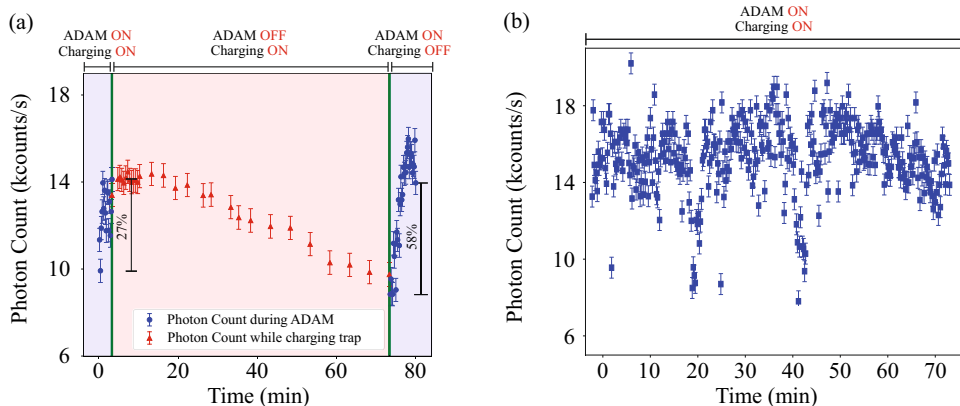


Figure 5. (a) Real time compensation with ADAM of laser charging induced stray electric field. The ion was optimized using ADAM (left blue points) then the photon count was noted whilst charging for 70 min (red points) then re-optimized (right blue points). Initial improvement from manually optimized settings was 27%. The second optimization improved the fluorescence by 58% from the charged conditions and returned it back to the optimum value of the first optimization within the error. (b) The trap was charged by hitting a UV laser to destabilize the ion and individual electrodes optimized using ADAM simultaneously for 70 min. The photon count fluctuates as a result of combination of fluctuations of power of the cooling laser power, algorithm search and charging irregularities. The optimizer keeps the fluorescence at the photon count similar to the case of optimizing after the charging is stopped (third section of (a)).

electrodes individually both with ADAM and MLOOP. The fit residual curve (difference between the experimental values and the theoretical fit) shows that optimizing individual electrodes, resulted in slight increase in heating instability near the resonance.

Testing under poor trap conditions. To test the live performance of the optimization protocol in a non-ideal situation, we deliberately charged the trap by shining 369.5 nm UV laser light onto the chip for 70 min. The power of the laser was $200 \pm 15\mu W$ and the Gaussian diameter of the focus was $120 \pm 10\mu m$. This process ejects electrons due to the photo-electric effect³⁴ and produces irregular and potentially unpredictable slow time varying electric fields within the trap. The process charged the trap significantly and made a noticeable reduction to the photon count. The ADAM algorithm was then tested both during charging and after charging was stopped. In both cases an improvement of fluorescence rate was observed.

The first experiment was performed to test the optimizing process after charging. In this test, starting with the optimal manual setting, ADAM individual electrode optimizer was able to obtain 27% improvement in the fluorescence rate (blue points on the left side of Fig. 5a). Then charging was induced onto the trap for 70 min and a clear decrease in photon count was seen that went even lower than the initial value (red points in Fig. 5a). At this point charging was stopped and ADAM was run again and fluorescence rate returned back to the previous optimum, within the error, in approximately 12 min. During the second optimization, the fluorescence goes higher than the stable final value for some iterations before the final. This is because of the same effect explained in “Gradient descent optimizer” section that the fluorescence might spike right after a change but go down slightly after stabilizing. Looking at the changes of individual electrodes, shown in Fig. 3b, we see that the main electrodes adjusted were those around the ion and some throughout the trap. The change in the laser horizontal position was negligible.

Another experiment was done by running ADAM during continuous charging for real-time compensation. Since we induce charging via laser scattering from the trap, the collected photons are both from the ion and the scattered laser and fluctuations in the intensity of scattered light confuses the optimizer. Despite that the optimizer did not lose the ion nor needed to abort the process. Figure 5b shows that the fluorescence rate, even after

a 70-min charging session, remained near the optimum value. After stopping the charging, the ion remained trapped for more than 8 h and was intentionally removed from the trap after this time.

Conclusion

Comparing the results of the gradient descent method and MLOOP shows that ADAM, the local optimizer, was a better performer in volatile conditions. This is because unlike MLOOP, ADAM does not need any training and can react faster to changes. MLOOP as a global optimizer was able to find settings with higher fluorescence but occasionally optimums were unstable if the defined parameter search range for the settings were large or if the machine learner ran for too long. The main drawback of MLOOP was that it was much slower than ADAM. In both cases photon collection times were the limiting factor.

Optimizing the individual electrodes improved the fluorescence by 78% for ADAM and 96% for MLOOP. ADAM showed its reliability in the charging test, returning the ion to the optimal fluorescence in 12 min after 70 min of purposely charging the trap with a UV laser. Improvement amounts depended greatly on the overall stability of the cooling laser and efficiency of the photon counting system.

To improve the speed of the gradient based optimizer, shorter readout times can be used although this increases variability in the value of the photon count. It is also possible to try local optimizers like SPSA³⁵ that approximate the gradient using only 2 readouts instead of 90. This improves the time needed for each iteration but because using this approximate gradient reduces the improvement in each iteration, the overall speed comparison to reach the same optimum can only be made when both are tried in practice. One possible problem with SPSA is that it cannot handle noise like ADAM and multiple readouts and averaging are needed in noisy conditions. If high amount of averaging is required, the algorithm may become very slow.

Received: 14 January 2022; Accepted: 8 April 2022

Published online: 29 April 2022

References

- Debnath, S. *et al.* Demonstration of a small programmable quantum computer with atomic qubits. *Nature* **536**, 63–66. <https://doi.org/10.1038/nature18648> (2016).
- Lekitsch, B. *et al.* Blueprint for a microwave trapped ion quantum computer. *Sci. Adv.* **3**, e1601540. <https://doi.org/10.1126/sciadv.1601540> (2017).
- Monroe, C. & Kim, J. Scaling the ion trap quantum processor. *Science* **339**, 1164–1169. <https://doi.org/10.1126/science.1231298> (2013).
- Blinov, B. B., Leibfried, D., Monroe, C. & Wineland, D. J. Quantum computing with trapped ion hyperfine qubits. *Quantum Inf. Process.* **3**, 45–59. <https://doi.org/10.1007/s11128-004-9417-3> (2004).
- Wineland, D. J. *et al.* Experimental issues in coherent quantum-state manipulation of trapped atomic ions. *J. Res. Natl. Inst. Stand. Technol.* **103**, 259–328. <https://doi.org/10.6028/jres.103.019> (1998).
- Kielpinski, D., Monroe, C. & Wineland, D. J. Architecture for a large-scale ion-trap quantum computer. *Nature* **417**, 709–711. <https://doi.org/10.1038/nature00784> (2002).
- Chiaverini, J. *et al.* Surface-electrode architecture for ion-trap quantum information processing. *Quantum Inf. Comput.* **5**, 419–439 (2005).
- Seidelin, S. *et al.* Microfabricated surface-electrode ion trap for scalable quantum information processing. *Phys. Rev. Lett.* **96**, 253003. <https://doi.org/10.1103/PhysRevLett.96.253003> (2006).
- Doret, S. C. *et al.* Controlling trapping potentials and stray electric fields in a microfabricated ion trap through design and compensation. *New J. Phys.* **14**, 073012. <https://doi.org/10.1088/1367-2630/14/7/073012> (2012).
- Amini, J. M. *et al.* Toward scalable ion traps for quantum information processing. *New J. Phys.* **12**, 033031. <https://doi.org/10.1088/1367-2630/12/3/033031> (2010).
- Kielpinski, D. Entanglement and decoherence in a trapped-ion quantum register. Ph.D. thesis (2001).
- Tanaka, U. *et al.* Micromotion compensation in a surface electrode trap by parametric excitation of trapped ions. *Appl. Phys. B* **107**, 907–912. <https://doi.org/10.1007/s00340-011-4762-2> (2012).
- Allcock, D. T. C. *et al.* Heating rate and electrode charging measurements in a scalable, microfabricated, surface-electrode ion trap. *Appl. Phys. B* **107**, 913–919. <https://doi.org/10.1007/s00340-011-4788-5> (2012).
- Narayanan, S. *et al.* Electric field compensation and sensing with a single ion in a planar trap. *J. Appl. Phys.* **110**, 114909. <https://doi.org/10.1063/1.3665647> (2011).
- Berkeland, D. J., Miller, J. D., Bergquist, J. C., Itano, W. M. & Wineland, D. J. Minimization of ion micromotion in a Paul trap. *J. Appl. Phys.* **83**, 5025–5033. <https://doi.org/10.1063/1.367318> (1998).
- Noek, R. *et al.* Trapping and cooling of $^{174}\text{Yb}^+$ ions in a microfabricated surface trap. *J. Korean Phys. Soc.* **63**, 907–913. <https://doi.org/10.3938/jkps.63.907> (2013).
- Allcock, D. T. C. *et al.* Implementation of a symmetric surface-electrode ion trap with field compensation using a modulated Raman effect. *New J. Phys.* **12**, 053026. <https://doi.org/10.1088/1367-2630/12/5/053026> (2010).
- Harlander, M., Brownnutt, M., Hänsel, W. & Blatt, R. Trapped-ion probing of light-induced charging effects on dielectrics. *New J. Phys.* **12**, 093035. <https://doi.org/10.1088/1367-2630/12/9/093035> (2010). arXiv:1004.4842.
- Seif, A. *et al.* Machine learning assisted readout of trapped-ion qubits. *J. Phys. B At. Mol. Opt. Phys.* **51**, 174006. <https://doi.org/10.1088/1361-6455/aad62b> (2018).
- Wigley, P. B. *et al.* Fast machine-learning online optimization of ultra-cold-atom experiments. *Sci. Rep.* **6**, 25890. <https://doi.org/10.1038/srep25890> (2016).
- Tranter, A. D. *et al.* Multiparameter optimisation of a magneto-optical trap using deep learning. *Nat. Commun.* **9**, 4360. <https://doi.org/10.1038/s41467-018-06847-1> (2018).
- Ghadimi, M. *et al.* Scalable ion-photon quantum interface based on integrated diffractive mirrors. *npj Quantum Inf.* **3**, 1–4. <https://doi.org/10.1038/s41534-017-0006-6> (2017).
- Kingma, D. P. & Ba, J. Adam: A method for stochastic optimization. (2017). arXiv:1412.6980
- Shappert, C. M. *et al.* Spatially uniform single-qubit gate operations with near-field microwaves and composite pulse compensation. *New J. Phys.* **15**, 083053. <https://doi.org/10.1088/1367-2630/15/8/083053> (2013).
- Blüms, V. *et al.* Laser stabilization to neutral Yb in a discharge with polarization-enhanced frequency modulation spectroscopy. *Rev. Sci. Instrum.* **91**, 123002. <https://doi.org/10.1063/5.0019252> (2020).
- Norton, B. G., Street, E. W., Petrasunas, M. J., Jechow, A. & Kielpinski, D. Millikelvin spatial thermometry of trapped ions. *New J. Phys.* **13**, 113022. <https://doi.org/10.1088/1367-2630/13/11/113022> (2011).

27. Budker, D., Kimball, D., Kimball, D. F. & DeMille, D. P. *Atomic Physics: An Exploration Through Problems and Solutions* (Oxford University Press, Oxford, 2004).
28. Zappacosta, A. Auto ion compensation. https://github.com/alexzappa11/Auto_Ion_Compensation (2021).
29. Metcalf, H. J., Van der Straten, P. & Van der Straten, P. *Laser Cooling and Trapping. Graduate Texts in Contemporary Physics* (Springer-Verlag, New York, 1999).
30. Ejtemaei, S., Thomas, R. & Haljan, P. C. Optimization of $yb171+$ fluorescence and hyperfine-qubit detection. *Phys. Rev. A* **82**, 063419. <https://doi.org/10.1103/PhysRevA.82.063419> (2010).
31. Berkeland, D. J. & Boshier, M. G. Destabilization of dark states and optical spectroscopy in Zeeman-degenerate atomic systems. *Phys. Rev. A* **65**, 033413. <https://doi.org/10.1103/PhysRevA.65.033413> (2002).
32. Ghadimi, M. *et al.* Multichannel optomechanical switch and locking system for wavemeters. *Appl. Opt.* **59**, 5136–5141. <https://doi.org/10.1364/AO.390881> (2020).
33. Price, K., Storn, R. M. & Lampinen, J. A. Natural computing series. In *Differential Evolution: A Practical Approach to Global Optimization* (Springer-Verlag, Berlin Heidelberg, 2005).
34. Wang, S. X. *et al.* Laser-induced charging of microfabricated ion traps. *J. Appl. Phys.* **110**, 104901, <https://doi.org/10.1063/1.3662118> (2011). [arXiv:1108.0092](https://arxiv.org/abs/1108.0092).
35. Spall, J. C. Implementation of the simultaneous perturbation algorithm for stochastic optimization. *IEEE Trans. Aerosp. Electron. Syst.* **34**, 817–823. <https://doi.org/10.1109/7.705889> (1998).

Acknowledgements

This research was financially supported by the Griffith University Research Infrastructure Programme, the Griffith Sciences equipment scheme, and Australian Research Council Linkage (LP180100096) Projects, ML is supported by Australian Research Council Future Fellowship (FT180100055), AZ was supported by Centre for Quantum Dynamics, Griffith University, Summer Scholarship, JS, and KS were supported by the Australian Government Research Training Program Scholarship.

Author contributions

A.Z. and M.G. developed the codes. A.Z., M.G., J.S., and K.S. performed the experiments. M.G., E.S. and M.L. supervised the research. A.Z., M.G. and M.L. prepared the figures. M.G., A.Z., E.S. and M.L. wrote the manuscript.

Competing interests

The authors declare no competing interests.

Additional information

Correspondence and requests for materials should be addressed to M.G.

Reprints and permissions information is available at www.nature.com/reprints.

Publisher's note Springer Nature remains neutral with regard to jurisdictional claims in published maps and institutional affiliations.



Open Access This article is licensed under a Creative Commons Attribution 4.0 International License, which permits use, sharing, adaptation, distribution and reproduction in any medium or format, as long as you give appropriate credit to the original author(s) and the source, provide a link to the Creative Commons licence, and indicate if changes were made. The images or other third party material in this article are included in the article's Creative Commons licence, unless indicated otherwise in a credit line to the material. If material is not included in the article's Creative Commons licence and your intended use is not permitted by statutory regulation or exceeds the permitted use, you will need to obtain permission directly from the copyright holder. To view a copy of this licence, visit <http://creativecommons.org/licenses/by/4.0/>.

© The Author(s) 2022

Appendix B

Calculations

B.1 Fluorescence distribution under state mixing

The integral in equation 3.105 is written explicitly and transformed into an integral over λ with the relation of equation 3.104,

$$\begin{aligned} \frac{\gamma_{L,b}}{k!} \int_0^T e^{-\gamma_{L,b}t} e^{-(R_D T + R_B t)} (R_D T + R_B t)^k dt \\ = \frac{\gamma_{L,b}}{R_B k!} e^{\frac{\gamma_{L,b} R_D T}{R_B}} \int_{R_D T}^{(R_B + R_D)T} e^{-(1 + \frac{\gamma_{L,b}}{R_B})\lambda} \lambda^k d\lambda. \quad (\text{B.1}) \end{aligned}$$

This form is identical to the equations of Wölk et al.[123]. In this form, the integral can be solved knowing the relation,

$$\int e^{-bt} t^{a-1} dt = -b^{-a} \Gamma(a, bt) + c \quad (\text{B.2})$$

to retrieve equation 3.106. Equation 3.111 is solved in the same manner using the different λ relation, equation 3.109.

B.2 Electric dipole calculation

This appendix will show that the rotating wave approximation applies to π -transitions driven by linearly polarized light and not to σ^\pm transitions driven by the appropriately circularly polarized light.

B.2.1 π -transitions

First consider the electric dipole for a π -transition. The vector direction for the electric dipole moment between hydrogen wavefunctions $\psi_{1,0,0}$ and $\psi_{2,1,0}$ can be found by calculating the angular integral as in Allen and Eberly[95, Eq. 2.10]. Only the angular component $Y_{l,m}(\theta, \phi)$ of the wavefunctions, $\psi_{n,m,l} = R_{n,l}(r)Y_{l,m}(\theta, \phi)$ is required. The angular components are $Y_{1,0}(\theta) = \cos\theta$ and $Y_{0,0} = 1$.

$$\begin{aligned} & \int_0^\pi \int_0^{2\pi} Y_{1,0}^*(\theta, \phi)(\sin\theta \cos\phi \mathbf{x} + \sin\theta \sin\phi \mathbf{y} + \cos\theta \mathbf{z}) Y_{0,0}(\theta, \phi) d\phi d\theta \\ &= \pi^2 \mathbf{z} \quad (\text{B.3}) \end{aligned}$$

The solution shows electric fields linearly polarized along the z-axis will couple best to the electric dipole. Using the field, $\mathbf{E}_0(t) = E_0 \cos(\omega t) \mathbf{z}$ and arbitrary electric dipole magnitude $|d_{eg}|$,

$$\begin{aligned} \hat{V}(t) &= -\mathbf{E}_0(t) \cdot (\mathbf{d}_{eg} |e\rangle \langle g| + \mathbf{d}_{eg}^* |g\rangle \langle e|) \\ &= -\frac{|\mathbf{d}_{eg}| E_0}{2} (e^{i\omega t} + e^{-i\omega t})(|e\rangle \langle g| + |g\rangle \langle e|). \quad (\text{B.4}) \end{aligned}$$

Transforming into the interaction picture yields,

$$\begin{aligned}
\hat{V}_I(t) &= e^{i\hat{H}t/\hbar}\hat{V}(t)e^{-i\hat{H}t/\hbar} \\
&= (|g\rangle\langle g| + e^{i\omega t}|e\rangle\langle e|)\hat{V}(t)(|g\rangle\langle g| + e^{-i\omega t}|e\rangle\langle e|) \\
&= -\frac{|\mathbf{d}_{eg}|E_0}{2}((e^{i(\omega+\omega_0)t} + e^{-i(\omega-\omega_0)t})|e\rangle\langle g| + (e^{-i(\omega+\omega_0)t} + e^{i(\omega-\omega_0)t})|g\rangle\langle e|) \\
\end{aligned} \tag{B.5}$$

where both resonant $\omega - \omega_0$ and counter-rotating $\omega + \omega_0$ terms are present. To solve the dynamics for simple Rabi oscillations where $\mathbf{d}_{eg}E_0 \ll \hbar\omega$, the $\omega + \omega_0$ terms can be omitted under the rotating wave approximation.

B.2.2 σ^+ -transitions

This same calculation can be performed for the $\psi_{1,0,0}$ and $\psi_{2,1,1}$ states as in equation 3.38. Given $Y_{1,1}(\theta, \phi) = -e^{i\phi} \sin \theta$,

$$\begin{aligned}
\int_0^\pi \int_0^{2\pi} Y_{1,1}^*(\theta, \phi) (\sin \theta \cos \phi \mathbf{x} + \sin \theta \sin \phi \mathbf{y} + \cos \theta \mathbf{z}) Y_{0,0}(\theta, \phi) d\phi d\theta \\
= -\frac{\pi^2}{2}(\mathbf{x} - i\mathbf{y}),
\end{aligned} \tag{B.6}$$

it is seen the vector agrees with the same electric dipole calculation by Allen and Eberly[95] in equation 3.38. Driving the electric dipole with a circularly polarized field, $E_0(t) = \frac{E_0}{\sqrt{2}}(\cos(\omega t)\mathbf{x} + \sin(\omega t)\mathbf{y})$ yields,

$$\begin{aligned}
\hat{V}(t) &= -\mathbf{E}_0(t) \cdot (\mathbf{d}_{eg}|e\rangle\langle g| + \mathbf{d}_{eg}^*|g\rangle\langle e|) \\
&= -\frac{\mathbf{d}_{eg}E_0}{2}((\cos(\omega t) - i\sin(\omega t))|e\rangle\langle g| + (\cos(\omega t) + i\sin(\omega t))|g\rangle\langle e|) \\
&= -\frac{\mathbf{d}_{eg}E_0}{2}(e^{-i\omega t}|e\rangle\langle g| + e^{i\omega t}|g\rangle\langle e|)
\end{aligned} \tag{B.7}$$

Note equation B.7 has only one frequency compared to equation B.4 with two counter-rotating frequencies. Transforming into the interaction picture,

$$\begin{aligned}
\hat{V}_I(t) &= e^{i\hat{H}t/\hbar} \hat{V}(t) e^{-i\hat{H}t/\hbar} \\
&= (|g\rangle\langle g| + e^{i\omega t}|e\rangle\langle e|) \hat{V}(t) (|g\rangle\langle g| + e^{-i\omega t}|e\rangle\langle e|) \\
&= -\frac{\mathbf{d}_{eg}E_0}{2} (e^{i(\omega-\omega_0)t}|g\rangle\langle e| + e^{-i(\omega-\omega_0)t}|e\rangle\langle g|) \quad (\text{B.8})
\end{aligned}$$

Owing to the circular electric field and the complex term in the electric dipole term, the interaction potential in the interaction frame has no counter-rotating terms, so no rotating wave approximation is required.

B.3 Detuned Ramsey unitary

The excited state population in section 4.2.6 is derived by calculating the effect of the unitary operators on the states $|g\rangle$ and $|e\rangle$. The unitary for a driven two level atom given its Hamiltonian(equation 3.48) is first solved,

$$\begin{aligned}
\hat{U}_I(t) &= e^{i\frac{\hat{H}}{\hbar}t} = e^{i\frac{\Omega'}{2}(\frac{\Delta}{\Omega'}\hat{\sigma}_z + \frac{\Omega}{\Omega'}\hat{\sigma}_x)t} \\
&= \hat{I} + i\frac{\Omega't}{2}\left(\frac{\Delta}{\Omega'}\hat{\sigma}_z + \frac{\Omega}{\Omega'}\hat{\sigma}_x\right) - \frac{(\frac{\Omega't}{2})^2}{2}\hat{I} - i\frac{(\frac{\Omega't}{2})^3}{6}\left(\frac{\Delta}{\Omega'}\hat{\sigma}_z + \frac{\Omega}{\Omega'}\hat{\sigma}_x\right) + \dots \\
&= \hat{I} \cos\left(\frac{\Omega't}{2}\right) + i\left(\frac{\Omega}{\Omega'}\hat{\sigma}_x + \frac{\Delta}{\Omega'}\hat{\sigma}_z\right) \sin\left(\frac{\Omega't}{2}\right). \quad (\text{B.9})
\end{aligned}$$

A $\pi/2$ -pulse will have duration $t = \frac{\pi}{2\Omega}$, and its effect on an atom in the ground state can be found

$$\hat{U}_I(\pi/2\Omega)|g\rangle = \left(\cos\left(\frac{\pi\Omega'}{4\Omega}\right) + i\frac{\Delta}{\Omega'}\sin\left(\frac{\pi\Omega'}{4\Omega}\right)\right)|g\rangle + i\frac{\Omega}{\Omega'}\sin\left(\frac{\pi\Omega'}{4\Omega}\right)|e\rangle. \quad (\text{B.10})$$

Afterwards, free evolution for time T is considered using the unitary $\hat{U}_0(T)$ which is equivalent to $\hat{U}_I(T)$ but setting $\Omega = 0$.

$$\begin{aligned}\hat{U}_0(T)\hat{U}_I(\pi/\Omega)|g\rangle &= (\hat{I} \cos(\frac{\Delta T}{2}) + i\hat{\sigma}_z \sin(\frac{\Delta T}{2})) \times \\ &\quad (\cos(\frac{\pi\Omega'}{4\Omega}) + i\frac{\Delta}{\Omega'} \sin(\frac{\pi\Omega'}{4\Omega}))|g\rangle + i\frac{\Omega}{\Omega'} \sin(\frac{\pi\Omega'}{4\Omega})|e\rangle \\ &= (\cos(\frac{\Delta T}{2}) + i\sin(\frac{\Delta T}{2}))(\cos(\frac{\pi\Omega'}{4\Omega}) + i\frac{\Delta}{\Omega'} \sin(\frac{\pi\Omega'}{4\Omega}))|g\rangle + \\ &\quad (i\cos(\frac{\Delta T}{2}) + \sin(\frac{\Delta T}{2}))\frac{\Omega}{\Omega'} \sin(\frac{\pi\Omega'}{4\Omega})|e\rangle.\end{aligned}\quad (\text{B.11})$$

Adding the final pulse makes the equation unweildy so instead, working backwards, $\langle e | \hat{U}_I(\pi/\Omega)$ is calculated,

$$\langle e | \hat{U}_I(\pi/\Omega) = (\cos(\frac{\pi\Omega'}{4\Omega}) - i\frac{\Delta}{\Omega'} \sin(\frac{\pi\Omega'}{4\Omega}))\langle e | + i\frac{\Omega}{\Omega'} \sin(\frac{\pi\Omega'}{4\Omega})\langle g |.\quad (\text{B.12})$$

Finally equations B.11 and B.12 are combined and the absolute square is found using an online equation solver to arrive at equation 4.6.

B.4 Comprehensive master equation model for

$^2S_{1/2} \leftrightarrow ^2P_{1/2}$ system

Similar to the theory in section 3.2.3, the valence electron population within the $^2S_{1/2}$ & $^2P_{1/2}$ manifolds interacting with the electric field of the Raman lasers can be described accurately using a Hamiltonian in the interaction picture relative to the $^2S_{1/2} F = 1 m_F = 0 \leftrightarrow ^2P_{1/2} F = 0$ transition. The bare atom Hamiltonian reads,

$$\begin{aligned}\frac{\hat{H}_0}{\hbar} &= -\Delta_{HF,S}|S,0,0\rangle\langle S,0,0| - \delta_B|S,1,-1\rangle\langle S,1,-1| + \delta_B|S,1,1\rangle\langle S,1,1| + \\ &\quad (\Delta_{HF,P} - \delta_B/3)|P,1,-1\rangle\langle P,1,-1| + \Delta_{HF,P}|P,1,0\rangle\langle P,1,0| + \\ &\quad (\Delta_{HF,P} + \delta_B/3)|P,1,1\rangle\langle P,1,1|\end{aligned}\quad (\text{B.13})$$

where ket states are labeled according to quantum numbers $|l, F, m_F\rangle$ and $\delta_B = \mu_B|B|/\hbar$. An incident laser's polarisation can be decomposed into the three orthogonal polarisations π , σ^- & σ^+ . Each addresses a set of transitions described by the three interaction Hamiltonians,

$$\begin{aligned}\frac{\hat{H}_\pi}{\hbar} &= \frac{\Omega_\pi}{2\sqrt{3}} e^{-i\delta t} \left(|P, 0, 0\rangle \langle S, 1, 0| - |P, 1, -1\rangle \langle S, 1, -1| + \dots \right. \\ &\quad \left. |P, 1, 0\rangle \langle S, 0, 0| + |P, 1, 1\rangle \langle S, 1, 1| \right) + h.c. \\ \frac{\hat{H}_{\sigma^-}}{\hbar} &= \frac{\Omega_{\sigma^-}}{2\sqrt{3}} e^{-i\delta t} \left((-|P, 1, 0\rangle + |P, 0, 0\rangle) \langle S, 1, 1| - \dots \right. \\ &\quad \left. |P, 1, -1\rangle (\langle S, 0, 0| + \langle S, 1, 0|) \right) + h.c. \\ \frac{\hat{H}_{\sigma^+}}{\hbar} &= \frac{\Omega_{\sigma^+}}{2\sqrt{3}} e^{-i\delta t} \left((|P, 1, 0\rangle + |P, 0, 0\rangle) \langle S, 1, -1| + \dots \right. \\ &\quad \left. |P, 1, 1\rangle (-\langle S, 0, 0| + \langle S, 1, 0|) \right) + h.c.\end{aligned}\tag{B.14}$$

Equation B.14 uses the Clebsch-Gordon coefficients as in figure 3.12 to determine the sign of interaction terms as well as the $\sqrt{3}^{-1}$ scaling factor. Lasers detuned by δ from $|S, 1, 0\rangle \leftrightarrow |P, 0, 0\rangle$ are described by equations B.13 and B.14. Dynamics of the system being driven by multiple lasers at different detunings and polarizations can be described by combining multiple instances of equation B.14 into one comprehensive Hamiltonian.

The twelve spontaneous emission collapse operators are also described, accounting for Clebsch-Gordon coefficient values and sign,

$$\begin{aligned}\hat{L}_1 &= \sqrt{\frac{\Gamma}{3}} |S, 1, -1\rangle \langle P, 0, 0| & \hat{L}_2 &= \sqrt{\frac{\Gamma}{3}} |S, 1, 0\rangle \langle P, 0, 0| \\ \hat{L}_3 &= \sqrt{\frac{\Gamma}{3}} |S, 1, 1\rangle \langle P, 0, 0| & \hat{L}_4 &= -\sqrt{\frac{\Gamma}{3}} |S, 0, 0\rangle \langle P, 1, -1| \\ \hat{L}_5 &= -\sqrt{\frac{\Gamma}{3}} |S, 1, -1\rangle \langle P, 1, -1| & \hat{L}_6 &= -\sqrt{\frac{\Gamma}{3}} |S, 1, 0\rangle \langle P, 1, -1| \\ \hat{L}_7 &= \sqrt{\frac{\Gamma}{3}} |S, 1, -1\rangle \langle P, 1, 0| & \hat{L}_8 &= \sqrt{\frac{\Gamma}{3}} |S, 0, 0\rangle \langle P, 1, 0| \\ \hat{L}_9 &= \sqrt{\frac{\Gamma}{3}} |S, 1, 1\rangle \langle P, 1, 0| & \hat{L}_{10} &= -\sqrt{\frac{\Gamma}{3}} |S, 0, 0\rangle \langle P, 1, 1| \\ \hat{L}_{11} &= -\sqrt{\frac{\Gamma}{3}} |S, 1, 0\rangle \langle P, 1, 1| & \hat{L}_{12} &= \sqrt{\frac{\Gamma}{3}} |S, 1, 1\rangle \langle P, 1, 1|\end{aligned}\tag{B.15}$$

A useful application of this comprehensive model is simulating the performance of the used Raman schemes omitting the motional coupling (figure B.1). From this model, the trend of Raman detuning against population transfer to the

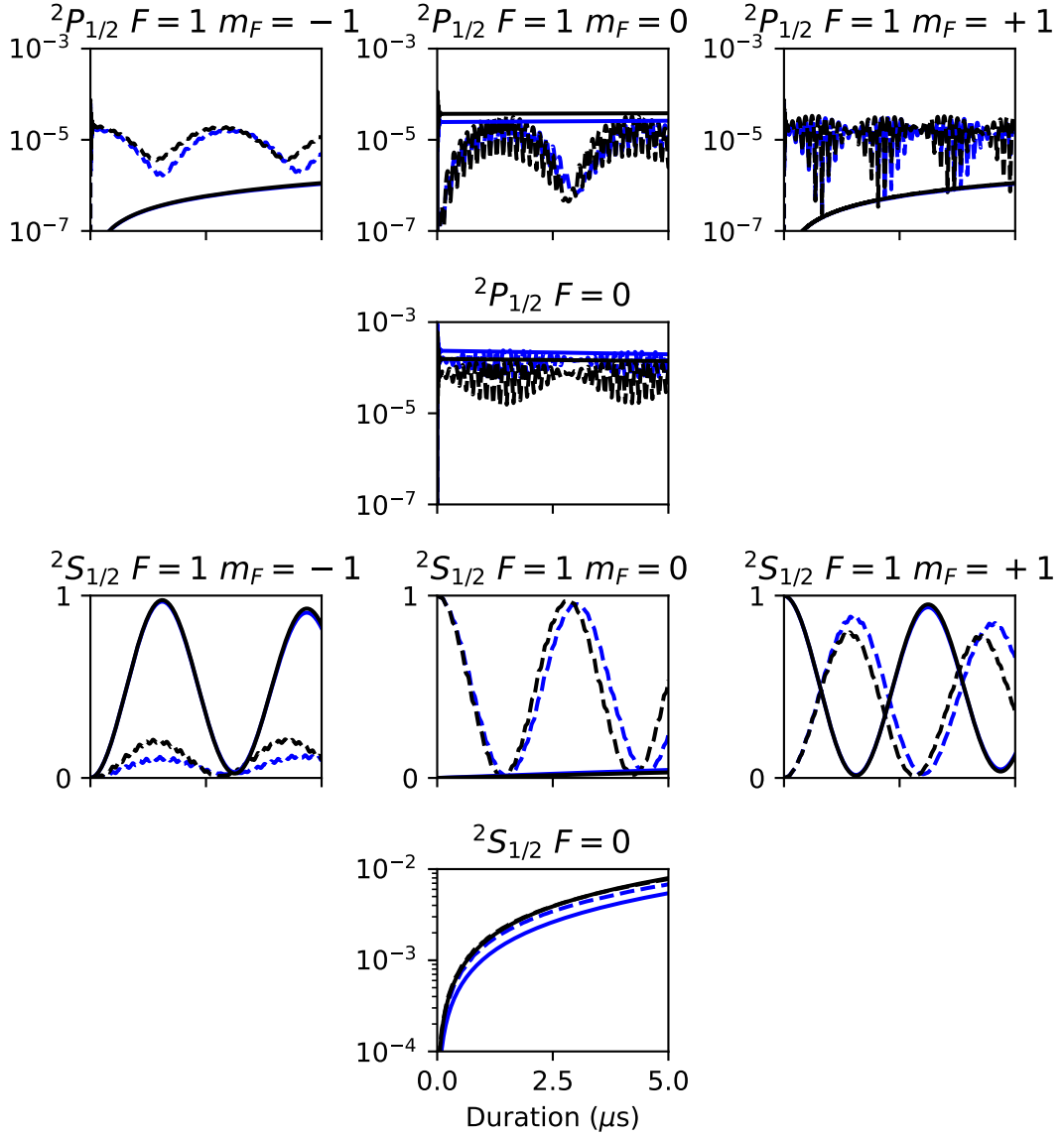


Figure B.1: Full 8-level Lindbladian simulation of Raman transitions. Sub-figures represent Grotrian diagram style sub-structure of $^2S_{1/2} \leftrightarrow ^2P_{1/2}$ system in $^{171}\text{Yb}^+$. Dashed lines represent simulations of the $|S, 1, 0\rangle \leftrightarrow |S, 1, 1\rangle$ Raman transition used in experiment. Solid lines represent the $|S, 1, 1\rangle \leftrightarrow |S, 1, -1\rangle$ scheme also used. Blue lines are with the Raman beams detuned -1 GHz from the $|S, 1, 0\rangle \leftrightarrow |P, 0, 0\rangle$ transition and black lines are with -2 GHz detuning. Rabi rates of individual Raman beams chosen to give equivalent Raman Rabi rates.

Zeeman sub-levels, as well as the effective Rabi rate of the Raman transition was found (figure B.2).

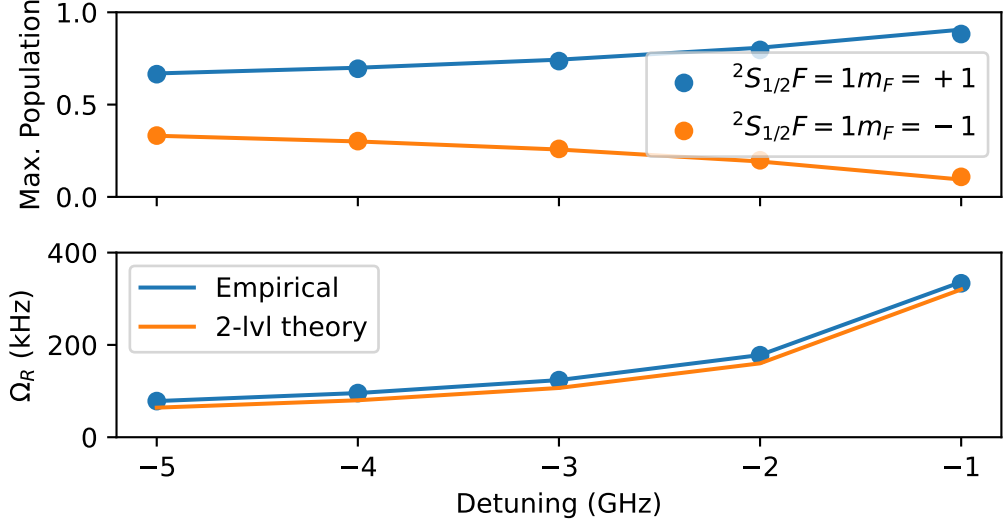


Figure B.2: (a) Results of simulations of the transfer of population from $|S, 1, 0\rangle \leftrightarrow |S, 1, \pm 1\rangle$. Empirical trends (equations 5.1 and 5.2 for trends in (a) and (b) respectively) were found. The empirical trend for Rabi rate is more accurate than the rate predicted under the 2 level adiabatic approximation for a simple Raman transition.

B.5 Raman self-interference

The Raman transition coupling states $|S, 1, -1\rangle \leftrightarrow |S, 1, 1\rangle$ ($|\uparrow\rangle \leftrightarrow |\downarrow\rangle$) via σ^\pm transitions has self-induced interference due to opposite Clebsch-Gordon coupling coefficients (figure 3.12) of $|S, 1, 1\rangle \leftrightarrow |P, 0, 0\rangle$ ($|\downarrow\rangle \leftrightarrow |e_1\rangle$, positive) and $|S, 1, 1\rangle \leftrightarrow |P, 1, 0\rangle$ ($|\downarrow\rangle \leftrightarrow |e_2\rangle$, negative) which are split in energy by $\hbar\Delta_{p,HF}$. Similar to equation 3.72, the Hamiltonian can be written as,

$$\begin{aligned}\hat{H}_0/\hbar &= \Delta |e_1\rangle \langle e_1| + (\Delta - \Delta_{p,HF}) |e_2\rangle \langle e_2| \\ \hat{H}_I/\hbar &= \frac{1}{2}(\Omega_P |\downarrow\rangle (\langle e_1| - \langle e_2|) + \Omega_S |\uparrow\rangle (\langle e_1| + \langle e_2|)) + h.c.\end{aligned}\tag{B.16}$$

After applying the adiabatic approximation to the Schrodinger equation as in equation 3.74, the coupled ODEs for the ground states becomes,

$$\begin{aligned}\dot{c}_\downarrow &= i \frac{\Omega_P \Omega_S}{4} \left(\frac{1}{\Delta} - \frac{1}{\Delta - \Delta_{p,HF}} \right) c_\uparrow + i \frac{\Omega_P^2}{4} \left(\frac{1}{\Delta} + \frac{1}{\Delta - \Delta_{p,HF}} \right) c_\downarrow \\ \dot{c}_\uparrow &= i \frac{\Omega_S^2}{4} \left(\frac{1}{\Delta} + \frac{1}{\Delta - \Delta_{p,HF}} \right) c_\uparrow + i \frac{\Omega_P \Omega_S}{4} \left(\frac{1}{\Delta} - \frac{1}{\Delta - \Delta_{p,HF}} \right) c_\downarrow\end{aligned}\quad (\text{B.17})$$

Which describes Rabi oscillations at Rabi rate

$$\Omega_R = \frac{\Omega_P \Omega_S}{2} \left(\frac{1}{\Delta} - \frac{1}{\Delta - \Delta_{p,HF}} \right) \quad (\text{B.18})$$

and a detuning of

$$\Delta_R = \frac{\Omega_S^2 - \Omega_P^2}{4} \left(\frac{1}{\Delta} + \frac{1}{\Delta - \Delta_{p,HF}} \right). \quad (\text{B.19})$$

Appendix C

Code

C.1 Ideal readout parameter estimation

Code used to determine optimal fidelity by optimizing the parameters for on-resonant saturation parameter s , readout duration T and ground-state $F = 1$ Zeeman shift δ_B . Code is used for determining optimal readout fidelity of different atomic species in section 2.2 and was adapted for determining optimal readout parameters as in section 4.2.1. It was adapted by fixing Zeeman shift to an experimentally determined value and by also extracting the threshold number by finding the argument of the minimum error in the parameter ‘errorn’.

```
import numpy as np
from numpy import pi
from scipy.special import gammaincc, factorial
from scipy.optimize import minimize

def poisson(n, lmbda):
    return np.exp(-lmbda) * lmbda ** n / factorial(n)

# P-state population from Berkeland and Boshier 2002 paper
```

```

def ionmodel171(s, Delta, theta, dB, Gamma):
    Omega = Gamma * (s/2) ** 0.5
    cost = np.cos(theta) ** 2
    sint = np.sin(theta) ** 2
    LW = (Gamma / 2) ** 2 + Omega ** 2 * (1 / 3) * cost * (
        1 - 3 * cost) / (1 + 3 * cost) + (
        cost / (1 + 3 * cost)) * (
        Omega ** 4 / (36 * dB ** 2) + 4 * dB ** 2)
    Pp0 = (3 / 4) * cost * sint / (1 + 3 * cost) \
        * Omega ** 2 * (1 / 3) / (Delta ** 2 + LW)
    return Pp0

```

```

def qbt_infidelity(stauddbn):
    # unpack tuple of saturation parameter, readout duration
    # and Zeeman splitting (natural linewidth units)
    s, T, dBn = stauddbn
    eta = 1e-3 # total detection efficiency
    k = 0 # index to select atom [Cd, Yb, Hg, Ba]
    n = np.arange(100)
    Gamma = [2*pi*50e6, 2*pi*19.6e6,
              2*pi*70e6, 1/7.92e-9]
    Gamma = Gamma[k] # Natural linewidth
    omegaHFP = [2*pi*2e9, 2*pi*2.105e9,
                2*pi*6.9e9, 2*pi*1.840e9]
    omegaHFP = omegaHFP[k] # P-state hyperfine splitting
    omegaHFS = [2*pi*14.5e9, 2*pi*12.642812e9,
                2*pi*40.5e9, 2*pi*9.931e9]
    omegaHFS = omegaHFS[k] # S-state hyperfine splitting
    dB = dBn*Gamma

```

```

delta = 0 # laser detuning from resonance

P = ionmodel171(s, delta, np.arccos(3 ** -0.5), dB, Gamma)

RB = eta*Gamma*P

RD = 0#1.39 * 343 * s + 166

Delta1 = omegaHFS + omegaHFP

Delta2 = omegaHFP

# dark and bright state lifetimes (Ejtemae et al. 2010)

gammaLd = 2/9 * Gamma * ((Gamma * (s/2) ** 0.5
                           )/(2*Delta1))**2

gammaLb = 2/27 * Gamma * ((Gamma*(s/2)**0.5)/(2*Delta2)
                           )**2 * (1-P)

def XBD(n): # B->D state mixing in readout

    term1 = -gammaLb/RB

    term2 = np.exp(RD*T*gammaLb/RB)

    term3 = (gammaLb/RB + 1) ** (-n-1)

    term4 = gammaintcc(n+1, (gammaLb/RB + 1)*(RB+RD)*T)

    term5 = gammaintcc(n+1, (gammaLb/RB + 1)*RD*T)

    return term1 * term2 * term3 * (term4 - term5)

def XDB(n): # D->B state mixing in readout

    term1 = gammaLd/RB

    term2 = np.exp(-(RD+RB)*T*gammaLd/RB)

    term3 = (-gammaLd/RB + 1) ** (-n-1)

    term4 = gammaintcc(n+1, (-gammaLd/RB + 1)*RD*T)

    term5 = gammaintcc(n+1, (-gammaLd/RB + 1)*(RD+RB)*T)

    return term1 * term2 * term3 * (term4 - term5)

```

```

# dark and bright distributions

pbrightn = np.exp(-gammaLb*T)*poisson(n, (RB+RD)*T) + XBD(n)

pbrightn[-1] = 1 - np.sum(pbrightn[:-1])

pdarkn = np.exp(-gammaLd*T)*poisson(n, RD*T) + XDB(n)

pdarkn[-1] = 1 - np.sum(pdarkn[:-1])

errorn = np.zeros_like(pbrightn)

for nn in n: # average fidelity given threshold count nn

    errorn[nn] = 0.5 * (np.sum(pbrightn[:nn]) +
                         np.sum(pdarkn[nn:]))

return np.min(errorn)

result = minimize(qbt_infidelity, (1.5, 1.5e-4, 0.3),
                   method='Powell',
                   bounds=((0, 3), (0, 7e-3), (0, 1)))

# Powell method seemed to search parameter space better
# than Nelder-Mead method.

print(100*(1-qbt_fid(result.x)))
print(result.x)

```

C.2 Angular Momentum Coupling Coefficient Calculator

Code written in Python is used to calculate the electric dipole angular momentum coupling terms. Equations are followed from Daniel Steck[96].

```

# Coupling coefficient for an electric dipole hyperfine transition
from scipy.special import factorial

# sub-function used in calculation of Wigner 6-j symbol

```

```

def Delta(a, b, c):
    return (factorial(a + b - c) * factorial(
        b + c - a) * factorial(
        c + a - b) / factorial(a + b + c + 1)) ** 0.5

def w6j(j1, j2, j3, l1, l2, l3): # Wigner 6-j symbol
    J = j1 + j2 + j3
    k1 = j1 + l2 + l3
    k2 = l1 + j2 + l3
    k3 = l1 + l2 + j3
    m1 = j1 + j2 + l1 + l2
    m2 = j2 + j3 + l2 + l3
    m3 = j3 + j1 + l3 + l1
    nmin = int(max(J, k1, k2, k3))
    nmax = int(min(m1, m2, m3))
    term1 = Delta(j1, j2, j3) * Delta(j1, l2, l3) * Delta(l1, j2,
        l3) * Delta(
        l1, l2, j3)
    term2 = 0
    for n in range(nmin, nmax + 1):
        term2 += (-1) ** n * factorial(n + 1) / (
            factorial(n - J) * factorial(n - k1) * factorial(
            n - k2) * factorial(
            n - k3) * factorial(
            m1 - n) * factorial(m2 - n) * factorial(m3 - n))
    return term1 * term2

```

```

def cgc(j1, j2, j3, m1, m2,
        m3): # <j1,m1;j2,m2|j3,m3> Clebsch-Gordon coefficient
    term1 = (m1 + m2) == m3
    term2 = (factorial(j1 + j2 - j3) * factorial(
        j1 + j3 - j2) * factorial(
        j2 + j3 - j1) / factorial(
        j1 + j2 + j3 + 1)) ** 0.5
    term3 = ((2 * j3 + 1) * factorial(j1 + m1) * factorial(
        j1 - m1) * factorial(
        j2 + m2) * factorial(
        j2 - m2) * factorial(j3 + m3) * factorial(j3 - m3)) ** 0.5
    nmin = max(j2 - j3 - m1, j1 + m2 - j3, 0)
    nmax = min(j1 - m1, j2 + m2, j1 + j2 - j3)
    term4 = 0
    for n in range(nmin, nmax + 1):
        term4 += (-1) ** n / (
            factorial(j1 - m1 - n) * factorial(
            j3 - j2 + m1 + n) * factorial(
            j2 + m2 - n) * factorial(
            j3 - j1 - m2 + n) * factorial(n) * factorial(
            j1 + j2 - j3 - n))
    return term1 * term2 * term3 * term4

```

```

I, Fe, Je, Fg, Jg, me, mg = (1 / 2, 0, 1 / 2, 1, 1 / 2, 0, 1)
term1 = (-1) ** (Fe + Jg + 1 + I)
term2 = ((2 * Fe + 1) * (2 * Jg + 1)) ** 0.5
term3 = cgc(Fe, 1, Fg, me, -(me - mg), mg)
term4 = w6j(Je, Jg, 1, Fg, Fe, I)

```

```

term5 = (2 * Je + 1) / (2 * Jg + 1)
coeff = term1 * term2 * term3 * term4 * term5
print(coeff)
# print(coeff**-2) # coefficents are typically represented as
# 1/sqrt(X)

```

C.3 Laser power stabilization algorithm

Pseudocode of the power stabilization method incorporated using Artiq and Sinara.

```

Require:  $S$                                 ▷ Setpoint target for photodiode voltage
Require:  $I$                                 ▷ Like i-value in a PID controller
Require:  $A_{min}$                             ▷ Minimum allowed output amplitude
Require:  $A_{max}$                             ▷ Maximum allowed output amplitude
Require:  $A$                                 ▷ Initial output amplitude

function RAIL( $A, A_{min}, A_{max}$ )          ▷ Limits A to min-max values
    if  $A < A_{min}$  then
         $A \leftarrow A_{min}$ 
    else if  $A > A_{max}$  then
         $A \leftarrow A_{max}$ 
    end if
    return  $A$ 
end function

 $A \leftarrow \text{RAIL}(A, A_{min}, A_{max})$ 
OUTPUTAMPLITUDE( $A$ )                      ▷ Updates RF amplitude of AOM
for  $n = 1$  to 100 do
    WAIT                                     ▷ Time delay for photodiode to respond
     $M \leftarrow \text{MEASUREPDVOLTAGE}$           ▷ Measures photodiode with ADC
     $A \leftarrow A - I \times (M - S)$             ▷ Compensates  $A$  according to  $M - S$ 

```

```

 $A \leftarrow \text{RAIL}(A, A_{min}, A_{max})$ 
 $\text{OUTPUTAMPLITUDE}(A)$ 
end for

```

C.4 Resonances Computed for Raman Thermometry

The resonances computed in the fit of the $\sim \pm 1.6$ MHz scan in figure 5.5.

Resonance (MHz)	k_x	k_y	k_z
0	0	0	0
± 0.25	± 1	∓ 1	0
± 0.33	∓ 1	± 1	± 1
± 0.58	0	0	± 1
± 0.75	0	± 1	∓ 1
± 0.83	± 1	∓ 1	± 1
± 1.00	± 1	0	∓ 1
± 1.16	0	0	± 2
± 1.33	0	± 1	0
± 1.58	± 1	0	0
± 1.91	0	± 1	± 1

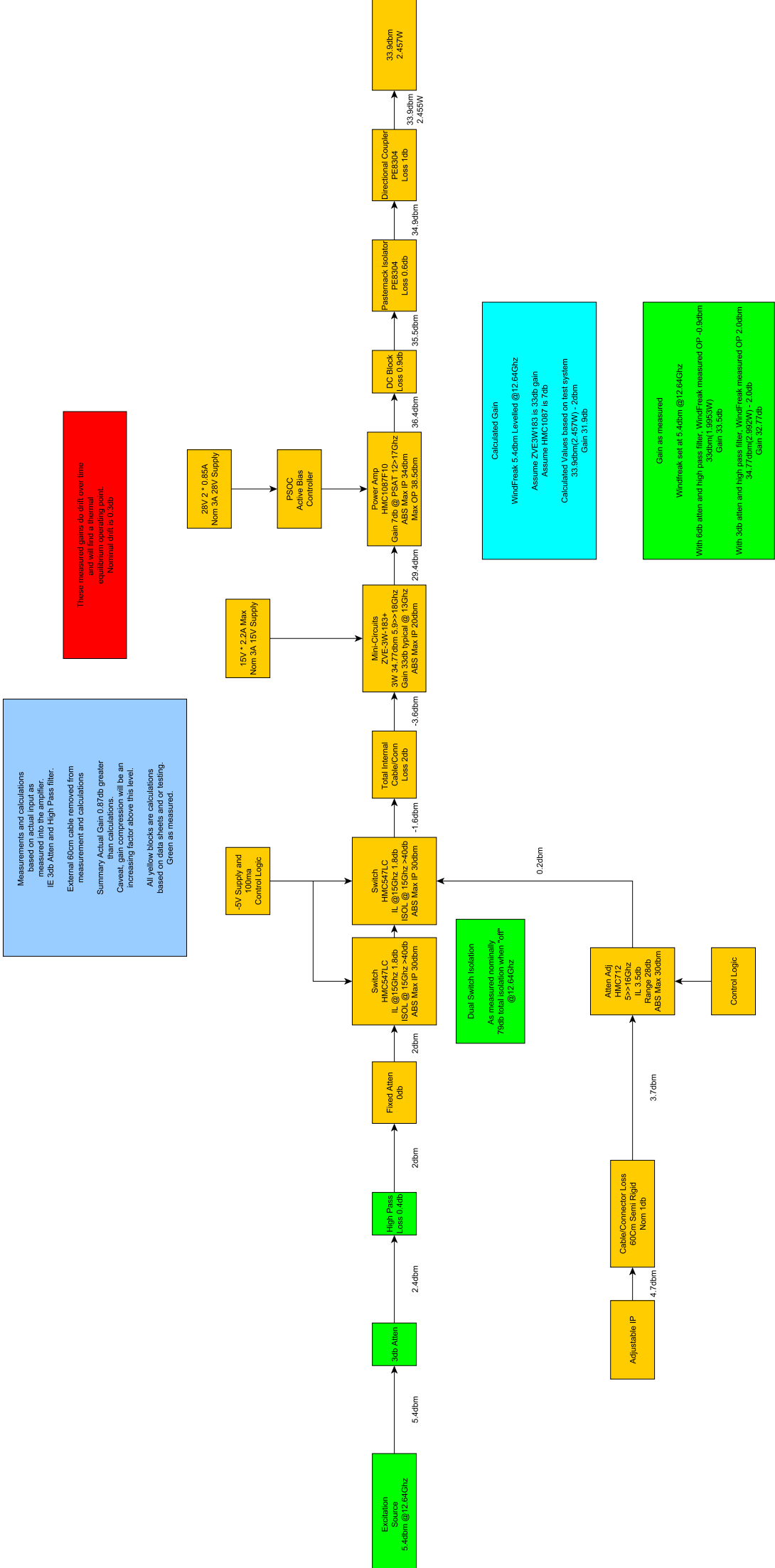
Table C.1: The resonances of different three dimensional mode combinations as given by equation 3.81 for $\omega_x/2\pi = 1.58$ MHz, $\omega_y/2\pi = 1.33$ MHz and $\omega_z/2\pi = 0.58$ MHz.

Upon retrospection, the resonances at 0.25 MHz, 0.33 MHz and 0.83 MHz could have been omitted because of their weak coupling. The 1.91 MHz resonance could have been omitted as well since it was outside the range of the scan.

Appendix D

Microwave amplifier schematic

A block diagram characterizing the microwave power through the amplifier system. The measurements and diagram are by our in-house electrical engineer.



Acronyms

ADC analog-to-digital converter. 108, 144, 220

AM amplitude modulation. 103, 144

AOM acousto-optic modulator. 1, 16, 26, 28, 103–105, 107, 108, 118, 145, 220

APD avalanche photo-diode. 25, 108, 111

CCD charge-coupled device. 23, 24, 176, 177

CPT coherent population trapping. 77, 83, 84

CW continuous wave. 1, 16, 26, 102, 104

DAC digital-to-analog converter. 97, 106, 148

DDS direct digital synthesis. 144

ECDL external cavity diode laser. 105

EIT electromagnetically-induced-transparency. 29, 34, 35, 177

EM electro-magnetic. 57, 60

EMCCD electron-multiplying charge-coupled device. 115, 117

EOM electro-optic modulator. 26, 27, 103, 104, 109, 111, 114–116

FM frequency modulation. 103

FWHM full width at half maximum. 60

GTRI Georgia Tech Research Institute. 96, 97, 146, 177

GUI graphical user interface. 97, 98

HCL hollow cathode lamp. 163, 176

HWP half-wave plate. 104, 117, 144, 168

LHC left hand circular. 79, 164–167

MOT magneto-optical trap. 177

MRI magnetic resonance imaging. 58

NIST National Institute of Standards and Technology. 19–21

NMR nuclear magnetic resonance. 58, 59

ODE ordinary differential equation. 54, 69, 138, 213

PBS polarizing beam splitter. 104, 144, 165–167

PID proportional-integral-derivative. 106, 107, 220

PMF probability mass function. 90–92, 109–111

PMT photo-multiplier tube. 25

POLEAS polarization enhanced absorption spectroscopy. 1, 154, 167–171, 173, 175, 176

PS polarisation spectroscopy. 154, 167–171, 173, 175, 176

QHO quantum harmonic oscillator. 37, 45, 46

QWP quarter-wave plate. 115, 144, 168

RF radio frequency. 20, 30, 39, 75, 96, 103–105, 108, 144–147, 149, 163, 220

RHC right hand circular. 79, 164, 165, 167

RMS root mean square. 44

RWA rotating wave approximation. 54

SAS saturated absorption spectroscopy. 102

SHE spin-heat engine. 1, 32, 33, 36

TDSE time-dependent Schrödinger equation. 46, 51, 53, 69, 73

TISE time-indepedent Schrödinger equation. 47

TTL transistor-transistor logic. 98, 105, 108

UV ultraviolet. 20, 24, 100, 101, 153

Bibliography

- [1] Jackson S. S. T. Wright, Tim Gould, André R. R. Carvalho, Salil Bedekhal, and Joan A. Vaccaro. Quantum heat engine operating between thermal and spin reservoirs. *Physical Review A*, 97:052104, 5 2018.
- [2] D. Hayes, D. N. Matsukevich, P. Maunz, D. Hucul, Q. Quraishi, S. Olmschenk, W. Campbell, J. Mizrahi, C. Senko, and C. Monroe. Entanglement of Atomic Qubits Using an Optical Frequency Comb. *Physical Review Letters*, 104(14):140501, apr 2010.
- [3] W. C. Campbell, J. Mizrahi, Q. Quraishi, C. Senko, D. Hayes, D. Hucul, D. N. Matsukevich, P. Maunz, and C. Monroe. Ultrafast gates for single atomic qubits. *Physical Review Letters*, 105(9):090502, aug 2010.
- [4] B. B. Blinov, C. Monroe, D. Stick, D. L. Moehring, K. Brickman, L. Deslauriers, M. J. Madsen, P. J. Lee, and R. Miller. Atomic qubit manipulations with an electro-optic modulator. *Optics Letters*, Vol. 28, Issue 17, pp. 1582-1584, 28:1582–1584, 9 2003.
- [5] K. Kim, S. Korenblit, R. Islam, E. E. Edwards, M. S. Chang, C. Noh, H. Carmichael, G. D. Lin, L. M. Duan, C. C. Joseph Wang, J. K. Freericks, and C. Monroe. Quantum simulation of the transverse Ising model with trapped ions. *New Journal of Physics*, 13(10):105003, oct 2011.
- [6] The Nobel Prize in Physics 1989. <https://www.nobelprize.org/prizes/physics/1989/summary/>.

- [7] The Nobel Prize in Physics 2012. <https://www.nobelprize.org/prizes/physics/2012/summary/>.
- [8] Volker Strobel. Pold87/academic-keyword-occurrence: First release. *Zenodo*, apr 2018.
- [9] S. M. Brewer, J. S. Chen, A. M. Hankin, E. R. Clements, C. W. Chou, D. J. Wineland, D. B. Hume, and D. R. Leibrandt. Al+ 27 Quantum-Logic Clock with a Systematic Uncertainty below 10-18. *Physical Review Letters*, 123(3):033201, jul 2019.
- [10] Xin Zheng, Jonathan Dolde, Varun Lochab, Brett N. Merriman, Haoran Li, and Shimon Kolkowitz. Differential clock comparisons with a multiplexed optical lattice clock. *Nature* 2022 602:7897, 602(7897):425–430, feb 2022.
- [11] Tobias Bothwell, Colin J. Kennedy, Alexander Aepli, Dhruv Kedar, John M. Robinson, Eric Oelker, Alexander Staron, and Jun Ye. Resolving the gravitational redshift across a millimetre-scale atomic sample. *Nature* 2022 602:7897, 602(7897):420–424, feb 2022.
- [12] J. M. Pino, J. M. Dreiling, C. Figgatt, J. P. Gaebler, S. A. Moses, M. S. Allman, C. H. Baldwin, M. Foss-Feig, D. Hayes, K. Mayer, C. Ryan-Anderson, and B. Neyenhuis. Demonstration of the trapped-ion quantum ccd computer architecture. *Nature* 2021 592:7853, 592:209–213, 4 2021.
- [13] Chris Ballance and Tom Harty. Oxford ionics — high performance quantum computing, 2021.
- [14] October 1, 2021 — IonQ Becomes First Publicly Traded, Pure-Play Quantum Computing Company. <https://ionq.com/news/october-01-2021-ionq-listed-on-nyse>.

- [15] J. C. Bergquist, Randall G. Hulet, Wayne M. Itano, and D. J. Wineland. Observation of Quantum Jumps in a Single Atom. *Physical Review Letters*, 57(14):1699, oct 1986.
- [16] Frank Diedrich and Herbert Walther. Nonclassical radiation of a single stored ion. *Physical Review Letters*, 58(3):203, jan 1987.
- [17] Q. A. Turchette, C. S. Wood, B. E. King, C. J. Myatt, D. Leibfried, W. M. Itano, C. Monroe, and D. J. Wineland. Deterministic Entanglement of Two Trapped Ions. *Physical Review Letters*, 81(17):3631, oct 1998.
- [18] Gleb Maslennikov, Shiqian Ding, Roland Hablützel, Jaren Gan, Alexandre Roulet, Stefan Nimmrichter, Jibo Dai, Valerio Scarani, and Dzmitry Matsukevich. Quantum absorption refrigerator with trapped ions. *Nature Communications*, 10:1–8, 12 2019.
- [19] D. Von Lindenfels, O. Gräb, C. T. Schmiegelow, V. Kaushal, J. Schulz, Mark T. Mitchison, John Goold, F. Schmidt-Kaler, and U. G. Poschinger. Spin heat engine coupled to a harmonic-oscillator flywheel. *Physical Review Letters*, 123:080602, 8 2019.
- [20] B. B. Blinov, D. L. Moehring, L. M. Duan, and C. Monroe. Observation of entanglement between a single trapped atom and a single photon. *Nature*, 428(6979):153–157, mar 2004.
- [21] Wolfgang Paul. Electromagnetic traps for charged and neutral particles. *Reviews of Modern Physics*, 62(3):531–540, jul 1990.
- [22] D. Wineland and H. Dehmelt. Line shifts and widths of axial, cyclotron and G-2 resonances in tailored, stored electron (ion) cloud. *International Journal of Mass Spectrometry and Ion Physics*, 16(3):338–342, mar 1975.

- [23] F. G. Major and G. Werth. High-Resolution Magnetic Hyperfine Resonance in Harmonically Bound Ground-State ^{199}Hg Ions. *Physical Review Letters*, 30(23):1155, jun 1973.
- [24] Zhang Jian-Ming, Zou De-Shu, Xu Chen, al, Jong Kyu Kim, Hong Luo, and Yangang Xi. Optical Detection of Ions Confined in a rf Quadrupole Trap. *Metrologia*, 13(3):167, jul 1977.
- [25] D. J. Wineland, R. E. Drullinger, and F. L. Walls. Radiation-pressure cooling of bound resonant absorbers. *Physical Review Letters*, 40(25):1639–1642, jun 1978.
- [26] W. Neuhauser, M. Hohenstatt, P. Toschek, and H. Dehmelt. Optical-Sideband Cooling of Visible Atom Cloud Confined in Parabolic Well. *Physical Review Letters*, 41(4):233, jul 1978.
- [27] W. Neuhauser, M. Hohenstatt, P. E. Toschek, and H. Dehmelt. Localized visible Ba+ mono-ion oscillator. *Physical Review A*, 22(3):1137, sep 1980.
- [28] R. Blatt, H. Schnatz, and G. Werth. Ultrahigh-Resolution Microwave Spectroscopy on Trapped $^{171}\text{Yb}^+$ Ions. *Physical Review Letters*, 48(23):1601, jun 1982.
- [29] R. Blatt, H. Schnatz, and G. Werth. Precise determination of the $^{171}\text{Yb}^+$ ground state Hyperfine separation. *Zeitschrift für Physik A Atoms and Nuclei* 1983 312:3, 312(3):143–147, sep 1983.
- [30] Ch Gerz, J. Roths, F. Vedel, and G. Werth. Lifetime and collisional depopulation of the metastable 5D 3/2-state of Yb+. *Zeitschrift für Physik D Atoms, Molecules and Clusters* 1988 8:3, 8(3):235–237, sep 1988.
- [31] H. Lehmitz, J. Hattendorf-Ledwoch, R. Blatt, and H. Harde. Population trapping in excited Yb ions. *Physical Review Letters*, 62(18):2108, may 1989.

- [32] R. Casdorff, V. Enders, R. Blatt, W. Neuhauser, and P. E. Toschek. A 12-GHz Standard Clock on Trapped Ytterbium Ions. *Annalen der Physik*, 503(1-3):41–55, jan 1991.
- [33] H. Harde, H. Lehmitz, J. Hattendorf-Ledwoch, and R. Blatt. Self-induced zeeman coherences in a Paul trap. *Applied Physics B* 1991 53:3, 53(3):131–137, sep 1991.
- [34] J. C. Bergquist, Wayne M. Itano, and D. J. Wineland. Recoilless optical absorption and Doppler sidebands of a single trapped ion. *Physical Review A*, 36(1):428, jul 1987.
- [35] M. G. Raizen, J. M. Gilligan, J. C. Bergquist, W. M. Itano, and D. J. Wineland. Ionic crystals in a linear Paul trap. *Physical Review A*, 45(9):6493, may 1992.
- [36] W M Itano, J C Bergquist, J J Bollinger, J M Gilligan, D J Heinzen, F L Moore, M G Raizen, and D J Wineland. Quantum projection noise: Population fluctuations in two l-evel systems. *PHYSICAL REVIEW A*, 47(5), 1993.
- [37] S. R. Jefferts, C. Monroe, E. W. Bell, and D. J. Wineland. Coaxial-resonator-driven rf (Paul) trap for strong confinement. *Physical Review A*, 51(4):3112, apr 1995.
- [38] C. Monroe, D. M. Meekhof, B. E. King, S. R. Jefferts, W. M. Itano, D. J. Wineland, and P. Gould. Resolved-Sideband Raman Cooling of a Bound Atom to the 3D Zero-Point Energy. *Physical Review Letters*, 75(22):4011, nov 1995.
- [39] D. Leibfried, D. M. Meekhof, B. E. King, C. Monroe, W. M. Itano, and D. J. Wineland. Experimental Determination of the Motional Quantum State of a Trapped Atom. *Physical Review Letters*, 77(21):4281, nov 1996.

- [40] D. Leibfried, D. M. Meekhof, C. Monroe, B. E. King, W. M. Itano, and D. J. Wineland. Experimental preparation and measurement of quantum states of motion of a trapped atom. *Journal of Modern Optics*, 44-11(12):2485–2505, 1997.
- [41] J. I. Cirac and P. Zoller. Quantum computations with cold trapped ions. *Physical Review Letters*, 74(20):4091–4094, 1995.
- [42] C. Monroe, D. M. Meekhof, B. E. King, W. M. Itano, and D. J. Wineland. Demonstration of a Fundamental Quantum Logic Gate. *Physical Review Letters*, 75(25):4714, dec 1995.
- [43] Ferdinand Schmidt-Kaler, Hartmut Häffner, Mark Riebe, Stephan Gulde, Gavin P.T. Lancaster, Thomas Deuschle, Christoph Becher, Christian F. Roos, Jürgen Eschner, and Rainer Blatt. Realization of the Cirac–Zoller controlled-NOT quantum gate. *Nature 2003* 422:6930, 422(6930):408–411, mar 2003.
- [44] Anders Sørensen and Klaus Mølmer. Quantum Computation with Ions in Thermal Motion. *Physical Review Letters*, 82(9):1971, mar 1999.
- [45] Anders Sørensen and Klaus Mølmer. Entanglement and quantum computation with ions in thermal motion. *Physical Review A*, 62(2):022311, jul 2000.
- [46] K. Wright, K. M. Beck, S. Debnath, J. M. Amini, Y. Nam, N. Grzesiak, J. S. Chen, N. C. Pisenti, M. Chmielewski, C. Collins, K. M. Hudek, J. Mizrahi, J. D. Wong-Campos, S. Allen, J. Apisdorf, P. Solomon, M. Williams, A. M. Ducore, A. Blinov, S. M. Kreikemeier, V. Chaplin, M. Keesan, C. Monroe, and J. Kim. Benchmarking an 11-qubit quantum computer. *Nature Communications*, 10:1–6, 12 2019.

- [47] J. J. García-Ripoll, P. Zoller, and J. I. Cirac. Speed optimized two-qubit gates with laser coherent control techniques for ion trap quantum computing. *Physical Review Letters*, 91(15), 2003.
- [48] D. Heinrich, M. Guggemos, M. Guevara-Bertsch, M. I. Hussain, C. F. Roos, and R. Blatt. Ultrafast coherent excitation of a $^{40}\text{Ca}^+$ ion. *New Journal of Physics*, 21(7):073017, jul 2019.
- [49] M. I. Hussain, D. Heinrich, M. Guevara-Bertsch, E. Torrontegui, J. J. García-Ripoll, C. F. Roos, and R. Blatt. Ultraviolet Laser Pulses with Multigigahertz Repetition Rate and Multiwatt Average Power for Fast Trapped-Ion Entanglement Operations. *Physical Review Applied*, 15(2):024054, feb 2021.
- [50] Mahmood Irtiza Hussain, Matthew Joseph Petrasius, Christopher D. B. Bentley, Richard L. Taylor, André R. R. Carvalho, Joseph J. Hope, Erik W. Streed, Mirko Lobino, and David Kielpinski. Ultrafast, high repetition rate, ultraviolet, fiber-laser-based source: application towards Yb^+ fast quantum-logic. *Optics Express*, 24(15):16638, jul 2016.
- [51] Kenji Shimizu, Jordan Scarabel, Elizabeth Bridge, Steven Connell, Moj Ghadimi, Ben Haylock, Mahmood Irtiza Hussain, Erik Streed, and Mirko Lobino. Ultrafast coherent excitation of an ytterbium ion with single laser pulses. *Applied Physics Letters*, 119(21):214003, nov 2021.
- [52] J. D. Wong-Campos, S. A. Moses, K. G. Johnson, and C. Monroe. Demonstration of Two-Atom Entanglement with Ultrafast Optical Pulses. *Physical Review Letters*, 119(23), dec 2017.
- [53] L. M. Duan, M. J. Madsen, D. L. Moehring, P. Maunz, R. N. Kohn, and C. Monroe. Probabilistic quantum gates between remote atoms through interference of optical frequency qubits. *Physical Review A - Atomic, Molecular, and Optical Physics*, 73(6):062324, jun 2006.

- [54] D. L. Moehring, P. Maunz, S. Olmschenk, K. C. Younge, D. N. Matsukevich, L. M. Duan, and C. Monroe. Entanglement of single-atom quantum bits at a distance. *Nature*, 449(7158):68–71, sep 2007.
- [55] Suryansh Upadhyay, Abdullah Ash Saki, Rasit Onur Topaloglu, and Swaroop Ghosh. A Shuttle-Efficient Qubit Mapper for Trapped-Ion Quantum Computers, apr 2022.
- [56] M Acton, K.-A. Brickman, P. C. Haljan, P. J. Lee, L. Deslauriers, and C. Monroe. Near-perfect simultaneous measurement of a qubit register. *Quantum Info. Comput.*, 6(6):465–482, September 2006.
- [57] David Hucul, Justin E. Christensen, Eric R. Hudson, and Wesley C. Campbell. Spectroscopy of a Synthetic Trapped Ion Qubit. *Physical Review Letters*, 119(10):100501, sep 2017.
- [58] C. Guet and W. R. Johnson. Relativistic many-body calculations of transition rates for Ca+, Sr+ and Ba+. *Physical Review A*, 44(3):1531, aug 1991.
- [59] G. Audi, O. Bersillon, J. Blachot, and A. H. Wapstra. The Nubase evaluation of nuclear and decay properties. *Nuclear Physics A*, 729(1):3–128, dec 2003.
- [60] R W Berends, E H Pinnington, B Guo, and Q Ji. Beam-laser lifetime measurements for four resonance levels of Yb II. *Journal of Physics B: Atomic, Molecular and Optical Physics*, 26(20):L701, oct 1993.
- [61] S. Olmschenk, K. C. Younge, D. L. Moehring, D. N. Matsukevich, P. Maunz, and C. Monroe. Manipulation and detection of a trapped Yb + hyperfine qubit. *Physical Review A*, 76(5):052314, nov 2007.
- [62] S. Ejtemaei, R. Thomas, and P. C. Haljan. Optimization of Yb+ fluorescence and hyperfine-qubit detection. *Physical Review A - Atomic, Molecular, and Optical Physics*, 82(6):063419, dec 2010.

- [63] D. J. Berkeland and M. G. Boshier. Destabilization of dark states and optical spectroscopy in Zeeman-degenerate atomic systems. *Physical Review A - Atomic, Molecular, and Optical Physics*, 65(3):13, feb 2002.
- [64] L. Deslauriers, P. C. Haljan, P. J. Lee, K. A. Brickman, B. B. Blinov, M. J. Madsen, and C. Monroe. Zero-point cooling and low heating of trapped $^{111}\text{Cd}^+$ ions. *Physical Review A - Atomic, Molecular, and Optical Physics*, 70:043408, 10 2004.
- [65] Peter T.H. Fisk, Matthew J. Sellars, Malcolm A. Lawn, and Colin Coles. Accurate measurement of the 12.6 GHz clock transition in trapped $^{171}\text{Yb}^+$ ions. *IEEE Transactions on Ultrasonics, Ferroelectrics, and Frequency Control*, 44(2):344–354, 1997.
- [66] J. Mizrahi, B. Neyenhuis, K. G. Johnson, W. C. Campbell, C. Senko, D. Hayes, and C. Monroe. Quantum control of qubits and atomic motion using ultrafast laser pulses. *Applied Physics B: Lasers and Optics*, 114(1-2):45–61, jan 2014.
- [67] D. Hayes, S. M. Clark, S. Debnath, D. Hucul, I. V. Inlek, K. W. Lee, Q. Quraishi, and C. Monroe. Coherent error suppression in multiqubit entangling gates. *Physical Review Letters*, 109(2):020503, jul 2012.
- [68] Christopher M. Seck, Mark G. Kokish, Matthew R. Dietrich, and Brian C. Odom. Raman sideband cooling of a $\text{Ba}^+ 138$ ion using a zeeman interval. *Physical Review A*, 93:053415, 5 2016.
- [69] Simon Webster. *Raman Sideband Cooling and Coherent Manipulation of Trapped Ions*. PhD thesis, St. John’s College, University of Oxford, 2005.
- [70] F. Schmidt-Kaler, J. Eschner, G. Morigi, C. F. Roos, D. Leibfried, A. Mundt, and R. Blatt. Laser cooling with electromagnetically induced

transparency: application to trapped samples of ions or neutral atoms.

Applied Physics B 2001 73:8, 73(8):807–814, mar 2014.

- [71] I. V. Inlek, C. Crocker, M. Lichtman, K. Sosnova, and C. Monroe. Multispecies Trapped-Ion Node for Quantum Networking. *Physical Review Letters*, 118(25):250502, jun 2017.
- [72] Peter Blythe. *Optical frequency measurement and ground state cooling of single trapped Yb + ions*. PhD thesis, University of London, 8 2005.
- [73] Sebastian Deffner. *Quantum Thermodynamics*. IOP Publishing, jul 2019.
- [74] Johannes Roßnagel, Samuel T. Dawkins, Karl N. Tolazzi, Obinna Abah, Eric Lutz, Ferdinand Schmidt-Kaler, and Kilian Singer. A single-atom heat engine. *Science*, 352:325–329, 4 2016.
- [75] John E. Shaw. Comparing Carnot, Stirling, Otto, Brayton and Diesel Cycles. *Transactions of the Missouri Academy of Science*, 42(2008):1–6, jan 2008.
- [76] C. T. Schmiegelow, H. Kaufmann, T. Ruster, J. Schulz, V. Kaushal, M. Hettrich, F. Schmidt-Kaler, and U. G. Poschinger. Phase-stable free-space optical lattices for trapped ions. *Physical Review Letters*, 116:033002, 1 2016.
- [77] Charles H. Bennett. The thermodynamics of computation—a review. *International Journal of Theoretical Physics* 1982 21:12, 21(12):905–940, dec 1982.
- [78] E. T. Jaynes. Information Theory and Statistical Mechanics. *Physical Review*, 106(4):620, may 1957.
- [79] E. T. Jaynes. Information Theory and Statistical Mechanics. II. *Physical Review*, 108(2):171, oct 1957.

- [80] Joan A. Vaccaro and Stephen M. Barnett. Information erasure without an energy cost. *Proceedings of the Royal Society A: Mathematical, Physical and Engineering Sciences*, 467:1770–1778, 6 2011.
- [81] Regina Lechner, Christine Maier, Cornelius Hempel, Petar Jurcevic, Ben P. Lanyon, Thomas Monz, Michael Brownnutt, Rainer Blatt, and Christian F. Roos. Electromagnetically-induced-transparency ground-state cooling of long ion strings. *Physical Review A*, 93(5):053401, may 2016.
- [82] L. Ratschbacher, C. Sias, L. Carcagni, J. M. Silver, C. Zipkes, and M. Köhl. Decoherence of a Single-Ion Qubit Immersed in a Spin-Polarized Atomic Bath. *Physical Review Letters*, 110(16):160402, apr 2013.
- [83] Tomas Sikorsky, Ziv Meir, Ruti Ben-shlomi, Nitzan Akerman, and Roee Ozeri. Spin-controlled atom–ion chemistry. *Nature Communications* 2018 9:1, 9(1):1–5, mar 2018.
- [84] L. Feng, W. L. Tan, A. De, A. Menon, A. Chu, G. Pagano, and C. Monroe. Efficient Ground-State Cooling of Large Trapped-Ion Chains with an Electromagnetically-Induced-Transparency Tripod Scheme. *Physical Review Letters*, 125(5):053001, jul 2020.
- [85] C. S. Roos, D. Leibfried, A. Mundt, F. Schmidt-Kaler, J. Eschner, and R. Blatt. Experimental Demonstration of Ground State Laser Cooling with Electromagnetically Induced Transparency. *Physical Review Letters*, 85(26):5547, dec 2000.
- [86] Dianqiang Su, Ruijuan Liu, Zhonghua Ji, al, Manuel Vogel, David E Pritchard, and Michael P Bradley. Atom traps compared with ion traps. *Physica Scripta*, 1995(T59):131, jan 1995.

- [87] Carl E. Wieman, David E. Pritchard, and David J. Wineland. Atom cooling, trapping, and quantum manipulation. *Reviews of Modern Physics*, 71(2):S253, mar 1999.
- [88] *NIST Digital Library of Mathematical Functions*. <http://dlmf.nist.gov/>, Release 1.1.3 of 2021-09-15. F. W. J. Olver, A. B. Olde Daalhuis, D. W. Lozier, B. I. Schneider, R. F. Boisvert, C. W. Clark, B. R. Miller, B. V. Saunders, H. S. Cohl, and M. A. McClain, eds.
- [89] Dalton T. Snyder, Wen Ping Peng, and R. Graham Cooks. Resonance methods in quadrupole ion traps. *Chemical Physics Letters*, 668:69–89, jan 2017.
- [90] H.J.W. Muller-kirsten. *Introduction To Quantum Mechanics: Schrodinger Equation And Path Integral (Second Edition)*. World Scientific Publishing Company, 2012.
- [91] Viorica N. Gheorghe, F. G. Major, and Günther Werth. *Charged Particle Traps II*. Springer-Verlag Berlin Heidelberg, 2009.
- [92] Patrick P. Hofer, Martí Perarnau-Llobet, L. David M. Miranda, Géraldine Haack, Ralph Silva, Jonatan Bohr Brask, and Nicolas Brunner. Markovian master equations for quantum thermal machines: local versus global approach. *New Journal of Physics*, 19(12):123037, dec 2017.
- [93] B G Norton, E W Streed, M J Petrasius, A Jechow, and D Kielpinski. Millikelvin spatial thermometry of trapped ions. *New Journal of Physics*, 13(11):113022, nov 2011.
- [94] E. Schrödinger. An Undulatory Theory of the Mechanics of Atoms and Molecules. *Physical Review*, 28(6):1049, dec 1926.
- [95] L. Allen and J. H. Eberly. *Optical Resonance and Two-Level Atoms*. Dover Publications, Inc., New York, 1987.

- [96] Daniel A. Steck. *Quantum and Atom Optics*. available online at <http://steck.us/teaching>, revision 0.12.6, 23 April edition, 2019.
- [97] D. L. Moskovkin and V. M. Shabaev. Zeeman effect of the hyperfine-structure levels in hydrogenlike ions. *Physical Review A*, 73(5):052506, may 2006.
- [98] A. S. Bell, P. Gill, H. A. Klein, A. P. Levick, Chr Tamm, and D. Schnier. Laser cooling of trapped ytterbium ions using a four-level optical-excitation scheme. *Physical Review A*, 44(1):R20, jul 1991.
- [99] V. Weisskopf and E. Wigner. Berechnung der natürlichen Linienbreite auf Grund der Diracschen Lichttheorie. *Zeitschrift für Physik* 1930 63:1, 63(1):54–73, jan 1930.
- [100] Jaideep Singh. The E1 & M1 Spontaneous Decay Rates for an Emitter Inside a Cavity Within a Medium. Technical report, Michigan State University, 2014.
- [101] Anthony E. Siegman. *Lasers*. University Science Books, 1986.
- [102] Bahaa E. A. Saleh and Malvin Carl Teich. *Fundamentals of photonics*. Wiley series in pure and applied optics. Wiley, New Jersey, 2nd ed. edition, 2007.
- [103] Igor Dotsenko. Raman spectroscopy of single atoms. *Diplom Theses, Bonn University*, 2002.
- [104] Ben Q Baragiola and Jason Twamley. Generating nonclassical states of motion using spontaneous emission. *New Journal of Physics*, 20(7):073029, jul 2018.
- [105] J. R. Johansson, P. D. Nation, and Franco Nori. QuTiP 2: A Python framework for the dynamics of open quantum systems. *Computer Physics Communications*, 184(4):1234–1240, apr 2013.

- [106] D. J. Wineland and Wayne M. Itano. Laser cooling of atoms. *Physical Review A*, 20(4):1521, oct 1979.
- [107] S. Alighanbari, M. G. Hansen, V. I. Korobov, and S. Schiller. Rotational spectroscopy of cold and trapped molecular ions in the Lamb–Dicke regime. *Nature Physics* 2018 14:6, 14(6):555–559, mar 2018.
- [108] J. Steinbach, J. Twamley, and P. L. Knight. Engineering two-mode interactions in ion traps. *Physical Review A*, 56(6):4815, dec 1997.
- [109] Rogerio de Sousa. Electron Spin as a Spectrometer of Nuclear-Spin Noise and Other Fluctuations. *Topics in Applied Physics*, 115:183–220, 2009.
- [110] Harrison Ball, William D. Oliver, and Michael J. Biercuk. The role of master clock stability in quantum information processing. *npj Quantum Information* 2016 2:1, 2(1):1–8, nov 2016.
- [111] Norbert Wiener. Generalized harmonic analysis. *Acta Mathematica*, 55(none):117–258, 1930.
- [112] John R. de Laeter and Nino Bukilic. The isotopic composition and atomic weight of ytterbium. *International Journal of Mass Spectrometry*, 252(3):222–227, jun 2006.
- [113] M Aymar, A Debarre, and O Robaux. Highly excited levels of neutral ytterbium. II. Multichannel quantum defect analysis of odd- and even-parity spectra. *Journal of Physics B: Atomic and Molecular Physics (1968-1987)*, 13(6):1089, mar 1980.
- [114] William F. Meggers. The Second Spectrum of Ytterbium (Yb II). *Journal of Research of the National Bureau of Standards. Section A, Physics and Chemistry*, 71A(6):396, nov 1967.

- [115] N. Yu and L. Maleki. Lifetime measurements of the $4f^{14}5d$ metastable states in single ytterbium ions. *Physical Review A*, 61(2):022507, jan 2000.
- [116] E Biémont, J-F Dutrieux, I Martin, and P Quinet. Lifetime calculations in Yb II. *Journal of Physics B: Atomic, Molecular and Optical Physics*, 31(15):3321, aug 1998.
- [117] Ann-Marie Mårtensson-Pendrill, David S. Gough, and Peter Hannaford. Isotope shifts and hyperfine structure in the 369.4-nm $6s - 6p_{1/2}$ resonance line of singly ionized ytterbium. *Physical Review A*, 49(5):3351, may 1994.
- [118] M. Roberts, P. Taylor, G. P. Barwood, W. R. C. Rowley, and P. Gill. Observation of the $2S1/2-2F7/2$ electric octupole transition in a single $^{171}\text{Yb}^+$ ion. *Physical Review A*, 62(2):020501, jul 2000.
- [119] P. Taylor, M. Roberts, S. V. Gateva-Kostova, R. B. M. Clarke, G. P. Barwood, W. R. C. Rowley, and P. Gill. Investigation of the $2S1/2-2D5/2$ clock transition in a single ytterbium ion. *Physical Review A*, 56(4):2699, oct 1997.
- [120] Y. Y. Jau, J. D. Hunker, and P. D.D. Schwindt. F-state quenching with CH₄ for buffer-gas cooled ^{171}Y b+ frequency standard. *AIP Advances*, 5(11):117209, nov 2015.
- [121] M. Roberts, P. Taylor, S. V. Gateva-Kostova, R. B. M. Clarke, W. R. C. Rowley, and P. Gill. Measurement of the $2S1/2-2D5/2$ clock transition in a single $^{171}\text{Yb}^+$ ion. *Physical Review A*, 60(4):2867, oct 1999.
- [122] Pengfei Wang, Chun-Yang Luan, Mu Qiao, Mark Um, Junhua Zhang, Ye Wang, Xiao Yuan, Mile Gu, Jingning Zhang, and Kihwan Kim. Single ion qubit with estimated coherence time exceeding one hour. *Nature Communications* 2021 12:1, 12(1):1–8, jan 2021.

- [123] Sabine Wölk, Christian Piltz, Theeraphot Sriarunothai, and Christof Wunderlich. State selective detection of hyperfine qubits. *Journal of Physics B: Atomic, Molecular and Optical Physics*, 48(7):075101, apr 2015.
- [124] Moji Ghadimi, Valdis Blums, Benjamin G. Norton, Paul M. Fisher, Steven C. Connell, Jason M. Amini, Curtis Volin, Harley Hayden, Chien Shing Pai, David Kielpinski, Mirko Lobino, and Erik W. Streed. Scalable ion-photon quantum interface based on integrated diffractive mirrors. *npj Quantum Information*, 3(1):1–4, dec 2017.
- [125] Edwin B. Wilson. Probable Inference, the Law of Succession, and Statistical Inference. *Journal of the American Statistical Association*, 22(158):209–212, 1927.
- [126] Sébastien Bourdeauducq, Whitequark, Robert Jördens, Yann Sionneau, Enjoy-digital, Cjbe, David Nadlinger, Hartytp, JBoulder, Daniel Slichter, Drew, Mntng, R-srinivas, Apatura-iris, Stewart Mackenzie, Z. Smith, Paweł K, Marius Weber, Kemstevens, Felix Held, and David Leibrandt. m-labs/artiq: 4.0, nov 2018.
- [127] SynthHD: Dual Channel RF Signal Generator With 10 MHZ - 15 GHZ.
- [128] GTRI Microwave I ion traps for QIP applications.
- [129] Thai M. Hoang, Yuan Yu Jau, Richard Overstreet, and Peter D.D. Schwindt. YbH⁺ formation in an ytterbium ion trap. *Physical Review A*, 101(2), feb 2020.
- [130] M. Harlander, M. Brownnutt, W. Hänsel, and R. Blatt. Trapped-ion probing of light-induced charging effects on dielectrics. *New Journal of Physics*, 12(9):093035, sep 2010.
- [131] Moji Ghadimi, Elizabeth M. Bridge, Jordan Scarabel, Steven Connell, Kenji Shimizu, Erik Streed, Erik Streed, Mirko Lobino, and

- Mirko Lobino. Multichannel optomechanical switch and locking system for wavemeters. *Applied Optics*, Vol. 59, Issue 17, pp. 5136-5141, 59(17):5136–5141, jun 2020.
- [132] Erik W. Streed, Jongchul Mun, Micah Boyd, Gretchen K. Campbell, Patrick Medley, Wolfgang Ketterle, and David E. Pritchard. Continuous and pulsed quantum zeno effect. *Physical Review Letters*, 97(26):260402, dec 2006.
- [133] Derek F. Kimball, Dmitry Budker, Evgeniy B. Alexandrov, Marcis Auzinsh, Simon M. Rochester, and Valeriy V. Yashchuk. Dynamic effects in nonlinear magneto-optics of atoms and molecules: review. *JOSA B*, Vol. 22, Issue 1, pp. 7-20, 22(1):7–20, jan 2005.
- [134] D. J. Berkeland, J. D. Miller, W. M. Itano, and D. J. Wineland. Laser-Cooled Mercury Ion Frequency Standard. *Physical Review Letters*, 80(10):2089, mar 1998.
- [135] S. Charles Doret, Jason M. Amini, Kenneth Wright, Curtis Volin, Tyler Killian, Arkadas Ozakin, Douglas Denison, Harley Hayden, C. S. Pai, Richart E. Slusher, and Alexa W. Harter. Controlling trapping potentials and stray electric fields in a microfabricated ion trap through design and compensation. *New Journal of Physics*, 14(7):073012, jul 2012.
- [136] Siu Kwan Lam, Antoine Pitrou, and Stanley Seibert. Numba. In *LLVM '15: Proceedings of the Second Workshop on the LLVM Compiler Infrastructure in HPC*, pages 1–6, Austin, Texas, 2015. Association for Computing Machinery (ACM).
- [137] N. Daniilidis, S. Narayanan, S. A. Möller, R. Clark, T. E. Lee, P. J. Leek, A. Wallraff, St Schulz, F. Schmidt-Kaler, and H. Häffner. Fabrication and heating rate study of microscopic surface electrode ion traps. *New Journal of Physics*, 13(1):013032, jan 2011.

- [138] R. J. Epstein, S. Seidelin, D. Leibfried, J. H. Wesenberg, J. J. Bollinger, J. M. Amini, R. B. Blakestad, J. Britton, J. P. Home, W. M. Itano, J. D. Jost, E. Knill, C. Langer, R. Ozeri, N. Shiga, and D. J. Wineland. Simplified motional heating rate measurements of trapped ions. *Physical Review A - Atomic, Molecular, and Optical Physics*, 76(3):033411, sep 2007.
- [139] Donald C. Morton. Atomic Data for Resonance Absorption Lines. II. Wavelengths Longward of the Lyman Limit for Heavy Elements. *The Astrophysical Journal Supplement Series*, 130(2):403–436, oct 2000.
- [140] Peng Yi Zhao, Zhuan Xian Xiong, Jie Liang, Ling Xiang He, and Bao Long Lu. Magneto-optical trapping of ytterbium atoms with a 398.9 nm laser. *Chinese Physics Letters*, 25(10):3631–3634, oct 2008.
- [141] C. E. Habermann and A. H. Daane. Vapor Pressures of the Rare-Earth Metals. *The Journal of Chemical Physics*, 41(9):2818, jul 2004.
- [142] A. M. van der Spek, J. J. L. Mulders, and L. W. G. Steenhuisen. Vapor pressure of rubidium between 250 and 298 K determined by combined fluorescence and absorption measurements. *JOSA B, Vol. 5, Issue 7, pp. 1478-1483*, 5(7):1478–1483, jul 1988.
- [143] Dipankar Das, Sachin Barthwal, Ayan Banerjee, and Vasant Natarajan. Absolute frequency measurements in Yb with 0.08ppb uncertainty: Isotope shifts and hyperfine structure in the 399-nm S01→P11 line. *Physical Review A - Atomic, Molecular, and Optical Physics*, 72(3):032506, sep 2005.
- [144] M. L. Harris, C. S. Adams, S. L. Cornish, I. C. McLeod, E. Tarleton, and I. G. Hughes. Polarization spectroscopy in rubidium and cesium. *Physical Review A - Atomic, Molecular, and Optical Physics*, 73(6):062509, jun 2006.

- [145] K Pahwa, L Mudarikwa, J Goldwin, 15 H Wang, P L Gould, and W C Stwalley. Polarization spectroscopy and magnetically-induced dichroism of the potassium D₂ lines. *Optics Express*, Vol. 20, Issue 16, pp. 17456-17466, 20(16):17456–17466, jul 2012.
- [146] Shaobing Zhu, Tao Chen, Xiaolin Li, and Yuzhu Wang. Polarization spectroscopy of ¹S₀ & ¹P₁ transition of neutral ytterbium isotopes in hollow cathode lamp. *JOSA B*, Vol. 31, Issue 10, pp. 2302-2309, 31(10):2302–2309, oct 2014.
- [147] Technical information wavelengthmeter ws8-2. <https://www.hightfinesse.com/en/wavelengthmeter/wavelengthmeter-further-information/technical-information-wavelengthmeter-ws8-2.pdf>.
- [148] D A Howe. Interpreting Oscillatory Frequency Stability Plots. In *IEEE International Frequency Control Symposium and PDA Exhibition*, 2002.
- [149] William Riley and David Howe. Handbook of frequency stability analysis, 2008-07-01 00:07:00 2008.

Other material separate from the body of the thesis and submitted as part,
or in support of the thesis.